UNIVERSITÁ DEGLI STUDI DELL'INSUBRIA
Dipartimento di Scienza ed Alta Tecnologia

Neutrino emission from Blazars

Candidate:
Chiara Righi

Supervisor:
Dr. Fabrizio Tavecchio

PhD. in Physics and Astrophysics
XXXI Cyle
22 Febbraio 2019

Dedicato a te, con il nostro motivetto della colazione e con le nostre passioni comuni che continuano a crescere anche se manchi ogni giorno. Dedicato anche a te che mi apettavi per giocare e mi hai insegnato a leggere e scrivere.....e tentato con i giorni della settimana. Dedicato spotrattutto a te, da cui non smetto mai di imparare ed alle nostre serate a cercare di capire come allineare il telescopio. Dedicato a te, che mi fai ridere con poco, che mi fai sentire vecchia ma mi rendi giovane ogni volta che parliamo. Dedicato a noi, che il nostro "pain" ogni tanto diventa "ehi!"

Overview

During the last decade, multi-messenger astronomy has become increasingly relevant for the astrophysical community. In this context the discovery of PeV neutrinos by IceCube in 2012, in clear excess to the expected atmospheric flux at very-high energy ($\gtrsim$ 100 TeV), marked the beginning of the high-energy neutrino astrophysics era. Differently from photons, neutrinos can carry information about the core of the astrophysical objects that produce them, giving us a better understanding of the internal composition of their sources. Moreover neutrinos are generally associated with hadronic interactions in their sources, so the detection of high-energy neutrinos can unravel the origin of the cosmic rays and ultra-high energy cosmic rays. The origin of these neutrinos is still an open issue. Their weak interaction makes it difficult to accumulate enough statistical evidence to uniquely identify their sources. Even with a km^3 detector, the number of expected astrophysical neutrino rate is not larger than ~ 10 events per year. At present, the IceCube detector, with a volume of 1 kilometer cube, detected ~ 80 neutrinos above 60 TeV since 2010. Waiting to accumulate enough events, several source classes have been considered as possible cosmic-rays accelerators and then high-energy neutrino emitters.

The quasi isotropic distribution of these events in the sky allows one to reject the hypothesis of an exclusively galactic nature of these neutrinos. Indeed, some analyses suggested two components, a galactic one at low energy (< 100 TeV) and an extragalactic one at higher energies. Among the possible extragalactic neutrino sources, Blazars start to stand out.

Blazars are associated to active galactic nuclei hosting a relativistic jet oriented close to our line of sight. The presence of jets and the strong non-thermal emission up to the TeV band makes them natural accelerators of particles. A characteristic of these objects is the variability of the emission at all frequencies. This gives information about the physical processes of the jet and the relation between different energy emission. The physical interpretation of their spectral energy distribution (SED), characterized by a peak at low energy (peaking in the optical-UV band) and a peak at high energy (in the γ-ray band), is still under debate. In fact, while the low energy emission is well described by the synchrotron emission of the relativistic leptons inside the jet, the high energy peak can be

described with hadronic or leptonic models. In September 2017 the spatial coincidence between a neutrino event detected by IceCube, with a good angular resolution, and a blazar, TXS 0506+056, was observed for the first time. This event is even more intriguing because of the high-state emission in γ-ray band of this blazar. Since then, the whole astroparticle community started to investigate these kind of objects as neutrino emitters. A multiwavelength campaign and several theoretical interpretation models were developed in the last year for the potential neutrino counterpart TXS0506+056.

During the three years of my PhD, I focused my attention on the study of blazar objects as neutrino emitters. In this thesis all my work on this topic is presented.

Chapter 1 describes the mechanisms of high-energy neutrino production and the main characteristics of detection, presenting IceCube telescope.

Chapter 2 presents the main source candidates in which neutrino emission can occur. In this set of astrophysical classes we focus on active galactic nuclei (AGN) and in particular on Blazars, describing the geometry and the radiation emission models (*Chapter 3*).

Chapter 4 shows the link between neutrino production and Blazars. We present the main SED interpretation models that describe both electromagnetic and neutrino emission. We describe in detail the channel to produce neutrinos in jets and then we show simple results for this phenomenon. Finally, in the last Chapters I focus on my main contributions to the neutrino emission modelling and observations. In particular *Chapter 5* shows the spine-layer scenario, a model of a structured jet that allows to consider Blazars as main neutrino emitters. Here comes my first contribution on the correlation between γ-ray emission and neutrino emission from Blazar.

Chapter 6 focuses on the study of a sample of BL Lac objects (a subclass of Blazars) detected above 50 GeV by the γ-ray Fermi satellite whose position in the sky is consistent with events recorded by IceCube. For this sample of sources we performed an observational optical and X-ray campaign and we built the SED and light-curve to search similar features between the different BL Lac candidates and TXS0506+056 source.

Given the lack of a clear detection of neutrinos from the brightest γ-ray BL Lac (as Markarian 421 or Markarian 501) after $\sim$ 8 years of acquisition by IceCube, together with the unexpected nature of TXS0506+056 as neutrino source, we proposed an alternative scenario in *Chapter 7*. Our hypothesis stands on a *"new"* photon populations as target to trigger the $p\gamma$ interaction, in particular the photons involved in the neutrino production come from the accretion flow.

We dedicate *Chapter 8* to discuss the main results of the thesis and the new prospects in this new field of astrophysics.

Table of contents

Chapter 1

Astrophysical Neutrinos

Of all particles, neutrinos are ideal astronomical messengers because of their weak propensity to interact with matter and their charge neutrality, which allow them to travel through the space without deflection. Differently from photons, neutrinos can carry information about the core of the astrophysical objects that produce them giving us a better understanding of the internal composition of their source (e.g. the case of solar neutrinos). Moreover they do not suffer absorption, unlike the case of γ-rays, which interact with the Cosmic Microwave Background (CMB) and Extragalactic Background Light (EBL), during their cosmic propagation. Neutrinos are generally associated with hadronic interactions in their sources, so the detection of high-energy neutrinos can unravel the nature of the cosmic rays. High-energy neutrinos are produced in sources where cosmic rays are accelerated, and their ability to travel without deflection by magnetic field makes them the perfect tracers of cosmic-rays sources. Unfortunately, their weak interaction makes difficult to detect them and then to identify their sources. Neutrinos are revealed when some secondary particle or radiation is produced in their (weak) interaction with some target. A *neutrino event* is defined by the observation of the charged lepton associated to the specific type of neutrinos by charged current (CC) interactions, or the hadronic (or nuclear) transformation caused by neutral current (NC) interactions.

Fig. **??** shows different astrophysical neutrino components. During this thesis we will focus on the high-energy neutrino, above 100 GeV. To observe these kind of neutrinos, in 1960 Markov proposed to *set up apparatus in an underground lake or deep in the ocean in order to separate charged particle directions by Cherenkov radiation.* Following this suggestion, at present, three high-energy neutrino detectors are currently in operation and one under construction: Baikal, ANTARES, IceCube and Km3NeT. With this detectors, a large volume of deep natural water (or ice), instrumented with light sensors, was transformed

into a Cherenkov detector that collects the light emitted by high energy particles produced after the interaction of neutrinos with matter.

In this chapter we provide a brief summary of the main characteristics of high-energy neutrino and its detectors.

1.1 Neutrino production

Cosmic rays (CR) have been studied for more than a century. We detected them up to ultra-high energies (10^7 TeV) but, due to the scrambling induced by cosmic magnetic field, we still do not know their sources and the acceleration mechanism. CRs can collide with a target producing unstable mesons, that decay giving neutrinos and gamma rays[1]. The two most plausible neutrino production mechanisms are the collision between accelerated protons and target protons (pp interaction) and the interaction between accelerated protons and target photons ($p\gamma$). Depending on the environment, one mechanism can be dominant with respect to the other (see **?**).

1.1.1 pp vs. $p\gamma$ mechanism

The interaction of an accelerated CR with gas or radiation produces pions that subsequently decay into neutrinos and gamma-rays. To study the relation between neutrino energy E_ν, gamma-rays energy E_γ, and the energy of cosmic rays E_p, it is necessary to focus on the pion decay and then on the difference between pp and $p\gamma$ interaction.

π channel

The main decay channels of charged pions are:

$$\pi^+ \to \mu^+ \nu_\mu \to e^+ \bar{\nu}_\mu \nu_\mu \nu_e;$$

$$\pi^- \to \mu \bar{\nu}_\mu \to e^- \bar{\nu}_\mu \nu_\mu \bar{\nu}_e$$

while the neutral pion decays in:

$$\pi^0 \to \gamma + \gamma.$$

we refer to these photons as pionic photons to distinguish them from others. Each neutrino from pion decay takes, an average, 1/4 of the pion's energy (see **?** for a complete handling).

[1] Even if *cosmic rays* are composed by atomic nuclei and protons, we will refer frequently to CR as "proton".

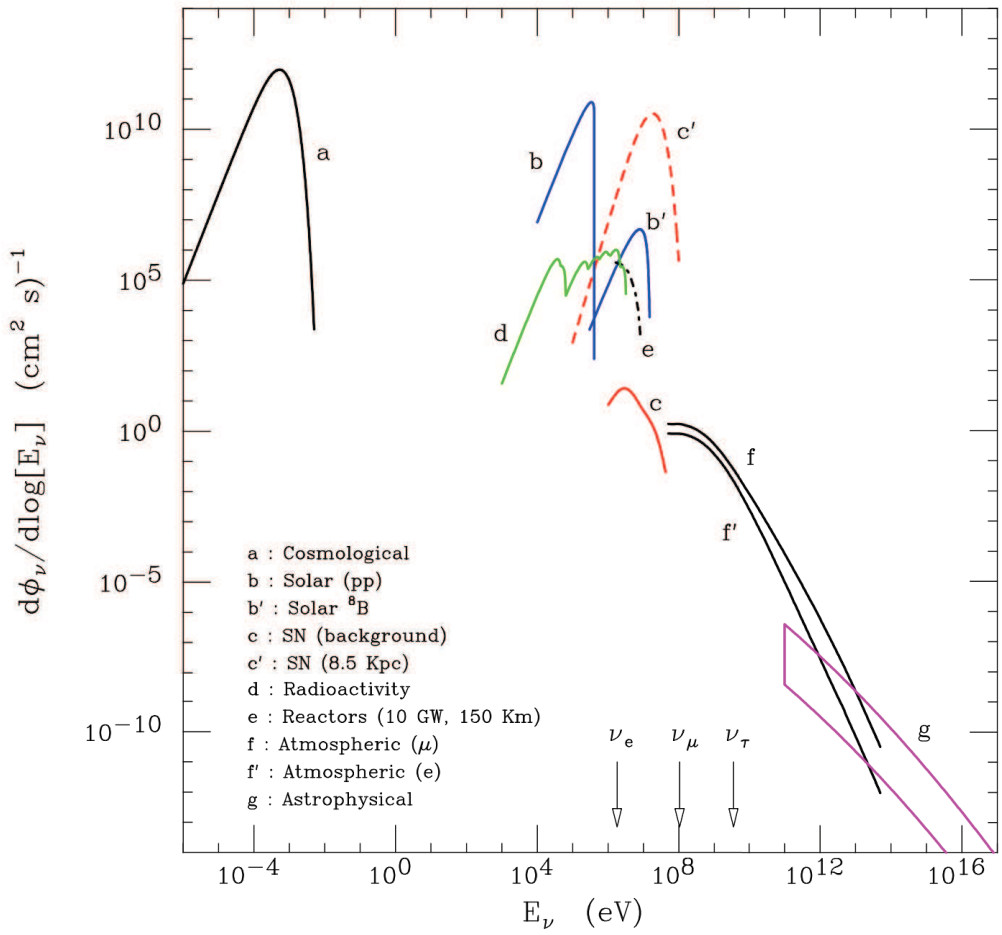

Fig. 1.1 Flux of various neutrino components at the surface of the Earth. The line that refers to cosmological neutrinos (e.g. relic of Big Bang) assumes that the neutrino mass is vanishing. The line that refers to Supernova neutrinos describes only ν_e. Different neutrino species have similar spectra, with differences difficult to appreciate in the figure. The line that describes geophysical neutrinos includes the ^{238}U and ^{232}Th decay chains (the flux weakly depends on geographical location). The atmospheric neutrino fluxes are calculated for the Kamioka location. Only the lowest energy part depends on the location. A range of prediction for the flux of astropysical neutrinos is shown. A more detailed atmospherical and astrophysical components are shown in fig. **??**. *Credits:* **?**.

$p\gamma$ channel

This interaction is considered the main channel of pion production inside the relativistic jet of active galactic nuclei (see Sec.**??** for other details). However other *alternative* scenarios are presented. In fact the neutrino production inside the jets could happen through the pp channel, when relativistic protons accelerated inside the jet interact with gas of clouds or stars that pass through the jet itself (see e.g. **?**, **?** for details). In the following a schematic selection of the main characteristics of this channel:

Energy threshold: The threshold for the $p+\gamma \to N+\pi$ reaction[2], could be found from kinematics considerations. Introducing the proton and photon four momenta, $P_p = (E_p, \overrightarrow{p_p})$, $P_\gamma = (\varepsilon, \overrightarrow{p_\gamma})$, and transforming to the center-of-mass frame, we could write an expression for the absolute value of the total four-momentum before and after the reaction. Before the reaction the invariant total momentum squared in the lab frame is:

$$s = (P_p + P_\gamma)^2 = m_p^2 + 2E_p\varepsilon(1-\beta\cos\theta)$$

while after the reaction (in the center of mass frame)

$$s = (P_N + P_\pi)^2 = m_N^2 + 2m_N m_\pi + m_\pi^2$$

Note that the expression is in the center-of mass frame and both nucleon and pion are at rest after the reaction. Equating the two expressions for the conserved s and assuming $\cos\theta = -1$ (assuming head-on collision), we find the condition for the possibility of the pion production

$$E_{p,th} = \frac{m_N m_\pi (1 + m_\pi/2m_N)}{2\varepsilon} \simeq 10^{17}\left[\frac{\varepsilon}{1\text{eV}}\right]^{-1}\text{eV} \tag{1.1}$$

Cross section: The cross section of the channel $p\gamma$ is composed by different contributions. The mechanism can produce the baryon Δ^+ that decays into $\pi^+ n$ (1/3 of cases) or $\pi^0 p$ (2/3 of cases). This channel result into a broad resonance which is the main contribution to the cross section close to the energy threshold ($\sim$ 150 MeV). Anther contribution at these energies is the *direct* production of pions that contribute nearly 30% to the total $\sigma_{p\gamma}$ from $\sim$ 250 MeV to $\sim$ 1GeV. There are also the *multi-pions* productions and the *diffraction* that give contributions at high-energies ($\geq$ 1GeV).

[2]With N,π equal to p,π^0 or n,π^+ respectively.

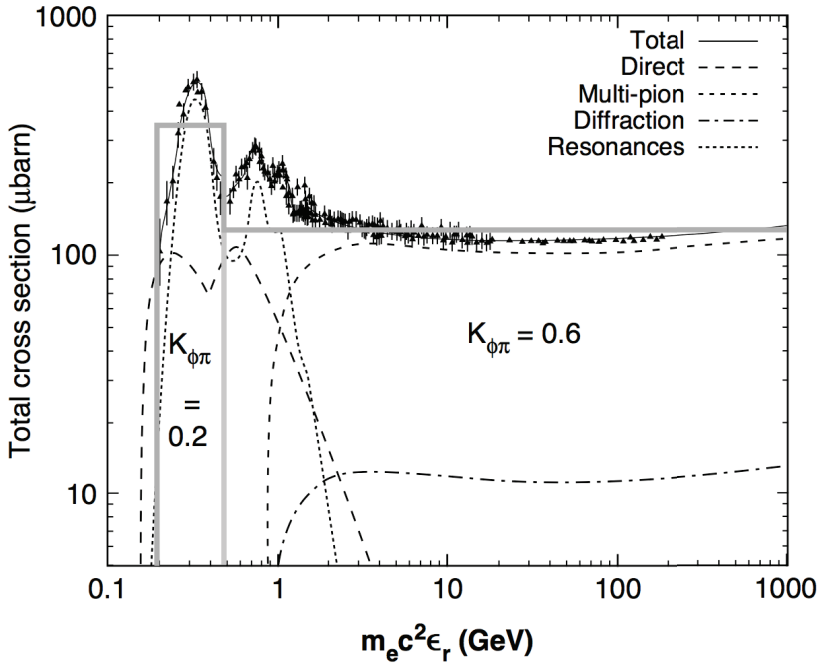

Fig. 1.2 Cross section of $p\gamma$ channel. Thick lines shown the two step-function approximations used in analytic expression. *Credits:* **?**.

Figure **??** show the total inelastic photomeson production cross section for the $p\gamma$ channel as a function of the photon's energy in the proton rest frame. **?** derive an analytic expression for the total and secondary production cross section approximating the photopion process as the sum of two channels. In this approximation, the low-energy step function takes into account the Δ resonance and the direct single-pion production (thick lines between 200 – 500 MeV in figure **??**). Here the cross section is approximated with $\sigma_{p\gamma} = 3.4 \times 10^{-28}\text{cm}^{-2}$ and the inelasticity factor $K_{p\gamma} = 0.2$[3]. At high-energies (> 500 MeV) the other two components are dominant and the cross section is approximated to $\sigma_{p\gamma} = 1.2 \times 10^{-28}\text{cm}^{-2}$, while $K_{p\gamma} = 0.6$.

A more detailed scenario is discussed in **?** and **?**.

Energy relations: the average energy for each neutrino turns out to be about the 5% of the primary proton's energy.

$$E_p \simeq 20 E_\nu$$

[3] In an inelastic collision the proton loses, on average, a fraction $K_{p\gamma}$ of its original energy, hence $K_{p\gamma}$ is the inelasticity of the collision.

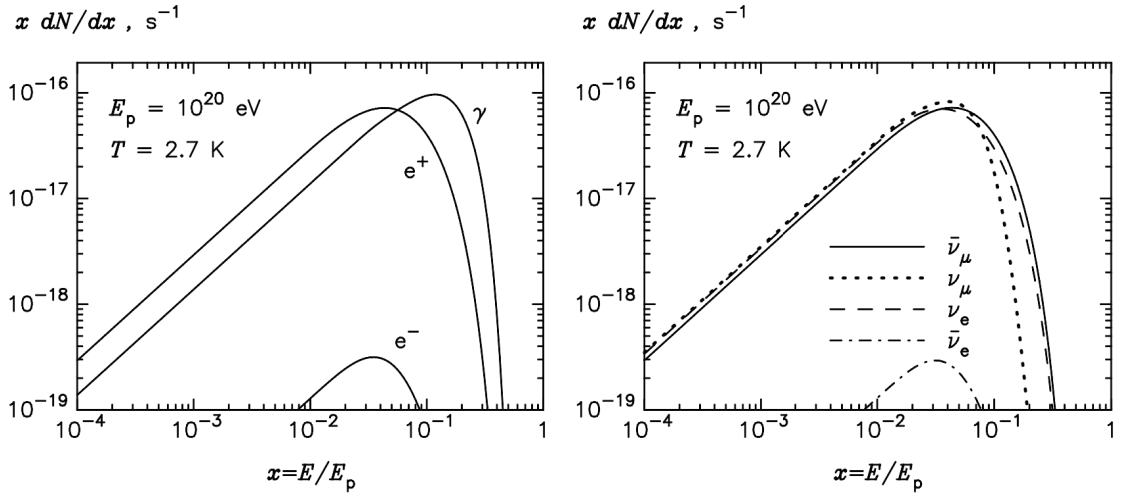

Fig. 1.3 The energy spectra of stable products of photomeson interactions of a proton of energy $E_p = 10^{20}$ eV with the 2.7 K cosmic microwave background radiation. Left panel: gamma-rays, electrons, and positrons. right panel: electron and muon neutrinos and antineutrinos. *Credits:* **?**.

The factor 20 comes from simple considerations. In fact, it is simply related to the fact that, on average, the pion takes 1/5 of the proton energy and each one of the four final particles earns the same energy. The resulting stable particles from the $p\gamma$ reactions obtain 1/20 of the energy of the relativistic proton. Fig. **??** supports the previous considerations. It show the energy spectra of γ-rays and electrons (left panels) and all neutrino types (right panels) produced by protons of energy 10^{20} eV interacting with blackbody radiation of temperature $T = 2.7$ K. The results depend only on the product $E_p \times T$, therefore they can be easily rescaled to a blackbody radiation of an arbitrary temperature. The e^+, e^- and ν spectra peak at ~ 0.05 of the proton energy. The γ-ray spectrum peaks at ~ 0.1 of the proton energy because of γ-rays come from the π^0 decay, and the pion energy is to be shared only by two particles (the two γ-rays) (see **?**).

Neutrino Spectrum: the spectrum of neutrinos produced by $p\gamma$ interaction is not dependent only on the spectrum of the primary protons. Because of the threshold in this kind of process, eq. **??**, the spectrum of photon target is relevant for the calculation of neutrino spectra. We will show, in fact, that the factor photomeson production efficiency $f_{p\gamma}$ (see Section **??** for details) is dependent on the target photon density through an integral in which the lower limit is the energy threshold that depends on the proton energy (for more details see **?** and **?**).

pp channel

In pp interaction mostly pions are created, with a smaller contribution of kaons (for more details see pp.278 **?**, **?** and **?**).

Energy threshold: From analogue kinematic considerations to those of the previous section, the energy threshold of this channel is

$$E_{p,th} = m_p\Big(1 + \frac{m_p^2 + 4m_\pi m_p}{2m_p^2}\Big); \tag{1.2}$$

which corresponds to a proton kinetic energy of:

$$E_{kin} = E_{p,th} - m_p \simeq 290\text{MeV}$$

Cross section: The cross-section of this reaction is also determined by the strong interaction and it is close to the geometrical cross-section of the proton, $\sigma_{pp} \simeq 4 \times 10^{-26}$ cm, depending on (growing with) the proton energy.

Energy relations: Similarly to the $p\gamma$ channel, the average energy for each neutrino turns out to be about the 5% of the primary proton's energy.

$$E_p \simeq 20E_\nu$$

Neutrino Spectrum: The shape of the neutrino spectra is, generally, the same of the accelerated protons spectrum (**?**).

1.2 Detecting High-Energy Neutrinos

Once produced, neutrinos do not take part in further interactions. Due to their cross-section (see fig. **??**), they substantially pass through the extragalactic background light (EBL) without interact. However, the flavor composition of the neutrinos that arrive at the Earth is not equal to the flavor composition at the emission because of the effects of flavor oscillations. The neutrino flavor composition at the source is approximately $\{\nu_e : \nu_\mu : \nu_\tau\} \approx \{1 : 2 : 0\}$, but the composition arriving at the detector is expected to be approximately an equal mix of ν_e, ν_μ and ν_τ, $\{1 : 1 : 1\}$ (**?**).

High-energy neutrinos interact predominantly with matter via deep inelastic scattering off nucleons. The neutrino-quark scattering happens through the exchange of a boson

($W^{\pm}$ or Z^0). We referred to *charged current* (CC) if the interaction happens through the $W^{\pm}$, while the exchange of a Z^0 leads the so called *neutral current* (NC) interaction (**?**).

1.2.1 Neutral current

The NC interaction leaves the neutrino state intact and the neutrino transfers a fraction of its energy to a nuclear target. The struck nucleus does not remain intact and its high-energy fragments typically initiate hadronic showers in the target medium. All neutrinos show the same behaviour interacting via NC; therefore with this process it is not possible to distinguish the flavor of the incoming neutrino. The average deposited energy in NC interactions is about 1/4 of the primary neutrino's energy, whereas the other part of the energy is carried away by the outgoing neutrino and it is not detectable. The cross section σ_{NC} of the interaction is shown in Fig.**??**. The neutrino-nucleon interaction is always higher than the anti-neutrino-nucleon one. The separation between the two channel is higher at lower energies (for more details see **?** or **?**).

1.2.2 Charged current

In a CC interaction a charged lepton that shares the neutrino flavor is produced. The average energy fraction transferred from the incoming neutrino to the charged lepton (e^-, μ^- or τ^-) is at level of 80% (about 3/4 of the ν energy) at these energies. The inelastic CC cross section on protons is at the level of 10^{-33} cm^2 at a neutrino energy of 10^3 TeV and it grows with the neutrino energy (see Fig.**??**, blue solid and dashed lines) (**?**, **?**).

Once generated, the three leptons have different behaviours:

Electron: High-energy electrons lose most of their energy by radiation. During their path (few meters), most of the energy is spent in the production of electromagnetic shower and only a small fraction is dissipated (transferred to the nuclear targets and released as hadronic shower).

Muon: High-energy muons can travel for some kilometers producing a so-called track. The average muon energy-loss rate can be describes as:

$$-\frac{dE_\mu}{dX} = \alpha + \beta E_\mu \tag{1.3}$$

where the coefficient α represents the ionization losses while βE_μ is the radiative term. X is defined as $X \equiv \rho(s)ds$, where ρ is the Earth density (in g cm^{-3}) and depends on the path

inside the Earth s, and ds is the length between the detector and the place of interaction νN (see Figure **??**). Both coefficients α and β depend on the energy; at TeV-PeV range they are respectively equal to $\simeq 2 \cdot 10^{-3}$ GeV cm^2 g^{-1} and $\simeq 5 \cdot 10^{-6}$ cm^2 g^{-1}. From equation **??** we can derive the muon energy after propagation on X (in g/cm^2):

$$E_{\mu,after} = (E_\mu + \frac{\alpha}{\beta})e^{-\beta X} - \frac{\alpha}{\beta}$$

In the same way we can derive the amount of matter needed to obtain $E_{\mu,after} = 0$:

$$X(E_{\mu,after}, E_\mu) = \frac{1}{\beta}\ln\frac{E_\mu + \alpha/\beta}{E_{\mu,after} + \alpha/\beta}$$

A muon with energy of $E_\mu \sim 10^6$ GeV loses all its energy in a range of ≈ 20 km (**?**).

Tau: The behaviour of a τ at high-energy is similar to e^-. Before decaying the tau travels for $\simeq 50$ m, and the losses are due to electromagnetic showers and hadronic showers due to dissipation with nucleons. A characteristic of a ν_τ event is the possibility to observe both the cascade due to the (anti)neutrino-nucleon interaction, and after few meters the tau decay cascade. This process is called "double bang". Furthermore the τ decay produces neutrinos, that carry away part of the energy (about 20% of the τ energy is not detectable (see **?**, **?**, **?** for details).

1.3 The neutrino telescopes

One particularly effective method to detect neutrinos is to observe the radiation of the hadronic cascade and the Cherenkov radiation given off by secondary charged particles produced in CC and NC interactions that travel faster then the speed of light in the medium (**?**).

The modern high-energy neutrinos detectors consist of strings of photo-multiplier tubes (PMT) distributed inside a transparent medium (water or ice). Since kilometer-scale detector is required, the PMT are located in natural Cherenkov media such as the water of a lake or a sea, or ice. At present there are three neutrino detectors operating in the world and one under construction:

- IceCube: located at the South Pole (detail in the next section) (**?**);
- ANTARES: located in the Mediteranean Sea, with a volume of 0.03 Km^3 (**?**);
- Baikal: a 1.5 Km^3 detector condutiong research in Lake Baikal (Russia) (**?**);

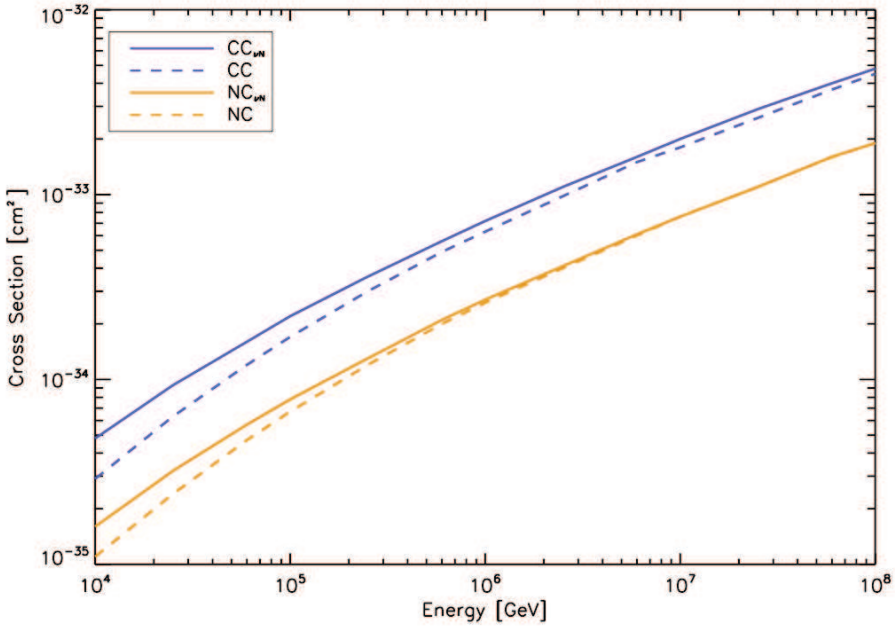

Fig. 1.4 Cross section for νN (solid lines) and $\bar{\nu} N$ (dashed lines) interactions. For both interactions the charged current (blue lines) and neutral current (orange lines) interactions are shown.

- Km3NeT: a new telescope under construction in the Mediterranean Sea that will have a volume of about 1 km^3. There are two different projects in construction: ARCA telescope, focuses on the high-energy neutrinos, and ORCA designed to study neutrino properties exploiting neutrinos generated in the Earth's atmosphere (**?**).

1.3.1 Why big telescopes?

The expected number of neutrino events depends upon the flux of high energy neutrinos F_ν, the number of target N and the cross section of deep inelastic scattering σ. Considering **?**, the upper bound of the high energy neutrino flux (all flavor) was expected to be order of:

$$\frac{d\phi}{dE} \simeq 5 \times 10^{-8} \frac{1}{\text{GeV cm}^2 \text{ sec sr}} \left(\frac{E}{1 \text{ GeV}}\right)^{-2}$$

Therefore, the flux in $T = 1$ year[4] is obtained by the following integral:

$$F_\nu \simeq \int_{E_{\text{min}}}^{E_{\text{max}}} 4\pi \times \frac{d\phi}{dE} \times T dE$$

[4]Note that 1 years $\simeq \pi \times 10^7$ s.

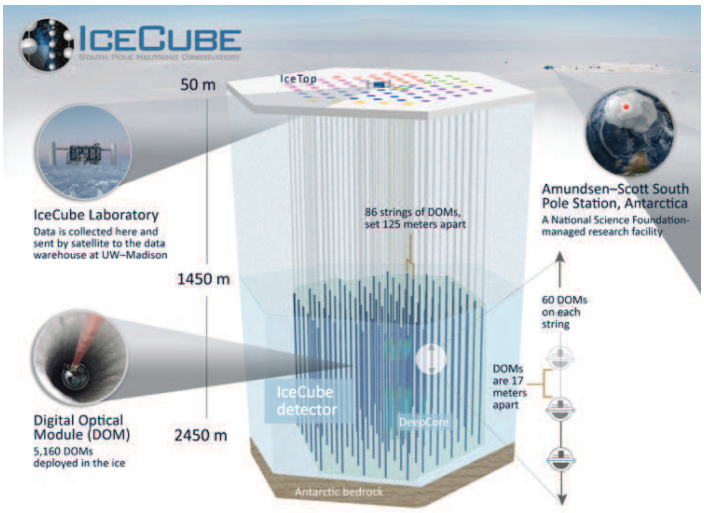

Fig. 1.5 Cartoon of IceCube detector. *Credits:* IceCube collaboration.

If we consider $E_{\min} = 100$ TeV and $E_{\max} = \infty$, the flux is equal to $F_\nu \simeq 2 \times 10^{-4}\ \nu/\mathrm{cm}^2$ year. The cross section of deep inelastic scattering at 100 TeV is order of $\sigma \approx 10^{-34}\ \mathrm{cm}^2$ (see figure **??**, then the the number of target is given by

$$N(V) = \frac{\rho V}{m_N} = 6 \times 10^{38} \frac{\mathrm{V}}{\mathrm{km}^3}$$

where ρ is the density of the detector's target that we assume $\rho = 1\ \mathrm{g\ cm}^{-3}$ that is exact for water and it is a good approximation for ice. m_N is the nucleon mass and it is equal to $\sim 1/6 \times 10^{-23} g$. V is the volume of the detector and it is our free parameter. Therefore the expected number of events above 100 TeV per year is expected to be:

$$F \times \sigma \times N(V) \simeq 10 \frac{\mathrm{events}}{\mathrm{years}} \frac{\mathrm{V}}{\mathrm{km}^3}$$

This is a rough and optimistic calculation (let us remember that we are using an upper bound on the high energy neutrinos flux). It is useful to have an idea of the volume required to observe high energy neutrinos.

This show that 1 km^3 is required to have at least few event per year.

1.3.2 IceCube

The IceCube detector (**?**) is located 1450 m below the geographic South Pole. It is a cubic kilometer of ice instrumented with 5160 digital optical modules (DOMs). Each DOM consists of a glass sphere containing PMT arranged along 86 strings (see Fig.**??**). Each

string is buried into the ice using hot water drills. Construction began in 2005, when the first IceCube string was deployed and collected enough data to verify that the optical sensors worked correctly.

The majority of the strings are located at 125 m of distance each other covering 1 km^2 on the surface. For each string, DOMs are attached every 17m. These distances are selected, through MonteCarlo simulations, in order to maximise the efficiency of the instrument. The parameters that fix these distances are, among others, the path of the leptons that produce Cherenkov light into the detector and the transparency of the material of the detector (water, or ice in this case).

At the surface IceCube is equipped with an array of 160 ice filled tanks (named *IceTop*) each one instrumented with two DOMs, that detect extensive atmospheric air showers induced by cosmic rays. The purpose of IceTop is to detect cosmic-ray air showers, with a threshold of about 300 TeV. This is useful in order to study the cosmic-ray flux and composition, but also as veto for the underground detector in order to reduce the background.

Atmospheric neutrinos are, in fact, the main source of background for the main target of IceCube, the study of astrophysical neutrinos. However, atmospheric neutrinos are a potential signal for other physics items, like the study of neutrino oscillations. In order to study also atmospheric neutrinos properties the detector was more densely instrumented towards its bottom using more efficient detector geometry for energies < 100 GeV. The sub-array is indicated in Fig.**??** *DeepCore*. DeepCore is composed by 6 strings with a distance of 72 m each other and the DOMs attached every 50 m (**?**).

The present configuration of the telescope was concluded on December 18, 2010. However, during the construction period, the strings already lowered into the Antarctic ice allowed publication of physics results for intermediate detector configurations (IC22 with 22 strings, IC40 with 40 strings and, etc. until IC86).

Neutrino Signature

Reconstruction of events depends on accurate timing (< 3 ns) and on the ability to measure the amount of Cherenkov light generated along the tracks of charged particles produced by the neutrino interactions. Basically, the arrival time of photons at the DOMs determines the trajectory and the amount of light determines the deposited energy. According to the flavour of the incoming neutrino and of the interaction, there are different categories of events inside the detector.

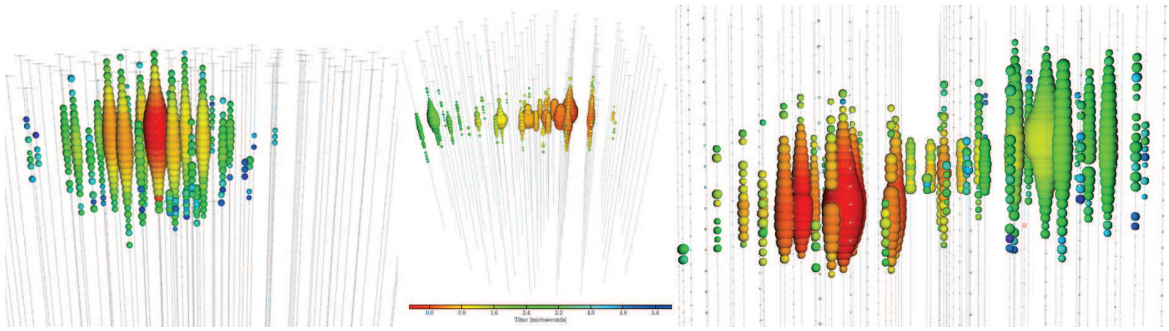

Fig. 1.6 IceCube HESE events. The grey string corresponds to the detector. Color and size of sphere corresponds to the arrival time (from red to green) and to the released energy (big sphere correspond to high energy) respectively. From left to right: Cascade, Muon track and simulation of a double bang (tau neutrino) event.

HESE: The high-energy neutrinos interacting inside the detector generate the so-called high-energy starting event (HESE) (**?**). This kind of event can be generated from any neutrino (ν_e,ν_μ,ν_τ). While ν_μ neutrinos can interact via CC channel inside the detector but the corresponding muon can escape generating a track, the other case of HESE events have the advantage that most of the neutrino energy remains inside the detector and this allows us to measure it with a $10-15\%$ resolution. In particular this class of events allows to measure the hadronic cascade from NC interaction, the electromagnetic and hadronic cascades from $\nu_{e,\mu}N$ CC interaction and the so-called double bang from $\nu_\tau N$ CC interaction. Note that in case of $\nu_\mu N$ CC interaction part of the energy is loss because of the long path of the generated muon. However the track generated by the muon allows us to have a better reconstructed direction of the incoming neutrino. Also the only way to recognise a ν_τ is to observe the double vertex of interaction into the detector. Since high-energy (> 100 TeV) tau neutrino production in the Earth's atmosphere is negligible, a tau neutrino detection would confirm the astrophysical origin of the observed neutrino signal and would help improve the precise measurement of astrophysical neutrino flavor ratios. At present IceCube Collaboration presented two tau neutrino candidate events identified in dedicated search (contributions at Neutrino Conference in Heidelberg, 2018).

Fig.**??** shows the three event classes forming part of HESE events. The colors represent the arrival time of the Cherenkov radiation (from red to green). The dimension of the spheres represents the deposited energy to the DOMs (larger dimension = more quantity of radiation observed by PMTs). On the left a typical cascade (that can be generated by NC interaction or $\nu_e N$ CC event) is shown. In the middle, a muon track with the vertex of the interaction contained in the detector visible. The right image shows a simulation of a

double bang events. The two vertex, one coincident with the ν_τ interaction and the other with the τ decay, are visible.

Throughgoing muons: Traditionally, neutrino searches focused on the observation of muon neutrinos that interact primarily outside the detector to produce kilometer-long muon tracks passing through the detector. The advantage of these events is that the effective volume of interaction for the ν_μ is higher than the HESE events. There are two conditions to have this kind of event:

- the interaction vertex should happen close enough to the detector, so that the muon arrives in the detector with sufficient energy to be seen;
- the muon should arrive from the region under the detector, namely, the region where the atmospheric muon background is rare or absent; in fact, the flux of atmospheric muons crossing the detector exceeds by several order of magnitude the flux of muons originated by cosmic and atmospheric neutrinos.

The muon tracks above ~ 100 TeV, are characterised by good reconstructed direction, with uncertainty around 1° on ice, that it can be less in water. The main limiting factor in the ice to improve the angular resolution is the scattering of the light by air trapped in the ice. The consequence is that up-going muon events are used for identification of the source (**?**).

Effective Area

The expected number of events per unit of time, dN, depends on the neutrino flux of the source $d\phi(E_\nu)$, and the effective area of the instrument $A_{eff}(E_\nu, \Omega, l)$. The effective area depends on the neutrino energy E_ν, on the direction of the incoming neutrino Ω and the neutrino flavor $l = e, \nu, \tau$. Each Collaboration releases a mean effective area calculated using Montecarlo simulations. However, it is possible to give an estimate of the effective area considering the following simplified analytical expression:

$$A_{eff}(E_\nu, \Omega, l) \approx e^{-\tau(\Omega, E_\nu, l)} N_n \sigma(E_\nu, l) \varepsilon(E_\nu) \tag{1.4}$$

where

- τ takes into consideration the neutrino flux attenuation and depends on the path s inside the Earth of the neutrino (and so it depends on the zenith angle Θ); it corresponds to:

$$\tau(\Omega, E_\nu, l) = \int_0^{s(\Omega)} \frac{\rho(s')}{m_p} \sigma(E_\nu, l) ds' \tag{1.5}$$

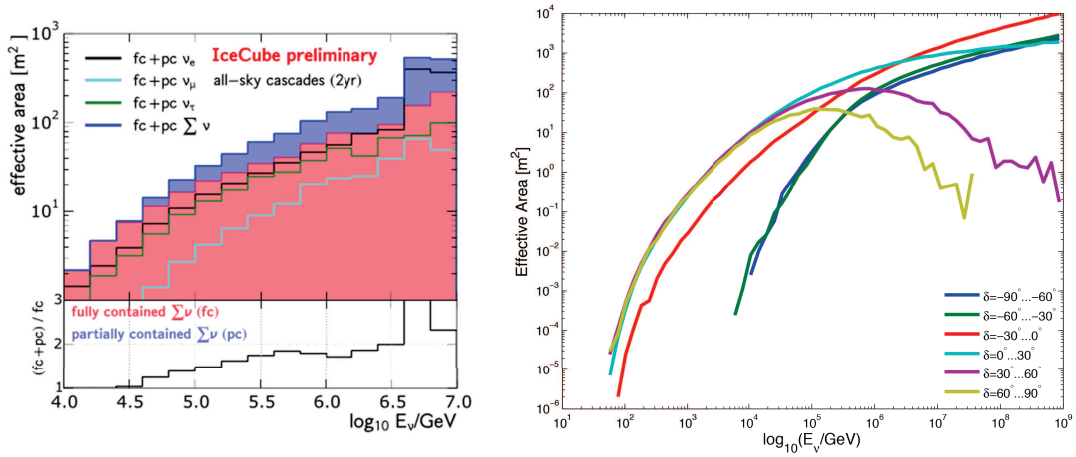

Fig. 1.7 Effective area for different kind of events in IceCube. *Left panel*: 2-year effective area of HESE event for combined fully and partially contained cascades (**?**); *Right panel*: Effective area of the complete IC86 for ν_μ point sources (**?**). Different declinations δ on the sky are plotted separately. The effect of the opacity is visible for $\delta > 30°$ and $E > 100$ TeV.

- The number of target nucleons N_n is given by $A\frac{\rho(s)}{m_p}ds$, where m_p is the mass of proton, A is the detector projected area (which in principle depends on the zenith angle) that we approximate to $\simeq 1\text{km}^2$. ρ is the Earth density (in g cm^{-3}) and depends on the path inside the Earth s and ds is the length between the detector and the place of interaction νN. Finally s and ds depends both from Ω. Figure **??** shows a cartoon of the incoming neutrino passing through the Earth and interacting a distance ds outside the detector.

- $\varepsilon(E_\nu) \leqslant 1$ is the efficiency of the detector. it takes into account the effective volume of the detector and the sensitivity of the instrument and the cuts applied during the analysis of the event.

Fig. **??** shows the effective area of IceCube detector for different neutrino events. In the left panel the all sky 2-year effective area of HESE events for different neutrino flavours (e: black line, μ: light blue line, τ: green line) is shown (**?**). The ν_μ cascade effective area is lower than the electronic and "tauonic" one because of selection criteria used in the analysis (see **?** and **?** for more details). **?**, in fact, reports that "*the effective areas for ν_e and ν_τ are higher than for ν_μ as this analysis was optimized for cascades and removed muon tracks*". The right panel, instead, shows the tracks effective area at different declination source bins (**?**). In this plot the contribute of the IceTop veto is clearly visible for the low declination angles ($-90° < \delta < -60°$ and $-60° < \delta < -30°$) at low energies. The optimal declination region in close to the equatorila line, while at declination angle $\delta > 30°$ the effect of Earth absorption is visible at high energies.

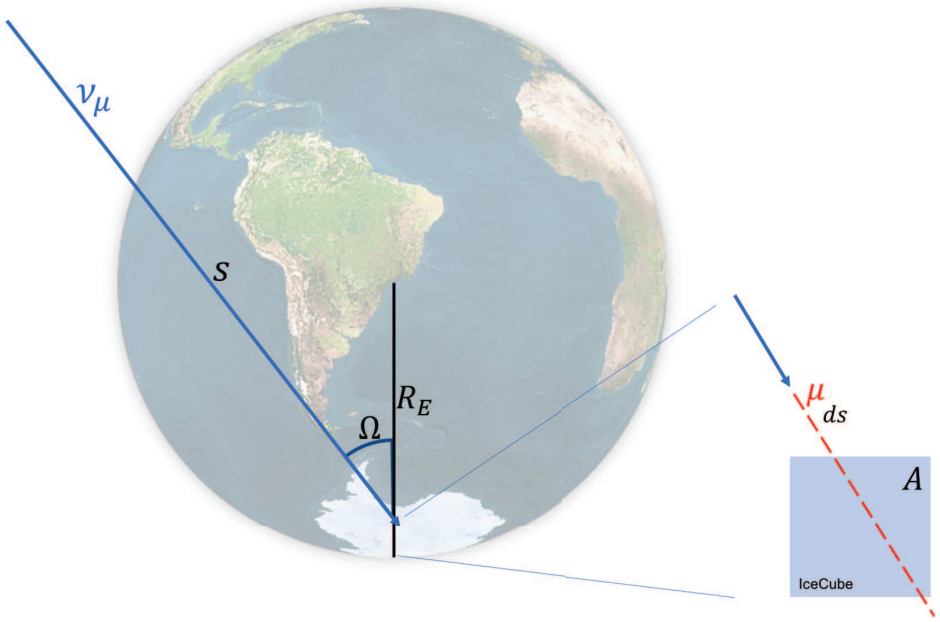

Fig. 1.8 Sketch of the path of a neutrino. The muon neutrino pass through the Earth and it can be interact outside the detector. The muon associated pass inside the detector producing Cherenkov radiation observable by the DOMs. In the figure the main quantities useful for the analytical expression of the effective area are shown.

Atmospheric Neutrinos

The majority of events observed by IceCube is imputable to the atmospheric background. These neutrinos are generated by the collision of cosmic rays with the atmosphere. In fact, during this interaction, secondary particles are produced among which a huge amount of pions and kaons. Mesons decay produce muons and neutrinos. Both of them are noise background for the identification of astrophysical neutrinos. The energy spectrum for both neutrinos and muons is $\sim E^{-3.7}$. IceCube has a veto system that refuses the events characterised by a coincident signal, that is produced by the muons in the veto and by the atmospheric neutrinos into the detector. The background affects predominantly the low energies (< 100 TeV) because of the steep spectrum and the Southern hemisphere since the atmospherical muons are absorbed by the Earth before to reach the detector (**?**, **?**, **?**).

There is another component of atmospheric background, the so-called *prompt*, due to the decay of heavy mesons ($c, \bar{c}, b, \bar{b} \rightarrow heavy - hadron + X \rightarrow \nu, \bar{\nu} + X' + X$). In this case the expected energy spectrum is $\sim E^{-2.7}$ but due to the low intensity of events, this background is not expected to be dominant.

Fig. **??** shows the best-fit ν spectra (**?**). IceCube data are represent with black dots. there are then different fits: The yellow and the red regions are the best fits for HESE

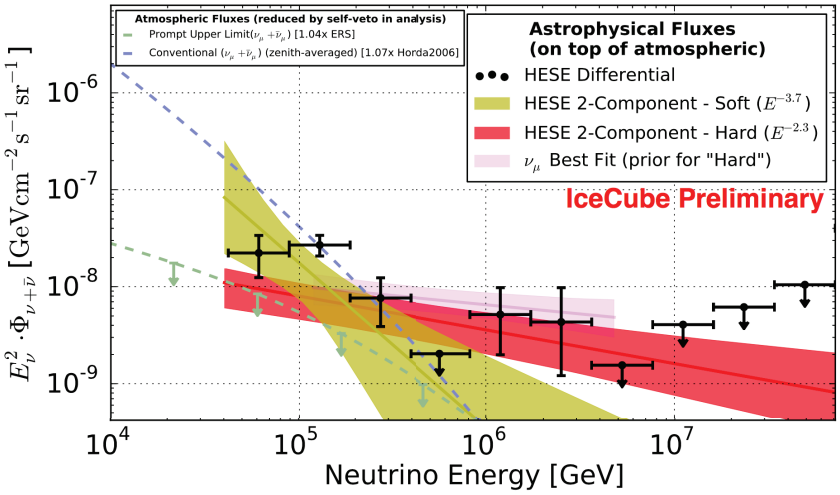

Fig. 1.9 Unfolded spectrum for six years of HESE neutrino events and six years Northern hemisphere track events. The yellow and red bands show the 1σ uncertainties on the result of a two-power-law fit. Superimposed is the best fit to eight years of the upgoing muon neutrino data (pink). Note the consistency of the red and pink bands. *Credits*: (**?**

events. The high-energy neutrino events are characterized by a spectral index of 2.13, which suggests that they can't have atmospherical origins. The pink spectrum is obtained from the measurement of the Northern Hemisphere muon neutrino flux, using IceCube data from 2009 to 2015. The dashed blu line is the best fit of the conventional $\nu_\mu + \bar{\nu}_\mu$ atmospherical neutrinos. The green line is the flux limit for prompt atmospheric neutrinos.

1.3.3 Status of the IceCube Observations

After eight years of data acquisition, IceCube observed an excess of events at energies beyond 100 TeV which cannot be associated to the atmospheric flux (**?**, **?**). The statistical significance of the excess, the astrophysical flux, is 6.7σ. Periodically the IceCube Collaboration publishes a list of detected events (both HESE and throughgoing events). At present the six-year data set contains a total of 83 neutrino events with deposited energies ranging from 60 TeV to 10 PeV. The data are reported in tables on **?** and **?** for HESE events (54 events) and in **?** for througoing events (29 events) (see also **?**).

In Figure **??** the arrival directions of the most energetic events in the eight-year upgoing $\nu_\mu + \bar{\nu}_\mu$ analysis ($\odot$) and the six-year HESE data sets are shown. The HESE data are separated into tracks ($\otimes$) and cascades ($\oplus$). The median angular resolution of the cascade events is indicated by thin circles around the best-fit position. The most energetic

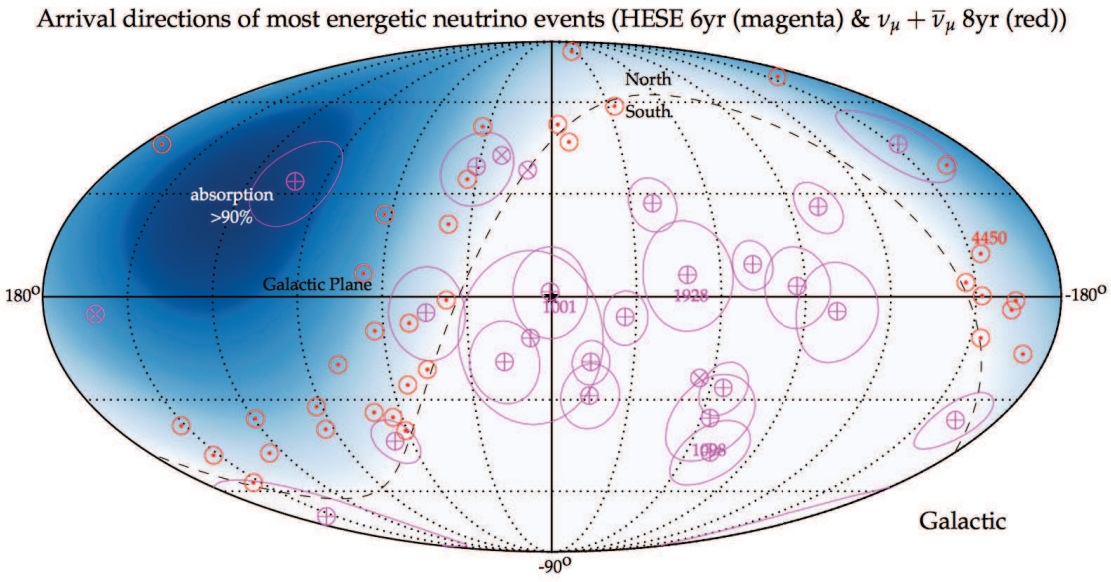

Fig. 1.10 Projection in Galactic coordinates of the arrival direction of neutrino events. In the plot the eight-year upgoing track analysis performed by the IceCube Collaboration with reconstructed muon energy $E_\mu \gtrsim 200$ TeV are shown (red $\odot$). The events of the six-year high-energy starting event (HESE) analysis with deposited energy larger than 100 TeV (tracks $\otimes$ and cascades $\oplus$) are also shown. The thin circles indicate the median angular resolution of the cascade events ($\oplus$). The blue-shaded region indicates the zenith-dependent range where Earth absorption of 100 TeV neutrinos becomes important, reaching more than 90% close to the nadir. The dashed line indicates the horizon and the star ($*$) the Galactic Center. The four most energetic events are highlighted with magenta numbers (HESE) and red number (tracks).

muons with energy $E_\mu > 200$ TeV in the upgoing $\nu_\mu + \bar{\nu}_\mu$ data set accumulate near the horizon in the Northern Hemisphere. Elsewhere, muon neutrinos are increasingly absorbed in the Earth before reaching the vicinity of the detector because of their relatively large high-energy cross sections. This causes the apparent anisotropy of the events in the Northern Hemisphere. Also HESE events with deposited energy of $E_{\rm dep} > 100$ TeV suffer from absorption in the Earth and are therefore mostly detected when originating from the Southern Hemisphere. After correcting for absorption, the arrival directions of cosmic neutrinos follow an isotropic distribution, suggesting a dominating extragalactic components. However an analysis of the possible galactic components at low energy is done in **?**, **?**, **?**.

The case of TXS 0506+056

In April 2016 IceCube set up a real time alert system **?**. Any track-like event with sufficient energy to have a high probability of being an astrophysical neutrino generates an alert in the form of a public Gamma-ray Coordinate Network circular within a minute of the event for possible follow-up by astronomical telescopes. About 10 alerts have been issued since the system began. The tenth such alert, IceCube-170922A, on September 22, 2017, reported a well-reconstructed muon neutrino with a significant probability to come from space rather than from the Earth's atmosphere. The energy deposited by this event was of 23.7 ± 2.8 TeV. To estimate the parent neutrino energy, the IceCube Collaborators performed simulations of the response of the detector array, considering that the muon-neutrino might have interacted outside the detector at an unknown distance. They assumed the best-fitting power-law energy spectrum for astrophysical high-energy muon neutrinos, $dN/dE \propto E^{-2.13}$ **?** where N is the number of neutrinos as a function of energy E. The simulations yielded a most probable neutrino energy of 290 TeV, with a 90% confidence level (C.L.) lower limit of 183 TeV, depending only weakly on the assumed astrophysical energy spectrum (**?**).

What makes this alert special is that, for the first time, telescopes detected enhanced γ-ray activity aligned with the cosmic neutrino within less than 0.1°, associated to a flaring blazar with redshift $z = 0.34$ (**?**), called TXS0506+056. Originally detected by Fermi and Swift satellite telescopes, the source was followed up by the MAGIC air Cherenkov telescope. Several other telescopes subsequently observed the flaring blazar; a complete report of the observations is reported in **?** and **?**.

Figures **??** and **??** summarise the multi-wavelength light curves and the changes in the broad-band spectral energy distribution (SED), compared to archival observations.

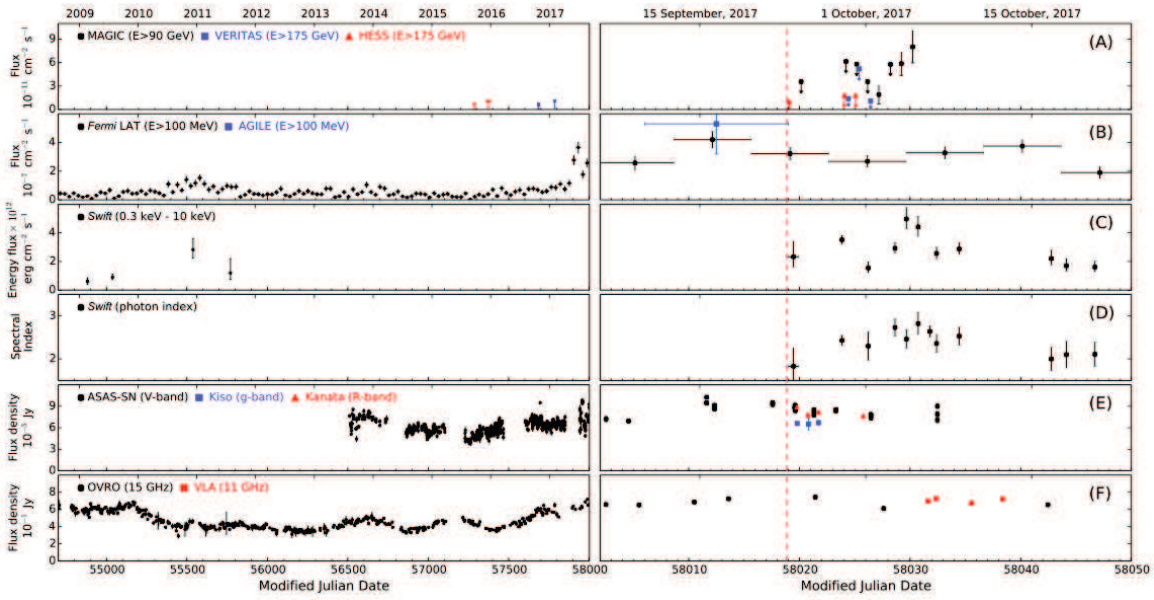

Fig. 1.11 Time-dependent multi-wavelength observations of TXS 0506+056 before and after IceCube-170922A. Significant variability of the electromagnetic emission can be observed in all displayed energy bands, with the source being in a high emission state around the time of the neutrino alert. From top to bottom: (A) VHE γ-ray observations by MAGIC, H.E.S.S. and VERITAS; (B) high-energy γ-ray observations by Fermi-LAT and AGILE; (C and D) X-ray observations by Swift XRT; (E) optical light curves from ASAS-SN, Kiso/KWFC, and Kanata/HONIR; and (F) radio observations by OVRO and VLA. The red dashed line marks the detection time of the neutrino IceCube-170922A. The left set of panels shows measurements between MJD 54700 (22 August, 2008) and MJD 58002 (6 September, 2017). The set of panels on the right shows an expanded scale for time range MJD 58002 - MJD 58050 (24 October, 2017). The Fermi-LAT light curve is binned in 28 day bins on the left panel, while finer 7 day bins are used on the expanded panel. A VERITAS limit from MJD 58019.40 (23 September, 2017) of $2.1 \times 10^{-10}\mathrm{cm}^{-2}\mathrm{s}^{-1}$ is off the scale of the plot and not shown.

Several models have been presented to describe the physics behind the neutrino and electromagnetic emission. Section **??** shows the so-called *spine-layer* scenario, applied to TXS 0506+056 SED (**?**), while section **??** shows an alternative scenario that consider the photons produced by the low accretion flow (*ADAF*), as target to the relativistic protons inside the jet **?**. Other scenarios are presented in **?**, **?**, **?**, **?**, **?**, **?**. A discussion of these results is given in Section **??**.

This coincidence detection triggered the IceCube Collaboration to reanalyse the data around the position of TXS 0506+056. In **?**, IceCube Collaboration shows an analysis including the entire 9.5 years of observations (from April 2008 to October 2017) performed with different configurations of the detector. To search for a neutrino signal at the coordinates of TXS 0506+056, they applied the standard time-integrated analysis **?** and time-dependent analysis (**?**) that they have been used in past searches (e.g. **?**, **?**).

They show the results of the time-dependent analysis performed at the coordinates of TXS 0506+056 for each of the six data periods. One of the data periods, from 2012 to 2015, contains a significant excess. The excess consists of 13 ± 5 events above the expectation from the atmospheric background. The significance depends on the energies of the events, their proximity to the coordinates of TXS 0506+056, and their clustering in time. This is illustrated in Fig. 2 of **?**, which shows the time-independent weight of individual events in the likelihood analysis during the data period. The significance of the excess, calculated 3.5σ, is due to both the number of events and their energy distribution.

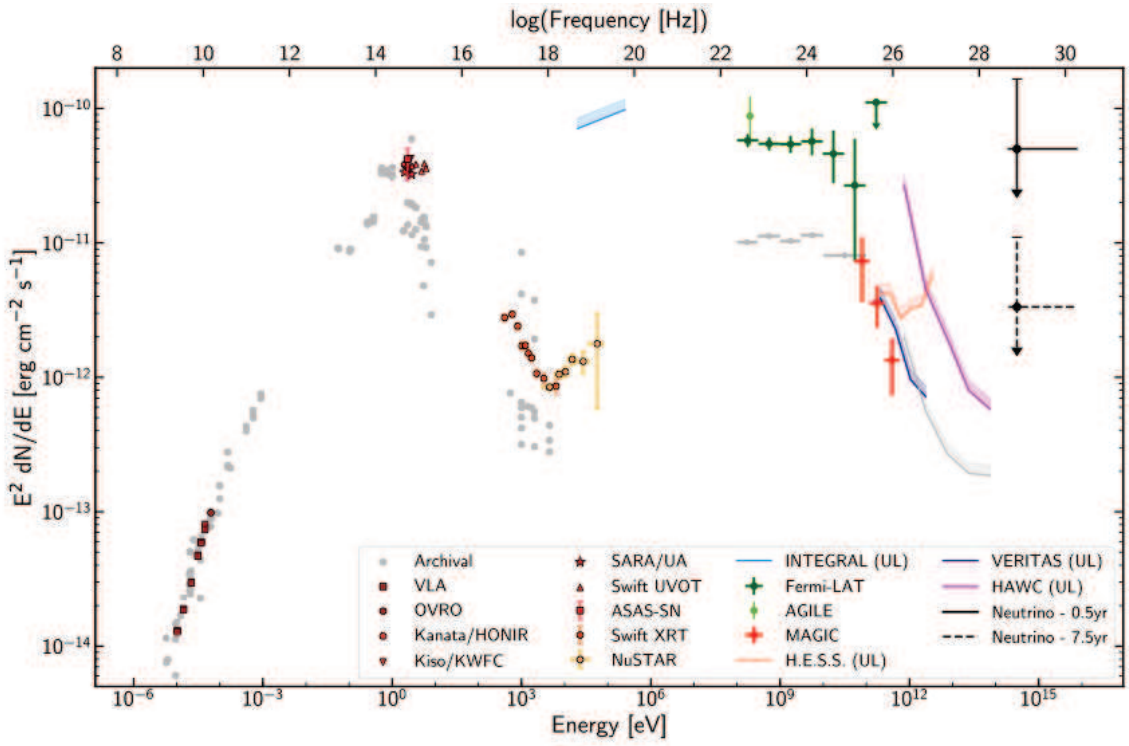

Fig. 1.12 The SED is based on observations obtained within 14 days of the detection of the IceCube-170922A event. See **?** to see all the telescopes that contributes to the realization of the SED. Archival observations are shown in grey to illustrate the historical flux level of the blazar. The γ-ray observations have not been corrected for absorption due to the EBL. SARA/UA, ASAS-SN, and Kiso/KWFC observations have not been corrected for Galactic attenuation. Even within this 14-day period, there is variability observed in several of the energy bands shown (see Figure **??**) and the data are not all obtained simultaneously. Representative $\nu_\mu + \bar{\nu}_\mu$ neutrino flux upper limits that produce on average one detection like IceCube-170922A over a period of 0.5 (solid black line) and 7.5 years (dashed black line) are shown assuming a spectrum of $dN/dE \propto E^{-2}$ at the most probable neutrino energy (311 TeV).

Chapter 2

Cosmic sources of high-energy neutrinos

In the previous chapter we discussed neutrino properties, the observational techniques and the status of the IceCube observations. At present, the spectrum of the neutrino events and the reconstructed directions of them, make impossible to distinguish between the two main channel of production pp or $p\gamma$. Due to the different environment, in fact, relativistic cosmic-rays (protons) can interact with radiation or gas producing pions and then neutrinos and γ-rays. Also, the reconstructed direction of the neutrino events is distributed isotropically in the Sky. This leads to exclude a unique galactic component. In particular in **??** we showed that the spectrum of the IceCube events can be interpreted as having two components: a galactic one at low energy, < 100 TeV, and an extragalactic component dominant above 100 TeV (**?**, **?**, **?**).

Then, the requirements of the neutrino sources should be:

- From the relation between protons and neutrinos energies, $E_p \sim 20E_\nu$, the candidate astrophysical high-energy neutrino sources should be also sources of HECRs; or they should be irradiated by a flux of cosmic rays from some other source(s).

- Moreover, due to the fact that during the pp or $p\gamma$ reactions both charged pions and neutral pions are created, it is reasonable to search neutrino sources from the most energetic sources of γ-rays, that they can be the result of π^0 decay.

In this chapter we give a brief overview of the main candidate neutrino source classes. We start describing the galactic candidates in which the pp channel is favourite, because of the rich environment of gas. Then we present the main extragalactic sources. In this case both scenarios (pp and $p\gamma$) are presented: cosmic rays can be accelerated in the jet and interact mainly with radiation pulling in the photo-meson reaction ($p\gamma$) or they can be produced by a supernovae explosion and then interact with the gas of the galaxy (pp) (for more details see **?**).

2.1 Cosmic-rays

The sources of CRs and UHECRs are still unknown and their link with astrophysical neutrinos is one of the best way to investigate on their nature. Their origin is expected to be both galactic and extragalactic. A reasonable starting point to study CRs is to establish some separation between those CRs that can potentially be accelerated inside the Galaxy and the ones that are thought to be produced outside the Milky Way (**?**, **?**).

In Fig. **??** the CRs spectrum recorded with different experiments is shown. The energy dependency of the flux of of cosmic rays is quite well described by a power law E^{-p} with p the spectral index, around 2.7 on average. After the low energy region dominated by cosmic rays from the Sun (the solar wind), the spectrum becomes steeper for energy values of less than around 1000 TeV (**?**). The point at which the change of slope takes place is called the *knee* and it is clearly visible in Fig. **??**. Around this energy the emission of CRs is probably dominated by astrophysical sources in our Galaxy. There is a substantial consensus that galactic CRs are somehow related to one or more types of supernova (SN) explosions and that acceleration is mainly due to diffusive transport in the proximity of strong shocks into the intergalactic medium (IGM) formed as a consequence of these explosions. However, there is no agreement on the fact that those CRs can actually reach the knee energy. At higher energies $\sim 10^9$ GeV, a hardening occurs, the so-called *ankle*; there are several arguments that support that the region above this energy is dominated by cosmic rays produced by extragalactic sources (see **?**, **?**, **?**,**?**). For even higher energies ($> 10^{11}$ GeV) the cosmic-ray spectrum presents a drastic suppression as expected from the interaction of long-traveling particles with the cosmic microwave background, remnant of the origin of the Universe.

The energy scale of CRs producing TeV-PeV neutrinos is above the cosmic-ray *knee* in the energy range from PeV to 10 PeV but below the CR *ankle* around 4×10^6 TeV. The underlying cosmic ray population responsible for the neutrino emission is hence not clearly identifiable as Galactic or extragalactic in terms of the energy.

2.2 Galactic sources

The directions of the events detected by IceCube suggest that the nature of the astrophysical neutrinos cannot be exclusively galactic. However, the Milky Way is an ideal environment for the pp channel, because of the abundant gas in which a relativistic cosmic-ray can travel through. Our galaxy can contribute to the neutrino spectrum by

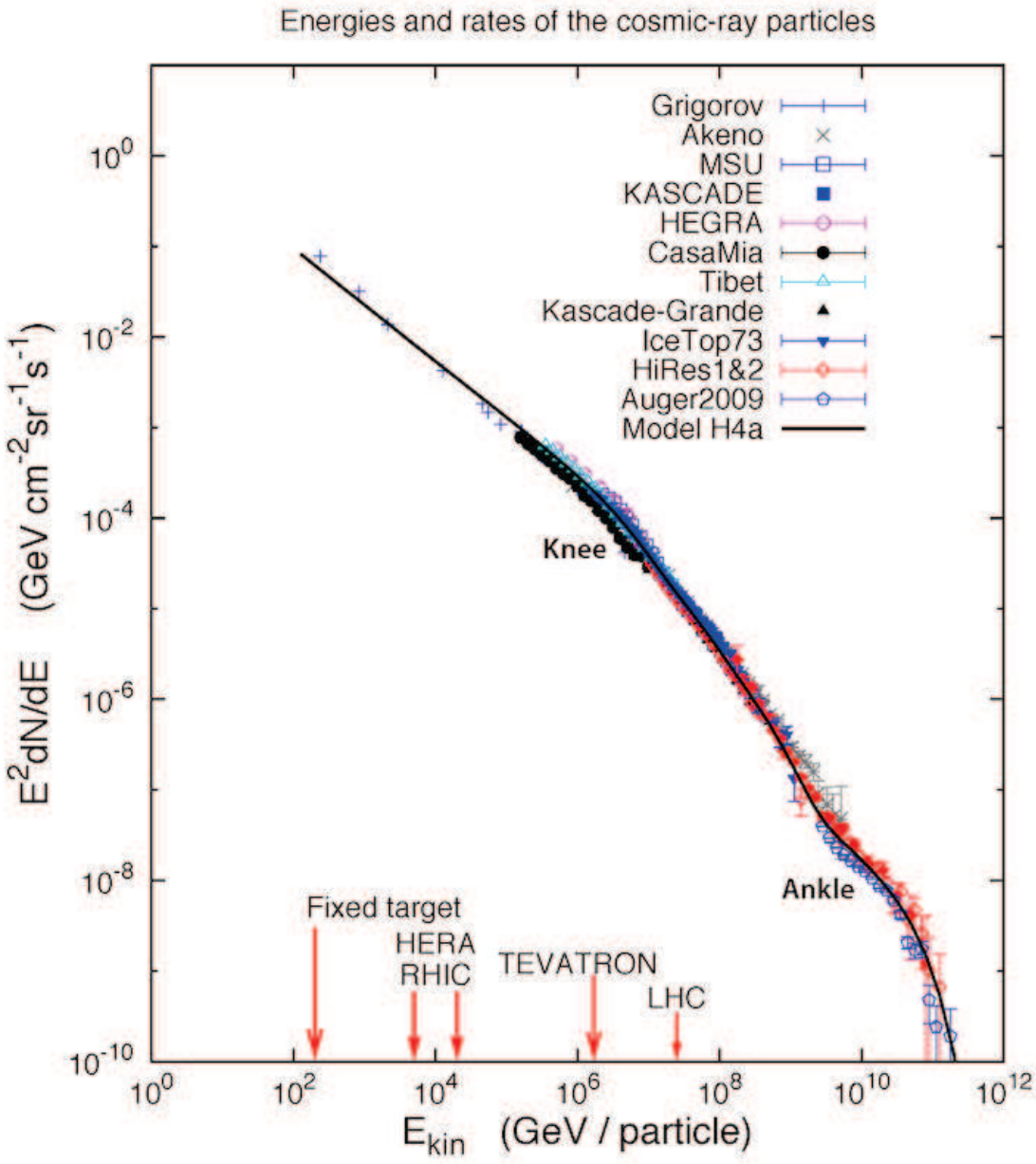

Fig. 2.1 Cosmic rays spectrum. The flux of cosmic rays decreases strongly with increasing particle energy. Slightly above an energy of 10^{15} eV, the slope of energy decrease changes. This leads to a bend in the spectrum, the *knee* of cosmic radiation. In the region around 10^{18} eV, also called the *ankle*, the slope changes again (it became hardering). According to the standard lore, below the knee, cosmic rays are thought to be of galactic origin, while above the ankle they are expected to be only extragalactic.

the diffuse neutrino emission of galactic CRs, the joint emission of galactic PeV sources or microquasars, and extended galactic structures like the Fermi Bubbles or the galactic halo.

2.2.1 Galactic diffuse emission

The events detected by IceCube corresponds to neutrinos with energies of a few PeV. Considering hadronic production via $p\gamma$ or pp interactions, this corresponds to an underlying CR population with energies $E_p \sim 20E_\nu$, reaching above the CR *knee*, but not necessarily above the *ankle* (see Figure **??**). The origin of CR detected in this region is still unknown. Since these range corresponds to the transition region of Galactic and extragalactic cosmic rays it is feasible that Galactic sources might be responsible for the emission. However, the absence of a strong anisotropy in the arrival direction of events and upper limits on the neutrino flux of individual point source emission limits the contribution of individual Galactic point sources (**?**).

A significant contribution to the observed diffuse flux is only possible for extended Galactic diffuse emission. A guaranteed contribution to the diffuse emission of the Galactic Plane is the hadronic emission produced by interactions of diffuse CRs with gas (**?**, **?**, **?**, **?**, **?**).

In general, this emission is expected to follow the local diffuse CR spectrum. Usually it is assumed that the average spectrum in our Galaxy is close to the observed one with a power-law $E^{-2.75}$ up to the knee at $3-4$ PeV, where the spectrum became softer. In the context of the IceCube observation, the all-sky integrated flux is unlikely to reach the observed level (**?**, **?**, **?**).

Another source of extended Galactic emission is the cumulative quasi-diffuse flux of Galactic sub-threshold sources. Various sources might reach the required large maximal energies necessary for the IceCube observation.

It was shown that candidate Galactic sources for the IceCube emission following the Galactic distribution of supernova remnants or pulsars can only maximally contribute at a level of 65% to be consistent with the HESE three-year data (**?**, **?**, **?**, **?**).

2.2.2 Extended galactic sources

The origin of the extended Galactic gamma-ray emission known as the *Fermi Bubbles* (**?**, **?**) is unclear, but leptonic (**?**) as well as hadronic (**?**, **?**) scenarios have been proposed, which can be distinguished via their corresponding neutrino emission (**? ?**). Figure **??** shows a two years γ-ray sky observed by Fermi satellite. the upper panel shows the smoothed all sky map detected in the energy region of $1-10$ GeV in which the galactic plane is clearly

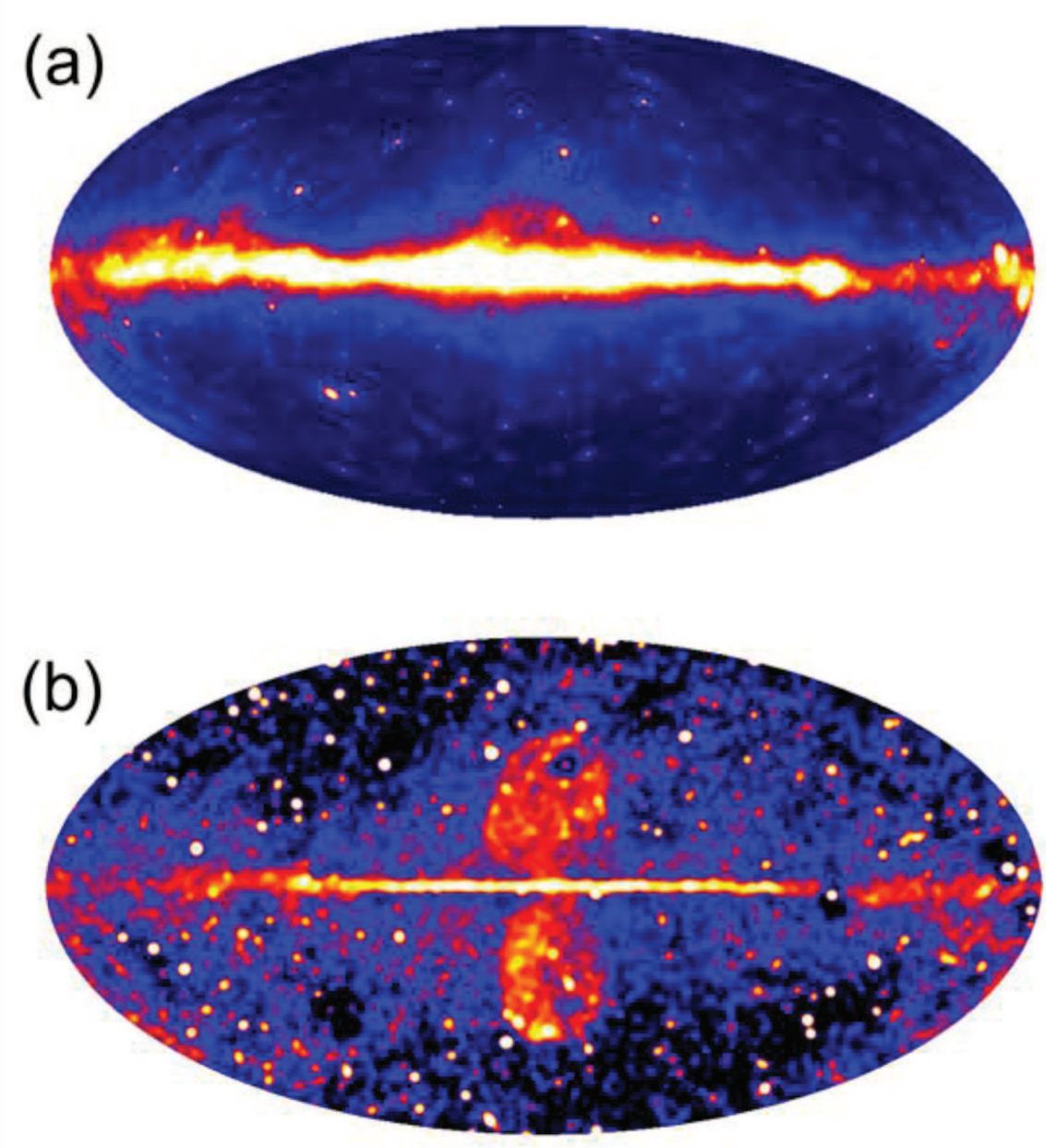

Fig. 2.2 Two years γ-ray sky map observed by Fermi satellite. a) is the smoothed all sky map (1-10 GeV) in with the galactic plane and the galactic centre are clearly visible. b) residual sky map in which the Fermi bubbles are turned up.

visible. The lower panel shows, instead, the residual sky map in the same energy band to turns up the Fermi bubbles.

IceCube's HESE three-year data show a weak statistical excess close to the Galactic Center in the search for anisotropies in the event arrival directions. This has motivated speculations about a possible hadronic contribution to the Fermi Bubbles (**?**, **?**, **?**, **?**). The maximum contribution of the Fermi Bubble region to the HESE three-year data has been shown to be limited to about 25% (**?**).

2.3 Extragalactic sources

Among extragalactic sources, we describe gamma-ray bursts, starbust galaxies and active galactic nuclei. However small contribution of the neutrino background can come also from other galaxies with the same emission of our Milky Way or from exotic processes such as dark matter annihilation (**?**).

2.3.1 Gamma Ray Bursts

Gamma Ray Bursts (GRBs) are short and intense flashes of γ-rays with typical energies between keV and a few MeV (**?** **?**). They reach luminosities (assuming isotropy) of 10^{54} erg/s, which makes them the most energetic phenomena in the Universe. The γ-ray emission, called *"prompt"*, is highly variable, with timescales as short as few milliseconds, and can last a fraction of a second (short GRBs, $t < 2$ s) or few tens of seconds (long GRBs, $t > 2$ s). GRBs are cosmological sources having average redshift $\langle z \rangle \sim 2.5$. The progenitors of long GRBs are thought to be very massive stars that collapse at the end of their life, while the progenitors of short GRBs are thought to be the merging of two neutron stars.

It has been argued that if a small fraction of the kinetic energy is channeled into acceleration of CRs, GRBs can supply the total power density of ultra high energetic cosmic rays. For this reason they are prominent candidates for the origin of UHECRs (**?**, **?**) as well as for high-energy neutrinos (**?**).

Long GRBs are the most likely candidates for productions of neutrinos. Variations of the the baryonic content leads to expanding shells with different relativistic Doppler factors that start to collide and form internal shocks. The strong γ-ray display is related to synchrotron emission of a population of high-energy electrons that may be accelerated in the shocks. Protons that can be co-accelerated in the shocks could start to interact with photons of the synchrotron spectrum and produce neutrinos via $p\gamma$ channel. The

corresponding emission is typically in the TeV-PeV energy region depending, also, to the radiation spectrum.

The expected rate of GRBs is ~ 1000 per year over the entire sky. IceCube Collaboration performed an analysis to search potential events coming from 807 GRBs during three years of data taking (**?**). However only five events were found in spatial and temporal coincidence with GRBs. This allows to put constraints on the contribution of neutrinos coming from GRBs to the observed neutrino diffuse emission; that are at least a factor ten lower than the measured flux. This also bounds some parameters on which the theoretical model is based, such as the bulk Lorentz factor Γ and the baryonic load of the jet. However, model adjustments might circumvent these limits. For instance, frequent population of low-power, i.e. sub-threshold, GRBs (**?**, **?**) that are mostly undetected by gamma-ray observatories could be responsible for the flux. Besides, neutrino emission is also expected in different models of the GRB mechanism, such as the neutrino emission in the prompt phase produced via pp interactions in the GRB progenitor (**?**) or in early internal shocks up to the photosphere or late internal or external shocks during the afterglow phase (**?**).

2.3.2 Star-forming Galaxies

In galaxies with active star formation (the so-called star-forming galaxies, SFGs), both γ-rays and neutrinos emission is expected because of the large rate of supernova explosions and the correspondingly high flux of CRs and gas. About 10% of the star-formation rate density in the Universe is operated by a subclass of SFGs, the so-called starburst galaxies (SBGs).

SBGs host transient starburst episodes, often triggered by galaxy merger events, which channel fresh gas towards the center of the merger remnant. In addition to an increasing stellar birth rate, observations indicate an increased magnetic field strength (**?**). For this reason, cosmic rays accelerated in and emitted from supernova remnant shocks can be confined longer than the pp interaction time scale with the denser interstellar gas (**?**, **?**, **?**, **?**).

As a hadronic pp scenario, the neutrino spectrum is expected to follow the initial cosmic ray spectrum of the sources up to an energy where the confinement timescale due to diffusion and winds become smaller than the pp interaction timescale. This naturally produces a cutoff in the spectrum above $0.1 - 1$ PeV neutrino energies (**?**,**?** **?**, **?**). Variations of this scenario illustrate the different intrinsic cosmic ray spectra of supernovae and hypernovae in star-forming and starburst regions that can introduce additional spectral features in the cumulative neutrino spectrum (**?**).

Unfortunately, the detection of individual starburst galaxies as neutrino point sources is expected to be challenging due to their large abundance, i.e. a small individual point-source contribution to the diffuse neutrino flux as seen in **?**.

2.3.3 Active Galactic Nuclei

Active galactic nuclei (AGNs) are compact regions at the centre of galaxies with a luminosity higher than the normal galaxies and whose radiation emission ranges from radio to TeV band (**?**). AGNs are potential sources of high-energy particles including neutrinos. Chapter **??** is dedicated to the structure of these objects, here we report the main characteristics that allows AGN to be candidates neutrino sources.

The radiation from AGN is believed to be a result of accretion of matter by a supermassive black hole at the centre of the host galaxy (see Section **??**, and **??**) . About ~ 10% of AGN produce a non-thermal emission through two relativistic jets (see Section **??**).

Most of the neutrino production scenarios assume $p\gamma$ interactions. Neutrino emission of AGNs, in fact, has been predicted for various cosmic ray production and interaction sites, including for example CRs accelerated in shocks in the jet and interacting with thermal radiation from the accretion disk or synchrotron radiation of the jet (**?**, **?**, **? ?**, see also Section **??**). Another indirect source of neutrinos could come from the interaction of high-energy CRs interacting with the cosmic radiation backgrounds after emission of blazars (**?**).

However, hadronic emission via pp interactions can happen if the target density is large enough (**?**) or if the CRs accelerated in the jet are able to escape and interact with matter of the host galaxy (**?**, **?**).

The event IC-170922A on September 2017 associated to a flaring Blazar, a subclass of AGN (see Section **??**), suggests that these sources could provide a contribution on the neutrino spectrum observed by IceCube.

2.4 Interpretation of present results

Apart from the case of TXS 0506+056 (see Section **??**) no source has been identified by IceCube with a significance $> 3\sigma$. The non detection of multiplets of neutrinos from any source (except a possible excess from TXS 0506+056 presented in **?**), fixes the proprieties of the class that can produce neutrinos. In fact, this condition, together with the diffuse neutrino flux detected by IceCube, implies an upper limit on the average distance of the source population and then also a lower limit on the density. The combined constraints

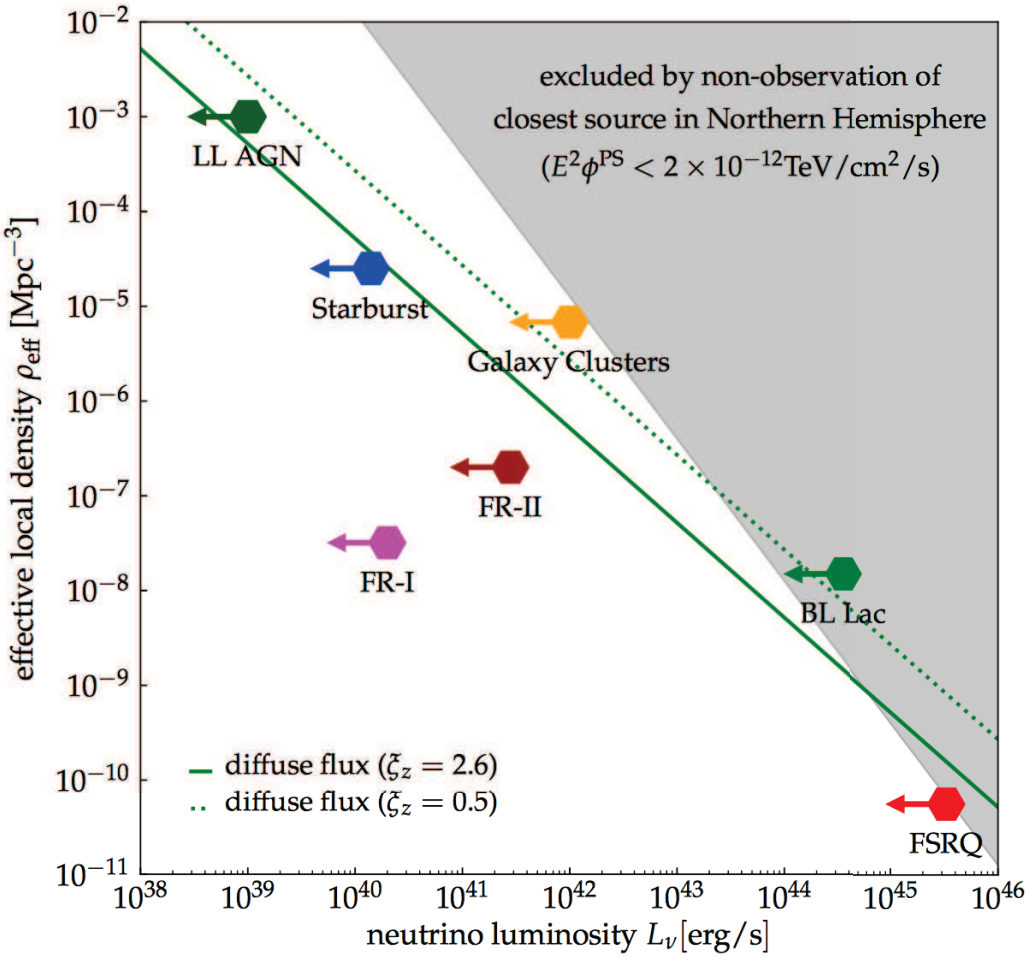

Fig. 2.3 The effective local density and (maximal) neutrino luminosity of various neutrino source candidates from **?**. The green solid (green dotted) line shows the local density and luminosity of the population of sources responsible for the diffuse neutrino flux of $E^2\phi \simeq 10^{-8}$ GeV cm^{-2} s-1 sr^{-1} observed with IceCube, assuming source evolution following the star-formation rate ($\xi_z \simeq 2.6$) or no source evolution ($\xi_z \simeq 0.5$), respectively. The gray-shaded area indicates source populations that are excluded by the non observation of point sources in the Northern Hemisphere ($f_{\rm sky} \simeq 0.5$) with discovery potential $E^2\phi \simeq 2 \times 10^{-12}$ TeV cm^{-2} s^{-1} (**?**).

on density and luminosity of sources is displayed in a so-called *Kowalski plot* (**?**) shown in Figure **??**. Figure shows the local density and luminosity of theorized neutrino sources from (**?**). The grey region is excluded by the non detection of individual point sources, assuming the discovery potential of IceCube in the Northern Hemisphere of $E^2\phi \simeq 2 \times 10^{-12}$ TeV cm^{-2} s^{-1} (**?**). The green lines show the combination of density and luminosity for sources at the level of the observed IceCube flux, assuming a source density evolution following the star formation rate (solid line) or no evolution (dotted line). From this Figure, IceCube is presently sensitive to source populations with local source densities smaller than, 10^{-8} M pc^{-3}. Much lower local densities, like those of BL Lacs FSRQs, are challenged by the non observation of individual sources. Some source classes, like Fanaroff-Riley (FR) radio galaxies, have an estimated neutrino luminosity that is likely too low for the observed flux. Note that these estimates depend on the evolution parameter ξ_z, and therefore the exact sensitivity estimate depends on the redshift evolution of the source luminosity density. Other analysis with similar conclusions were presented in **?** and **?**. In addition, this simple estimate can be refined by considering not only the closest source of the population but the combined emission of known local sources (**?**).

In the figure LL AGN stays for low-luminosity AGN (**?**), FR-I, FR-II, BL Lac and FSRQ are subclasses of AGN (See next Chapters). The position of BL Lac class (green dot) on the plot of Figure **??** is not in disagreement with the event of IC-170922A/TXS 0506+056. In fact, in this plot all BL Lacs are considered as neutrino emitters. In the next Chapters we will show that this is not true.

Note that the position of the classes into the plot of Figure **??** are to be consider as upper limits. In fact it is assumed that each class is liable of the entire neutrino diffused emission detected by Icecube. However, it is accepted from the astrophysical Community that the neutrino background observed by IceCube is a sum of components coming from different sources. In other words, each class provides a percentage of the entire neutrino spectrum that we observe (**?**, **?**, **?**).

Chapter 3

Active Galactic Nuclei

The term Active Galactic Nuclei (AGN) generally refers to the highly energetic phenomena that can be observed in the nuclei of some galaxies. The output of this kind of emission largely exceeds the total luminosity emitted from the host galaxy, showing typical luminosities in the range $\sim 10^{44} - 10^{48}$ erg s^{-1}. AGNs are, in fact, the most luminous persistent sources of electromagnetic radiation in the Universe. The radiation emitted from these nuclear regions can cover the whole electromagnetic spectrum, from radio wavelengths to very high-energies. These features cannot be attributed to stellar emission. The current model assigns this peculiar phenomena to the accretion process of matter onto a Super Massive Black Hole (SMBH), residing at the centre of the host galaxy, with masses that range between 10^6 and 10^{10} $M_\odot$. The energy emitted is thought to be produced by the gravitational infall of matter inside an accreting structure, that is heated to extremely high temperatures and dissipates the stored heat with different levels of efficiency.

The capability of these objects to emit radiation at high-energies makes AGNs potential sources of high-energy particles including neutrinos. High-energy neutrino emission from AGN have been discussed since the late 70s at least. If protons are accelerated by, for example, the diffusive shock acceleration mechanism, because the optical and X-ray radiation density is rather high in the vicinity of a SMBH, the CRs may efficiently interact with the ambient photons.

Both observational and theoretical multi-wavelength efforts have helped us understand the physics of AGN, which also lead to different proposals for CR acceleration and associated neutrino production in AGN.

In this chapter we present the main characteristics of AGNs and we focus on blazars, a subclass of radio-loud AGNs with a jet pointing to Earth.

3.1 Structure of AGNs

Due to the anisotropy of their structure, AGNs present phenomenological differences each other. This led, at first, to study AGN objects as different class sources. In fact, between the 70s and the 80s, there was a huge proliferation of phenomenological classes, that at the beginning were not connected to the same physical process. Later on, it was understood that most of the differences between various classes can be described as a different viewing angles under which we observe a single class of objects (**?**). This is the basic assumption on which the unified model of AGN is based. Figure **??** shows a cartoon summarising the structure of AGNs. In the following the main components of AGN structure are described.

3.1.1 Super Massive Black Hole and accretion flow

This system is the main engine of the whole AGN: the accretion process is thought to be one of the main responsible for the overall emission. Many models have been proposed for the accretion process, describing both high- and low-accretion rate processes. Some of these models will be described in Chapter **??**, but as a first raw description, at high accretion rates the most simple model is the geometrically thin, optically thick accretion disc (**?**). In the case of low accretion rates, instead, the particle density is so low that the energy exchange time scale between electrons and protons becomes larger than the accretion time scale, the accretion flow becomes thick and optically thin and small efficient; an example of description is given in **?**.

3.1.2 Broad Line and Narrow Line Regions

These structures are formed by clouds of partially (BLR) or totally (NLR) ionized plasma, at a distance from the central SMBH respectively of $R_{\rm BLR} \sim 0.1-1$ pc and $R_{\rm NLR} \sim 100$ pc. The vicinity of the BLR to the central engine causes the plasma orbits with a very high velocity around it ($v_{\rm BLR} \sim 10^3 - 10^4$ km s^{-1}) and then a production of Doppler broadened emission lines through recombination, following the ionization from photons emitted mainly by the accretion structure. The most prominent lines are: Lyα, CIV, MgII ecc. (see **?**). The luminosity emitted from the BLR is hence a very good tracer of the ionizing luminosity of the accretion structure, and of its overall luminosity. The average line spectra of AGNs are very similar over a wide range of luminosity, as shown in Figure **??**. This suggests that in addition to temperature, particle densities and ionization parameters are quite similar. An important exception to this statement is the behaviour of the C$_{IV}$ at $\lambda = 1549$Å emission line; relative to the continuum, C$_{IV}$ is weaker in more luminous objects (i.e., its equivalent

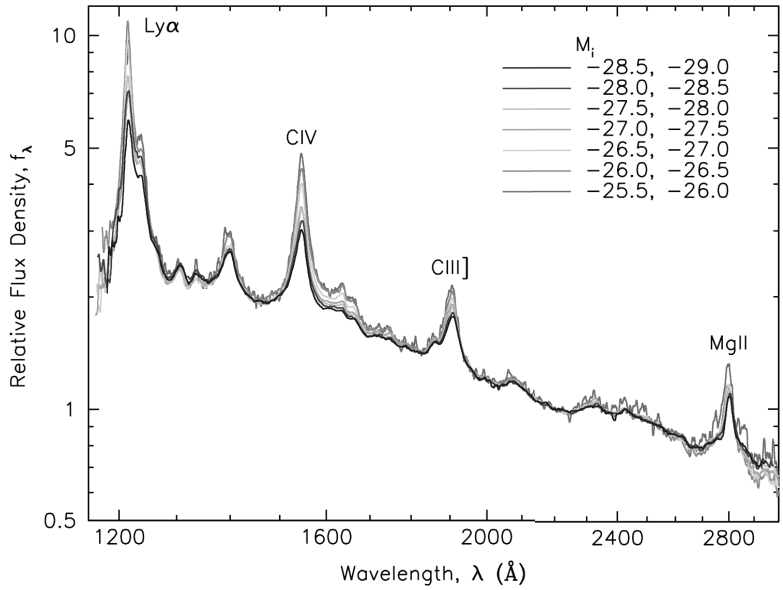

Fig. 3.1 Composite quasar spectra from the same small range of redshift but at different luminosities from the Sloan Digital Sky Survey. The flux density have been normalized at 2200Å.

width decreases with luminosity), a well-known anticorrelation known as the *Baldwin Effect* (**?**).

In the case of NLR, plasma has smaller velocity ($v_{\rm NLR} \sim 100-500$ km s^{-1}) that can be easily derived from the narrower emission lines emitted. Along with the different width, these lines can be clearly distinguished from those emitted by the BLR, because they include also "forbidden" lines, that can be produced only thanks to the lower-density conditions of the NLR itself, so that recombination can happen by spontaneous de-excitation, and not by collision events.

3.1.3 Dusty Torus

At a distance from the central black hole of $\sim 1-10$ pc an obscuring dusty structure, not necessarily toroidal, is present. This structure is responsible for the different spectral features across the various AGN sub-classes since it obscures the optical emission from the innermost structures (i.e. BLR, accretion continuum emission) under some viewing angles. The original unified model described this structure as an actual torus of dust, emitting in the IR wavelength range ($T \sim 10^3$ K). However, at present, different models are take into considerations. The most discussed model describes a clumpy distribution of dust all around the nucleus (first introduced by **?**). This would ascribe the different

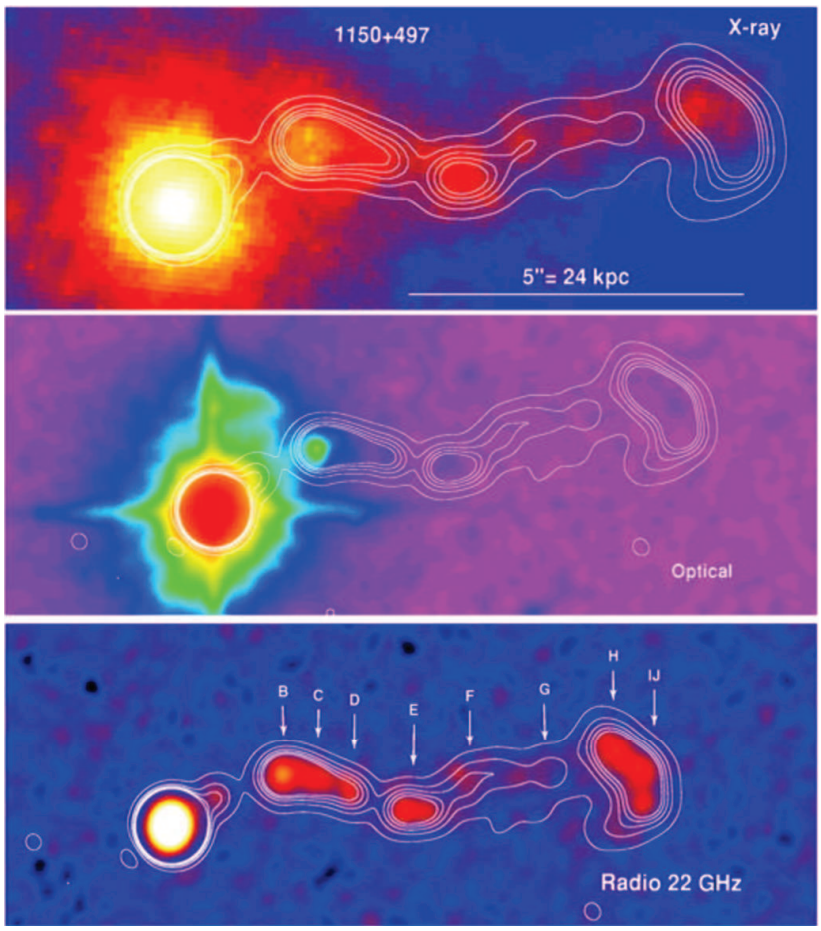

Fig. 3.2 Observations of a jet at different wavelength. The panel on top shows X-ray emission, the middle one the Optical emission while the Radio emission is shown in the bottom panel. It is clearly visible the nucleus (in the left) and the so-called *knots* of the jet. *Credits:* **?**.

spectral features also to the probability of a single clump of dust to be located along our line-of-sight (see e.g. **?**).

3.1.4 Relativistic Jet

About 10% of AGN show intense radio emission. For this reason, they are classified as radio-loud AGN. The criterion traditionally followed in order to classify these objects refers to the ratio between the rest-frame radio ($\nu \sim 5$GHz) and optical (blue band B) fluxes: $R = F_{5\mathrm{GHz}}/F_B$. Specifically, an AGN is defined radio-loud when $R > 10$, otherwise it is classified as a radio-quiet. The strong radio emission is generally associated to the presence of a relativistic jet, that can have a size in a range from a few tens of kpc to Mpc (**?**).

The structure is formed by two relativistic collimated outflow, a jet and a counter-jet, emitted symmetrically with respect to the central AGN nucleus. The plasma inside the jets moves relativistically (**?**), as can be inferred from the superluminal motion observed clearly in the collimated sections of these structures. Besides the relativistic bulk motion, the emitting particles are relativistic also in the comoving frame of the jet. This allows it to emit at all frequencies, up to γ-rays. The main emission mechanisms are Inverse Compton and synchrotron emission.

In Chapter **??** the main emission processes and jet models are described. Jets extend up to Mpc scales, and can terminate with extended structures called lobes, where the jets decelerate likely because of their interaction with the surrounding matter. While the jet emission is highly anisotropic, because of relativistic beaming, the lobes emit a strong, isotropic radio-emission thanks to the plasma deceleration.

The production mechanism of the relativistic jet is still unknown, and highly under debated. The two main processes considered to be connected to the jet formation are the electromagnetic extraction of energy and angular momentum from an accretion disc (likely thanks to magnetic reconnection), and the extraction of rotational energy from the spinning SMBH (**?**, **?**, **?**).

3.2 Unified Model of AGNs

As mentioned above, the viewing angle under which we observe an AGN highly affects its phenomenology (**?**). The emission from a relativistic jet is highly anisotropic because of relativistic beaming, and therefore its observed flux can be very different under different viewing angles. From another point of view, the presence of a dusty structure affects the optical emission. If the dust is located along our line-of-sight, the optical emission from the most central region will be partially or completely absorbed by the torus itself, and re-emitted in the IR. This affects also the spectral features in this wavelength range. For this reason, one of the first classifications introduced for AGN was indeed based on differences observed in the optical spectrum.

Radio quiet AGNs

Historically, the first classification of AGNs was done by Seyfert in 1943 (**?**). Observing the optical spectra of a set of spiral galaxies characterised by a bright core, Seyfert divided the sample into two groups: *Type 1 Seyfert galaxies* show both broad and narrow emission lines, while *Type 2* only the narrow components. With the unification of the AGNs this can be explained by the absorption from the dusty torus of the BLR radiation due to the

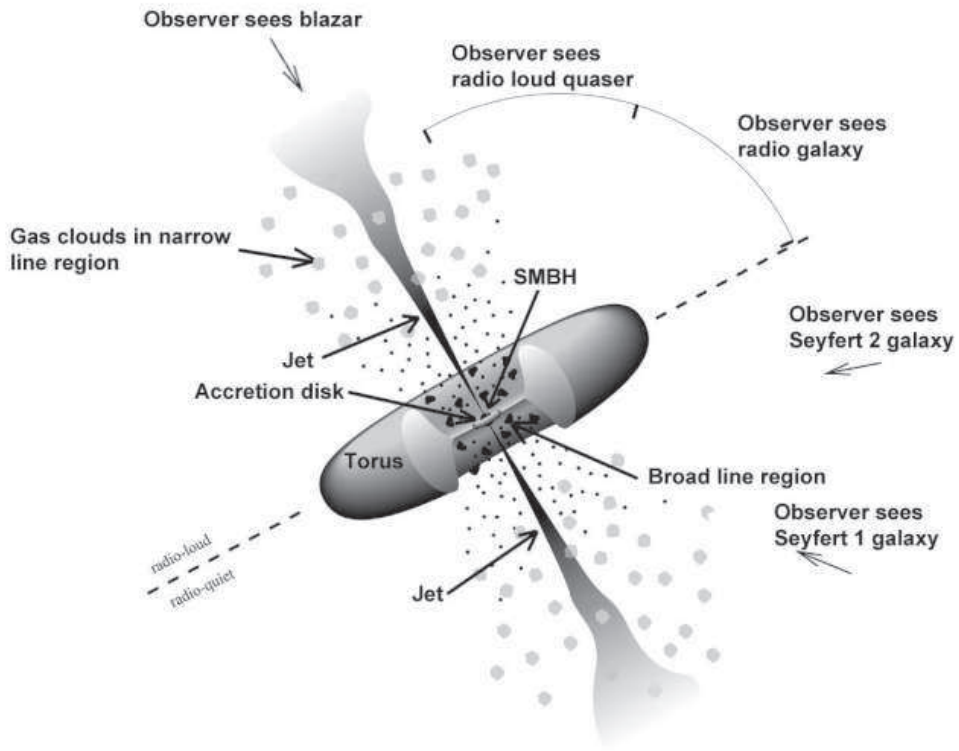

Fig. 3.3 Schematic view of the AGN unified model. *Credits:* **?**.

inclination of the AGN to the line-of-sight (see fig. **??**). Support to this theoretical model comes from polarimetric observations of Seyfert type 2 (NGC 1060 as first by **?** and then, for example, **?**). The polarized light coming from Sayfert type 2 show, in fact, the broad emission lines that were missing from the total light spectrum. This can be explain by the possibility that some fraction of the light emitted from the innermost region is scattered by free electrons in the direction of the observer. This scattered light would leave its signature in polarized light.

Radio loud AGNs

According to the radio dominance over the optical emission, AGNs can be divided into radio-loud or radio-quiet. Because of high luminosity and a strong radio emission, radio-loud AGNs are easier to detect than radio-quiet objects and then they were the first to be discovered. However radio-loud AGNs are only 10% of the whole class. Usually the host galaxies of radio-loud AGNs tend to be more massive than those of radio-quiet AGNs (e.g., **?**) and they produce a powerful jet component which provides significant radio emission through synchrotron radiation. For this reason the radio emission is a good tracer of the presence of a jet.

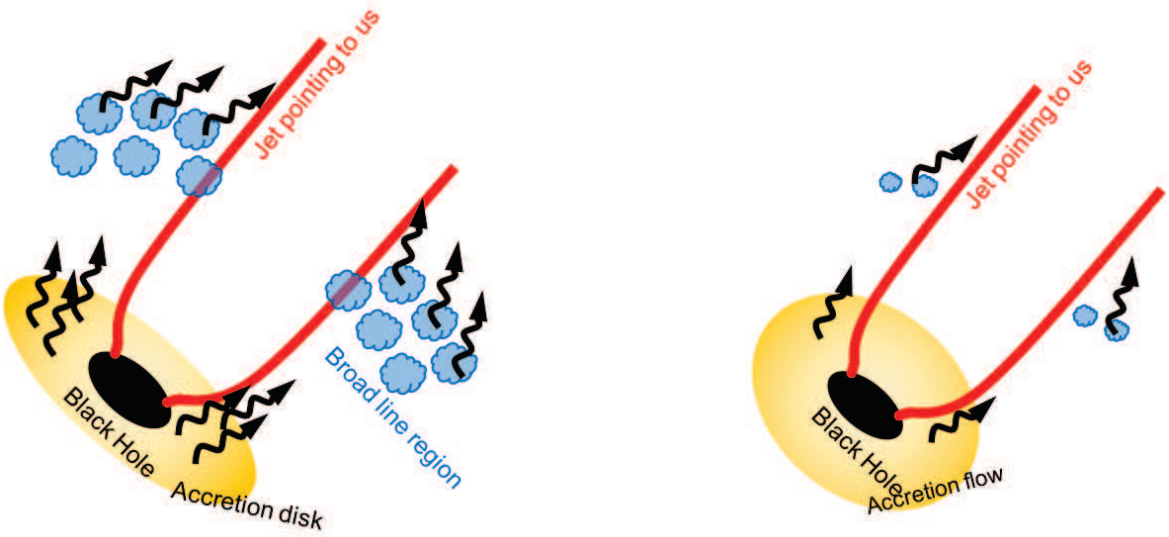

Fig. 3.4 Schematic view of blazars subclasses. FSRQs (in the left) present a rich radiation environment. The disk is supposed to be a optically thick, geometrically thin disk **?**. The present of broad emission lines in the optical spectra suggest the presence of the BLR. BL Lac objects (right panel) are instead less powerful than FSRQ, the disk is probably inefficient, an advected dominated accretion flow. Due to the weak or absent emission lines, the BLR is absent or poor.

Also in this case there is an historical classification of this kind of objects introduced by **?**. They classified a sample of *radio-galaxies* based on the relative position of the hot spot on the radio map. The low-luminosity Fanaroff-Riley class I (FR-I) are galaxies which show a rather compact emission arising close to the core, while the high-luminosity FR-II objects have the structure dominated by the radio lobes and most of the emission appears to come from the far end of the extended emission. The morphology difference between the two classes leads to believe a different physical scenario. This is strengthened by the different luminosity of the two classes. It exist, in fact, a dividing luminosity of $L_R = 10^{32}$ erg s^{-1} Hz^{-1} sr^{-1} at a frequency of 175 MHz to divide FR-I from FR-II. The two classes show two different jet behaviours on the kpc scale: on that scale, in FR-I jets the plasma seem to propagate more slowly than in FR-II. Also, FR-I were shown to have generally a lower accretion rate than FR-II (**?**).

Hypotheses that connected the different FR-I/-II features to the central engine (i.e. accretion) were introduced, to explain the observed differences (see more details in Chapter **??**).

Those radio-loud AGNs with their relativistic jets directed towards us are classified as blazars. Radio-galaxies are therefore thought to be the *parent population* of blazars.

3.3 Blazars

When the angle-of-view of radio-loud AGNs is only few degrees, we are observing a blazar. Blazars are quite peculiar sources, and should be rare indeed. Roughly, 10% of AGNs are radio-loud, and only ~ 1% of these, assuming random isotropically distribution of the sources, should have its axis aligned with our line-of-sight within 15°. Blazars are dominated by high variability. This is can be explained physically by the presence of the jet. As already said in **??**, the jet structure is still little-known, but the observations of the movement of the knots through the direction of the jet, suggest that the emission can vary. Observations of Blazars confirm that they are the most variable AGN subclass (**?**, **?**., **?**, **?**).

Blazar are prominent emitters from the radio frequencies all the way up to the very high energies above 1 TeV. One of the tracers of a Blazar is the radio emission coming from the jet. Their probable parent population is represented by FR-I and FR-II radiogalaxies with the jet oriented on the line of sight of the Earth. The optical emission is due to the synchrotron radiation of the relativistic electrons in the jet (more details in Section **??**). The X-ray emission is a delicate band in which several components contribute to the emission that we observe (see Section **??**). Finally Blazar can emit γ-ray photons due to leptonic (and, possibly, hadronic) emission (see Section **??**).

These characteristics make them a perfect environment to accelerate particles at high-energies. For this reason they have been considered as UHECRs birthplace, and then also high-energy neutrino emitters.

Blazars are generally divided in Flat Spectrum Radio Quasars (FSRQs) and BL Lacertae objects (BL Lacs). Also in this case the classification arises from observations. In particular, FSRQ and BL Lacs are classified based on the rest frame equivalent width (EW) of their broad emission lines: BL Lacs have $EW < 5$Å, while FSRQs have $EW > 5$ Å(**?**). This classification implies that while FSRQs show emission lines usually seen in quasars (hence the name), BL Lacs are characterised by the weakness or even absence of optical lines.

Figure **??** and **??** show typical spectra for FSRQ (**?**) and BL Lac (**?**). See also **?**. A physical interpretation of this difference can be connected to the different accretion mechanism. The emission lines observed in the optical spectrum should come from the broad line region of the blazar. Now we think that the absence or weakness of the lines in BL Lacs is not due to a particularly amplified continuum, but it is an intrinsic property. In fact, the BLR is irradiated by the ionizing photons produced by the accretion structure and therefore a difference in the broad emission lines could reflect a difference in the accretion luminosity. In the case of an efficient accretion (as the Shakura-Sunyaev disc), the BLR produces extremely luminous emission lines (see Section **??**). On the other hand, a radiatively inefficient accretion mechanism would not induce the BLR to produce

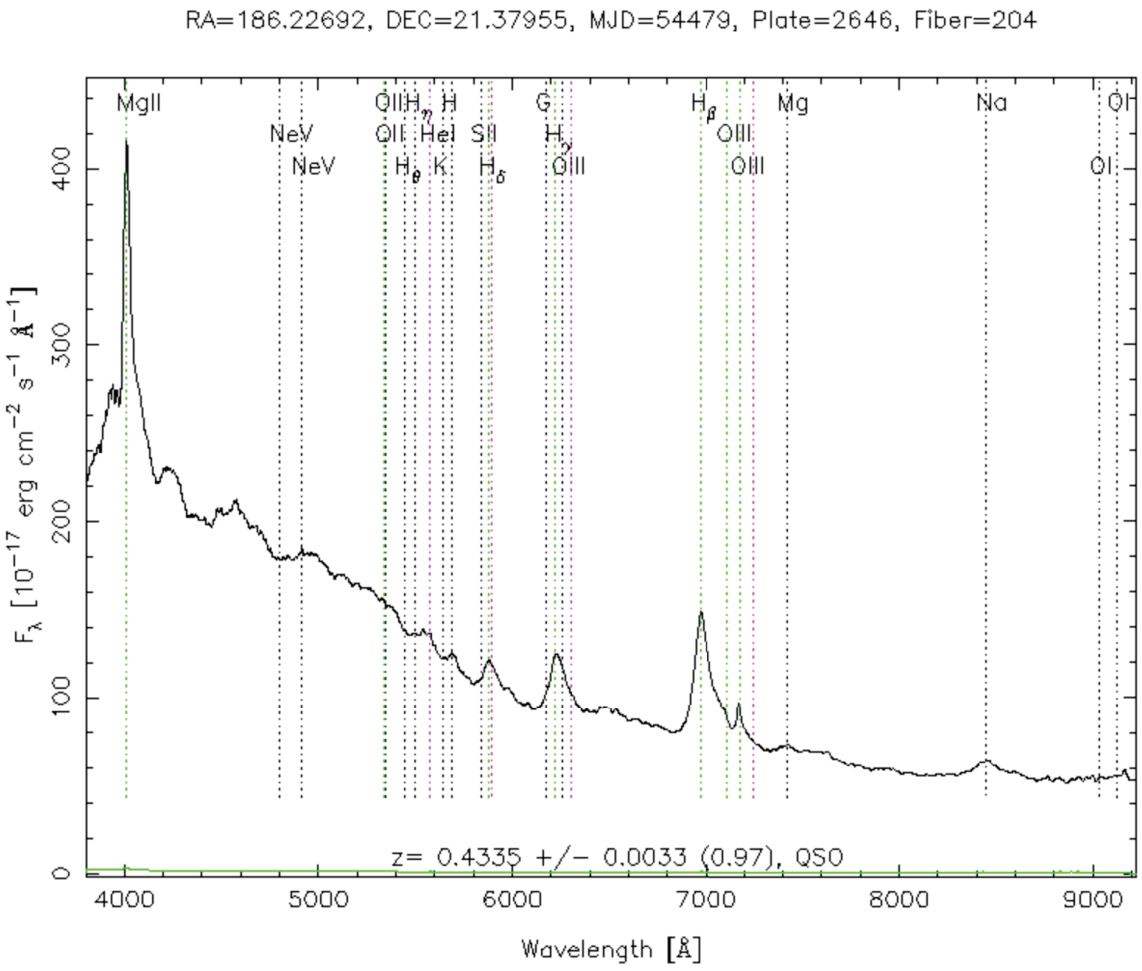

Fig. 3.5 Spectrum of FSRQ PKS 1222+261 taken with the Sloan Digital Sky Survey in January 2008. For each emission line the corresponding element is signed.

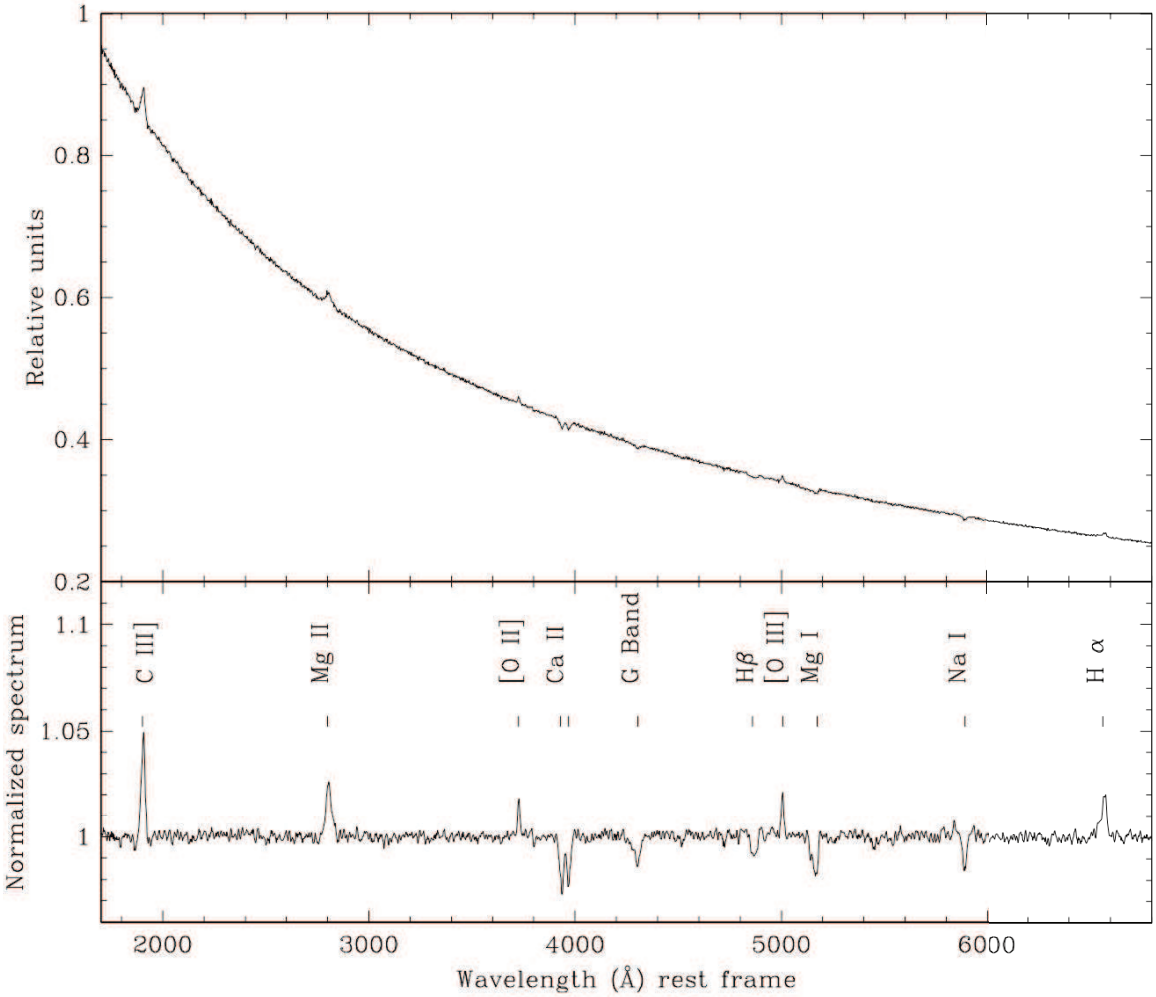

Fig. 3.6 Mean spectrum of BL Lac objects obtained combining the 23 objects in which intrinsic spectral features are detected. The first panel reports the mean spectrum assuming for the continuum a power law with index $\alpha = 0.90$ (which corresponds to the mean spectral index of the whole BL Lac sample). In the second panel normalized spectrum is shown (**?**).

emission lines. Since the EW can be considered a good measure of the line emission dominance over the underlying continuum, the EW classification could correspond to a physical intrinsic difference between the two classes. FSRQs show strong emission lines, being therefore linked to a radiatively efficient accretion process, such as a Shakura-Sunyaev disc, while the lineless BL Lacs were connected to radiatively inefficient accretion flows (RIAF), like the Advection-Dominated Accretion Flow (ADAF) (see Chapter **??**). The presence of a disc in FSRQs is confirmed from direct observations (see e.g. **?**).

Figure **??** shows a geometrical interpretation of the two subclasses of blazars. FSRQs (on the left) present a rich radiation environment. The disk is supposed to be a optically thick, geometrically thin disk (**?**). The presence of broad emission lines in the optical spectra suggests the presence of the BLR. BL Lac objects (on the right) are instead less powerful than FSRQ, the disk is probably inefficient, an advected dominated accretion flow. Due to the weak or absent emission lines, the BLR is absent or faint.

3.3.1 Spectral Energy Distribution of Blazars

As already mentioned, blazars emission covers the entire electromagnetic spectrum, from radio to γ-rays. This is a signal of the non-thermal processes at work in the jet. To easily have a comparison of source luminosities in different bands, it is common to plot the energy flux per logarithmic interval of frequency, $\log(\nu F_\nu)$, vs. $\log(\nu)$. This plot is the so-called *spectral energy distribution* (SED) and it is standard for multiwavelength studies.

The SED of blazars, shows two broad bumps, the so-called "double bump" shape. An example of the distribution of the data for a FSRQ (top panel) and a BL Lac object (bottom panel) over the SED is shown in Figure **??**. In both cases the double bump shape is clearly visible. The first bump peaks in the optical-UV band and it is typically ascribed to the synchrotron emission of the relativistic jet. The second one peaks in the γ-ray band and its nature is still under debate.

Another important feature of the blazar SED is its variability, that tends to be more intense and rapid at high energies, a feature that can be exploited in order to understand the mechanisms at work (see Chapter **??**). Quasi-simultaneous variability in different spectral bands is often (but not always) observed, suggesting that most of the flux is produced in a single region of the jet. Radio emission is an exception. As we already said the parental population of Blazars are radiogalaxies. In particular it is common to associate FR-II as parent population of FSRQs and FR-I to BL Lacs. In the models the emission from Blazars (both BL Lac and FSRQs) is assumed to come from a blob of radius $R_{\rm jet}$ to a certain distance from the SMBH and with a Lorentz factor Γ (see more details in the next Chapter). The entire emission of Blazar is assumed to happen close to the

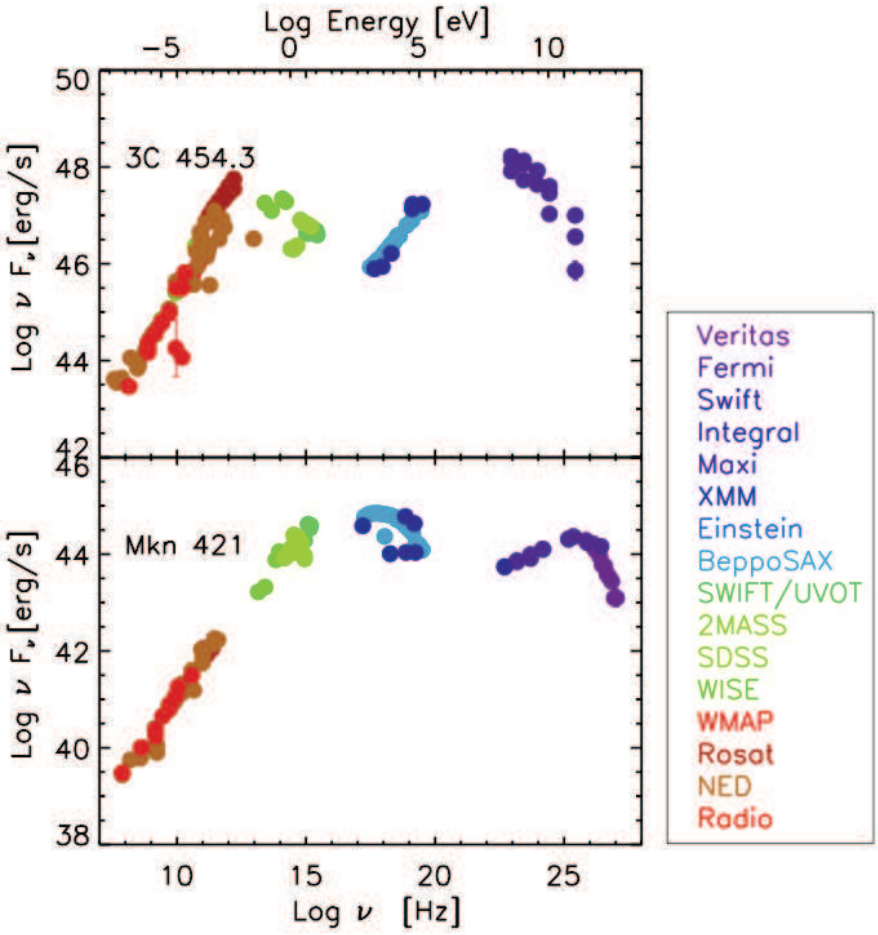

Fig. 3.7 An example of the characteristic SED of a FSRQ (3C 454.3 on the top) and a BL Lac object (Mkn 421 bottom panel) built with archival data. The main features are two broad bumps, arguably due to non-thermal processes in the relativistic jet.

SMBH, in the inner region of the jet. The models, in fact, assume a blob at a certain distance from the BH (< pc) and derive the spectrum coming from this region. In the case of the radio emission, this way to perform the models do not work well. In fact in the next Chapters often you see that the fit model do not work from radio emission (in particular for low energies). This can be easily explained since the radio band is dominated from the emission coming from the external region of the jet (> pc).

3.3.2 The Blazar Sequence

One of the first systematic analysis of the SED of the whole blazar class has been performed in **?**. The work presents a statistical study of a sample of 126 blazars observed at different wavelengths. They divided the sample of blazars by radio-luminosity subclasses and they

built an average SEDs for each *luminosity-bin*.
One of the main results is a homogeneus SED shape, characterised by two components, the first peaked at frequencies in the range $10^{13} - 10^{17}$ Hz, the second at about $10^{21} - 10^{24}$ Hz. Moreover, it seems that a trend of the peaks depending on the luminosity bin is present: the most powerful sources have the peaks at lower energies, while low luminosity ones peak at much higher energies.

Last, the higher luminosity-bin shall be composed mostly of FSRQs while BL Lacs are usually less bright. The SED of the higher luminosity-bin (and then of FSRQs) shows the second peak higher than the first one. This can be described by the so-called External Compton (EC) component emission (see section **??**).

Against the blazar sequence

The *blazar sequence* has been discussed for several years in the blazar-community. The main objection is that it could be the result of selection effects that are operating (e.g. **?**, **?**, **?**, **?**, **?**, etc). It is true, in fact, that in **?** most of the sources had not been observed at high-energies. Of all 126 blazars only 37 were observed in γ-ray band. In other words, the old sequence described the *tip of the iceberg* of the γ-ray emission of blazars considering only the brightest objects at high-energies.

Due to the main objection to the sequence, considering that as a a result of selection effects, **?** proposed the *simplified scenario* for blazars, completely alternative to the blazar sequence. The authors suggest that there is no physical link between the luminosity and the overall shape of a blazar. It means that, differently from the result of the sequence, it is possible to find BL Lacs objets at high redshift and luminous, such as FSRQs at low distances and with low luminosity. Then, for, this simplified scenario, both at high and low luminosities, we have both red (positions of the two peaks of the SED at low energy/frequency) at and blue (positions of the two peaks of the SED at high energy/frequency) blazars. Only observations of red BL Lacs or blue FSRQs can demonstrate this alternative scenario.

Blazar sequence 2.0

Motivated by these arguments, in **?** we have reported the systematic analysis of the whole blazars, with known redshift, belonging to the most recent γ-ray catalogue released by the Fermi Collaboration. This catalogue is the 3LAC sample that covers all the blazars detected by *Fermi* satellite after 4 years of operations (**?**). In this case the new analysis contains a more extended complete sample down to deeper sensitivity limits. The new

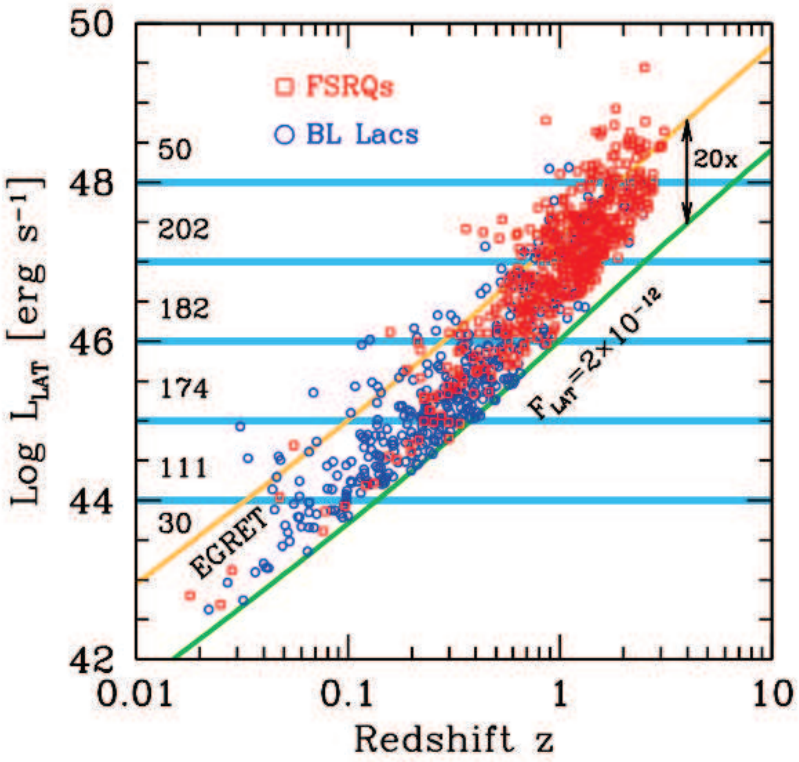

Fig. 3.8 The γ-ray luminosity (in the rest frame 0.1 – 100 GeV band) as a function of redshift for all blazars in the 3LAC catalog with known redshift. The solid lines refer to approximately the sensitivity limit of EGRET (onboard the CGRO satellite (orange line) and the Fermi/LAT sensitivity of the 3LAC sample, that is ~ 20 times deeper. The horizontal lines divide the sample into 6 γ-ray luminosity bins, and the corresponding total number of sources in each bin is indicated. Red squares refer to FSRQs, blue circles to BL Lacs, following the classification of the 3LAC catalog (**?**).

sample contains 747 objects classified as BL Lacs (299) or FSRQs (448). Figure **??** shows the average (over 4 years) γ-ray luminosity as a function of redshift. Blue circles are BL Lacs, red squares are FSRQs, as defined by **?**. It is clear that BL Lacs have lower redshifts and smaller γ-ray luminosities than FSRQs.
We divided these blazars into 6 γ-ray luminosity bins. The number of sources in each bin is reported in Figure **??**. Each bin spans a decade in γ-ray luminosity, for an easy comparison with the old sequence, whose radio luminosity bins were also a decade. For each luminosity-bin we obtain an average SEDs using a phenomenological model. We performed a study for the entire sample of blazars, but, for the first time, we analysed the trend of the SEDs for both FSRQs and BL Lacs separately. The main results are:

- The existence of sequence is confirmed with this new analysis. Figure **??** shows a comparison between the old and the new sequence. Bearing in mind that the luminosity-bins for the two analysis are different (the old sequence follow the radio luminosity-bin while the new one the γ-ray luminosity bin), the trends are coherent each others.

- When considering BL Lacs and FSRQs separately, we discover that the trend is different. Focusing first on FSRQs, we note that the overall shape of the SEDs does not change much, except for the Compton dominance (CD, it is the ratio between the Compton peak and the synchrotron one, see **?** for more details), that increases with the γ-ray luminosity. Contrary to the overall sequence, the γ-ray slope is almost constant, as well as the inferred peak frequencies of the synchrotron and the high energy components. Therefore, FSRQs show trends, but only in Compton dominance and in the X-ray slope. They do not become redder when more luminous (the pattern we called *sequence*).

  On the contrary, BL Lacs show a different behaviour. BL Lacs, in fact, show a remarkable trend for the entire SED, that changes by changing the bolometric luminosity. The peak frequencies become smaller as the luminosity increases: ν_S (the frequency of the first peak) goes from $\sim 10^{17}$ Hz to $\sim 10^{12}$ Hz increasing the luminosity L_γ by 4 orders of magnitude. Similarly, ν_C decreases by more than 4 orders of magnitude, with most of the change occurring around $L_\gamma \sim 10^{46}$ erg s^{-1}. The Compton dominance changes by one order of magnitude in the entire luminosity range, indicating that in BL Lacs the synchrotron and the high energy components are almost equal.

- When we put together all blazars, the sequence becomes more evident, and more similar to the original one. This is because, at high luminosities, the properties of

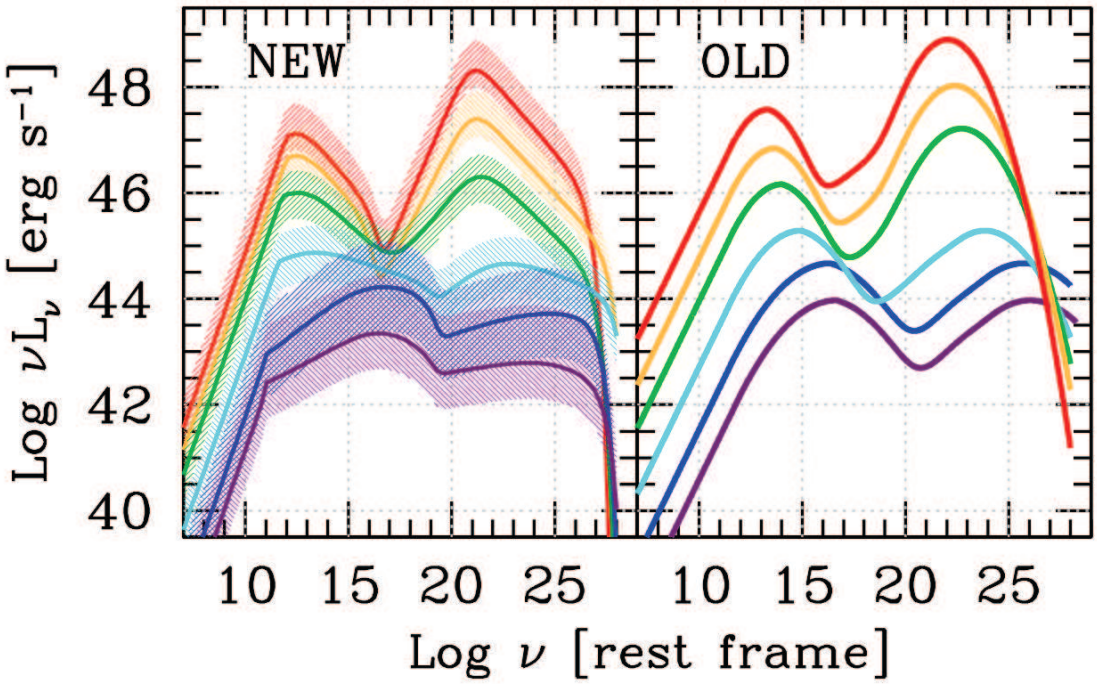

Fig. 3.9 Comparison between the new and the original blazar sequence for all blazars. Note that the original blazar sequence considered 5 radio luminosity bins, while the new one considers bins in the γ-ray band (**?**).

the average SED are dominated by FSRQs, while BL Lacs dominate the average SED at low L_γ.

A physical interpretation of these observations will be done in next Section. The blazar sequence can be, in fact, fruitfully interpreted in terms of the source physics. To do it we need to introduce the main emission processes of the jet.

3.3.3 Interpretation of the blazar sequence

Coming back to the blazar sequence, the SED modelling was performed using an analytical function as presented in the next paragraph. However the physical interpretation of the sequence is given in terms of leptonic model.

Phenomenological SEDs

The entire non–thermal SED of all blazars can be described by two broad humps and a flat radio spectrum. The simplest analytical function to approximate such a broad band SED is a single power in the radio, connecting to a smoothly broken power law, describing the low energy hump, plus another smoothly broken power law that describes the high energy hump. The most remarkable deviations to this simple description are related either to the emission from the accretion disc and the torus (in the optical–UV and the far IR, respectively) and the emission of the host galaxy visible at low redshifts. Therefore we propose to describe the entire non–thermal SED with the following prescription, completely phenomenological. In the radio band we have

$$L_{\rm R}(\nu) = A\nu^{-\alpha_{\rm R}}; \quad \nu \leq \nu_{\rm t} \tag{3.1}$$

where $\nu_{\rm t}$ is where the flat part ends. It can be interpreted as the self–absorption frequency of the most compact jet emitting region. This power law connects with:

$$L_{\rm S+C}(\nu) = L_{\rm S}(\nu) + L_{\rm C}(\nu);\ \nu > \nu_{\rm t} \tag{3.2}$$

describing the low and the high frequency part, respectively. The low energy part (that can be associated to synchrotron flux) is assumed to be:

$$L_{\rm S}(\nu) = B\,\frac{(\nu/\nu_{\rm S})^{-\alpha_1}}{1+(\nu/\nu_{\rm S})^{-\alpha_1+\alpha_2}}\,\exp(-\nu/\nu_{\rm cut,S});\ \nu > \nu_{\rm t} \tag{3.3}$$

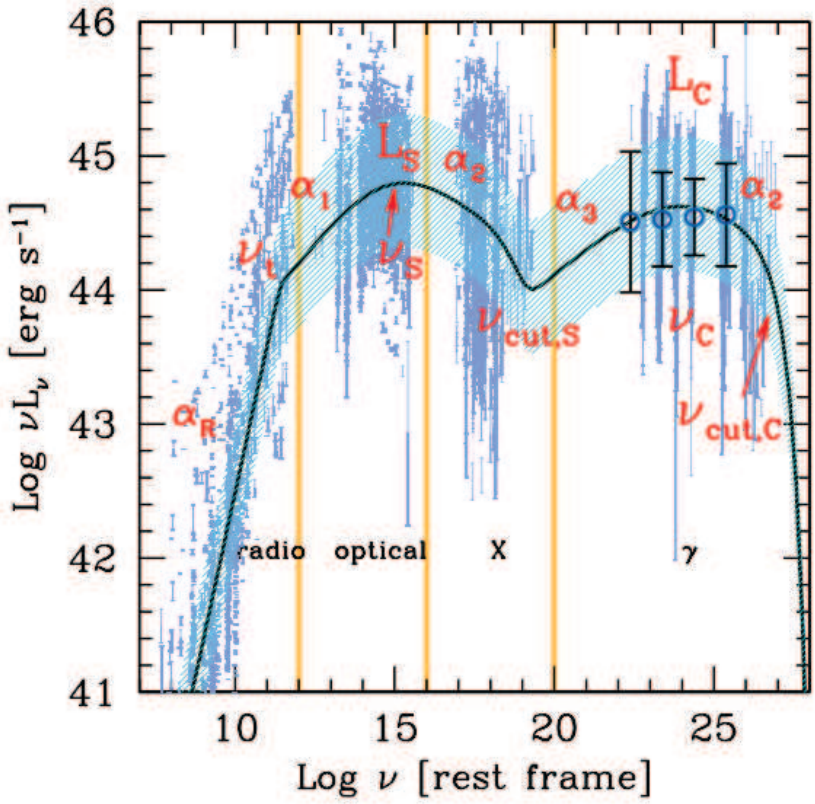

Fig. 3.10 Sketch illustrating the phenomenological description of the average SED of the blazars in each luminosity bin. In this example we show the SED of the BL Lacs in the bin $45 < log(L_\gamma/\mathrm{erg\ s^{-1}}) < 46$. We show the data of each source, with no averaging. The hatched stripe corresponds to 1σ of the dispersion of points around the fitting law showed with the black solid line. The red labels correspond to the needed parameters.

while the high energy part (that can be associated to the inverse Compton flux) is:

$$L_{\rm C}(\nu) = C\,\frac{(\nu/\nu_{\rm C})^{-\alpha_3}}{1+(\nu/\nu_{\rm C})^{-\alpha_3+\alpha_2}}\,\exp(-\nu/\nu_{\rm cut,C});\ \nu > \nu_{\rm t} \tag{3.4}$$

The constants A, B, C are obtained requiring:

- The radio spectrum and $L_{\rm S+C}(\nu)$ connect at $\nu_{\rm t}$;
- at $\nu_{\rm S}$ (the peak of the synchrotron spectrum), the luminosity is $L_{\rm S}(\nu_{\rm S})$;
- at $\nu_{\rm C}$ (the peak of the inverse Compton spectrum), the luminosity is $L_{\rm C}(\nu_{\rm C})$. This is parametrized giving the Compton dominance parameter CD, namely the ratio of the $\nu L(\nu)$ Compton and synchrotron luminosities.

In total, we have 11 parameters, all univocally related to observables. They are:

- the three typical frequencies $\nu_{\rm t}$ (self–absorption), $\nu_{\rm S}$ (peak frequency of the synchrotron spectrum), $\nu_{\rm C}$ (peak frequency of the high energy spectrum);
- the two cut–off frequencies $\nu_{\rm cut,S}$ and $\nu_{\rm cut,C}$ of the synchrotron and high energy spectra, respectively;
- the four slopes $\alpha_{\rm R}$ (radio), α_1 (connecting $\nu_{\rm t}$ with $\nu_{\rm S}$), α_2 (the slope after the synchrotron and the high energy peak), α_3 (the slope before the high energy peak).
- the two $\nu L(\nu)$ luminosities at the synchrotron and the high energy peaks.

We found that the same $\alpha_{\rm R} = -0.1$ can describe all sources, so the free parameters become 10. Consider also that the high energy cut–offs are not well determined, but are not very important for the description of the SED. Consider also that all parameters are observable quantities.

Physical interpretation of the Blazar sequence

The fact that FSRQs follow a clear trend in Compton dominance, while the peak frequencies ν_S and ν_C are almost constant, can be explained in terms of a nearly constant radiative cooling rate. We have already shown that the structure of a FSRQ is quite complex and the presence of the disk, the BLR the torus, etc. makes the environment of the FSRQs rich of soft photons (see Figure **??**). We will show that the external radiation plays a key role on the electromagnetic and neutrino emission of these objects (see Section **??**). The energy density of the external radiation $U'_{\rm ext}$ is proportional to Γ^2 (see **?**). Then if Γ is

approximately the same in different sources, the cooling rate is the same in FSRQs of different power. In fact the same cooling rate implies the same relevant electron energies and constant peak frequencies.

Furthermore the Compton dominance increases with total power in FSRQs. This can be explained in terms of magnetic energy density U'_B decreasing with luminosity. The ratio $U'_{\rm ext}/U'_B$, in fact, determines the value of the Compton dominance (see more details in **?**).

For BL Lacs, instead, the main radiation mechanism for the high energy hump is the synchrotron Self-Compton process (see Section **??**). It strongly depends upon the synchrotron radiation energy density in the comoving frame that is an increasing function of the observed luminosity. Therefore the cooling is not constant, but it is more severe in more powerful BL Lacs. As a consequence, the energy of the electrons emitting at the SED peak could be smaller (due to the larger cooling) in high luminosity BL Lacs, and both ν_S and ν_C would be smaller.

Chapter 4

Photons and neutrinos from Blazars

In order to consider blazars as neutrino emitters it is necessary to fully understand the physics behind the emission of the jet. The complex structure of an AGN makes hard the reconstruction of the entire physical processes that happen close to the inner regions and the central engine. Moreover, the nature, and then the composition, of the jet itself is still unknown. A relativistic jet is a highly collimated outflows from a supermassive black hole that transport matter, energy and momentum from the central engine to remote locations. The essential ingredients of the emitting volumes we call "knots" and "hot spots" are: a magnetic field (average value $\leq 1\mu$G at large kpc scale distance, and $1-10$ G close to inner region, < pc scale), a rather broad (in energy) distribution of relativistic electrons (and/or positrons) and photons. It is reasonable also the presence of cold (thermal) and/or hot (relativistic) protons. Most of the published works on jet composition are based on attempts to find evidence for the particle content: either pairs ($e^+ - e^-$) or normal plasma ($p - e^-$) or a mixed composition. The detection of neutrinos coming from blazars could give a boost to solve the question of jet content.

The spectral energy distribution of these objects puts some constraints to several models that try to reproduce the observations. The first bump composing the SED is produced by a population of relativistic electrons in the jets by synchrotron emission. This is clearly indicated by the high degree of polarisation of the optical radiation. The origin of the second component at high-energies is still under debate. The two competing scenarios are the *hadronic* and the *leptonic* models. In the first one the relativistic protons in the jet play a key role for the emission through $p\gamma$ channel or proton synchrotron, while the leptonic model attributes the origin of second bump to the electrons, by means of the *Inverse Compton* (IC) scattering processes.

This Chapter provides a brief description of the most important physical ingredients involved in the blazar phenomenology.

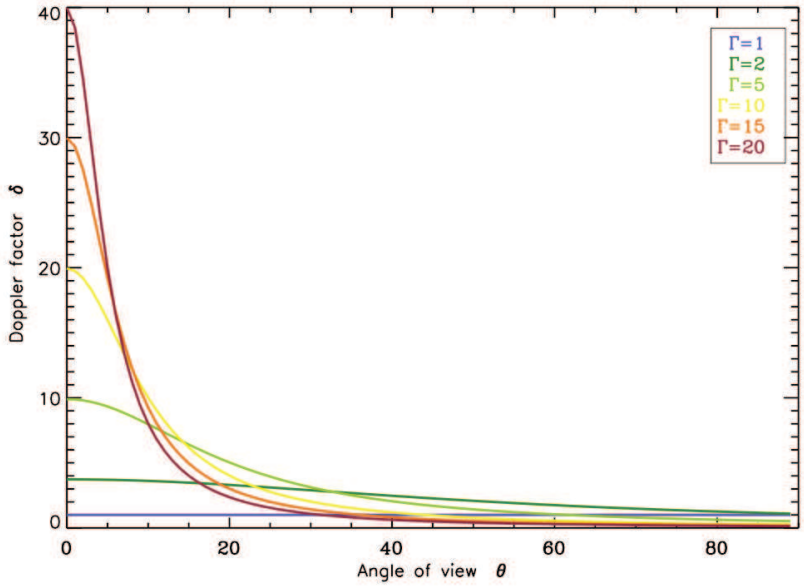

Fig. 4.1 Plot of the relativistic Doppler factor δ as a function of the viewing angle θ, for different values of Lorentz factor: $\Gamma = 1$ (blue line), $\Gamma = 2$ (dark green line), $\Gamma = 5$ (light green line), $\Gamma = 10$ (yellow line), $\Gamma = 15$ (orange line), $\Gamma = 20$ (red line). At $\theta = 0$ $\delta = 2\Gamma$, while at $\theta = 1/\Gamma$ $\delta = \Gamma$.

4.1 Relativistic effects

In order to produce non-thermal spectra that extend up to TeV γ-rays, particles need to be accelerated up to very high energies. We remand to Chapter 17 of **?** for a detailed discussion on the acceleration processes that can occur inside the jet. Here we want to introduce the main effects of the relativistic motions of the jet.

4.1.1 Doppler factor

Owing to the relevance of the relativistic effects that impact on the emission of the jet, it is suitable to introduce the main parameters that will be in use throughout the thesis. Let's consider a source moving with bulk speed $\beta \equiv v/c$ and *Lorentz factor* $\Gamma \equiv 1/\sqrt{1-\beta^2}$. The emission properties as seen by an observer located at an angle θ with respect to the direction of motion are strongly affected by both relativistic and Doppler effect. It is useful to introduce the so-called relativistic *Doppler factor* that takes into account both contributions and it is defined as

$$\delta \equiv \frac{1}{\Gamma(1-\beta\cos\theta)} \tag{4.1}$$

Table 4.1 Useful relativistic transformations

$\nu = \nu'\delta$	frequency
$t = t'/\delta$	time
$V = V'/\delta$	volume
$\sin\theta = \sin\theta'/\delta$	sine
$\cos\theta = (\cos\theta' + \beta)/(1 + \beta\cos\theta')$	cosine
$I(\nu) = \delta^3 I'(\nu')$	specific intensity
$I = \delta^4 I'$	total intensity
$j(\nu) = j'(\nu')\delta^2$	specific emissivity
$k(\nu) = k'(\nu')/\delta$	absorption coefficient

where $1/\Gamma$ express the special relativistic component while $1/(1-\beta\cos\theta)$ is the Doppler effect part. For Blazars usually the angle of view is assumed to be $\theta \sim 1/\Gamma$ and then $\cos\theta \sim \beta$ and $\delta \sim \Gamma$. Table **??** collects some of the most common transformations, useful when dealing with high energy cosmic sources. In the table the fundamental quantities used in high-energy astrophysical field are listed. Note that the observed frequencies, ν, are Doppler boosted with respect to the ones emitted, ν': $\nu = \delta\nu'$.

Figure **??** shows the observed δ as a function of the viewing angle θ and for different values of the Lorentz factor Γ.

4.1.2 Superluminal motion in jets and its consequences

High-resolution radio observations allow us to resolve individual emission components (the so-called *knots*) within the relativistic jets of radio-loud AGN. In many of these objects, these components appear to move across the sky with projected speeds faster than the speed of light, in some extreme cases with apparent transverse speeds of $v_\perp \sim 50c$. The accepted explanation for this phenomenon was first proposed by **?**. It turns out that this is merely a consequence of the finite speed of light, and does not pose any contradiction to special relativity.

Let us assume, as illustrated in Figure **??**, that the radio knot moves with a relativistic speed $v = c\beta$ along the jet, which is directed at a small angle θ with respect to our line-of-sight. Now, consider the apparent speed at which an observer on Earth would see this knot move across the sky between points A and B in Fig. **??**. If l is the distance between A and B, then the knot will move from A to B in a time (measured in the rest frame of the AGN) $\Delta t = l/(\beta c)$. The projected distance across the sky is given by $s = l\sin\theta = v\Delta t sin\theta$. Now, consider that the light emitted from the knot at point A has to travel an extra distance $x = v\Delta t\cos\theta$ to reach the observer, compared to light emitted at point B. Hence, the observer will see the knot moving from A at point B not in a time Δt later, but only at a

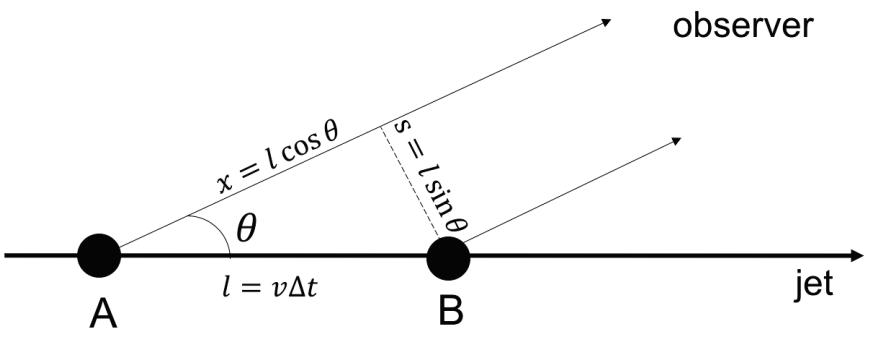

Fig. 4.2 Illustration of the geometry assumed to explain the superluminal motion of radio knots in AGN.

time $\Delta t_{\rm obs} = \Delta t - x/c = \Delta t(1-\beta\cos\theta)$. Hence, the apparent motion across the sky which the observer measures, is given by

$$v_\perp = \frac{s}{\Delta t_{\rm obs}} = \frac{v\sin\theta}{(1-\beta\cos\theta)} \tag{4.2}$$

For any given value of Γ , there is a preferred angle at which the apparent speed is maximum. It is straightforward to show that this happens for

$$\cos\theta_{\rm sl} = \beta \tag{4.3}$$

This value of $\theta_{\rm sl}$ is called the *superluminal angle* or *critical angle*.
At this angle, $\sin\theta = \sqrt{1-\cos^2\theta_{\rm sl}} = 1/\Gamma$, and the apparent transverse speed is therefore

$$v_\perp(\theta_{\rm sl}) = \frac{v/\Gamma}{(1-\beta^2)} = v\Gamma \tag{4.4}$$

Hence, for any given value of Γ , the speed can apparently reach a value of above c (**?**). For Blazar usually it is assumed that the angle of view is the critical angle, then $\theta \sim 1/\Gamma$ and $\delta \sim \Gamma$ assumes values in the range $10-20$.

4.2 SED interpretation

Electromagnetic emission can be divided into two components: thermal and non-thermal radiation. Thermal radiation is associated to particles, distributed in thermal equilibrium, according to Boltzman law. In sources in thermal equilibrium and with the opacity $\tau >> 1$, outcoming radiation has the typical shape of a black body.

Non-thermal radiation is associated to particles out of equilibrium, usually following a power-law, originating from other processes, such as the movement of charged particles in a magnetic field.

Blazars presents both thermal and non-thermal emission coming, respectively, from disk, torus, BLR, or from the jet. Due to the geometry of Blazars, the non-thermal emission of the jet usually dominates the thermal components from the inner regions.

4.2.1 Hadronic model

In hadronic models, both primary electrons and protons are accelerated to ultrarelativistic energies, with protons exceeding the threshold for $p\gamma$ photo-pion production on the soft photon field in the emission region. While the low-frequency emission is still dominated by synchrotron emission from primary electrons, the high-energy emission is dominated by proton synchrotron emission (depending on the intensity of the magnetic field B), π^0 decay photons, synchrotron and Compton emission from secondary decay products of charged pions, and the output from pair cascades initiated through these high-energy emissions intrinsically absorbed by $\gamma\gamma$ pair production (**?**, **?**, **?**,**?**).

The fast variability at high-energy that in some cases characterises blazar objects is one of the main issues against the pure hadronic model, since the cooling time for protons is characteristically very long. Moreover the classical "double bump" shape of the Blazar SED is not well described by the hadronic radiation spectrum that is typically flat in $\nu L(\nu)$ (see Figure **??**).

Figure **??** show a lepto-hadronic model (**?**) fit on BL Lac PG1553+113 for the period 2005-2009 and the neutrino flux for the corresponding IceCube event (ID 17). The data are obtained from **?**.

Bethe-Heitler pair production

A process that competes with the photo-meson channel, but is dominant at lower energies, is Bethe-Heitler pair production. In astrophysical environments, the process is more often realized when ultrarelativistic protons collides with low-energy photons,

$$p + \gamma \rightarrow e^+ + e^- + p$$

The process is energetically allowed when

$$\gamma_p \epsilon > m_e c^2$$

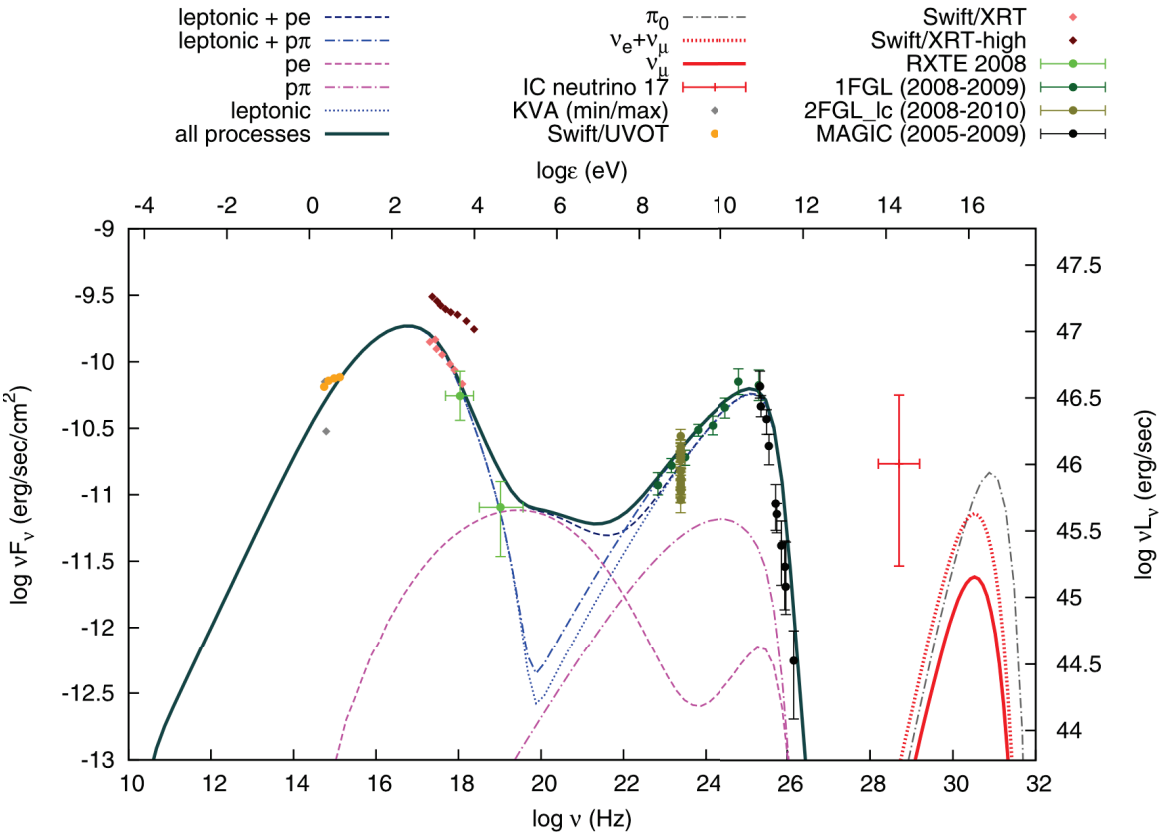

Fig. 4.3 SED of BL Lac PG 1553+113 for the period 2005-2009 and the neutrino flux for the corresponding IceCube event (ID 17). The data are obtained from **?**. Grey diamonds correspond to the KVA minimum and maximum fluxes and orange circles are the Swift/UVOT observations. Light and dark red diamonds are observations from Swift/XRT in 2005 corresponding to an intermediate and high flux level, respectively. With light green circles (from top to bottom) are plotted the average RXTE flux and the average 15-150 keV Swift/BAT flux. Green circles represent the average Fermi/LAT spectrum (2008 August-2009 February) and black circles the MAGIC observations over the periods 2005-2006 and 2007-2009. This figure shows the hadronic components: Bethe-Heitler spectrum (dashed pink line) and the cascade from photomeson (dotted-dashed pink line). The proto-synchrotron is missing. Also the leptonic model is plotted (dotted blue line). *Credits*: **?**.

where $\gamma_p = E_p / m_p c^2$ is the proton Lorentz factor, ϵ is the soft photon energy, and m_e is the mass of electron. The maximum energy of the electron (positron) is determined by the kinematics of the process

$$E_{e,\max} = \begin{cases} 4\gamma_p^2 \epsilon, & \text{if } m_e c^2 \ll \gamma_p \epsilon \ll m_p c^2 \\ m_p c^2 \gamma_p = E_p, & \text{if } \gamma_p \gg m_p c^2 \end{cases} \tag{4.5}$$

The pairs injected into the emitting region through this process have been computed using the analytical formulae by **?** (in which the Bethe-Heitler cross section is expressed following the work by **?**). For typical hadronic parameters of the emission region in a jet, the pairs are energetic enough to trigger an electro-magnetic cascade. In figure **??** the Bethe-Heitler contribute is clearly visible (pink dashed line called "pe"). We will see that this component play a fundamental role in the lepto-hadronic model (see discussion in the Chapter 8).

4.2.2 Leptonic model

In leptonic models, the radiative output throughout the electromagnetic spectrum is assumed to be dominated by leptons (electrons and possibly positrons), while protons that are likely present in the outflow, are not accelerated to sufficiently high energies to contribute significantly to the radiative output. The high-energy emission is then most plausibly explained by Inverse Compton scattering of low-energy photons by the same electrons producing the synchrotron emission at lower frequencies (**?**, **?**, **?**, **?**, **?**).

We refer to **?**, **?** and **?** for a standard description of the two main physical processes that occur in the leptonic scenario: the synchrotron emission and the Inverse Compton one. Here we want to introduce the main characteristics that are useful for the next discussions.

Synchrotron: Synchrotron emission is responsible for the peak in the UV to X-ray range. In other words, the first peak on the Blazar SED is well described by the synchrotron emission of relativistic electrons inside the jet.

The average synchrotron power emitted, P_S, by a single electron assuming an isotropic distribution, is given by:

$$P_s = \frac{4}{3} \sigma_T c U_B \gamma^2 \beta^2 \tag{4.6}$$

where σ_T is the Thomson scattering cross section, U_B is the magnetic energy density, γ and β are respectively the particle Lorentz factor and the velocity of the particle (**?**).

Inverse Compton: The Inverse Compton (IC) scattering is a physical process that occurs when the electron is in motion and can transfer some of its energy to a photon with less energy. There are two regimes in which the Inverse Compton scattering can happen, that are called the Thomson and the Klein-Nishina regimes. The latter case, occurring when the energy of the target photon in the frame of the electron is of the order of $m_e c^2$, is quite complex, a quantitative treatment is reported in **?**. In the Thomson regime, the energy loss rate of the electron is given by

$$P_{\rm IC} = \frac{4}{3}\sigma_T c U_{\rm rad}\gamma^2\beta^2 \tag{4.7}$$

Note the similarity with the synchrotron energy loss. The radiation energy density $U_{\rm rad}$ is related to the luminosity $L_{\rm rad}$ by

$$U_{\rm rad} = \frac{L_{\rm rad}}{4\pi R^2 c}$$

This relation is valid if we measured $U_{\rm rad}$ outside the source, at a distance R from its center.

Even if the leptonic model can fit well the SED of blazars, a pure leptonic model can't explain the emission of neutrinos. A lepto-hadronic model is then the only way to explain both the shape and the fast variability of the electromagnetic SED and the neutrino emission from Blazars. In our work we will use this scenario in which the electromagnetic SED is dominated by the leptonic emission but the jet is able to accelerate protons at high-energies to produce neutrinos detectable by IceCube. Among leptonic models there are different scenarios that require both *one zone* model and *multi-zone* model.

Synchrotron Self Compton: The most popular one zone model is the *Synchrotron Self-Compton* (SSC) scheme (see e.g. **?**). The SSC model assumes that target photons involved in the Inverse Compton are those emitted by synchrotron radiation by the same relativistic electrons with which they scattered via IC. With this assumption the two peaks of the SED are strongly linked due to the fact that the electron population that produce the synchrotron peak is the same that scatter to produce the second peak. This model involves few parameters and at present it is the most constrained model for BL Lacs. Figure **??** shows the resulting SED models, for Mkn421, obtained with two variability timescales: $t_{\rm var}$ = 1 day (red curve) and $t_{\rm var}$ = 1 hr (green curve). The model describes very satisfactorily the entire measured broadband SED (**?**). This model is able to extract the main characteristics of the jet, as the value of the magnetic field, with few considerations.

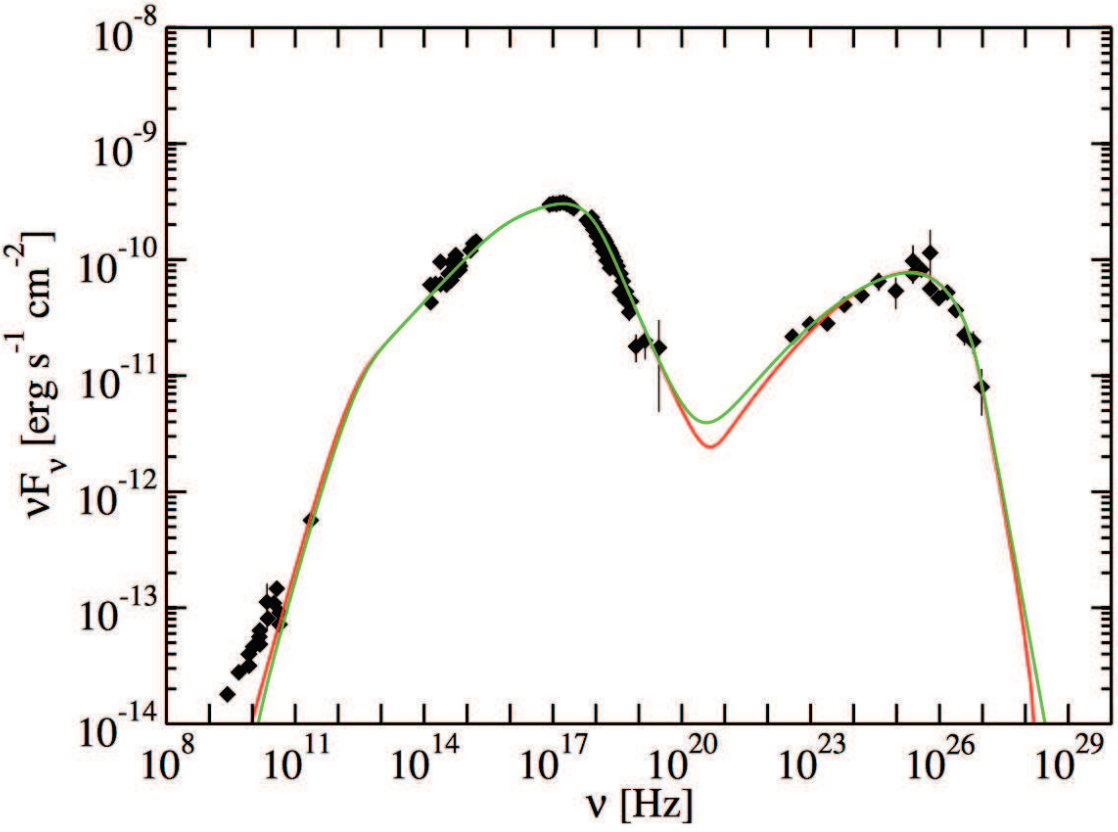

Fig. 4.4 SED of Mrk 421 with two one-zone SSC model fits obtained with different minimum variability timescales: $t_{\rm var}$ = 1 day (red curve) and $t_{\rm var}$ = 1 hr (green curve). *Credits*: **?**.

In fact, the ratio between the two peak frequencies $\nu_{\rm IC}/\nu_S$ allows to find $B'\delta$:

$$B'\delta = \frac{3\pi m_e c}{2e}\frac{\nu_S^2}{\nu_{\rm IC}}(1+z)$$

In the SSC model it happens that relativistic electrons are in a region with some radiation and magnetic energy densities. Then they will emit by both the synchrotron and the Inverse Compton scattering processes. The ratio of the two luminosities will be:

$$\frac{L_S}{L_{\rm IC}} = \frac{P_S}{P_{\rm IC}} = \frac{U'_B}{U'_{\rm rad}}$$

External Compton: Another popular leptonic model is the *External Compton* (EC) in which the target soft photons for the IC scattering do not originate in the jet, but are preferentially provided by the central region of the AGN: directly from the accretion disk or reprocessed by the BLR or by the torus. The photons emitted from the disk may interact with the gas clouds in two ways: they can be simply reflected by free electrons (Thomson scattering) or absorbed and reemitted, mainly in the broad optical lines. The energy density of this external radiation as seen in the blob rest frame is amplified by a factor Γ^2. For this reason in some cases this radiation can be dominant in comparison with the synchrotron one produced inside the jet. The EC model is particularly suitable to model FSRQs. In fact, according to the *blazar sequence*, the second peak of the the FSRQ SED is typically higher than the synchrotron one. A good explanation is given by the EC since in addition to the SSC model, the radiation of the BLR (if the distance of the blob d is less of ~ 0.2 pc) or of the torus ($d >$1 pc) can be involved in the high energy component. Figure **??** shows the overall optical to γ-ray SED of the FSRQ 3C 454.3 at five different epochs during 2009 November and December and an additional one ("low") representative of a low γ-ray state. We can see the large variability amplitude of the γ-ray flux, which spectrum is instead remarkably less variable **?**. In the case of BL Lacs, instead, the poor radiation environments allows one to neglet external targets to produce γ-ray photons. However there is the possibility to consider the photons coming from the inefficient disk (ADAF) as external radiation that can interact with both relativistic electrons and protons inside the jet (see Chapter **??**).

Multi-zones: Concerning *multi-zone* models, we refer to those models that consider contributions from different regions of the jet where the physical parameters can assume different sets of values. This kind of models are more complex and usually with more parameters. This can allow to reach more easily an agreement with the observations. As

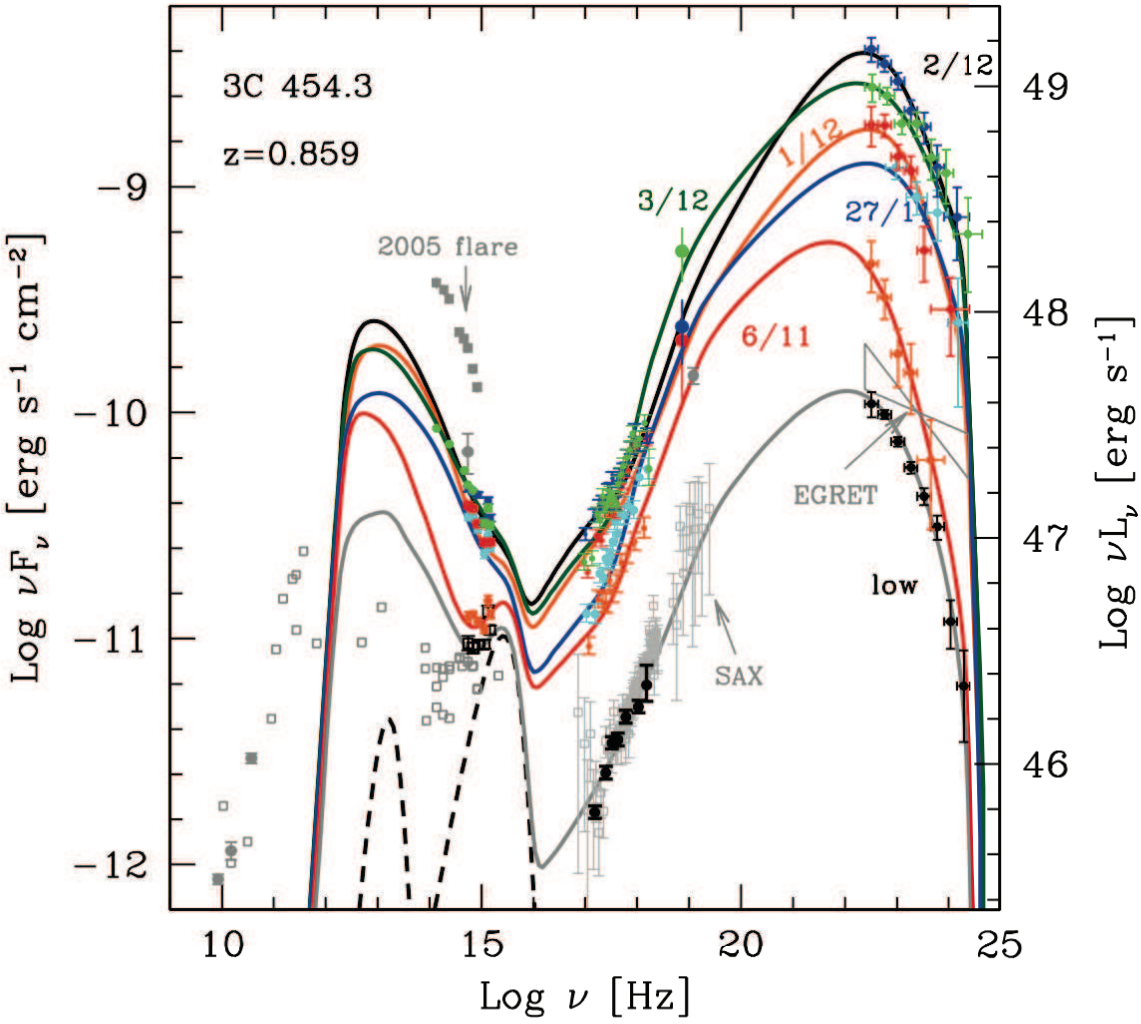

Fig. 4.5 The SED of 3C 454.3 at six selected epochs: 2009 November 6 and 27; 2009 December 1, 2 and 3 plus the previous "low" γ-ray state (see text). The different SED are labelled. The result of the modelling, including the accretion disc component, its X-ray corona contribution and the IR emission from the torus (dashed black lines) are also shown. For the SED of November 6, it shown, for illustration, the contribution of the EC and SSC components. Note that both are necessary to explain the X-ray spectrum, according to the modelling. *Credits*: **?**.

an example of inhomogeneous model, the *spine-layer* model (**?**) assumes that the jet is structured in a inner, faster and narrower spine and a surrounding, slower and less collimated layer, reproducing within the jet the structure observed in VLBI radio maps. In Chapter **??** a more detailed description of this model is presented.

The pure leptonic model cannot explain blazar as neutrino emitters. There are several *lepto-hadronic* models to explain both electromagnetic, neutrinos and in some cases also cosmic-ray spectra. In the following sections and Chapters we present lepto-hadronic models in which the same photons involved in the interaction with relativistic electrons are also involved in the $p\gamma$ reaction. In this way the electromagnetic SED can be dominated by the leptonic emission, but at the same time the neutrino production is also possible. A reasonable assumption on this model is that the accompanying UHE γ-ray photons (from π^0 decay and emitted by the $e^{\pm}$ pairs from the charged pions decay) are readily reprocessed through electromagnetic cascades, leaving the sources as a low-level, flat, MeV-GeV component.

4.3 Neutrino production in Blazars

In Section **??** the main channels to produce high-energy neutrinos are explained. Due to the environment rich of photons, the $p\gamma$ interaction is dominant in Blazars. Relativistic protons accelerated inside the jet can interact with photons of the jet itself or coming from external regions. Here we want to focus on the main features of this channel and the photons involved in this process. In the following we derive the ν emission calculated with simple assumptions, showing the different shapes of the neutrino spectrum by varying the main parameters.

4.3.1 Photomeson production efficiency

The photomeson production efficiency $f_{p\gamma}$ is a parameter depending on the proton cooling time $t_{p\gamma}(E_p)$ and the time on which protons escape from the region of neutrino production[1] or loose energy through adiabatic expansion. It is determined by the ratio:

$$f'_{p\gamma}(E'_p) = \frac{t'_{\rm dyn}}{t'_{p\gamma}(E'_p)} \tag{4.8}$$

[1] All physical quantities as measured in the jet comoving frame are primed.

where $t'_{\rm dyn} \approx R/c$ is the dynamical timescale, R is the radius of the region of proton acceleration, and $t'_{p\gamma}(E'_p)$ is the energy loss timescale for protons via $p\gamma$ channel.
In particular the inverse of the photo-meson cooling time is given by:

$$t^{-1}_{p\gamma}(E'_p) = c\int_{\epsilon_{\rm th}}^{\infty} d\epsilon \frac{n'_t(\epsilon)}{2\gamma'_p\epsilon^2}\int_0^{2\epsilon\gamma'_p} d\epsilon_r \sigma_{p\gamma}(\epsilon_r)K_{p\gamma}(\epsilon_r)\epsilon_r; \tag{4.9}$$

where n_t is the numerical density of the photons target that here is assumed as isotropic, $\gamma'_p = E'_p/m_pc^2$ is the proton Lorenz factor, and $\epsilon_{\rm th}$ is the threshold energy of the process. The cross section $\sigma_{p\gamma}$ and the inelasticity $K_{p\gamma}$ of the approximation, provided in **??**, can be used to solve the integral of equation **??**.

For a better understanding of equation **??** we report the calculation proposed in **?**. Assuming a generale spectral number density $n_t(\epsilon,\Omega) = dN_t/d\epsilon d\Omega dV$, they derive the photohadronic interaction rate $\dot{N}_{\rm sc}$ for ultrarelativistic hadrons in a radiation field, as given by:

$$\dot{N}_{\rm sc}(\gamma_p) = c\oint d\Omega\int_0^{\infty} d\epsilon(1-\beta_p\mu)n_t(\epsilon,\Omega)\sigma_{p\gamma}(\epsilon_r) \tag{4.10}$$

where $\mu = \cos\theta$, with θ the angle between the direction of the interacting photon and proton and $\epsilon = h\nu/m_ec^2$. In an inelastic collision, for example the pion production, an ultrarelativistic proton loses, on average, a fraction $K(\epsilon_r)$ of its original energy (as seen in Section **??**). Then the equation **??** can be written as:

$$t^{-1}_{p\gamma}(\gamma_p) = c\int_0^{\infty} d\phi\int_{-1}^{+1} d\mu(1-\beta_p\mu)n_t(\epsilon,\Omega)\sigma_{p\gamma}(\epsilon_r)K_{p\gamma}(\epsilon_r) \tag{4.11}$$

in which the only difference between the previous equation is the presence of $K_{p\gamma}(\epsilon_r)$ and the division of the integral in the solid angle Ω into the two angles ϕ and θ. Assuming now an isotropic radiation field, $n_t(\epsilon,\Omega) = n_t(\epsilon)/4\pi$ and ultrarelativistic protons, $\gamma_p \gg 1$, $\beta_p \to 1$, and rewriting the integral in the variable μ as depending on ϵ_r using the relation between the two variables: $\epsilon_r = \gamma_p\epsilon(1-\beta_p\mu)$, we obtain equation **??**.

4.3.2 Neutrino spectrum

A good approximation of the neutrino spectrum is given by:

$$E_\nu L_\nu(E_\nu) \approx \frac{3}{8} f_{p\gamma}(E_p)E_pL_p(E_p) \tag{4.12}$$

where 3/8 is the fraction of the proton energy given to neutrinos (**?**). As already said, in this case, the neutrino spectrum depends on the proton energy distribution but also on the

photon target spectrum. The dependency of the photon spectrum is contained into $f_{p\gamma}$. In fact, the energy loss timescale for protons $t_{p\gamma}$ depends on the target photon density $n_t(\epsilon)$ and on the energy threshold (see Section **??**). The consequence is that the spectrum of neutrinos does not simply follows the shape of proton spectrum.

As already said, the complex structure of Blazars ensures that there are several emitting components that can produce the photon target for the relativistic protons inside the jet. In the following we show the main hypothesis taken into consideration in literature. Due to the different structures, that characterised the two subclasses of Blazar, we will distinguish FSRQs from BL Lacs.

4.3.3 Cosmic ray spectrum

To calculate the neutrino spectrum coming from a source (blazar in our case) it is necessary to do some assumptions about the CR spectrum involved in the $p\gamma$ reaction.

It is reasonable to assume that the population of CR (protons) distribution is parameterised by a cut-offed power-law:

$$L_p(E_p) \approx k_p E_p^{-n} \exp\left(-\frac{E_p}{E_{\rm cut}}\right) \tag{4.13}$$

The main parameters are:

- L_p: the total injected luminosity of relativistic protons. $L_p = \int_{E_{\rm min}}^{E_{\rm max}} L_p(E_p) dE_p$;
- n: the spectral index;
- $E_{\rm min,max}$: the upper and lower limit of the energy of relativistic protons involved in the photomeson production.

4.3.4 Target photons spectrum

As sketched in Figure **??**, the neutrino emission can result from the interaction of p with non-thermal photons in the jet, or with external photons. In the following each component is studied independently for both FSRQs and BL Lacs.

Non-thermal component

With non-thermal component we refer to the radiation produced in the jet, that is the synchrotron radiation (and the Inverse Compton emission in some cases) produced by relativistic electrons in the jet. The synchrotron emission is clearly visible in the SED for

both FSRQs and BL Lacs. Usually this component can be approximated by a power-law as reported in equation **??**. In this model the photon target density is fixed (mostly of the times), while the parameters detailing the relativistic protons population involved in the $p\gamma$ interaction are free. In particular the main parameters that affect the neutrino spectrum are:

- $R_{\rm jet}$: the radius of the blob inside the jet in which the interaction $p\gamma$ is assumed to take place. Consequently the distance from the SMBH of this blob is assumed to be $d \approx R_{\rm jet}/\theta_{\rm jet} \approx R_{\rm jet}\Gamma$ since $\theta_{\rm jet} \approx 1/\Gamma$ (see Section **??**)[2].

- δ: the Doppler factor that is the same for the entire jet (we are assuming a *one zone* model) is usually suppose to be $\delta \sim 15-20$ in the case of FSRQs and $\delta \sim 10-15$ in case of BL Lacs.

- n: The spectral index of equation **??**. In general we assumed $2 < n < 3$. The maximum limit coincides with the spectral index observed in the CR-rays spectrum between the knee and the ankle.

- $E_{\rm cut}$: The cutoff energy of equation **??**. This parameter fixes also the maximum value of energy of the CRs involved in the interaction with the target photons. It is usually fixed in a range 10^{17} eV $< E_{\rm cut} < 10^{19}$ eV.

A distinction between FSRQs and BL Lacs is necessary because of their different proprieties.

FSRQs To apply this model to the subclass of FSRQs we consider the same sample used for the *blazar sequence 2.0*. We select those blazars listed as "FSRQ" in the 3FGL catalogue and with known redshift z. A classification for five luminosity bins (from 10^{44} erg s^{-1} $< L_{\rm LAT} < 10^{45}$ erg s^{-1} to $L_{\rm LAT} > 10^{48}$ erg s^{-1}) was performed for these 448 FSRQs. For each luminosity bin we used the formulae in section **??** to find the average SED showed in fig. **??**.

In section **??** the main characteristics of the *blazar sequence 2.0* have been already discussed. Here we remark only that FSRQ form a sequence, but only in Compton dominance (the ratio between the two frequency peaks of the SED) and in the X-ray slope. They do not become redder when more luminous. Then the synchrotron emission from FSRQs seems to not change shape and position for different luminosity bins. This means that for

[2]Note that we are assuming to be at the superluminal angle $\theta_{\rm jet} = \theta_{\rm sl}$.

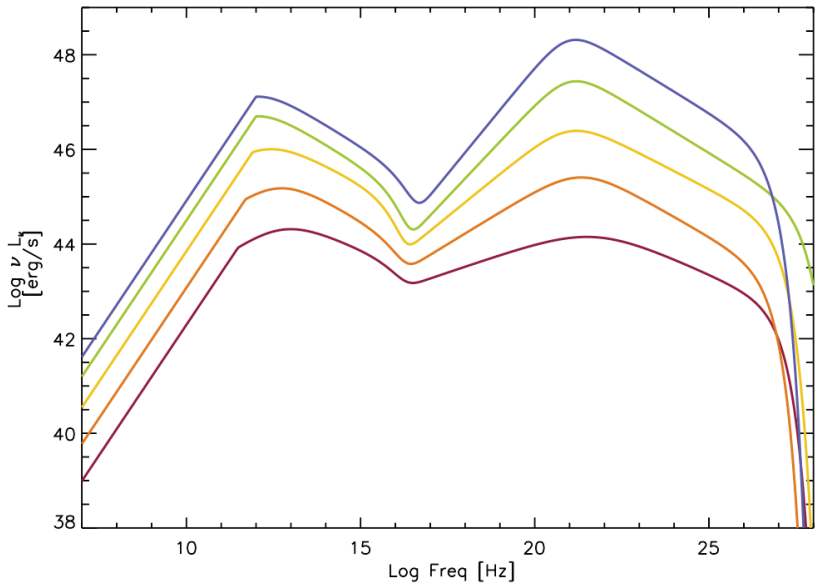

Fig. 4.6 FSRQs sequence. The different curves represents a different luminosity bin, from FSRQs with $L_{\rm LAT} > 48$ (blue curve) to $44 < L_{\rm LAT} < 45$ (dark red curve) in steps of 10.

equal proton spectrum the neutrino spectrum for different luminosity bins will have the same shape (but different levels).

Fig. **??** shows different neutrino spectra changing the main parameters. For all four spectra the fixed parameters are:

- The cosmic-ray luminosity $L_p = 10^{45}$ erg s^{-1}. Even if keeping this parameter fixed is not physically realistic, this allows to have an idea of the importance of the target photon distribution. A more realistic scenario is given in the next section;
- The radius of the blob containing the protons $R_{\rm jet} = 10^{16}$ cm;
- The minimum energy of the accelerated protons inside the jet that can be involved in the photomeson reaction, $E_{\rm min} = 3 \times 10^{11}$ eV. This parameter is important because it is linked with the total injected luminosity of the protons L_p. In fact protons at low energy do not contribute to the high-energy neutrino emission ($E_p \approx 20 E_\nu$). However, due to the distribution of protons assumed (equation **??**), the choice of $E_{\rm min}$ is dictated to do not have a too large proton power.

The parameters that change between the four spectra are then: n, $E_{\rm cut}$ and δ. In particular, solid lines are derived using: $n = 2$, $E_{\rm cut} = 10^{17}$ eV and $\delta = 20$. The variation of the spectral index of cosmic rays n implies a reshaping of the neutrino spectrum. This is shown in the short-dashed line in which $n = 2.7$ (the others parameters are fixed).

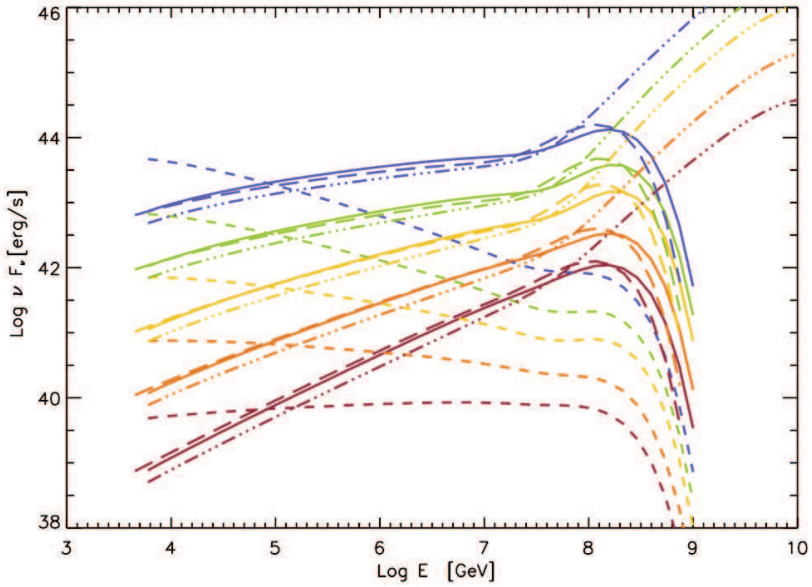

Fig. 4.7 Neutrino spectra for different luminosity bins of FSRQs. Each colour corresponds to the bins in figure **??**. On the basis of the parameters fixed to build the solid line, short-dashed line varies n, three-dotted dashed line varies $E_{\rm cut}$ while long-dashed line varies δ.

As already said, $E_{\rm cut}$ changes the maximum energy of the protons involved in the $p\gamma$ reaction. Three-dotted-dashed lines show the neutrino spectrum using $E_{\rm cut} = 10^{19}$ eV. In this case the photons involved in the photo-meson reaction can have higher energy and as a consequence, also photons at lower energies can intervene in the interaction, as clear from the energy threshold equation already presented in Equation **??**:

$$\epsilon \simeq \frac{10^{17}}{E_p} \text{eV}$$

If $E_p = 10^{19}$ eV, the photons with minimum energy involved in the reaction are photons with $\epsilon \simeq 10^{-2}$ eV which corresponds to mid infrared photons ($\sim 10^{12}$ Hz). The slope variation of the neutrino spectrum at $\sim 10^8$ GeV reflects the spectrum of the target photons. For this reason the neutrino spectrum change slope at high energies.
In the last neutrino spectrum (long-dashed line) only the Doppler factor parameter is changed, $\delta = 15$. The neutrino spectrum shifts only in energy with a weak variation of the shape.

Fig. **??** is useful to understand the effect of the main parameters to the shape of the neutrino spectrum. It stands to reason that the real situation should be more complicated.

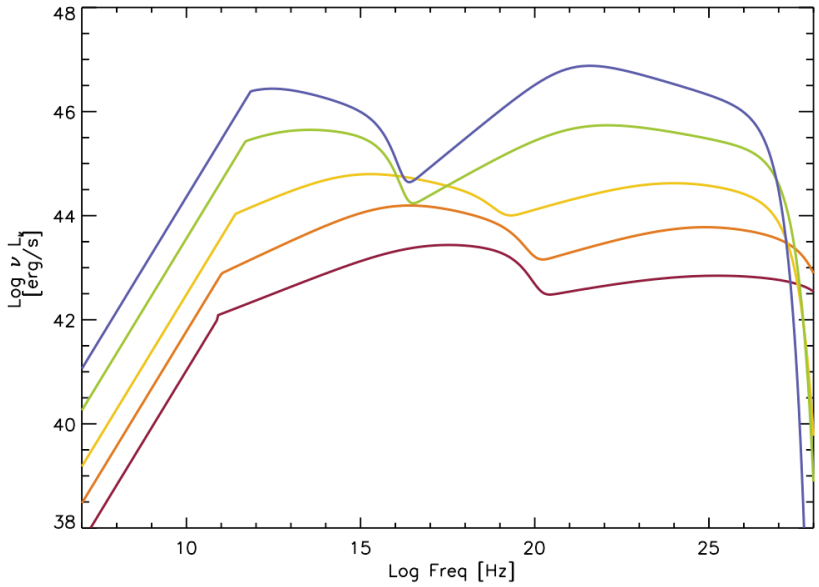

Fig. 4.8 BL Lacs sequence. The different curves represent a different luminosity bin, from BL Lacs with $L_{\rm LAT} < 10^{43}$ erg s^{-1} (blue curve) to 10^{47} erg s$^{-1} < L_{\rm LAT} < 10^{48}$ erg s^{-1} (dark red curve).

For example a more physical scenario could be described by the variation of L_p between the different luminosity bins of FSRQs.

BL Lacs A similar analysis can be carried out for BL Lacs. Also in this case the *blazar sequence 2.0* presents a trend specific for BL Lac SEDs. The main difference with the previous case is that the synchrotron shape of the BL Lac SEDs varies for different luminosity bins. A main result of the *blazar sequence 2.0* is, in fact, that the position of ν_S and ν_C changes for BL Lacs. The synchrotron peaks from IR region to high luminosity: $\nu_S = 8 \times 10^{11}$ Hz for 10^{47} erg s$^{-1} < L_{\rm LAT} < 10^{48}$ erg s^{-1} while $\nu_S = 8 \times 10^{16}$ Hz for $L_{\rm LAT} < 10^{43}$ erg s^{-1} (see Table 1 of **?** for details). Differently from the FSRQs case, now we expect a dependence of the neutrino spectrum on the lumimosity bins of BL Lacs even for a fixed CR spectrum. Fig. **??** shows the average SEDs for the 299 BL Lacs selected from the 3FGL catalogue as already presented in **?**. The variation of the shapes for the different luminosity bins is evident.

As in the analysis of FSRQs, we fixed some parameters. The fixed parameters are, as in the case of FSRQs: $L_p = 10^{45}$ erg s^{-1}, $R_{\rm jet} = 10^{15}$ cm and $E_{\rm min} = 3 \times 10^{11}$ eV. Note that in this case $R_{\rm jet}$ is a factor 10 lower than the case of FSRQs. In fact, consider a small $R_{\rm jet}$, allows us to maximise the neutrino emission. Moreover, in contrast to FSRQs, in BL Lac objects fast variability is observed (**?**). This suggests that the region of emission is smaller than the FSRQs one. The other parameters are chosen as follows:

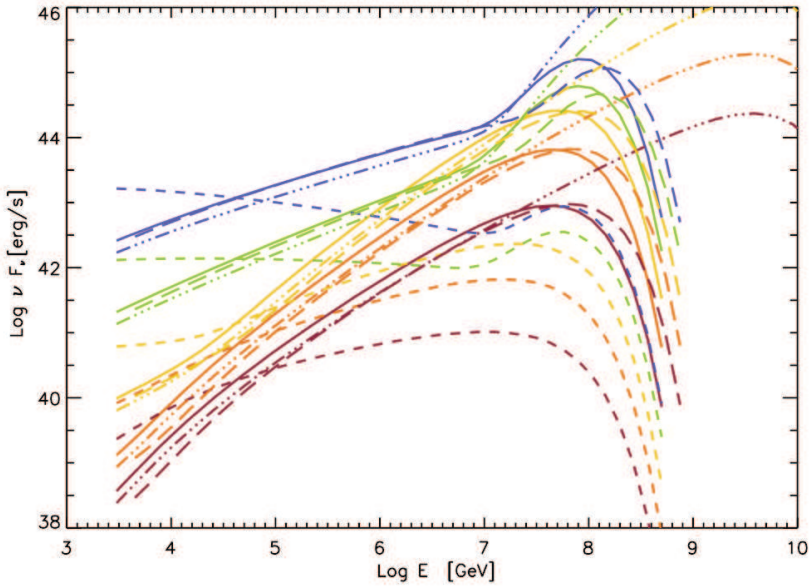

Fig. 4.9 Neutrino spectra for different luminosity bins of BL Lacs. Each colour corresponds to the bins in figure **??**. On the basis of the parameters fixed to build the solid line, short-dashed line varies n, three-dotted dashed line varies $E_{\rm cut}$ while long-dashed line varies δ.

- solid line: $\delta = 10$, $n = 2$, $E_{\rm cut} = 10^{17}$ eV
- short-dashed line: $\delta = 10$, $n = 2.7$, $E_{\rm cut} = 10^{17}$ eV
- three-dotted-dashed line: $\delta = 10$, $n = 2$, $E_{\rm cut} = 10^{19}$ eV
- long-dashed line: $\delta = 15$, $n = 2$, $E_{\rm cut} = 10^{17}$ eV

Note that the last two luminosity bins at high energies are likely contaminated by FSRQs wrongly classified as BL Lacs. Unlike the FSRQs case, here the neutrino spectra present different shape due to the photon target trend. The low luminosity bins do not present a change of the slope at $\sim 10^7$ GeV. This because the synchrotron peak is less pronounced and then the shape of the photons involved in the $p\gamma$ luminosity does not present any pronounced peak as in the case of the high luminosity bins or the FSRQs case.

There is another way to classify BL Lacs given by the Fermi Collaboration. Due to the shift of the peaks in the SED sequence, BL Lacs can be divided according to the position of the synchrotron peak ν_S. In this classification there are three different subclasses:

- Low synchrotron peak BL Lacs (LSP or LBL) in with $\nu_S < 10^{14}$ Hz.

- Intermediate synchrotron peak (ISP or IBL), in which 10^{14} Hz $< \nu_S < 10^{15}$ Hz.;
- High synchrotron peak (HSP or HBL) with $\nu_S > 10^{15}$ Hz.

This classification is unrelated to the gamma-ray band luminosity, $L_{\rm LAT}$, as the classification in the blazar sequence. Then it is not properly correct to associate the luminosity bins $10^{47} < L_{\rm LAT} < 10^{48}$ erg s^{-1} and $10^{46} < L_{\rm LAT} < 10^{47}$ erg s^{-1} to the LSP BL Lacs, $10^{45} < L_{\rm LAT} < 10^{46}$ erg s^{-1} to ISP and the last two bins to HSP, even if the majority of objects owned these bins respect the Fermi classification. A more accurate discussion about this Classification is done in Section **??**. There we performed the same analysis on neutrino emission using as photons target the average SED of LSP, ISP and HSP BL Lacs.

External Photons for FSRQs

In the case of FSRQs, external radiation such as the BLR and the tours radiation can interact with relativistic protons inside the jet and trigger the photomeson reaction. For BL Lacs the situation is more complex and we will discuss the potential external radiation field in the next chapter.

BLR Section **??** already presents a description of the broad line region as composed by clouds of ionized plasma surrounding the inner region of an AGN. These clouds are visible thanks to the broad emission lines in the optical spectrum. We will consider the BLR radiation significant for the neutrino production only in FSRQs. In the case of BL Lacs the emission lines in the optical spectrum are weak or even missing, leading to suppose that the accretion flow is inefficient. The BLR luminosity is strongly linked to the disk luminosity of the AGN.

The BLR is assumed to be a shell at a distance:

$$R_{\rm BLR} = 10^{17} L_{\rm d,45}^{1/2} \text{ cm} \tag{4.14}$$

where, for simplicity we consider the bolometric disc luminosity $L_{\rm d,45}$. This implies that the energy density of the line photons for an observer at rest with the black hole is constant:

$$U_{\rm BLR} = f_{\rm BLR} \frac{L_{\rm d,45}}{4\pi R_{\rm BLR}^2 c} = 2.65 \times 10^{-2} \text{ erg cm}^{-3} \tag{4.15}$$

where $f_{\rm BLR}$ is considered to be 0.1 and it is the fraction of $L_{\rm d}$ reprocessed in lines, especially the Lyman α line, and the continuum. The spectral shape of the BLR observed in the comoving frame of the jet can be approximate as a blackbody peaking at a factor Γ times

the rest-frame frequency of the Lyman α line (see **?** and **?** and **?** for further details). The energy density within $R_{\rm BLR}$ in the rest frame,

$$U_{\rm BLR}(\nu) = \xi \frac{2h\nu^3}{c^2} \frac{1}{e^{\frac{h\nu}{kT}} - 1} \tag{4.16}$$

where T is the temperature of the blackbody, and ξ is a normalization factor and it can be determine from equation **??** and **??**:

$$\xi = \frac{U_{\rm BLR}}{\int_0^\infty U_{\rm BLR}(\nu)} d\nu$$

Finally an observer comoving with the jet emission measures $U'_{\rm BLR}$ given by:

$$U'_{\rm BLR} = U_{\rm BLR}\Gamma^2 \tag{4.17}$$

To represent the energy density of the BLR we chose $T = 10^4$ K that corresponds to a blackbody with a peak (in νF_ν), in the comoving frame, around a frequency $\nu^{\rm BLR}_{\rm peak} = 2 \times 10^{14}\Gamma$ Hz (see **?** for a detailed discussion).

Torus An analogous discussion can be performed for the torus. Also in this case the shape can be approximated with a blackbody radiation with a temperature in the infrared band. We select $T = 10^3$ K to have a blackbody peaking at $\nu^{\rm IR}_{\rm peak} = 2 \times 10^{13}$ Hz.

We approximate the result of **?** by assuming that the torus reprocesses half of the disc radiation (corresponding to an opening angle of 60°). The typical distances of the torus, $R_{\rm IR}$, is assumed to scale as $L_{\rm d}^{1/2}$, yielding a constant temperature ($\propto L/R^2_{\rm IR}$). From the result of **?** we then set

$$R_{\rm IR} = 10^{18} L^{1/2}_{\rm d,45} \text{ cm}$$

and the corresponding radiation energy density, as measured in the jet comoving frame, is

$$U'_{\rm IR} = f_{\rm BLR} \frac{L_{\rm d,45}\Gamma^2}{4\pi R^2_{\rm BLR} c} = 3 \times 10^{-4} \text{ erg cm}^{-3} \tag{4.18}$$

Fig.**??** shows the spectra for a typical source of the luminosity bin $L_{\rm LAT} > 10^{48}$ erg s^{-1}. The grey dots are the data of 3C 454.3, one of the most studied FSRQ in this bin. The black line is the average SED of this bin calculated in the FSRQ sequence. The blackbody approximate emission of the BLR (dotted line) and the Torus (dotted-dashed line) are shown. Three neutrino spectra are also shown. Assuming a proton spectrum with $L_p = 10^{45}$ erg s^{-1}, $n = 2$, $E_{\rm cut} = 10^{17}$ eV, $E_{\rm min} = 10^{11}$ eV and with a Lorentz factor $\Gamma = 20$, we use as photon

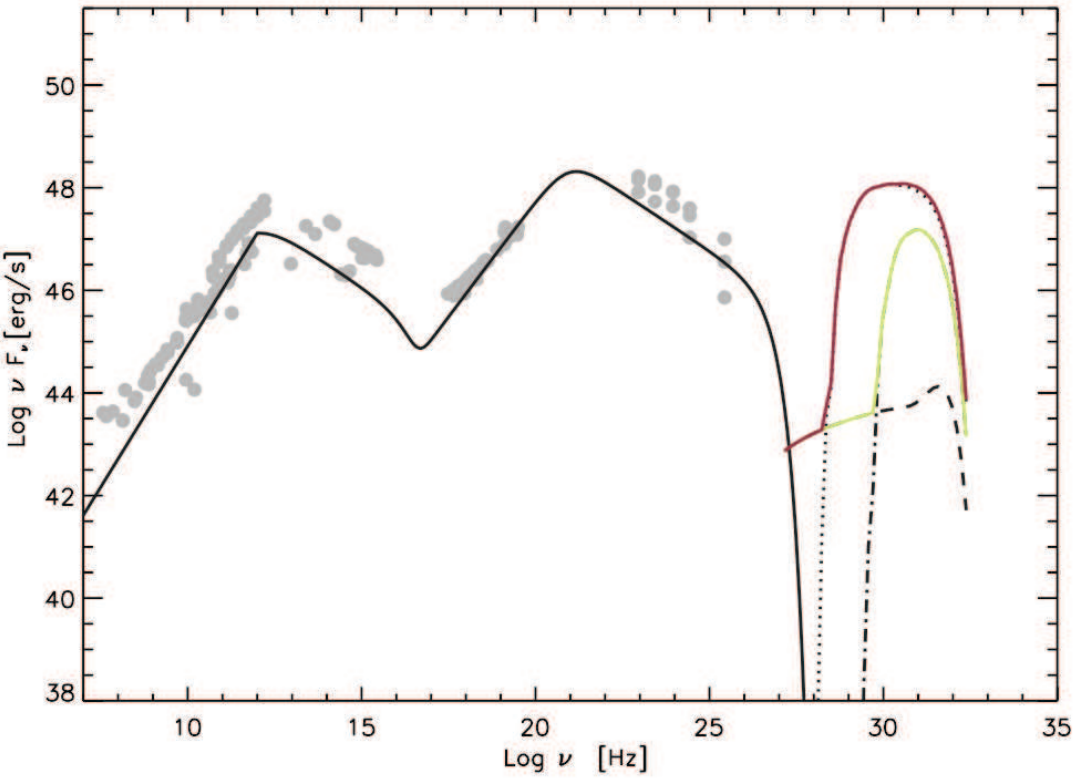

Fig. 4.10 SED for a typical FSRQs belonging to the luminosity bin $L_{\rm LAT} > 10^{48}$ erg s^{-1}. Grey dots are the data of 3C454.3, black line shows the average SED of this luminosity bin derived with the phenomenological model. The two dotted line are respectively the blackbody spectrum of the BLR and the corresponding neutrino spectrum. Dotted-dashed lines are respectively the torus and its neutrino spectrum. Dashed line is the neutrino spectrum using as photon target the synchrotron radiation of the jet. Red and green lines are the expected neutrino spectrum inside and outside the BLR.

targets the BLR radiation (dotted line), the torus emission (dotted-dashed line) and the synchrotron radiation of the jet (dashed line). The influence of the external radiation to the neutrino output depends also on the distance position, d, of the emitting blob. If $d < R_{\rm BLR}$ the neutrino spectrum output is influenced by all three components and the final output is reported with the red line shown in figure **??**, while the green line is the neutrino spectrum in case $d > R_{\rm BLR}$. In fact in this case the BLR photons cannot be involved in the interaction with protons, and then only the external photons from the torus and the synchrotron ones intervene on the reaction.

Chapter 5

Spine-Layer Model

In the previous chapter the link between electromagnetic SED and neutrino emission is presented. The assumption that blazars are neutrino emitters, binds the characteristics of the interpretative model. In particular, even if the pure leptonic model (typically the Synchrotron Self-Compton) reproduces well the blazar SED data, it cannot explain the neutrino emission due to the fact that the main ingredient to produce high-energy neutrinos are relativistic protons. On the other hand, a pure hadronic model is not always able to mimic the electromagnetic emission of the Blazar, or some of its characteristics such as the rapid variability. Lepto-hadronic (LH) models, in which both electrons and protons are accelerated in the jet, are introduced to explain both EM and neutrino SED. There are several LH models that can be applied, in which the main difference is the photon target interacting with relativistic particles. In the previous chapter a LH model in which both relativistic leptons and protons interact with synchrotron radiation of the jet was presented. In this case FSRQs and BL Lacs present a different neutrino spectrum due to the differences between the photon target spectra. Another model, applied in the previous chapter to FSRQs, is to use as photon target for the $p\gamma$ reaction the radiation emitted by external environment of the jet such as BLR and Torus. The result is that the expected neutrino luminosity is higher than the one produces with synchrotron emission due to relativistic effects and the high photon target density observed by protons inside the jet. In this chapter we want to investigate alternative LH models for BL Lac objects to explain both EM and neutrino emission. Initially, the focus on BL Lac object as neutrino emitters was motivated by the results presented in **?**. Authors showed that there is a weak spatial correlation between neutrino direction and BL Lac object detected above 50 GeV by Fermi (BL Lacs of the 2FHL catalogue). This, together with the results presented by **?**, lead us to consider BL Lac as main neutrino emitters. In particular **?**, shows the possibility to reproduce the whole neutrino spectrum observed by IceCube exclusively

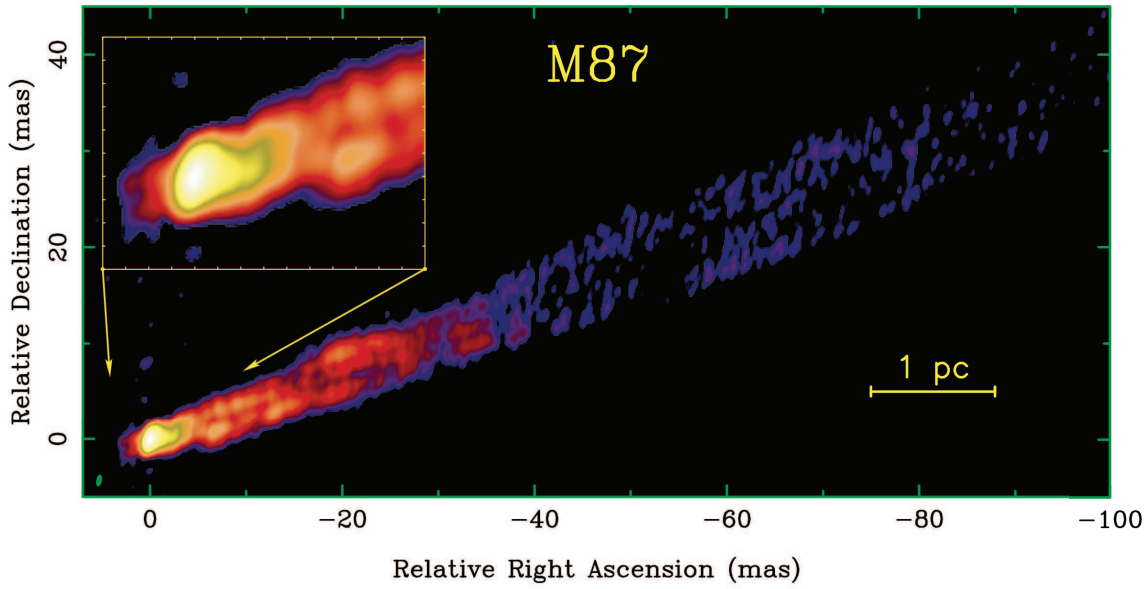

Fig. 5.1 VLBA 2 cm logarithmic false-color image of the M87 jet.

with the BL Lac objects if the jet is structured. In fact, the jet can present two different Lorentz factor: one for the fast inner region, and another for the slower layer. We show the theoretical and observational evidences supporting the existence of this structure, called *spine-layer*. This model can be used to explain the γ-ray emission, the second peak of the SED, assuming that synchrotron radiation produced by leptons in the layer interact with relativistic electrons in the spine, but also to produce high-energy neutrinos, using relativistic protons in the spine.

5.1 Observations

The bright and rapidly variable TeV emission of BL Lacs implies that at the scales where this emission originates, the jet should be highly relativistic. This is necessary in order to avoid the absorption of TeV photons by the IR radiation produced co-spatially to the TeV emission (**?**, **?**). Since the small angle of view of blazars does not allow to study in detail the longitudinal structure of their jet, it is convenient to observe the jet features of their parent population, the radiogalaxies, in order to understand the jet emission. There are several observations supporting the unified model in which the parent population of FSRQs are FRII, while FRI are the corresponding radiogalaxies of BL Lacs (**?**).

Recent observational evidence coming from high resolution radio observations, suggests the presence of a structure of the jet (**?**, **?**, **?**, **?**). This observational and phenomeno-

logical arguments are supported also by numerical simulations (**?**). A nice example is given in **?** in which the peculiar galaxy M87 in the Virgo Cluster was observed with the NRAO Very Long Baseline Array (VLBA, **?**) at 2 cm wavelength. M87 is one of the closest radio galaxies, and as such it has one of the few jets which can be well-resolved on sub-parsec scales in a direction transverse to the flow. A detailed study of the morphology at different wavelength was performed in **?**. High dynamic range images constructed from observations made in the year 2000 describe the two-dimensional structure of the jet out to nearly 0.2" (16 pc) and show the presence of a faint counterfeature. This is visible in Figure **??** where the 2 cm image constructed from observations made with the VLBA plus one VLA antenna is shown. A tapered image, made with twice the beam size from the same data, shows structure out to nearly 0.2". As seen in Fig. **??**, the jet appears bifurcated, starting at about 0.4 pc from the core, characteristic of a limb-brightened cylindrical or conical jet. The M87 jet appears to be highly collimated, with re-collimation observed between 2 pc where the opening angle is about 16°, and 12 pc where the opening angle is only 6° to 7°.

Similar results were obtained for NGC 1275 (**?**), other radiogalaxies (**?**, **?**, **?**) and also the BL Lac Mkn 501 (**?**).

The observation of a limb-brightened structure suggests, then, the presence of a faster central core and a slower sheath for the inner jet.

Apart from observational evidence, a spine-layer configuration for the jet has been proposed in the past on the basis of theoretical arguments (**?**). In addition, the existence of a velocity structure has also been suggested to explain some observed properties of radiogalaxies, such as their magnetic field configuration (**?**, **?**), and to overcome problems in unifying radiogalaxies with BL Lac objects (**?**).

5.2 Theoretical model

From the previous section it is clear that there are observational evidences of the presence of a structure of the jet in BL Lacs. **?** proposed that if the entire jet is rapidly decelerating in the γ-ray zone, then the base of the jet, still moving fast, will see the radiation produced at the end of the deceleration zone relativistically boosted. This "extra" radiation will favour inverse Compton emission, making it possible to derive less extreme values for the physical parameters with respect to a pure one-zone SSC model. There is an alternative hypothesis that the jet is structured not in the radial, but in the transverse direction, being composed by a slow layer and a fast spine. This alternative model is presented in **?**. Here

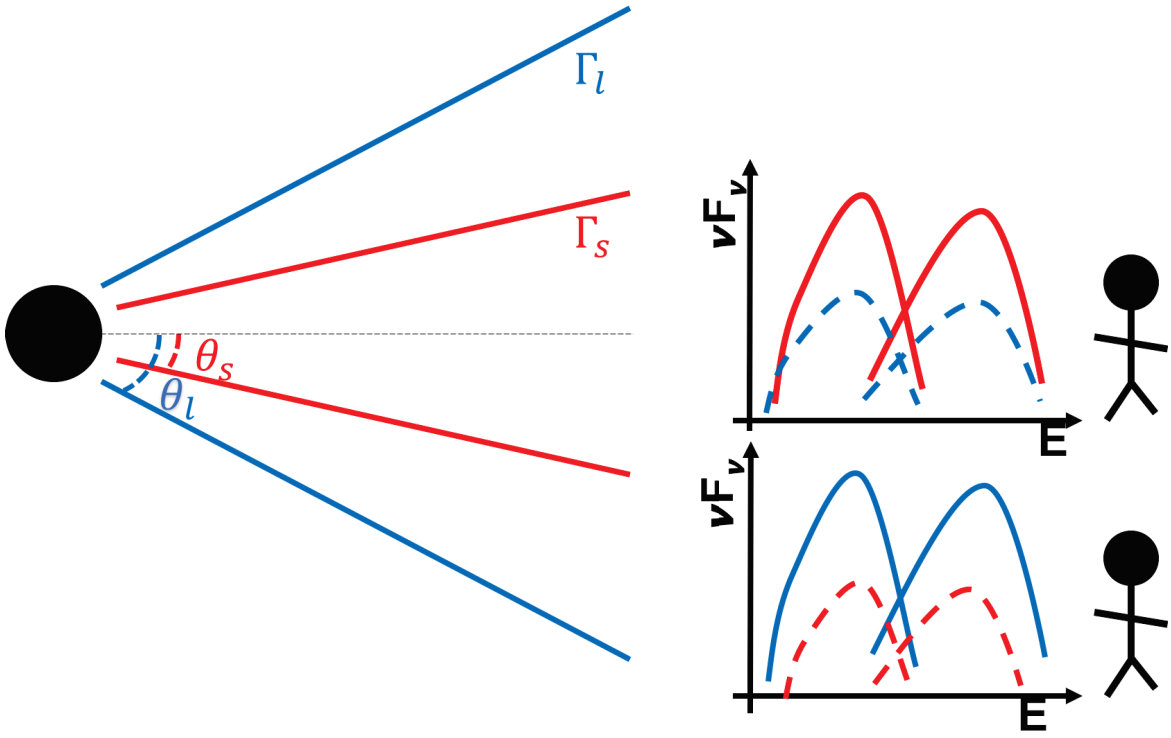

Fig. 5.2 Cartoon illustrating the spine-layer SED at different viewing angles.

we want to give the main informations of this model presented in **?** and relevant for our application.

The structured jet can be approximated as a structure of two coaxial cylinders: the external hollow cylinder for the layer and the inner cylinder for the spine. Since the plasma inside the two cylinders moves at different velocities, $\Gamma_s > \Gamma_l$ are the Lorentz factors of the spine and of the layer and $c\beta_s$ and $c\beta_l$ are the corresponding velocities, we will distinguish the different frames with no primes for the observer frame, primed quantities in the rest frame of the spine and double primed quantities in the frame of the layer.

Fig. **??** represents a schematic view of the spine layer structure as seen by an observer to the Earth. Due to the different Lorentz factor of the jet regions, the beaming angle of the jet is different (remember that $\theta \sim 1/\Gamma$). For angles of view $\theta < \theta_s$, the spine region is brighter that the layer (upper right schematic SED). This corresponds to the first part of the jet of Figure **??**. At larger angles of view, instead, the observer cannot see the deboosted spine emission, but for $\theta_s < \theta < \theta_l$ the layer is still visible.

Fig. **??** illustrates a cartoon of the the assumed geometry for the spine-layer model. We consider a cylinder for the layer with an external radius R_2, internal radius R and width $\Delta R_l''$, as measured in the comoving frame of the layer. The comoving volume of the layer

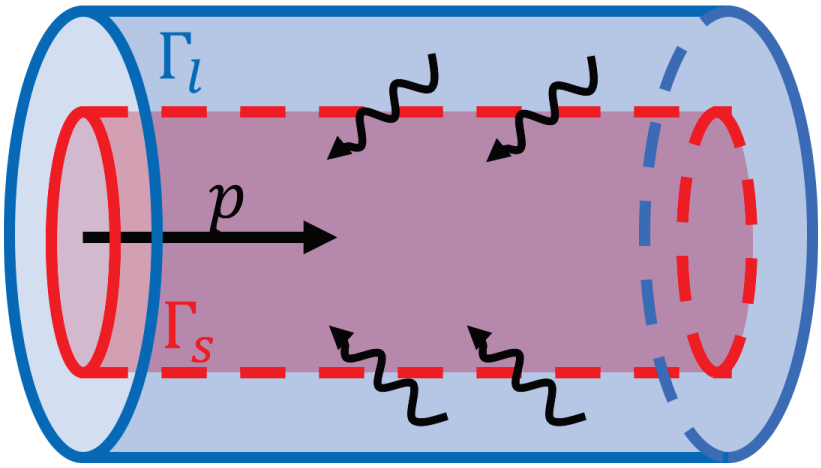

Fig. 5.3 Cartoon illustrating the spine-layer model.

is then $V_l'' = \pi(R_2 - R)^2 \Delta R_l''$. For the spine, instead, the inner cylinder has the same R and a width $\Delta R_s'$, as measured in the comoving frame of the spine. The active volume of the spine is then $V_s' = \pi R^2 \Delta R_s'$.

Since the spine and the layer move with different Lorentz factors, the radiation emitted by the spine (layer) is seen boosted by the layer (spine). With respect to a comoving observer at the same distance from the spine (layer), the radiation energy density is enhanced by a factor $\sim (\Gamma')^2$, with Γ' given by

$$\Gamma' = \Gamma_s \Gamma_l (1 - \beta_s \beta_l) \tag{5.1}$$

Both structures emit by the synchrotron and the inverse Compton processes. The energy distribution of the emitting electrons, $N(\gamma)$, is assumed to extend down to $\gamma_{\rm min}$, and to have the shape:

$$N(\gamma) = \begin{cases} K\gamma^{-n_1}\left[1 + \left(\frac{\gamma}{\gamma_b}\right)^{n_1 - n_2}\right] e^{-\frac{\gamma}{\gamma_{\rm cut}}}; & \text{if } \gamma > \gamma_{\rm min} \\ 0; & \text{if } \gamma \leq \gamma_{\rm min} \end{cases} \tag{5.2}$$

The normalization (i.e. K) of this distribution is found by imposing that $N(\gamma)$ produces a given intrinsic synchrotron luminosity, which is an input parameter of the model.

As a consequence of the structure of the jet there is the influence that one region has to the other and viceversa. This *feedback* increases the inverse Compton flux, since both the spine and the layer see an enhanced radiation energy density. Furthermore, while the synchrotron and the SSC emission in the comoving frame are assumed to be isotropic, the inverse Compton process between electrons of the layer (spine) and seed

photons produced by the spine (layer) is highly anisotropic. In fact, **?** found the pattern of the emitted radiation from a moving blob immersed in a bath of seed photons (e.g. corresponding to the radiation produced by the broad line region of a powerful blazar), and pointed out the fact that in this case the external Compton radiation is more beamed than the synchrotron and SSC emission.

In our case the component contributing to the external radiation (from layer to spine and viceversa) is not at rest with respect to the distant observer, but moves. To find the pattern of the emitted radiation it is convenient to move to the comoving frame of the emitter of the seed photons. As already shown in Section **??**, the Doppler factor δ is a parameter that allows to consider the relativistic effects. It is defined in equation **??** as depended on the Lorenz factor Γ and the viewing angle θ. Note that in this scenario the situation is more delicate and Γ and θ are to be consider according to the frame we are considering. Furthermore we defined $\delta_{l,s}$ ($\delta_{s,l}$) as the beaming factor of the radiation produced in the layer (spine) as observed in the spine (layer).

Consider now the seed photons produced by the layer, and an observer comoving with the layer. In this frame, the spine is moving with Γ', and the photon frequencies produced by the spine are blueshifted by the Doppler factor $\delta_{s,l}$. Going to the frame of the distant observer, these photons are further blueshifted by δ_l. But the distant observer will see the same photons blueshifted by δ_s. This implies $\delta_{s,l}\delta_l = \delta_s = 1/\delta_{l,s}$ (further details can find in **?**).

In the frame of the spine the external Compton radiation produced by the layer follows a pattern $\propto \delta_{l,s}^{4+2\alpha}$ (see details on **?**, where α is the spectral index of the emission [$F(\nu) \propto \nu^{-\alpha}$], while the synchrotron and SSC emission follow the usual pattern $\propto \delta_{l,s}^{3+\alpha}$. If $I'(\nu')$ is the monochromatic intrinsic intensity produced by the spine, we have

$$\begin{aligned} I(\nu) = I'(\nu)\delta_{l,s}^{4+2\alpha}\delta_s^{3+\alpha} = I'(\nu)\delta_s^{3+\alpha}\left(\frac{\delta_l}{\delta_s}\right)^{1+\alpha}; \qquad \text{(EC)} \\ I(\nu) = I'(\nu')\delta_s^{3+\alpha}; \qquad \text{(S,SSC)} \end{aligned} \tag{5.3}$$

An example of application of this model to the most studied TeV BL Lacs object is given in **?** in which the authors reproduce the SED of Mkn 421. As already said in section **??**, the one-zone SSC model parameters are uniquely specified once the SED bumps (namely, peak frequencies and luminosities) and the variability time-scale are well characterized (**?**). The latter observable determines the value of the source size, through the causality relation $R \approx c\,t_{\rm var}\delta/(1+z)$. The values of the peak frequencies and luminosities can be linked to the other physical parameters, most notably the magnetic field and the particle density and energy. Fig. **??** left panel, provide an excellent description of both the synchrotron and the

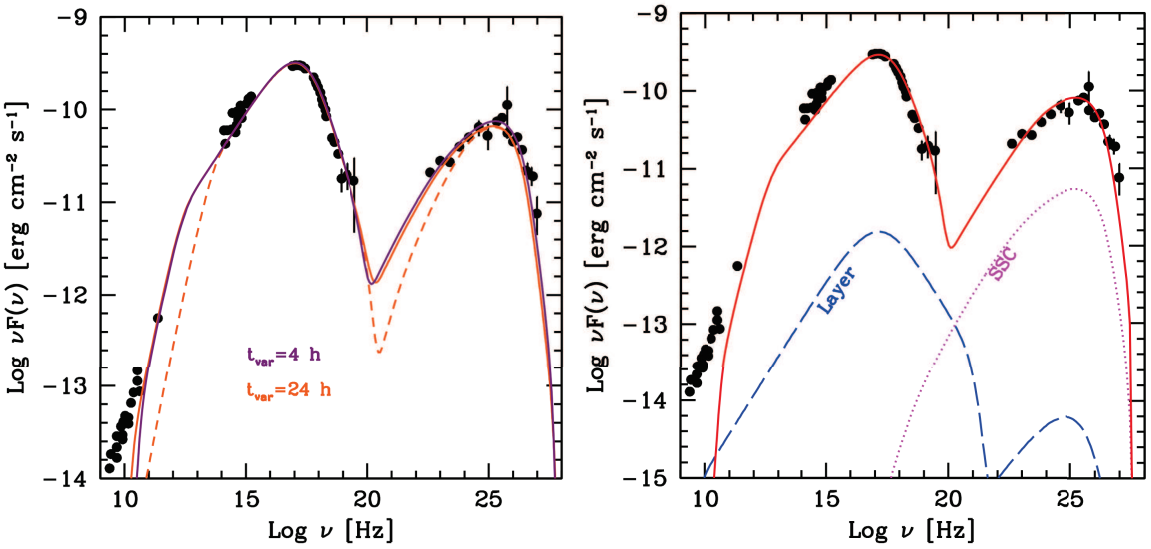

Fig. 5.4 SED of Mkn 421 (black, from Abdo et al. 2011) reproduced with the SSC model (left panel) and spine-layer model (right panel). *Left panel:* The violet and orange solid lines show the theoretical SED calculated with the SSC model for two different value of the variability time-scale with the parameters. *Right panel:* The dashed blue line shows the emission from the layer. The magenta dotted line reports the SSC emission from the spine (**?**).

IC peak. On the other hand the same SED can be well fitted by a spine-layer model (see **?** for details about the parameters used). In this case the large radiation energy density available for the IC emission – provided by the layer – increases the IC luminosity and allows one to reproduce the SED in equipartition conditions.

5.3 Neutrino emission

For simplicity (as in **?**), for the study of neutrino emitters considering the spine-layer model, we will not take into account the fact that the radiation field of the layer in the spine frame (dominating the photo-meson reactions) is anisotropic (**?**). With this approximation the target radiation field of the layer in the observer frame can be parameterized by a smoothed broken power-law function with indices α_1, α_2:

$$L(\epsilon) = K\left(\frac{\epsilon}{\epsilon_0}\right)^{-\alpha_1}\left[1+\left(\frac{\epsilon}{\epsilon_0}\right)^{\alpha_1-\alpha_2}\right] \tag{5.4}$$

whose normalization K is given by the total observed luminosity $L_t = \int L(\epsilon)d\epsilon$, while ϵ_0 is the SED peak energy.

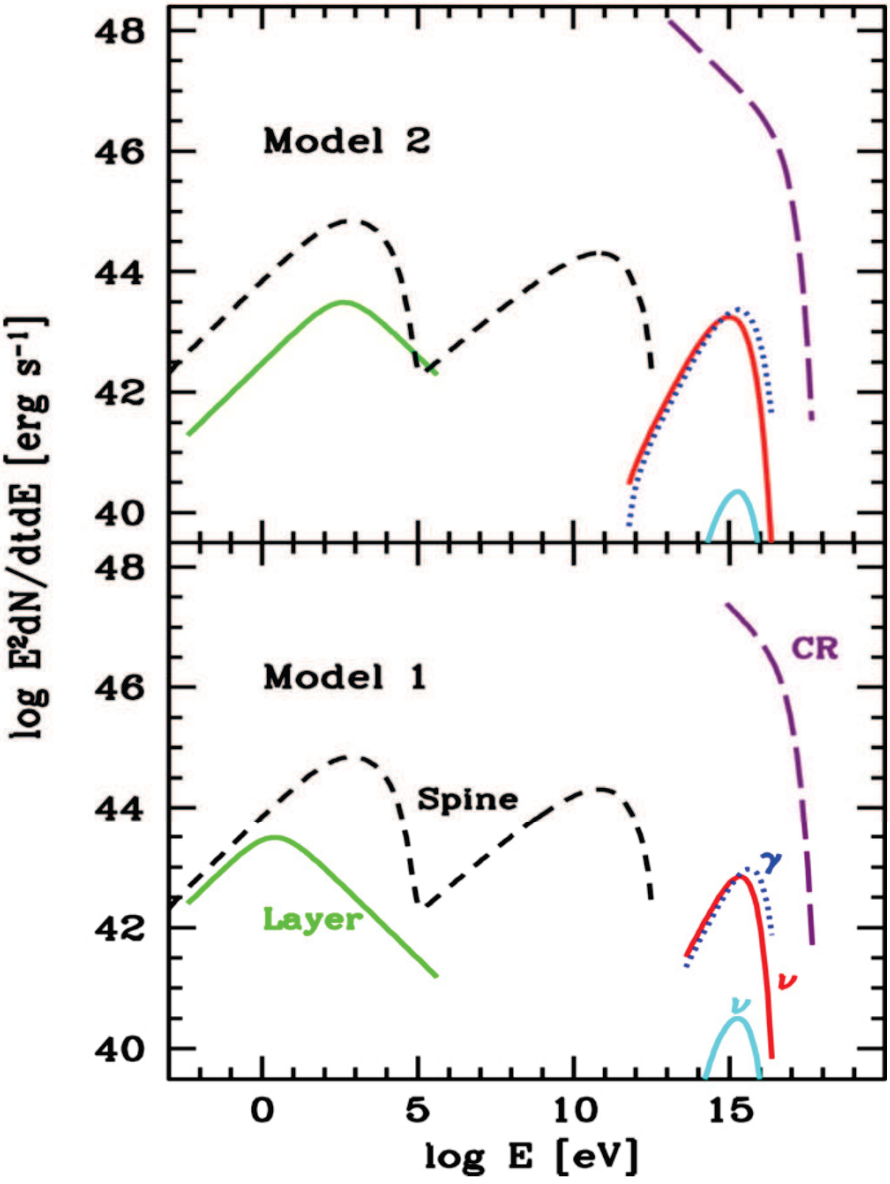

Fig. 5.5 Luminosities of the different components in the observer frame for models 1 (bottom) and 2 (top). The solid green line shows the layer soft emission while, for comparison, the black dashed line is the blazar spectrum template (assumed to be emitted by the spine). The violet long-dashed line shows the spectrum of the high-energy protons. The solid red and the dotted blue lines show the luminosity of neutrinos (all flavors) and γ rays produced through photo-meson reactions. For comparison, the cyan solid line shows the neutrino luminosity considering the internal synchrotron photons as targets for the photo- meson reaction.

The corresponding photon number density in the layer frame is

$$n''(\epsilon'') = \frac{L(\epsilon)}{4\pi R_2^2 c \delta_l^3 \epsilon''} \tag{5.5}$$

where $\epsilon'' = \epsilon/\delta_l$ with δ_l the Doppler factor of the layer frame.

Using equations **??**, as CRs spectrum, and **??**, as photon target density, in **??** we are able to derive the neutrino spectrum. Note that equation **??** must be transformed from the spine frame to the observer frame using the standard transformations: $E_\nu L_\nu(E_\nu) = E'_\nu L'_\nu(E'_\nu)\delta_s^4$ and $E_\nu = \delta_s E'_\nu$.

Summarizing, the model is specified by the following 11 parameters: the jet radius, R_2, the spine and layer Lorentz factors Γ_s and Γ_l, the observed layer radiative luminosity L_l, the peak ϵ_0 of its energy distribution [in $\epsilon L(\epsilon)$], the spectral slopes n_1 and n_2 of $L_l(\epsilon)$, the spine comoving CR luminosity L'_p, the CR power-law index n, the minimum and the cut-off energy $E'_{\rm min}$, $E'_{\rm cut}$. As already partially shown in the previous chapter, not all parameters have the same importance in determining the shape and the level of the resulting neutrino spectrum. The choice of the values of some parameters is guided by the results of the modelling of HBL emission. For definiteness, the jet radius is fixed to $R_2 = 10^{15}$ cm (e.g., **?**), $\Gamma_s = 15$, $\Gamma_l = 2$, and $\delta_s = 20$. Consequently, $\delta_l = 3.7$ and $\Gamma_{\rm rel} = 4$. The observed luminosity of the low-energy emission component of the layer is constrained from above, since we demand that the observed SED of HBL is dominated by the spine. For the low- and high-energy slopes we assume the customary values $\alpha_1 = 0.5$ and $\alpha_2 = 1.5$.

More important is the role of the peak energy of the layer emission ϵ_0 which regulates, through the photopion threshold condition, eq. **??**, the possible values of the minimum CR energy and the position of the maximum of the neutrino emitted luminosity. In fact, increasingly larger values of ϵ_0 allow for lower values of $E'_{\rm min}$ and thus lower energies of the produced neutrinos. On the other hand, due to the steep CR distribution, decreasing $E'_{\rm min}$ leads to increase the total CR power required to produce a given neutrino output.

Fig. **??** shows the importance of the layer shape to reproduce the neutrino spectra observed by IceCube. In the two panel the SED of a typical BL Lac with high-energy synchrotron peak (the so called HBL or HSP with $\nu_S > 10^{15}$ that correspond to $\gtrsim 10^3$ eV) is shown (dashed black line). This observed radiation is assumed to be emitted by the spine. The synchrotron emission of the layer as seen by the observer is represented by the green solid line. Assuming to use this radiation as photon target for the relativistic protons in the spine, the γ-rays and ν spectrum obtained by the $p\gamma$ emission is shown (respectively with dotted blue line and red solid line). For comparison the cosmic-ray spectrum (dashed

purple line) and the neutrino spectrum using the synchrotron radiation of the spine (cyan solid line) are also shown.

5.4 Interpretation of TXS 0506+056 with spine-layer model

In **?** the spine-layer model was applied to the case of TXS 0506+056 flare. The source is not a high-synchrotron peak BL Lacs (it is defined as IBL in the Fermi catalogue and it would belong to the 10^{46} erg s^{-1} < $L_{\rm LAT}$ < 10^{47} erg s^{-1} luminosity bin of the Blazar sequence), and then the spine-layer scenario is not proven for this source. However, as discussed in **?** and **?**, the model is expected to be relevant also for this kind of sources. The fit of the SED is shown in figure **??**. It is obtained following the considerations in the previous section **??**. The electromagnetic SED is well described by leptonic emission: synchrotron emission for the first peak and Inverse Compton of the relativistic electrons in the spine with the synchrotron photons from the layer for the high energy peak. In this analysis, also all relevant hadronic processes, described in Section **??** have been taken into account. In particular photo-meson-induced cascade emission (**?**), Bethe-Heitler (BH) pair cascade emission (**?**), and synchrotron radiation from protons (**?**) and muons have been included. For protons of sufficiently high energy, the gamma-rays resulting from photo-meson reactions can be energetic enough to undergo electron-positron pair production interactions with low-energy photons ($\gamma\gamma \rightarrow e^+e^-$), thereby triggering secondary pair cascades (**?**). This process redistributes the energy of photons down to lower energies until it falls below the threshold for $\gamma\gamma$ interactions and escape, generally resulting in a spectrum with roughly equal power over a broad energy range (from optical to VHE for the cases shown below).

From the spectral properties of the external radiation fields considered here, $\gamma\gamma$ transparency is expected below a few hundreds of GeV, the energy band best accessible to MAGIC. The direct products of $p\gamma$ reactions including neutrinos and photons are described using the analytical treatment of **?**. The secondary pair cascading processes were implemented following the formalism of **?** and extending it to include Inverse Compton in addition to synchrotron processes for the pairs. An additional hadronic component arises from BH pair production ($p\gamma \rightarrow pe^+e^-$), which can be observationally relevant in some cases. Gamma-ray emission via synchrotron radiation of protons or muons is mostly unimportant for the range of magnetic fields and proton energies considered here, except for a limited region of parameter space.

Figure **??** shows results for models corresponding to the low (bottom panel) and high states (upper panel). The enhanced luminosity for external Compton emission relative to

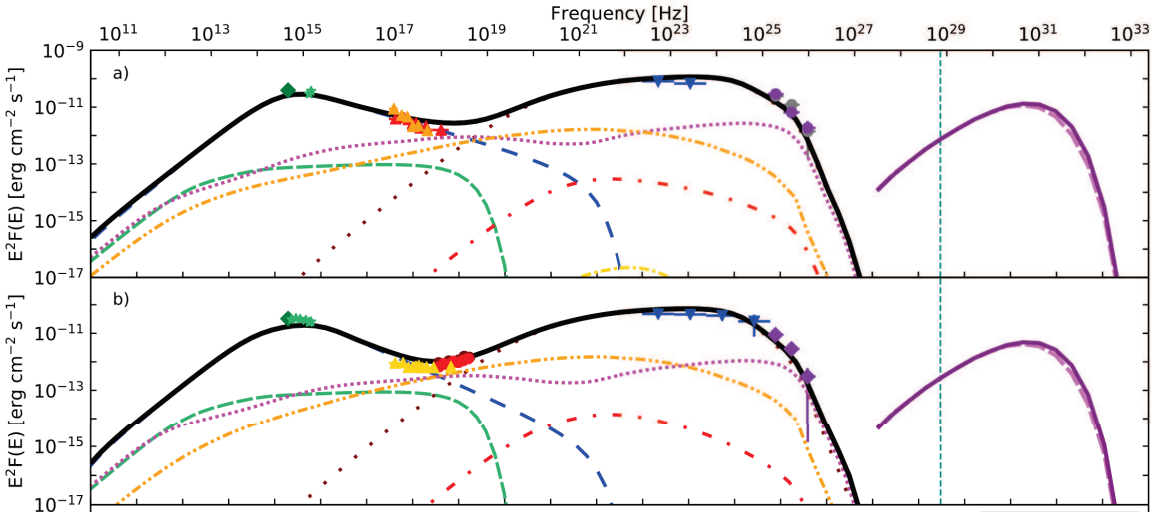

Fig. 5.6 Spectral energy distribution for the enhanced VHE gamma-ray emission state (a), MJD 58029 to 58030) and the lower VHE gamma-ray emission state (LS, b)) modelled with the jet-sheath scenario with $E_{p,\mathrm{max}} = 10^{16}$ eV. Symbols corresponding to data-points from different facilities and observation epochs are described in the legend. The curves represent individual emission components while the thick black curve shows the total predicted emission. The leptonic emission from the jet includes synchrotron (dashed blue), synchrotron-self-Compton (SSC, red dashed dotted), and external Compton (EC) emission (dark red dotted). Synchrotron emission from the sheath is denoted by the light green dashed line. The hadronic emission components are photo-meson-induced cascade (purple dotted), Bethe-Heitler pair cascade (yellow dash-dotted) and muon-synchrotron (yellow dotted). Predicted (anti-)neutrino spectra are marked by (light-)magenta (dashed) solid lines, the blue vertical line shows the energy ~ 290 TeV of the observed neutrino. *Credits:* **?**.

the other emission components at small viewing angles is important for adequately reproducing the MWL SEDs. Most notably, the prominent spectral steepening observed at a few tens of GeV by MAGIC confirms the internal $\gamma\gamma$ absorption that is robustly expected as a consequence of $p\gamma$ production of a ~ 290 TeV neutrino. Thus, this model reinforces the association between the multi-messenger signals. While the bulk of the gamma-rays are inferred to be external Compton emission from electrons, a non negligible contribution can arise from cascade emission induced by protons, most notably in the hard X-ray and VHE gamma-ray bands.

From the analysis of this event, the importance of the X-band came up. In fact, in this band, there are several contributions: the BH cascade (yellow dotted-dashed line in figure **??**), the photo-meson cascade (pink dotted line in figure **??**) and the leptonic contribution of the synchrotron emission (dashed blue line in figure). The slope of the X-ray region gives constraints on the lepto-hadronic model and then can help on the understanding of the physics of the jet. We will discuss about this in section **??**.

5.5 Relation with γ-ray emission

To give an estimate of the neutrino flux from a specific BL Lac in the framework of the spine-layer model in **?**, we assumed a relation between the neutrino emission and the γ-ray emission. The neutrino emission is linked to γ-ray emission due to the π^0 decay. As in the case of ν, the expected spectrum for γ-ray produced by photo-meson reaction, is given by equation **??** but substituting $1/2$ instead of $3/8$. Note that if the neutral pion takes $1/5$ of the energy of the relativistic proton, then each γ-ray from the pion decay obtain half of the pion energy. This means that $E_\gamma \simeq 1/10 E_p$ (see Figure **??**). However these photons, corresponding to PeV gamma-rays, have never been observed. A reason should be the presence of the Extragalacting Background Light that can interact with high-energy γ-ray (see **?**). Moreover it is reasonable to consider opaque the jet region in which this kind of γ-rays are produced with neutrinos (see **?** and **?** for details on the relation between the photo-meson production efficiency $f_{p\gamma}$ and the absorption $\tau_{\gamma\gamma}$). It means that γ-rays from the π^0 decay are promptly absorbed through scattering with the soft photons and, after reprocessing, leave the jet at much lower energies, in the MeV-GeV. This is also supported in the previous section **??** by the modelling of TXS0506+056.

It is however reasonable to search a relation between the neutrino flux and the observed γ-ray emission, even if they are originated by different processes. Note that the next considerations are valid not only for the spine-layer model but for all models in which the photon targets, interacting with protons, are the same that are comptonized by

relativistic electrons. Furthermore, the next considerations are valid only for those models in which the photon target shape is the same for all the sources. For example we will see in Chapter **??** that the spectrum of the accretion flow that we consider as photon target for the neutrino emission, changes for different subclass of BL Lac. In that case we cannot apply the consideration in the following for the entire class of BL Lac but only for each subclasses separately.

The total, energy integrated, neutrino luminosity can be expressed as:

$$L_\nu = \epsilon_{\rm p} Q'_{\rm p} \delta_s^4, \tag{5.6}$$

where the total CR injected power is:

$$Q'_{\rm p} = \int Q'_{\rm p}(E'_{\rm p})\, dE'_{\rm p}, \tag{5.7}$$

and the averaged efficiency $\epsilon_{\rm p}$ is:

$$\epsilon_{\rm p} = \frac{1}{Q'_{\rm p}} \int f_{p\gamma}(E'_{\rm p})\, Q'_{\rm p}(E'_{\rm p})\, dE'_{\rm p}. \tag{5.8}$$

In general, the IC (i.e., high-energy γ-ray) luminosity can be formally expressed in exactly the same way:

$$L_\gamma = \epsilon_{\rm e} Q'_{\rm e} \delta_s^4, \tag{5.9}$$

where now $\epsilon_{\rm e}$ and $Q'_{\rm e}$ refer to the relativistic electrons. Using Eq. **??** and **??** one can write the ratio of the gamma-ray and neutrino fluxes of a given source as:

$$\frac{F_\nu}{F_\gamma} = \frac{L_\nu}{L_\gamma} = \frac{\epsilon_{\rm p}}{\epsilon_{\rm e}} \frac{Q'_{\rm p}}{Q'_{\rm e}}. \tag{5.10}$$

In the spine layer scenario, the soft radiation field in the spine frame is dominated by the relativistically boosted layer radiation. In these conditions, both efficiencies, $\epsilon_{\rm p}$ and $\epsilon_{\rm e}$ depend on the same photon field, $n'_{\rm ph,l}$ and thus their ratio, $\epsilon_{\rm p}/\epsilon_{\rm e} \equiv \xi_{\rm ep}$ depend only on the details of the injection and cooling processes. As a zero-order approximation, one can assume that these properties are universal for all the (quite similar) BL Lac jets, namely that $\xi_{\rm ep}$ is on average constant (with, of course, some dispersion) in the BL Lac population. Furthermore, we find it reasonable to assume that the ratio between the power injected into relativistic electrons and that injected into high-energy protons is, on average, the same in different sources, both depending on the total power carried by the jet, $P_{\rm jet}$, that

is, $Q'_{\rm p} = \eta_{\rm p} P_{\rm jet}$ and $Q'_{\rm e} = \eta_{\rm e} P_{\rm jet}$, so that $Q'_{\rm p}/Q'_{\rm e} = \eta_{\rm p}/\eta_{\rm e} \approx const$. With these assumptions, we derive that F_ν/F_γ is, on average, the same in all HBL, $F_\nu/F_\gamma = \xi_{\rm ep}\eta_{\rm p}/\eta_{\rm e} \equiv k_{\nu\gamma}$.

Therefore, in our scheme, *the bolometric neutrino flux from a given BL Lac is directly proportional to its high-energy gamma-ray flux*,

$$F_\nu = k_{\nu\gamma} F_\gamma \tag{5.11}$$

Note that this relation is independent on the luminosity of the source. This allows us to consider all the BL Lacs objects of the 2FHL catalogue and not only those with redshift z known. This theoretically-inspired assumption is consistent with the results of **?**, who present the evidence for a spatial correlation between the reconstructed arrival direction of neutrinos (including both hemispheres, thus both HESE and though-going muon) and BL Lac objects emitting very high-energy γ-rays (> 50 GeV).

The Second Catalog of Hard Fermi-LAT Sources (2FHL) (**?**, **?**) includes all the sources detected at energies above 50 GeV by the Large Area Telescope onboard *Fermi* over 80 months of data. The high-energy band covered by the 2FHL closely matches the expected maximum of the IC component produced by the spine. Hence, it is reasonable to consider the 2FHL flux as a good proxy for F_γ. Therefore, using the relation derived above for each source, $F_{\nu i} = k_{\nu\gamma} F_{\gamma i}$, it is possible to derive the expected flux of neutrinos.

The constant can be derived under the assumption that the total neutrino diffuse flux measured by IceCube, $F_{\nu,tot}$ is entirely due to the contribution of the high-energy-emitting BL Lacs. This is a strong assumption and at present there are several considerations suggesting that the diffuse neutrino background observed by IceCube is a composition of neutrino emission from different classes (in particular the BL Lac contribution should be around $\sim 20-25\%$, see e.g. **?**, **?**, **?**). We can write that $F_{\nu,\rm BL\,Lac} = \eta_{\rm BL\,Lac} F_{\nu,tot}$. In the following we will consider $\eta_{\rm BL\,Lac} = 1$. Since the neutrino flux for each source is directly proportional to the corresponding gamma-ray flux, we can write:

$$F_{\nu,\rm BL\,Lac} = \eta_{\rm BL\,Lac} F_{\nu,tot} \equiv \sum_i F_{\nu i} = \sum_i k_{\nu\gamma} F_{\gamma\, i} = k_{\nu\gamma} \sum_i F_{\gamma i} = k_{\nu\gamma} F_{\gamma,tot}, \tag{5.12}$$

in which we use the fact that $k_{\nu\gamma}$ is (approximately) the same for all sources. Here $F_{\gamma,tot}$ is the total high-energy gamma-ray flux from BL Lacs (see below).

The next step is to convert the neutrino energy flux for each source, $F_{\nu\, i}$, to the neutrino number flux, $\Phi_i(E_\nu)$, using:

$$F_{\nu\, i} = \int_{E_1}^{E_2} \Phi_i(E_\nu) E_\nu \, dE_\nu, \tag{5.13}$$

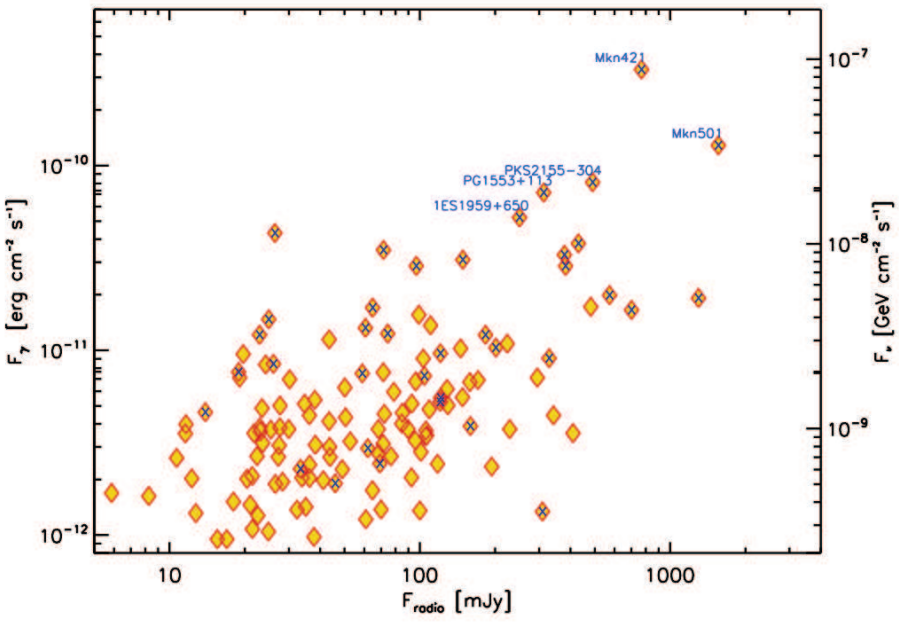

Fig. 5.7 Radio flux versus the high-energy γ-ray flux ($E > 50$ GeV) of the 132 BL Lacs belonging to the 2FHL catalogue. Blue crosses indicate sources detected in the TeV band. The vertical axis on the right reports the muon neutrino flux (in the 0.1-10 PeV band) predicted with the scaling discussed in the text. We also show the names of the brightest sources.

where the interval $[E_1, E_2]$ is the range of neutrino energies. We assume that each source emits a neutrino spectrum with the same shape of the overall neutrino spectrum reconstructed through the IceCube detections, that is, a power law distribution (more on this later):

$$\Phi_i(E_\nu) = \phi_i \left(\frac{E_\nu}{E^\star}\right)^{-\Gamma}, \tag{5.14}$$

where $E^\star$ is the energy of normalization. Therefore, from Eqs. **??**-**??** we can derive the neutrino number flux normalization ϕ_i as:

$$\phi_i = F_{\nu i}\, E^{\star\,-\Gamma}\, \frac{2-\Gamma}{E_2^{2-\Gamma} - E_1^{2-\Gamma}}. \tag{5.15}$$

Finally the number of neutrinos N_ν expected from a given HBL object of the 2FHL catalogue depends on the rate of high energy neutrino R_ν and the exposure time $T_{\rm exp}$ as follows:

$$N_\nu = R_\nu\, T_{\rm exp} = T_{\rm exp} \int_{E_1}^{E_2} A_{\rm eff}(E_\nu)\Phi_i(E_\nu)\, dE_\nu, \tag{5.16}$$

where $A_{\rm eff}(E_\nu)$ is the effective area of the neutrino detector.

Table 5.1 Expected 0.1-10 PeV flux (in units of 10^{-8} GeV cm^{-2} s^{-1}) and detection rate (yr^{-1}) of muon neutrinos R_ν for the brightest 2FHL BL Lacs with IceCube at declination $60° < \delta < 90°$, $30° < \delta < 60°$,$0° < \delta < 30°$ respectively. The numbers identify sources in the sky map of Fig. **??**.

	Name	F_ν	R_ν
	$60° < \delta < 90°$		
1	1ES1959+650	1.38	0.27
2	1ES0502+675	1.14	0.22
3	S50716+71	0.44	0.08
4	1RXSJ013106.4+61203	0.25	0.05
5	4C+67.04	0.25	0.05
6	Mkn180	0.24	0.05
7	MS0737.9+7441	0.13	0.02
8	RXJ0805.4+7534	0.08	0.02
9	S40954+65	0.07	0.01
10	S41749+70	0.07	0.01
	$30° < \delta < 60°$		
11	Mkn421	8.77	4.89
12	Mkn501	3.41	1.90
13	PG1218+304	0.92	0.52
14	3C66A	0.87	0.49
15	1H1013+498	0.87	0.49
16	1ES0033+595	0.82	0.46
17	1ES2344+514	0.69	0.39
18	1ES1215+303	0.52	0.29
19	B32247+381	0.37	0.21
20	B30133+388	0.35	0.19
	$0° < \delta < 30°$		
21	PG1553+113	1.89	2.47
22	PKS1424+240	1.00	1.30
23	PG1218+304	0.92	1.20
24	TXS0518+211	0.87	1.14
25	1ES0647+250	0.75	0.99
26	1ES1215+303	0.52	0.69
27	RXJ0648.7+1516	0.45	0.59
28	1RXSJ194246.3+10333	0.41	0.54
29	RBS0413	0.32	0.42
30	1H1720+117	0.25	0.33

5.5.1 Application and results

? found a significant probability of association between the positions of the BL Lacs belonging to the 2FHL catalogue - defined as BL Lac with synchrotron peak frequency larger than 10^{15} Hz - with flux $F(>50\,\mathrm{GeV}) \gtrsim 2\times10^{-11}$ ph cm^{-2} s^{-1} and a selected sample of neutrinos, including both HESE (four years) and through-going ν_μ (two years), detected by IceCube above 60 TeV. For illustration, in Fig. **??** we report the radio flux versus the γ-ray energy flux (integrated over the 50-2000 GeV band using the spectral parameters of the 2FHL) for the 132 HBL of the 2FHL (for the selection we used the phenomenological estimate of the synchrotron peak frequency provided in the 3rd Catalog of AGN Detected by the *Fermi*-LAT, abbreviated to 3LAC).

Our aim is to provide the neutrino counts expected from each 2FHL BL Lacs in view of the possible identification of the extragalactic neutrino sources based on a positional correlation with detected neutrinos. For this reason, it is justified to specialise our treatment and focus it on the through-going muon neutrinos, ν_μ. Indeed, muons leave well-defined and long tracks that are easier to reconstruct, determining the best ($<1^\circ$) angular resolution in order to look for possible associations with point-like sources as BL Lacs. In the case of IceCube this implies focusing on the component coming from the northern hemisphere. On the contrary, KM3NeT will be sensitive to through-going muons originating mainly from neutrinos coming from the southern hemisphere.

The IceCube collaboration published both the spectrum of the so-called high-energy starting events (HESE), dominated by cascade-like events triggered within the detector volume by neutrinos from the the southern sky (**?**) and that derived from analyzing only the (high-energy, $E \gtrsim 100$ TeV) muon-like northern events (**?**, **?**). The derived spectral parameters are in tension, with the through-going muon signal providing a spectrum harder ($\Gamma = 1.91\pm0.20$ using events with $E > 170$ TeV, **?**) than that ($\Gamma = 2.50\pm009$, **?**) derived from HESE data with an extension to low energy ($E > 60$ TeV). Interestingly, if only high-energy HESE events ($E > 100$ TeV) are selected, the tension reduces. This could be considered as evidence for hardening of the spectrum at high-energy, possibly related to two spectral components (galactic and extragalactic) (see the detailed discussion in **?**). Moreover, if extragalactic, the high neutrino flux below 60 TeV would imply an accompanying gamma-ray flux exceeding the high-energy extragalactic γ-ray background (e.g., **?**). It is also worth adding that it is unlikely that the neutrino spectrum predicted by the structured jet model extends below 100 TeV, since this would imply a relatively large cosmic-ray power (**?**). Summing up, there is evidence supporting the scenario in which lower energy neutrinos ($\lesssim 100$ TeV) are derived from another population (possibly galactic) of sources. All this justifies the use of the spectral parameters obtained with the

through-going muon analysis (we used the parameters derived from the first four years of IceCube, **?**) in the following section of paper.

Following the procedure discussed in Section **??**, the first step is to derive the constant of proportionality between the γ-ray and the neutrino flux from Eq. **??**.

The total (muon) neutrino flux $F_{\nu,tot}$ is calculated by integrating the power law spectrum provided by **?** in the range 100 TeV-10 PeV. The result is $F_{\nu,tot} = 4.85 \times 10^{-7}$ GeV cm^{-2} s^{-1}.

The second quantity needed is the total high-energy γ-ray flux from the neutrino-emitting BL Lac population, $F_{\gamma,tot}$. An obvious upper boundary to this flux is provided by the total (i.e., resolved+unresolved) observed extragalactic high-energy γ-ray background (**?**). Above 50 GeV (the low-energy threshold of the 2FHL) the background intensity is 2.4×10^{-9} ph cm^{-2} s^{-1} sr^{-1}. On the other hand, we calculated that the contribution of the detected BL Lac of the 2FHL (50-2000 GeV, flux sensitivity limit $\approx 8 \times 10^{-12}$ ph cm^{-2} s^{-1}) to the background (assuming isotropy) is 7.2×10^{-10} ph cm^{-2} s^{-1} sr^{-1}, corresponding to approximately one third of the total background intensity above 50 GeV. Through accurate simulations, **?** estimated that (resolved and unresolved) point sources with fluxes larger than 10^{-12} ph cm^{-2} s^{-1} (the majority of which are assumed to be blazars, but not necessarily all HBL) should account for approximately 90% of the background. On the other hand, we must also point out that **?** found that the correlation between the IceCube neutrinos and the 2FHL BL Lac holds only with sources with relatively high-flux ($\gtrsim 1.8 \times 10^{-11}$ ph cm^{-2} s^{-1}). Given these uncertainties and in view of the fact that, in any case, the differences involve relatively small factors, in the following we use the value of the flux $F_{\gamma,tot}$ obtained by summing the 2FHL BL Lac only, keeping in mind that derived neutrino fluxes should be considered as upper limits since, if also BL Lac with smaller flux would contribute, the derived neutrino fluxes could be lower by a factor ≈ 3. The total energy flux in the 50-2000 GeV band (approximating well the bolometric gamma-ray output, since the high-energy peak is commonly found at 100 GeV) of the 2FHL sources, $F_{\gamma,tot}$, can be directly performed using the spectral information of the 2FHL, giving $F_{\gamma,tot} = 1.14 \times 10^{-6}$ GeV cm^{-2} s^{-1}. Therefore, for the value of the constant we obtain $k_{\nu\gamma} = F_{\nu,tot}/F_{\gamma,tot} = 0.46$.

The vertical axis on the right of Fig. **??** reports the neutrino flux for each 2FHL BL Lac calculated with the scaling above. With these fluxes at hand we can predict the expected count rate for IceCube and KM3NeT. In the following we separately describe the results.

IceCube: We already presented IceCube detector in Section **??**. It is the largest operating neutrino detector, encompassing an instrumented cubic kilometer of ice. In the case of ν_μ

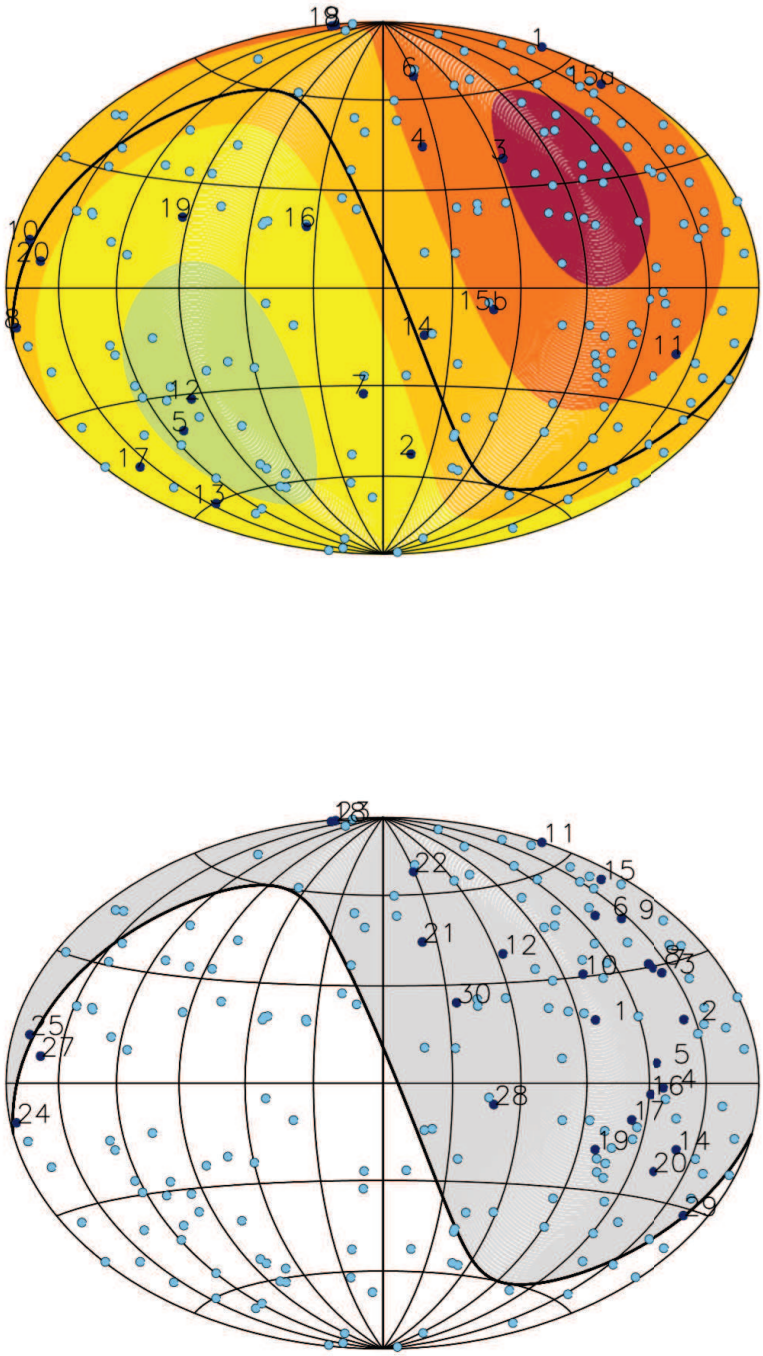

Fig. 5.8 Sky maps in galactic coordinates with the position of 2FHL HBL (light blue and blue) for IceCube (lower panel) and KM3NeT (upper panel). The blue points are the brightest HBL and the associated number is reported in Tables 1 and 2. For the plot of KM3NeT, the different color indicates the different range of object declination-dependant visibility; red: $> +60°$ and visibility percentage $< 20\%$, dark-orange: $+25° \div +60°$ and visibility percentage $20 \div 45\%$,orange: $-12° \div +25°$ and visibility percentage $45 \div 60\%$, yellow: $-53° \div -12°$ and visibility percentage $60 \div 100\%$ and green: $< -53°$ and visibility percentage 100%. Lower map: Visibility plot of IceCube. The gray region is 100% of muon neutrino visibility, and the white is near 0%.

, detected from the up-going through-going muons, the effective area of the instrument depends on the declination of the source (see Section **??** and Fig. **??**), since the angle-dependent absorption by the Earth starts to affect the detected flux above ≈ 100 TeV. The actual effective area in ranges of declinations ($60° < \delta < 90°$, $30° < \delta < 60°$, $0° < \delta < 30°$) is provided by **?**. The number of neutrinos expected for the brightest 2FHL sources with an effective exposure of one year and divided in ranges of declination are reported in Table **??** and shown in Fig. **??** (lower panel).

Very few sources present a rate exceeding 1 event yr^{-1}. Interestingly, among them are two of the best candidates proposed by **?**, Mkn 421 and PG 1553+113. 1ES 1959+650, from which AMANDA possibly detected three neutrinos during a burst in 2002 (**?**) is not expected to be so bright. In considering these numbers one must remember that they are upper boundaries to the actual values, since, as discussed above (Sect. 4), neutrino fluxes (and count rates) smaller by a factor ∼ 3 are compatible with the γ-ray background. Note also that PKS 2155-304, among the brightest 2FHL HBL and thus among the most intense neutrino sources, being a southern object does not enter into our list.

KM3NeT: KM3NeT (e.g., **?**) will be a new undersea neutrino telescope that could detect all-flavor neutrinos. Presently it is under construction in the Mediterranean sea.

The expected effective area as a function of declination, as that used above for IceCube, is not available yet. Therefore we chose to rely on the declination-averaged effective area provided by **?**. Note that, as opposed to the case for IceCube, for KM3NeT, a given source in the sky is below the horizon (and thus the up-going muon technique can be applied) for only a fraction of a year. **?** provide the effective exposure time of sources located at different declinations, that, is the fraction of time for which the source is below the horizon and thus data can be obtained. In Table **??** we thus report the expected neutrino counts for one year taking into account the effective exposure of the different sources (also reported in the Table).

In Fig. **??** we also show a sky map in galactic coordinates reporting the HBL of the 2FHL (light blue points) and, in blue, the best candidates for KM3NeT (upper panel) and IceCube (lower panel). For KM3NeT the colored areas indicate regions of the sky with different exposures from red (minimum) to green (maximum). In Fig.**??** we report the calculated neutrino flux as a function of the 2FHL γ-ray flux for the sources reported in Tables **??**-**??**.

Table 5.2 Expected 0.1-10 PeV flux (in units of 10^{-8} GeV cm^{-2} s^{-1}) and detection rate of muon neutrinos R_ν (yr^{-1}) for the brightest 2FHL BL Lacs with KM3NeT with different thresholds on the zenith angle (horizon and +10°). We also report the fraction of the observational time for which each source is below the threshold. The numbers identify the sources in the sky map, Fig. **??**.

	Name	F_ν	R_ν	Visibility at horizon	R_ν	Visibility at 10°
1	Mkn421	8.77	4.59	0.30	5.80	0.39
2	PKS2155-304	2.15	2.23	0.60	2.53	0.69
3	Mkn501	3.41	1.65	0.28	2.26	0.39
4	PG1553+113	1.89	1.42	0.44	1.66	0.51
5	PKS0447-439	0.76	0.87	0.67	1.02	0.79
6	PKS1424+240	1.00	0.67	0.39	0.79	0.46
7	PKS2005-489	0.51	0.63	0.72	0.75	0.86
8	TXS0518+211	0.87	0.59	0.39	0.72	0.48
9	PG1218+304	0.92	0.55	0.34	0.69	0.44
10	1ES0647+250	0.75	0.47	0.36	0.60	0.46
11	3C66A	0.87	0.38	0.25	0.54	0.36
12	1RXSJ054357.3-55320	0.30	0.40	0.78	0.52	1.00
13	PKS0301-243	0.43	0.44	0.59	0.49	0.66
14	1H1914-194	0.45	0.44	0.57	0.49	0.63
15^a	1H1013+498	0.87	-	-	0.48	0.32
15^b	1RXSJ194246.3+10333	0.41	0.32	0.45	-	-
16	PKS1440-389	0.36	0.41	0.66	0.47	0.76
17	1ES0347-121	0.39	0.35	0.53	0.40	0.60
18	1ES1215+303	0.52	0.31	0.34	0.39	0.44
19	1RXSJ101015.9-31190	0.32	0.34	0.60	0.39	0.69
20	RXJ0648.7+1516	0.45	0.33	0.42	0.38	0.49

5.5.2 Discussion

In this work we presented a heuristic framework to connect the γ-ray flux produced through the inverse Compton inside a structured jet of a HBL and the (hypothetical) neutrino flux. The scheme is motivated by the findings of **?** and in **?**.

The dependence on the gamma-ray flux makes possible to derive neutrino fluxes for BL Lacs, without secure redshift measurements. This is quite important since approximately 50% of the HBL of the 2FHL have uncertain z. We also note that, although based on a specific model, assuming a structured BL Lac jet, the linear correlation found between γ-ray and neutrino fluxes has already been suggested in the past for blazars (e.g., **?**, **?**).

We derived the expected number of muon neutrinos for the BL Lac of the 2FHL catalogue for both IceCube and KM3NeT provide a list of sources and expected numbers. Our study is focused on the through-going ν_μ because the angular resolution is well-defined in the detectors. Our analysis takes into account the structural differences between the detectors. We have used the effective area at different declinations for IceCube and the effective area for muon neutrino for all declinations for KM3NeT. A major difference between the two detectors is their latitude; IceCube is located at the South Pole and therefore the sources always have the same visibility throughout the year. Different is the case of KM3NeT, that has a range of declinations for which the sources are only partially visible during the year. For this reason, for our calculation we considered the visibility as a function of source declination for the muon-track analysis for tracks below the horizon and up to 10° above the horizon, given by KM3NeT collaboration. We calculated the expected number of neutrinos from HBL both for tracks below the horizon and for tracks up to 10° above the horizon; the difference between the two values is a factor of approximately 1.2. A more detailed study will be done when the effective area to the various declinations for KM3NeT is made available.

From our calculations we derive IceCube fluxes consistent with observations, predicting that for only a few γ-ray bright BL Lacs do we expect a handful of neutrinos detectable throughout few years of operation. The majority of the sources, however, have fluxes implying rates of the order of $\lesssim$0.1 events yr^{-1}, for which a clear association is thus problematic.

TXS0506+056 belong to the 2FHL catalogue. In particular with IceCube we expected a neutrino rate of ~ 0.25 event yr^{-1}. This result is compatible with the observation of a neutrino from this source.

For KM3NeT, on the other hand, we foresee an appreciable neutrino flux for several sources. We report 20 BL Lacs for which the expected rate is > 0.3 events yr^{-1}. For the brightest sources (Mkn 421, PKS 2155–304, Mkn 501), the event rate would likely be high

enough to allow a firm identification. We would like to point out that, for as far as the identification of the sources is concerned, KM3NeT and the proposed upgraded IceCube Gen2 (**?**) are expected to play a relatively valuable role. In particular, both are expected to have an improved (sub-degree) angular resolution for through-going muon neutrinos[1], which will greatly help studies of the correlation between the direction of the neutrino revealed and an extragalactic (or galactic) source. Moreover, having two instruments covering both hemispheres it will be possible to investigate better possible south-north anisotropies and spectral differences.

The structured jet model that we adopt is based on the assumption that the emission we observe from HBL is (almost) totally produced by leptons through synchrotron and IC mechanisms (although it is applicable to all cases in which one predicts a linear relation between neutrino and γ-ray fluxes). Protons (or hadrons) are only responsible for the observed neutrino flux (as shown in Section **??**). The accompanying UHE γ-ray photons (from π^0 decay and emitted by the $e^{\pm}$ pairs from the charged pions decay) are readily reprocessed through electromagnetic cascades, leaving the sources as a low-level MeV-GeV component. This is different from what is instead envisaged in lepto-hadronic models (e.g., **?**, **?**), predicting a luminous and hard MeV-GeV emission. Indeed, observations in the hard-X-ray band by the *NuSTAR* satellite (sensitive up to 80 keV), revealing a steep continuum up to the highest energies, seem to leave little room for this bright hard-X/soft gamma component (e.g., **?** for Mkn 421), expected to have a luminosity only slightly below that of the observed high-energy peak.

[1] The preliminary estimate for Km3NeT is ($< 0.2°$) (**?**).

Chapter 6

A multiwavelength view of BL Lacs neutrino candidates

Following the results of the previous Chapter, we decided to investigate those BL Lacs of the Second Catalog of Hard Fermi-LAT Sources (2FHL; **?**) that are in spatial coincidence with a neutrino event. A possible association of an HESE IceCube event with and HSP was suggested by **?**. A quite strong support to the idea that a a fraction of the neutrino flux is associated to BL Lacs comes from the recent possible association between a muon track event with an exceptionally good reconstructed direction and the active BL Lac TXS 0506+056 (Kopper & Blaufuss 2017, Tanaka et al. 2017, **?**, **?** see also **??** and **??**).

To further investigate the hypothesis of BL Lacs as sources of neutrino events, we started a program aimed at obtaining a better multiwavelength characterization of the emission properties of these sources, and their modelling. First of all, we define a sample of 2FHL BL Lacs potentially associated to IceCube events. Then, we complemented very sparse existing MW data, with observations with the Neil Gehrels *Swift* Observatory (hereafter *Swift*) for three candidates of our sample, and with REM campaigns for two others sources. The final datasets allowed us to assemble (non-simultaneous) SED for the sources.

We obtain a better characterisation of the SED for the sources of our sample. A prospective extreme Blazar, a very peculiar low synchrotron peak (LSP) source with a large separation of the two peaks and a *twin* of TXS0506+056 come up. We also provide the gamma-ray light curves to check the trend of the sources around the neutrino detection but the data do not reveal any pattern to the sources.

6.1 Selection of the BL Lac neutrino candidates

Following the results of **?** and **?** mentioned in the previous Chapter, we would like to assemble a sample of high-energy emitting BL Lacs to be correlated with the neutrino events. The best catalogue including this type of objects is the 2FHL catalogue. In fact, this catalogue consists of all sources detected above 50 GeV from the *Fermi* satellite. Even if the most recent Fermi catalogue, the 3FHL, comprises more sources (711 instead of the 193 BL Lacs of the previous one), it includes all the sources detected at lower energies (above 10 GeV). For this reason we consider the 2FHL catalogue more suitable to select high-energy emitting BL Lacs.

To create a sample of BL Lacs belonging to the 2FHL catalogue and investigate a spatial correlation with a neutrino event, we use the list of neutrino events reported in **?**. For the HESE events, **?** used the list provided by the IceCube Collaboration in **?**, including the events recorded during the period 2010-2012. To reduce the background by atmospheric neutrino events they selected only the events with a reconstructed energy, $E_\nu \geq 60$ TeV. Moreover, to limit the number of counterparts, only the events with angular uncertainty $\leq 20^\circ$ have been used. For the tracks, **?** considered the list given in **?**. For these tracks they assumed an average angular uncertainty of 0.4°, except for the 2.6 PeV event, for which the median angular error is 0.27° as reported in Schoenen & Raedel (2015). Since a recent release of muon tracks events (from the northern hemisphere) is given in **?**, we combine the HESE list by **?** with this more recent list of tracks. The position and the corresponding uncertainty of the neutrino events included in our sample are reported in the sky map shown in Fig.**??** (HESE: orange circles; muon tracks: red circles), together with the 193 BL Lac of the 2FHL (blue crosses).

We selected all the BL Lacs whose positions lie within the (large) angular uncertainty of the HESE events. We list all the BL Lacs found to satisfy the above selection criteria in Table **??**. For the track events, instead, we choose to consider significant any case in which there is a BL Lac at a distance less than 2.5° from the reconstructed centroid of the neutrino direction. We chose this value, which for some events is larger then the 90% C.L. angular uncertainty provided by IceCube Collaboration in **?**, to account for systematic differences between the reconstructed direction reported in the two different lists released by the IceCube Collaboration (respectively **?** and **?**). Note also than in both lists the angular errors are statistical errors only and do not include systematics. Then it is reasonable to consider a larger angular uncertainty. Due to the large uncertainty associated to the reconstructed position of HESE, for 12 of these events we found more than one BL Lac inside the error circle of a single event. Given the ambiguity on the potential candidates, in this exploratory work we only considered the HESE events with only one association.

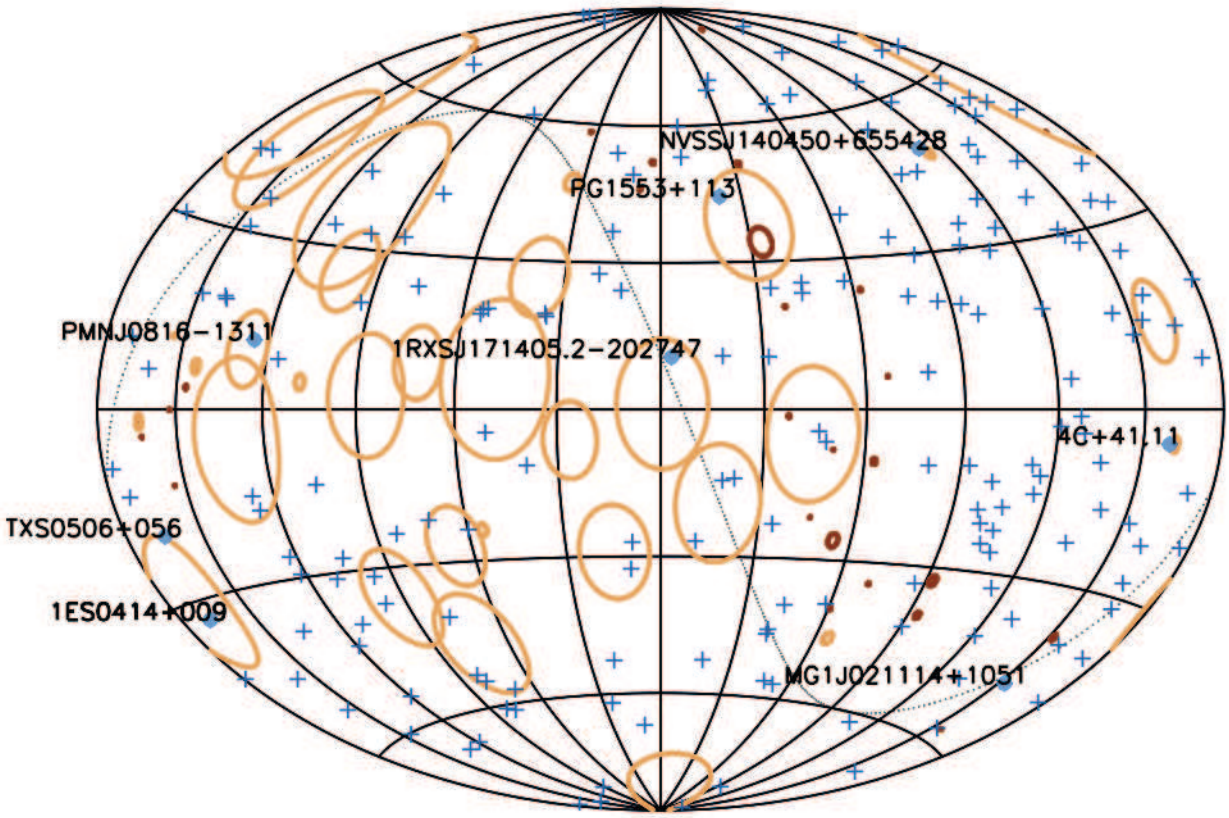

Fig. 6.1 Sky map in galactic coordinates reporting the reconstructed direction of the neutrinos detected by IceCube.The dotted black line is the equatorial line, the orange circles correspond to the angular uncertainty associated to 30 HESE events from **?** and the red dots indicate the direction of 29 muon tracks taken from **?**. The light blue crosses show the position of the 2FHL BL Lacs objects. We also indicate the sources in our sample (Table 2) with blue dots.

In fact, bearing in mind that the aim of this work is to study a clean sample of candidate neutrino emitting BL Lacs, we considered only the events in one-to-one correspondence with a only one BL Lac.

For the track events, we found one case in which the position of the associated BL Lac lies within the (small) angular uncertainty, namely MG1J021114+1051. As said above, to be conservative, we decided to include also two other sources, for which the distance from the corresponding neutrino position is less than 2.5°. The total number of selected sources is therefore 7. Two of them, 1ES0414+009 and PG1553+113, are TeV sources already well studied in literature (e.g. **?**). Therefore in the following we only focus our attention on the remaining poorly known 5 sources, whose properties are listed in Table **??**. To these sources we also add TXS 0506+056, that satisfy our selection criterium but

ID ν	Source name	Class
9	RXJ0950.2+4553	ISP
	Ton1015	HSP
	Ton0396	HSP
	1H1013+498	HSP
	Mkn421	HSP
11	RXJ1022.7-0112	HSP
	PMNJ0953-0840	HSP
	NVSSJ102658-174858	HSP
12	PKS2005-489	HSP
	PMNJ1936-4719	HSP
14	1RXSJ171405.2-202747	HSP
17	PG1553+113	HSP
19	1ES0505-546	HSP
	1RXSJ054357.3-55320	HSP
20	RBS0351	HSP
	PKS0229-581	ISP
	PKS0352-686	HSP
22	PMNJ1921-1607	HSP
	1H1914-194	HSP
	1RXSJ195815.6-30111	HSP
26	Ton0396	HSP
	MG1J090534+1358	HSP
27	PMNJ0816-1311	HSP
30	PMNJ0810-7530	ISP
	PKS1029-85	HSP
33	RXJ1931.1+0937	HSP
	1RXSJ194246.3+10333	HSP
35	1RXSJ135341.1-66400	HSP
	MS13121-4221	HSP
	1RXSJ130737.8-42594	HSP
	1RXSJ130421.2-43530	HSP
39	TXS0628-240	HSP
	PMNJ0622-2605	HSP
41	1ES0414+009	HSP
51	87GB061258.1+570222	LSP
	GB6J0540+5823	HSP

Table 6.1 List of all BL Lacs of the 2FHL catalogue in spatial correlation with a HESE neutrino event detected by IceCube and in the list of **?**. As expected the majority are HSP, defined as BL Lacs with the synchrotron peak $\nu_S > 10^{15}$ Hz.

Source name	α (J2000)	δ (J2000)	z	A_B	ν ID
Single 2FHL BL Lac inside the angular uncertainty of the HESE events					
PMNJ0816-1311	124.113	-13.197	$> 0.288^*$	0.296	27^a
1RXSJ171405.2-202747	258.521	-20.463	-	1.579	14^a
2FHL BL Lac with a distance max of 2.5° from a ν_μ					
4C+41.11	65.983	41.834	-	2.665	13^a
NVSSJ140450+655428	211.206	65.908	0.363	0.049	47^a
MG1J021114+1051	32.804	10.859	0.200	0.539	23^b
TXS 0506+056	77.358	5.693	0.336	0.392	IC170922A^c

Table 6.2 List of candidates neutrino sources studied in this work. For each source the equatorial (J2000) coordinates are reported (in degrees), the redshift, the A_B extinction coefficient from Schlafly & Finkbeiner (2011) (recalibration of the **?** infrared-based dust map) and the ID of neutrino detected by IceCube. The neutrino ID is taken from: *a*: **?**, *b*: **?**, *c*: IceCube Collaboration et al. 2018. Bold face characters identify the name of those sources for which we obtained dedicated *Swift* pointings. $*$: see Pita et al. (2014).

whose potentially associated neutrino event was not included in the lists considered above. This is the most plausible association observed so far and in our study we can use TXS 0506+056 as a benchmark case to discuss the other potential candidates (**?**). An important point to note is that not all selected sources are HSP, the BL Lac subclass favoured by the **?** analysis. In fact, even TXS 0506+056, whose synchrotron component peaks in the optical band, is classified as an intermediate synchrotron peak (ISP, 10^{14}Hz$< \nu_S < 10^{15}$Hz). Bold face is used for the sources for which we requested dedicated *Swift* observations. For MG1J021114+1051 and TXS 0506+056 we also obtained optical and IR observations with the Rapid Eye Mount (REM) telescope. For the other sources we only used archival data. The source TXS 0506+056 will be discussed in detail in the next section.

6.2 Data analysis

In the following, we describe the analysis performed on the *Swift*/XRT, *Swift*/UVOT, REM and *Fermi*/LAT data.

6.2.1 REM data

The Rapid Eye Mount telescope (REM) is a 60-cm robotic telescope located at the ESO La Silla Observatory. It includes an optical camera with the Sloan filters g, r, i, z and a near-infrared camera equipped with J-H-K filters. In these bands we observed MG1

Period	Filters					
	J	H	K	g	r	i
MG1J021114+1051						
01Oct2016/25Nov2016	-	-	17.088 ± 0.010	15.111 ± 0.025	14.578 ± 0.022	14.163 ± 0.032
TXS 0506+056						
30Sep2017	12.781 ± 0.056	11.945 ± 0.035	11.205 ± 0.100	15.013 ± 0.026	14.547 ± 0.020	14.174 ± 0.032
01Oct2017	12.632 ± 0.042	11.930 ± 0.051	11.061 ± 0.064	14.867 ± 0.022	14.361 ± 0.022	14.037 ± 0.033

Table 6.3 Observation period and filter used for the observation with REM telescope.

Source name	*b*	*m2*	*u*	*v*	*w1*	*w2*
1RXSJ171405.2-202747	19.55 ± 0.32	> 20.93	> 19.41	18.45 ± 0.28	> 20.27	> 21.13
4C+41.11	21.32 ± 0.42	> 21.45	21.22 ± 0.53	20.07 ± 0.32	> 21.08	> 21.69
NVSSJ140450+655428	> 20.18	> 20.53	> 19.78	> 19.38	> 20.00	> 20.84
PMN J0816-1311	17.19 ± 0.03	16.24 ± 0.03	16.25 ± 0.03	16.82 ± 0.04	16.18 ± 0.03	16.29 ± 0.03
MG1 J021114+1051	14.55 ± 0.01	14.46 ± 0.02	14.38 ± 0.02	14.02 ± 0.02	14.13 ± 0.02	14.58 ± 0.01
TXS 0506+056^h	15.06 ± 0.02	14.46 ± 0.02	14.27 ± 0.02	14.61 ± 0.02	14.35 ± 0.03	14.58 ± 0.02
TXS 0506+056^l	15.74 ± 0.04	15.42 ± 0.08	15.04 ± 0.03	15.24 ± 0.04	15.27 ± 0.03	15.60 ± 0.03

Table 6.4 *Swift*/UVOT observed magnitudes. Statistical uncertainties only are reported: systematic error is always lower than 0.03 mag. For TXS 0506+056 there are two states: h: high state of the source on 27/09/2017 (MJD: 58023.752), l: low state of the source on 25/07/2009 (MJD: 55037.512).

J021114+1051 and TXS 0506+056. Data reduction was carried out following the standard procedures, with the subtraction of an averaged bias frame dividing by the normalised flat frame. The photometric calibration was achieved by using the 2MASS and APASS catalogues. In order to minimise any systematic effect, we performed differential photometry with respect to a selection of non-saturated reference stars. Table 3 shows the observation period of these sources and the magnitude obtained at different filters.

Source name	Exp. time [ks]	Γ	N_H [10^{21} cm^{-2}]	χ^2_{red}(d.o.f.)	$F_{0.3-10keV}$ [10^{-12} erg cm^{-2} s^{-1}]
1RXSJ171405.2-202747	10.14	1.973 ± 0.053	1.56	1.259 (37)	3.55 ± 0.17
4C+41.11	27.70	1.578 ± 0.103	3.38	0.772 (12)	0.64 ± 0.55
NVSSJ140450+655428	10.78	2.349 ± 0.089	0.171	1.083 (12)	1.44 ± 0.05
PMNJ0816-1311	6.87	2.296 ± 0.026	0.81	1.394 (128)	19.97 ± 0.05
MG1J021114+1051	18.98	2.176 ± 0.027	0.616	1.201 (121)	5.79 ± 0.11
TXS 0506+056^h	4.947	2.606 ± 0.089	1.11	1.016 (21)	3.07 ± 0.25
TXS 0506+056^l	4.491	2.139 ± 0.288	1.11	0.282 (2)	0.86 ± 0.15

Table 6.5 Results of the *Swift*/XRT data analysis. For TXS 0506+056 there are two states: h: high state of the source on 27/09/2017 (MJD: 58023.752), l: low state of the source on 25/07/2009 (MJD: 55037.512).

6.2.2 *Swift*

Swift is a satellite equipped with several instruments (**?**). For all sources listed in Tab. 2, we had snapshot observations for both optical/UV and X-ray data. Comparing the different observation we noticed low variability and then we sum all the observations to increment the signal to noise ratio. In particular, we asked and obtained observation time for three sources of our sample (the bold face reported in Table 2). The observations were performed in the period October 2016-July 2017. For the other sources instead we re-analysed the archival data. In particular MG1J021114+1051 were observed in the period March 2010-November 2011 (data were already published, see Chandra et al. 2014 for details) while PMN J0816-1311 was observed by *Swift* in 2009.

Swift/UVOT data

The satellite *Swift* includes a 30 cm diffraction-limited optical-UV telescope (UVOT) (**?**) equipped with six different filters that covered the $170-650$nm wavelength range, in a 17 arcmin × 17 arcmin FoV. From the High Energy Astrophysics Science Archive Research Center (HEASARC[1]) data base we download the UVOT images in which our target sources were observed. For all the sources the analysis was performed with the `fappend`, `uvotimsum` and `uvotsource` tasks[2]. Due to the position of 1RXSJ171405.2-202747 full-stars field (see Fig.**??**) we perform a dedicated analysis. For the other sources we use a source region of 5 arcsec and the background was extracted from a source-free circular region with radius equal to 20 arcsec. The extracted magnitudes were corrected for Galactic extinction using the values of **?**, reported in the second to last column of Table **??** and applying the formulae by Pei 1992 for the UV filters, and eventually were converted into fluxes following Poole et al. 2008. Table 4 reports the observed Vega magnitudes in the Swift/UVOT v, b, u, $m1$, $m2$, and $w2$ filters, together with statistical uncertainties. Systematic uncertainties are never greater than 0.03 mag and therefore dominated by statistical ones in the vast majority of cases.

Swift/XRT data

Swift/XRT (**?**) data were analysed by using HEASOFT v6.20 software package. We analysed the spectra of the sources with XSPEC v.12.9.1 (Dorman & Arnaud, 2001) in order to extract the flux in the $0.3-10$ keV energy band and the photon index Γ, using the χ^2 minimization. For all sources an absorbed power-law model provides a good description of the spectrum.

[1]https://heasarc.gsfc.nasa.gov/docs/archive.html
[2]https://heasarc.gsfc.nasa.gov/docs/software/lheasoft/

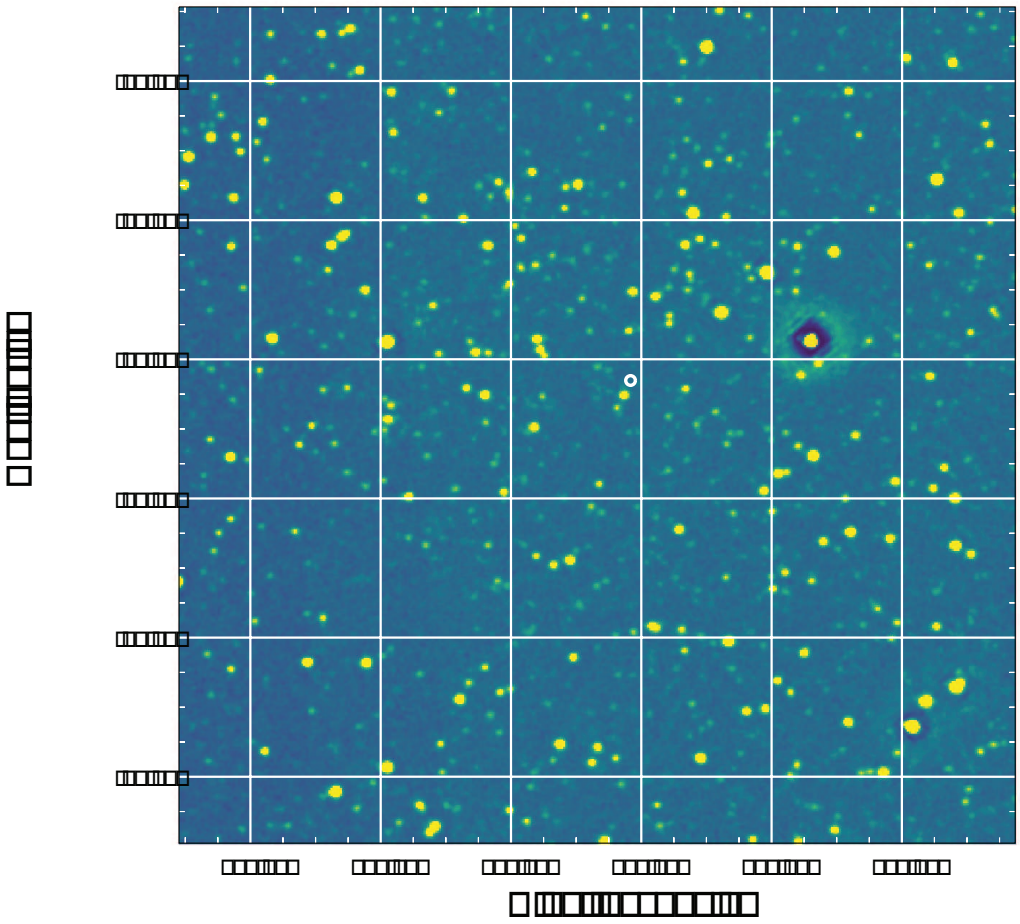

Fig. 6.2 Position map of the source 1RXS J171405.2-202747 in the *Swift*/UVOT B filter. The position of the source is highlighted by the white circle.

In all cases the fits are compatible with an absorption column, $N_{\rm H}$, fixed to the Galactic value. Table 5 shows the best fit parameters.

6.2.3 *Fermi*/LAT data

Fermi-LAT data analysis was performed using the Fermi Science Tools (v10r0p5) and PASS8 response Functions (P8R2_SOURCE_V6). Gamma-ray data were selected running *gtselect* for SOURCE events class, collected within 20° from the source under investigation; the chosen zenith angle cut was 90°. GTIs were prepared running *gtmktime* to select good quality data, collected during standard data taking mode. Livetime cubes were prepared taking into account the chosen zenith angle cut.

Gamma-ray light curves were produced in the energy range 0.3-100 GeV with a bin size of 4d and 16d for all sources. To cover possible active states lasting for several months, as observed in the case of TXS0506+056, we show the light curve in an interval of 300 days centred around the associated neutrino event. The flux reported for the chosen time-bins of the light curves is obtained with the standard unbinned likelihood analysis. The sources input files for the unbinned likelihood was prepared starting from the sources positions and spectral templates reported in the 3FGL catalog (**?**). For the investigated source, normalization and spectral parameters were allowed to vary. For sources within 10° from the investigated source, the normalization factor only was allowed to vary, and all the spectral parameters were fixed to their catalog value. For sources outside 10° from the investigated source, the normalization and all the spectral parameters were fixed to their catalog value.

In Fig. **??** we show the light curve for our sample of source (including PG1553+113 and 1ES0414+009). Due to the low flux, we show the 16 days bin light curve for all the source except for PG1553+113 and TXS0506+056 that are bright enough to have a good light curve with 4 days bin. The red vertical line shows the arrival time of the neutrino in spatial correlation with the source and the orange horizontal line is the mean flux of the source in the range 0.3-100 GeV reported in the 3FGL Fermi catalogue.

From Fig. **??** it is clear that for the most of the sources there is no significant γ-ray activity at the time of the neutrino detection (except the case of TXS0506+056). The light-curve of TXS0506+056 is consisted with the one present in IceCube Collaboration et al. (2018), Padovani et al. (2018), Keivani et al. (2018) and Veritas Collaboration (2018).

6.2.4 The case of 1RXSJ171405.2-202747

The study of 1RXSJ171405.2-202747 needed of a careful analysis because of the position of the source. It is in fact very close to the galactic center and therefore in a region full of stars and other sources (see Fig. **??**). For this reason we check carefully every data related to this source to be sure the effective association with our source.

Within the 3FGL gamma-ray catalog (**?**) the accuracy in the position of 3FGL J1714.1-2029 is 3.6 arcmin (95% c.l.). 1RXS J171405.2-202747 is identified as its X-ray counterpart. At 2.0 arcmin from the γ-ray source there is a radio source (**?**): NVSS J171405-202748 (with an accuracy on the position of radio source of 2.4 arcsec R.M.S.); while at 4.9 arcmin (just oustide the γ-ray error circle) there is NVSS J171402-202525. NVSS J171357-203653 is at 7.5 arcmin, NVSS J171442-202631 at 8.7 arcmin, all the other NVSS sources are more than 10 arcmin apart from the γ-ray source.
An X-ray source was observed and detected with Swift several times at celestial coordinates: α = 17 14 05.4, δ=-20° 27' 49", with an error of 3", coincident with the position of 1RXS J171405.2-202747 and of NVSS J171405-202748. No X-ray counterpart is found for NVSS J171402-202525.
In the following we will assume the detected *Swift* source as the X-ray counterpart of 3FGL J1714.1-2029; and NVSS J171405-202748 as the radio counterpart of the γ-ray source.
There is a weak near IR counterpart for NVSS J171405-202748 found in the 2MASS catalog (**?**), with celestial coordinates α=17 14 05.43, δ=-20° 27' 49.09" and positional error of 0.15 arcsec. A brighter NIR object (α =17 14 05.44, δ= -20° 27' 54.27") is found at 6.1 arcsec from NVSS J171405-202748, just outside the radio source error circle. We will consider the first near IR source as the counterpart for NVSS J171405-202748.

Summing-up all *Swift*/XRT observations, an absorbed power-law model does not fit to the data (reduced χ^2=2.2, see Table 5). A log-parabolic (Tramacere et al. 2007) model fit to the data: Using the *eplogpar* function ($F(E) = \frac{K}{E^2} 10^{-\beta(log(\frac{E}{E_P})^2)}$), the estimated parameters (for a confidence level of 90%) are: peak energy $E_P = 1.83^{+0.32}_{-0.27}$, curvature term $\beta = 0.86^{+0.36}_{-0.32}$, unabsorbed flux (in the 0-3-10 keV energy range) $F = (5.0^{+0.3}_{-0.4})10^{-12}$ erg cm^{-2} s^{-1}. The χ^2 is 5.9 for 15 degree of freedom, the null hypothesis probability is 0.92.

6.3 Spectral Energy Distributions

The Spectral Energy Distributions (SED) of the 6 sources, built by using archival data (green) and the data described above, are shown in Figs. **??**-**??**.

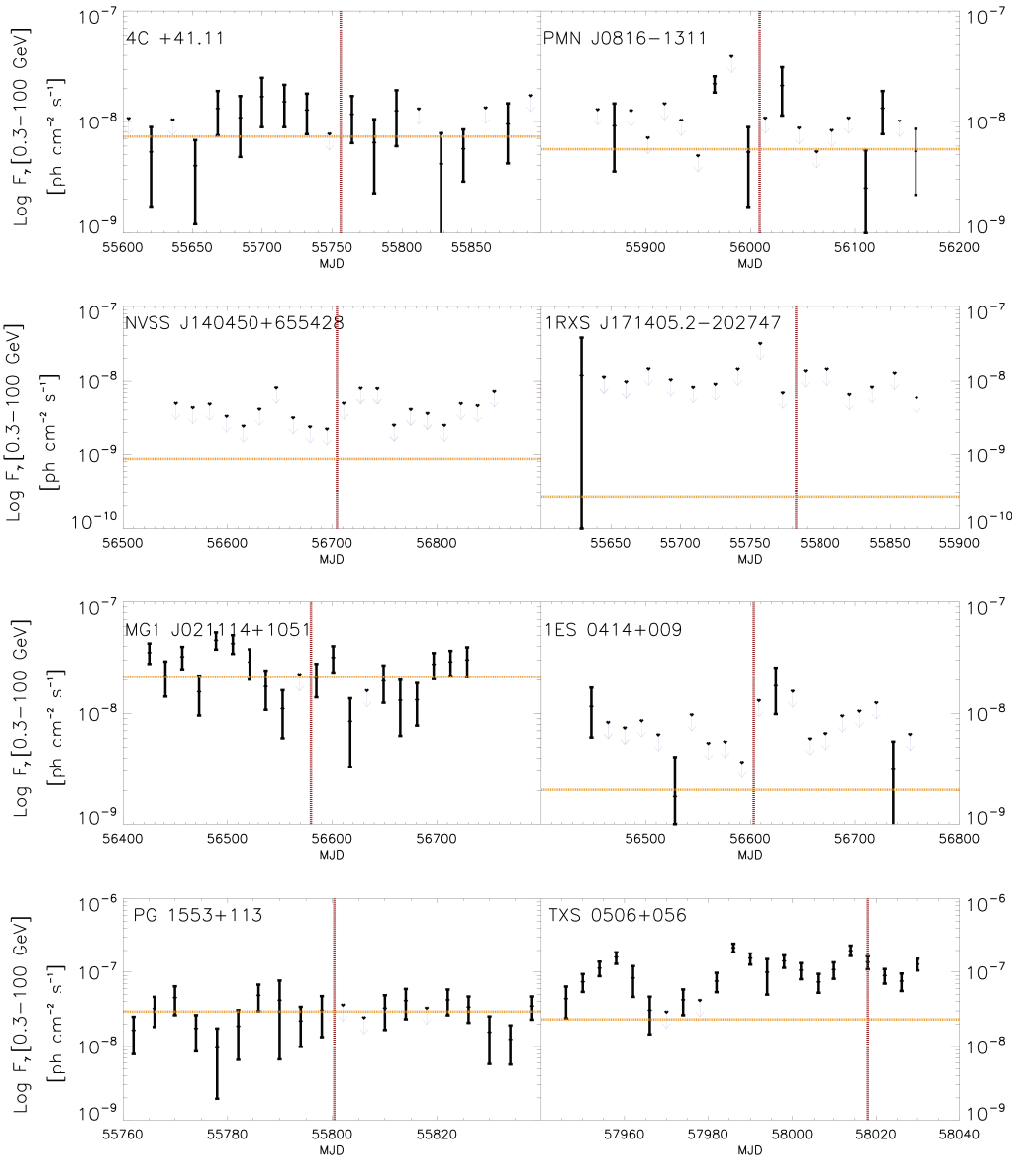

Fig. 6.3 γ-ray light curve of all 8 candidate sources. The bin is 16 days apart from PG1553+113 and TXS 0506+056 in which the bin is 4 days. The horizontal orange line represents the mean flux reported on the 3LAC catalogue. The data do not show flares in correspondence with the neutrino emission (red vertical line). However a discussion about the expected coincidence between a neutrino event and a γ-ray flare is in Section **??**.

We remark that the observational data from *Swift* and REM are not simultaneous. Moreover *Swift* spectra have been obtained from short snapshots performed over several months (see section **??**). Furthermore, there are very few data during the neutrino detection. The SED can therefore only provide time average information and cannot be used for detailed modelling of the electromagnetic and neutrino output.

The SED display a large variety of shapes. In particular, two sources (PMN J0816-1311 and NVSS J1404+65) clearly belong to the HSP population, with a peak frequency of the synchrotron component above 10^{15} Hz. MG1 J021114+1051 and TXS 0506+056 display a quite notable similarity and fulfil the criteria to be defined ISP. The SED of the remaining two sources have a less clear nature.

As discussed above, the analysis of the data of 1RXS J1714-20 is complicated by its position on the sky, close to the galactic plane. In particular, the confusion introduced by the complexity of the field makes difficult to understand the correct association of some of the data found in literature. For this reason we made a careful selection of the archival data. The concave X-ray spectrum from XRT, modelled with a log-parabolic fit (see section 3.5 for detail), suggests a peak around 1 keV. Such a large synchrotron peak frequency resemble a characteristic feature of the so-called extreme BL Lacs (e.g. Costamante et al. 2001, Bonnoli et al. 2015, Costamante et al. 2018). Besides a peak in the X-ray band, these peculiar sources display a quite hard gamma-ray continuum, often peaking in the TeV band. The optical band, instead, is dominated by the emission from the host galaxy. The data for 1RXS J1714-20 are consistent with both characteristics. The LAT data track a hard spectrum peaking above 100 GeV. The exceptional hardness of the spectrum is confirmed by the fact that this source belongs to the 2FHL (selection above 50 GeV) but it is absent in the 3FHL (selection above 10 GeV). Unfortunately, the description of the optical emission is poor. However, the UVOT upper limits together with the 2MASS datapoint are consistent with the emission from a typical elliptical host galaxy of BL Lac objects (for comparison, the dashed line reports the template for a giant elliptical by Silva et al. 2004).

The SED associated to 4C+41.11 is puzzling. The archival and the UVOT data locate the maximum of the synchrotron peak in the IR band. The hard XRT spectrum suggests that the X-ray continuum is associated to the second bump, likely peaking in the LAT energy band. The position of the synchrotron peak define 4C+41.11 as a LSP. However, the flat LAT spectrum (photon index ≈ 2) is quite atypical for this class (Ackermann et al. 2015). The shape of this SED is quite similar to the case of AP Lib, another LSP with an unusually hard LAT spectrum. This particular SED is quite difficult to be reproduced with standard one-zone emission models (e.g. Tavecchio et al. 2010) and possibilities to overcome this problem include the addiction of other components, possibly from the

large-scale jet (Hervet et al. 2015, Sanchez et al. 2015, Zacharias & Wagner 2016), or the contribution of hadronic processes **?**.

The case of TXS0506+056 has raised the attention of the whole high-energy astrophysics community (see Sections **??** and **??**). The facts that the source was in an high-state in the γ-ray band during the neutrino detection, that the event was a muon track event with a very good reconstructed direction (less than 1°) and the detection for the first time in the TeV band, make this event unique and particularly relevant. **?** showed the optical spectrum of the sources taken with the Gran Telescopio CANARIAS (GTC) with which, thanks to the emission lines of [OII],[OIII] and [NII], they attested a redshift of $z = 0.3365 \pm 0.0010$. Here we report both the high state, with data taken in the period 27/09/2017-01/10/2017, and the low state, data of 25/07/2009.

Together with the electromagnetic output, in Figs. **??**-**??** we also report the inferred level of the neutrino emission. In particular, the orange circles have been derived calculating the expected neutrino flux, F_{ν_c} required to have one neutrino detected during the seven years of operation of IceCube and assuming the energy estimated for that event. To this aim we use the declination-dependent effective area provided by **?** for track events and the one performed in **?** for the HESE. The light blue triangles instead show the flux, $F_{\nu_{R17}}$ derived by using the model of **?**, which assumed that BL Lacs belonging to the 2FHL account for the entire observed neutrino diffuse emission and that for each source the neutrino flux is correlated to its γ-ray flux. The fact that the brightest BL Lac sources of 2FHL catalogue are absent from our sample (such as Mkn421 or Mkn 501), suggests an overestimation of the flux $F_{\nu_{R17}}$. This raises a question about the neutrino emission from *Mkn-like* sources (see next Chapter). Note that in **?** we considered only the northern hemisphere, for this reason, for the 1RXS J 1714-20, we present only F_{ν_c}.

The requirement to produce a sizeable neutrino emission, implies that a fraction of the electromagnetic output derives, at least, from the γ-rays and the pairs injected in the source after the decay of neutral and charged pions. To properly model these processes (in particular the associated electromagnetic cascades) one needs to fully implement all the processes as in e.g., **?** and **?**. However, the paucity of soft target photons provided by the synchrotron component alone, requires the existence of external sources, such as the photons from the accretion flow **?** (see next Chapter) or those envisioned in the spine-layer scenario (e.g. **?**, as discussed in the previous Chapter).

6.4 Discussion

Following the idea that BL Lacs can be the emitters of high-energy neutrinos detected by IceCube, we started a observational campaign of a sample of candidates. From a list of 30 HESE + 29 muon tracks events respectively from **?** and **?**, and the BL Lac of the 2FHL catalogue of Fermi, we obtain a sample of 8 candidate neutrino BL Lacs spatially correlating with IceCube events. Two of the sources are very well-known high-energy emitting BL Lacs detected also in the TeV band (PG1553+113 and 1ES0414+009). For the other six sources we obtained observations with REM and *Swift* (optical, UV and X-ray band), to have a more accurate description of the synchrotron peak. Adding also archival data we derive the spectral energy distribution, that show a variety of shapes. As expected (since we started from 2FHL objects), the majority of sources are HSP, i.e. display a synchrotron peak at frequencies $\nu_S > 10^{15}$Hz, but, over a total of 8 sources, 3 appear to belong to the LSP or ISP subclasses. Assuming the detection of only one neutrino in 7 years with IceCube, we calculate the expected muon neutrino energy flux ($F_E = N \cdot E / A_{\rm eff} t$, with $N = 1$, $t = 7$y and $A_{\rm eff}$ the muonic effective area at the specific declination and energy and E the reconstructed neutrino energy), obtaining values in the range $10^{-12} < F_\nu < 10^{-11}$ erg cm^{-2} s^{-1}. We also compare this values with the expected muon neutrino flux obtained in a previous work **?**. The latter are systematically lower than those derived above assuming the detection of one neutrino in seven years. However, in considering this result, it is important to keep in mind that these fluxes – whose derivation assume, for instance, a constant flux of the sources (even if the large scale variability is one of the main characteristic of this class) and that this class is the unique emitter of the IceCube events – are affected by large uncertainties (e.g. $\eta_{\rm BL} < 1$ as introduced in the previous Chapter).

To investigate the possibility that the neutrino emission is associated to a particularly active state of the sources we have derived the light curves in the LAT band. While in the case of TXS 0506+056 the neutrino detection (Sep. 2017) coincides with a long lasting active state starting in April 2017 (see **?**), none of the other sources show such a significant increase of activity close to or in correspondence of the epoch of the neutrino detection. Small amplitude variability possibly correlated with the neutrino detection occurred in MG1 J021114+1051, PMN J0816-1311 and in 1ES 0414+009. However the quality of the data prevent any conclusion. A dedicated analysis of the correlation between the LAT light curves and possible excesses recorded by IceCube around the position of these sources could be interesting. However, we note that a strict correlation between neutrino emission and γ-ray activity is questionable also for TXS 0506+056, as proved by the potential neutrino emission found in 2014/2015 by **?** in coincidence with a rather quite gamma-ray

state (**?**). A strict link between gamma-ray emission and neutrinos is also excluded by modelling of the multimessenger SED of TXS 0506+056 in the framework of the photo-hadronic scenario (see previous Chapter), which suggests that the cascade and Bethe-Heitler components cannot be dominant in the high-energy band. The low sensitivity of present neutrino detectors with the pronounced variability of the sources make difficult the assessment of correlations between γ-ray flares and the neutrino emission.

A potential problem of the framework linking BL Lacs and the neutrino diffuse emission is represented by the absence of any clear association of neutrinos with the two brightest representative of the class, Mkn 421 and Mkn 501 (see also discussions in Aartsen et al. 2018b). In fact, there are no events associated with Mkn 501, while Mkn 421 is only potentially associated to a cascade events whose reconstructed direction is characterized by a very large angular uncertainty (Padovani & Resconi 2014, Petropoulou et al. 2015). The lack of events clearly correlated with these sources, after 7 years of activity by IceCube, raises doubts about the role of HSP as important neutrino emitters. Indeed, estimates based on the high-energy γ-ray flux as proxy (e.g., **?**) suggest that these two sources alone should provide $\sim 50\%$ of the entire muon neutrino emission attributable to BL Lacs. In **?** we specifically derived the expected significance of a possible detection by IceCube of Mkn 421, obtaining a significance of 3σ after 8 years. The lack of any excess around the position of these two sources, together with the possible observation of a neutrino emission by TXS 0506+056 source (not a HSP), bring us to ponder about the photon component involved on the photo-meson reactions. In **?** and **?**, the photons produced in the external and slow sheath of the jets is thought to play a role on the neutrino productions. This scenario is applied to the high-energy emitting BL Lacs, those sources in which there are the strongest indications supporting the presence of the spine-layer structure. The problems with Mkn 421 and Mkn 501 lead us to propose that the radiatively inefficient radiation flow can provide a radiation field that would favour LSP sources as neutrino emitters and would disfavour ISP and HSP objects **?**. This is the motivation of the model discussed in the next Chapter.

A possible continuation of the study described in this paper could be the extension to the BL Lac objects of the Third Catalog of Hard Fermi-LAT Sources (3FHL; Ajello 2017), which contains the sources detected in 7 years above 10 GeV by Fermi. This catalogue is composed of $\sim 50\%$ HSP and $\sim 50\%$ ISP+LSP. Table 7 shows the spatial correlation with the same sample of neutrino events and the BL Lacs of the 3FHL catalogue. A in-depth study of the SED and the light curve of these sources will be pursued.

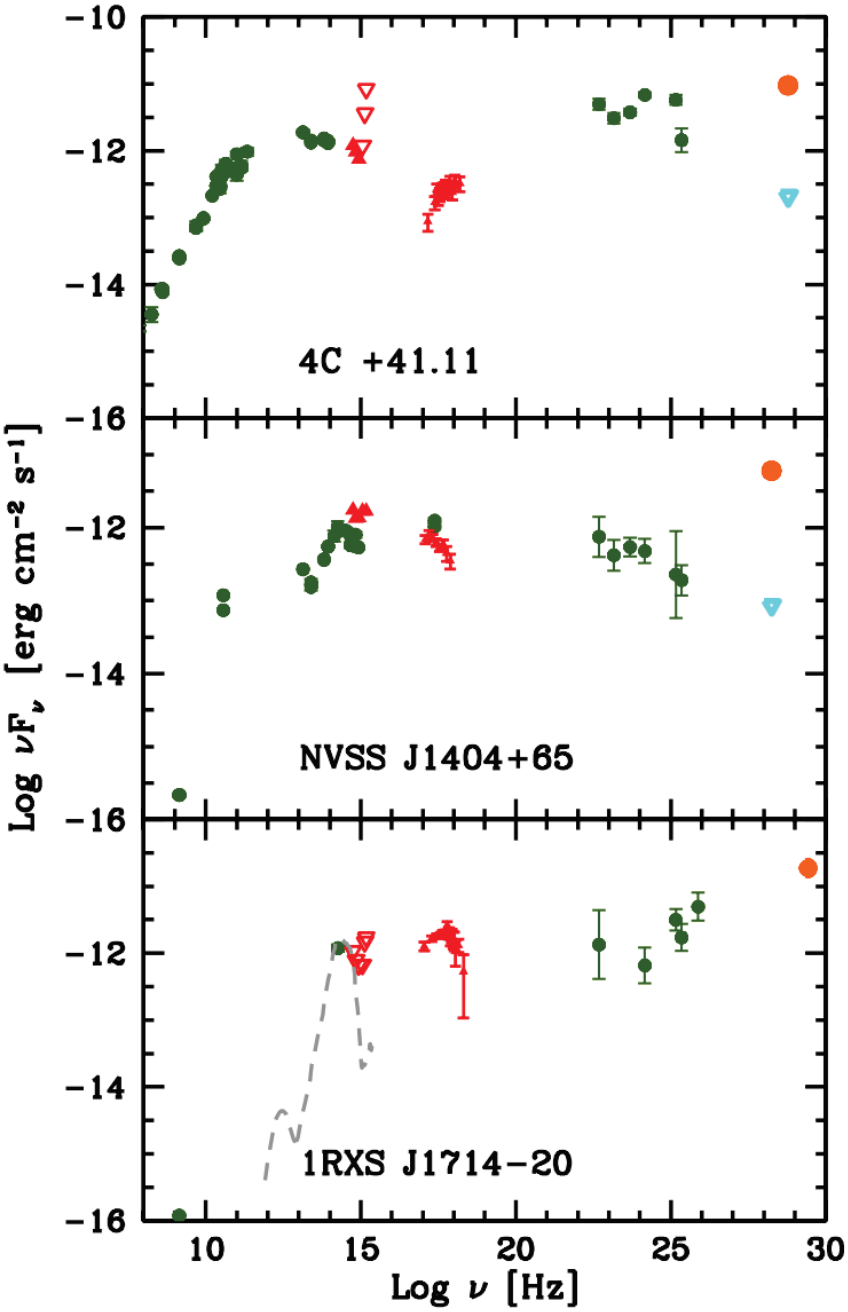

Fig. 6.4 Spectral energy distributions for three of BL Lac neutrino candidates. Green dots are archival data (by ASDC), red filled up-pointing triangle are *Swift*/UVOT and *Swift*/XRT data. *Swift*/UVOT upper limits are indicated with red down-pointing triangle. Orange dots corresponds to the expected neutrino flux, assuming one neutrino in 7 years of observation by IceCube, and using the effective area at the energy of the neutrino associated with the BL Lac. Light-blue triangle is the neutrino flux calculated in **?**. Due to the declination of 1RXSJ1714-20 (below the equator), the neutrino flux calculated in **?** is missing.

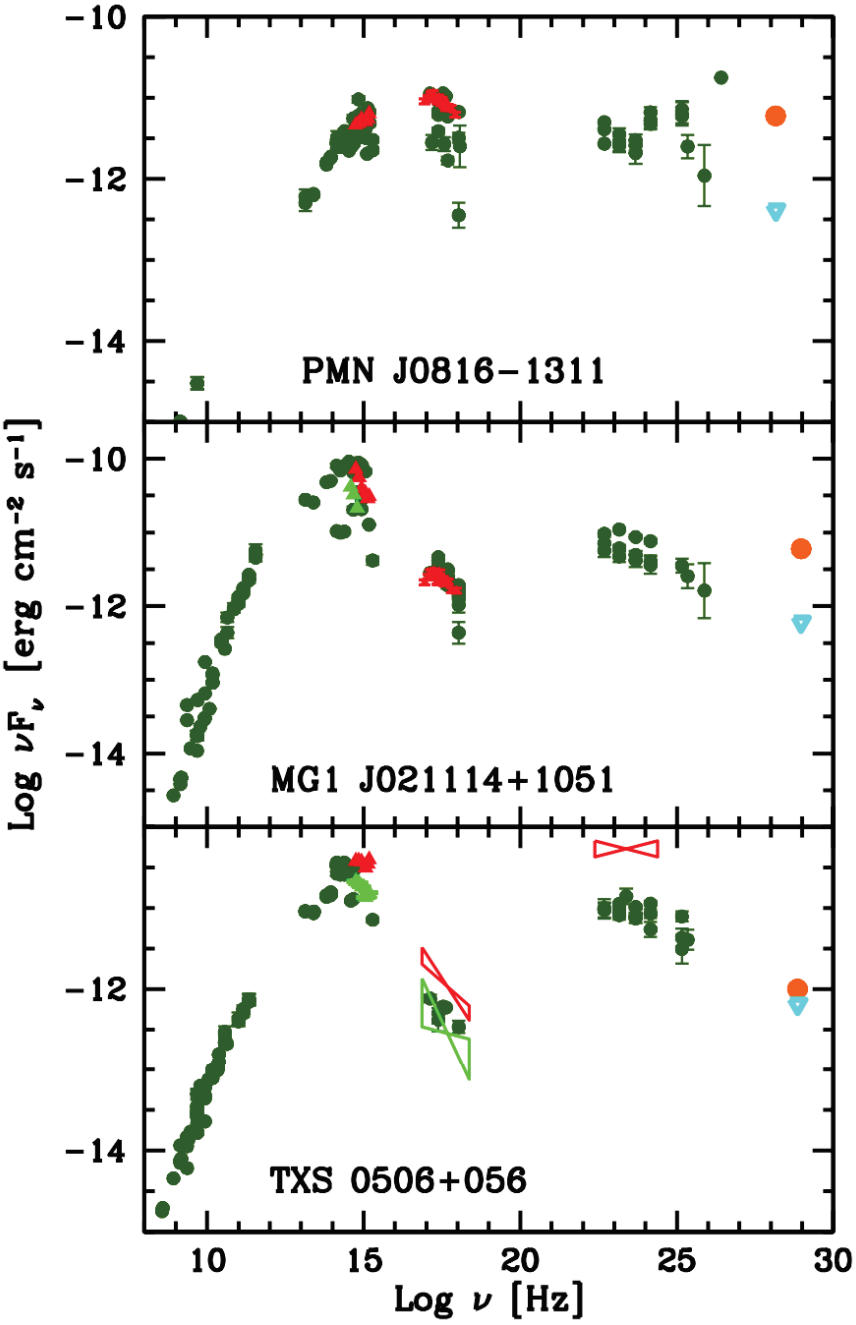

Fig. 6.5 Spectral energy distributions for three of BL Lac neutrino candidates. Green dots are archival data (by ASDC), red filled up-pointing triangle are *Swift*/UVOT and *Swift*/XRT data. *Swift*/UVOT upper limits are indicated with red down-pointing triangle. Light green up-pointing triangle are REM data (for MG1 J021114+1051and TXS0506+056) and *Swift*/UVOT estimation (only for TXS 0506+056). Orange dots corresponds to the expected neutrino flux, assuming one neutrino in 7 years of observation by IceCube, and using the effective area at the energy of the neutrino associated with the BL Lac. Light-blue triangle is the neutrino flux calculated in **?**.

Source name	α (J2000)	δ (J2000)	z	Class	ν ID
Single 3FHL BL Lac inside the angular uncertainty of the HESE events					
PKS1101-536	165.967	-53.950	-	LSP	4^a
1RXSJ094709.2-254056	146.789	-25.683	-	-	46^b
NVSSJ173146-300309	262.945	-30.052	-	-	14^a
3FHL BL Lac with a distance max of 2.5° from a ν_μ					
NVSSJ140450+655428	211.206	65.908	0.363	HSP	47^a
4C+41.11	65.983	41.834	-	LSP	13^a
MG1J021114+1051	32.804	10.859	0.200	ISP	23^b
TXS 0506+056	77.358	5.693	0.336	ISP	$*^c$
PMNJ2227+0037	336.992	0.618	2.145	ISP	44^b
PMNJ0152+0146	28.165	1.788	0.080	HSP	1^d
MG3J225517+2409	343.779	24.187	-	LSP	3^d
RXJ1533.1+1854	233.296	18.908	0.307	HSP	12^d
RXJ2030.8+1935	307.738	19.603	-	-	5^d
1ES0229+200	38.202	20.288	0.140	HSP	16^d

Table 6.6 List of candidates neutrino sources of 3FHL. Bold face characters identify the sources of 3FHL studied in this paper. The neutrino ID is taken from: *a*: **?**, *b*: **?**, *c*: Aartsen et al. 2018, *d*: **?**. We show the redshift reported in NED.

Chapter 7

The emission of radiatively inefficient accretion flows as target for neutrino emission

In the previous Chapters we already point out the importance of the photon target spectrum involved in the $p\gamma$ reaction. The photon spectrum shape influences the neutrino emission due to the presence of the photon density $n_t(\epsilon)$ in the Equation **??**. This influence is regulated by the threshold energy of the $p\gamma$ interaction (equation **??**). The event correlated with the flaring BL Lac TXS0506+056 point out the so-called *Markarian problem* we are going to talk about in the next Chapter (see **??**). Briefly, TXS0506+056 is not one of the brightest γ-ray sources and it is not a typical high-energy synchrotron peak BL Lac (HSP or HBL) for which there are observational evidences of the presence of a structured jet. The observation of a neutrino event from that source raises questions about the photon population involved in the neutrino emission. We already pointed out that by considering a simple scenario in which neutrinos are produced by the interaction of HECRs with synchrotron radiation produced by the relativistic electrons inside the jet cannot allow to produce the required neutrino flux (see Section **??** and **?**). In this scenario, in fact, the power of cosmic rays should be too high (in excess of 10^{48} erg/s) to produce the inferred flux of neutrinos. On the other hand, the spine-layer structure is thought to charcterize the jet of high-energy BL Lac objects, such as Mkn421 or Mkn501. The non detection of a neutrino from one of these sources can be interpreted in several ways. One of this is to reconsider the photon target population involved in the $p\gamma$ reaction. In this Chapter we present an alternative scenario in which we consider as target the radiation produced by the radiatively inefficient accretion flow onto the central BH. In fact as already discussed in **??**, BL Lacs present weak or absent emission lines in the optical spectrum. This with

the low power of the jet lead the AGN community to consider the BLR poor or completely absent in the BL Lac structure. We already stressed the link between the BLR and the accretion disk in Sections, **??** and **??**.

7.1 Accretion flow models

Different models have been proposed to describe the accretion of matter onto black holes. They can be grouped in two different categories: *cold* (efficient) and *hot* (inefficient) accretion flows, which correspond to accretion at high and low accretion rates, respectively. Cold accretion flows consist of cool optically thick gas accreting in a disc-like geometry. The most prominent examples are presented in (**?**; **?**; **?**) and **?**;**?**; **?**; **?**; etc.).

On the other hand, hot accretion flows are virially hot and optically thin. They occur at low mass accretion rates, and are generally characterized by lower radiative efficiency than the standard thin disc. Moreover, their radiative efficiency strongly decreases by decreasing the mass accretion rate. The thermal stability of these structures is generally guaranteed by energy advection. The most popular model for hot accretion flows is the advection dominated accretion flow (ADAF; **?**, **?**, **?**, **?**, **?**, **?**).

7.1.1 Radiatively efficient accretion disc

? introduced for the first time an accretion model based on the formation of a disc around a black hole. During accretion, matter is moving in a geometrically thin and optically thick disc. The plasma moves in Keplerian motion, and approaches the central black hole only if there is an efficient mechanism to transfer outwards the angular momentum. The magnetic field transport driven by the infalling matter, along with the turbulent motions of the matter itself, enable the angular momentum transfer.

The total energy release and therefore the spectrum of the emitted radiation are determined mainly by the mass accretion flow, i.e. the rate of matter inflow $\dot{M}$. Hence, the total disc luminosity L_d is given by the gravitational energy release through the relation:

$$L_d = \xi \dot{M} c^2$$

where ξ is the efficiency of the whole process and in general it is $\xi \sim 0.08 - 0.1$.

An upper critical luminosity is defined by the Eddington luminosity $L_{\rm Edd} = 4\pi G M_{\rm BH} m_p c/\sigma_T$. This is the luminosity at which radiation pressure is intense enough to stop the gravitational infall, and therefore accretion itself (defined in spherical geometry). In this sense,

the Eddington luminosity is generally assumed as an upper stability limit of the Shakura-Sunyaev disc. Numerically:

$$L_{\rm Edd} = 1.3 \times 10^{38} \frac{M_{BH}}{M_\odot} {\rm erg\ s^{-1}} \tag{7.1}$$

Corresponding to $L_{\rm Edd}$, an Eddington accretion rate can be defined as $\dot{M}_{\rm Edd} = \eta_{\rm acc} L_{\rm Edd}/c^2$ (e.g.**?**) where $\eta_{\rm acc}$ is a normalization parameter that does not contain physical information.

Because of the density and the optical thickness of the plasma, each element of the disc emits as a black body. The temperature of each element is determined by its distance from the central black hole, and closer to the black hole, the elements are hotter. Therefore, the most central regions of the disc are responsible for the most intense emission. The convolution of the black bodies with different temperatures and surface areas is a multicolor black body. In the case of a black hole with a mass $M_{\rm BH} \sim 10^6 - 10^9$ M$_\odot$, the spectrum peaks in the UV-soft X range. Photons with this energy are the most efficient in the ionization of plasma with the same properties as the BLR (see sections **??** and **??**).

7.1.2 Radiatively inefficient accretion disc

In the standard disc model, at very low accretion rates the particle density is so low that the energy exchange time scale between electrons and protons becomes larger than the accretion time scale. Most of the dissipated energy remains stored within the protons/ions, and an effective radiating disc model is no more plausible. The radiative disc model should occur only at accretion rate values larger than a critical value $\dot{m}_c$, i.e.

$$\dot{m} = \frac{\dot{M}}{\dot{M}_{\rm Edd}} > \dot{m}_c \tag{7.2}$$

where $\dot{m}_c \sim 10^{-2}$ **?**. Below this critical value the accreting flow is *advection* dominated, so that most of the viscously dissipated energy is advected radially with the flow. This is the fundamental feature of the Advection Dominated Accretion Flow (ADAF; **?**, **?**, **?**; **?**, **?**).

Figure **??** reports the relation between the temperature T and $\dot{m}$ for an accreting $10M_\odot$ black hole with viscosity parameter $\alpha = 0.3$ and ratio of gas pressure to total pressure $\beta = 0.5$, and focus on a radius $r = 10^3$. At very low $\dot{m}$ and very high $\dot{m}$, there is only one solution allowed for the temperature T of the system, therefore there is only one kind of flow allowed. However, for intermediate values of $\dot{m}$, there are three separate solutions. The uppermost branch, with a large value of T, is the advection-dominated branch discussed in **?**. This corresponds to the situation in which the fraction of the viscously dissipated

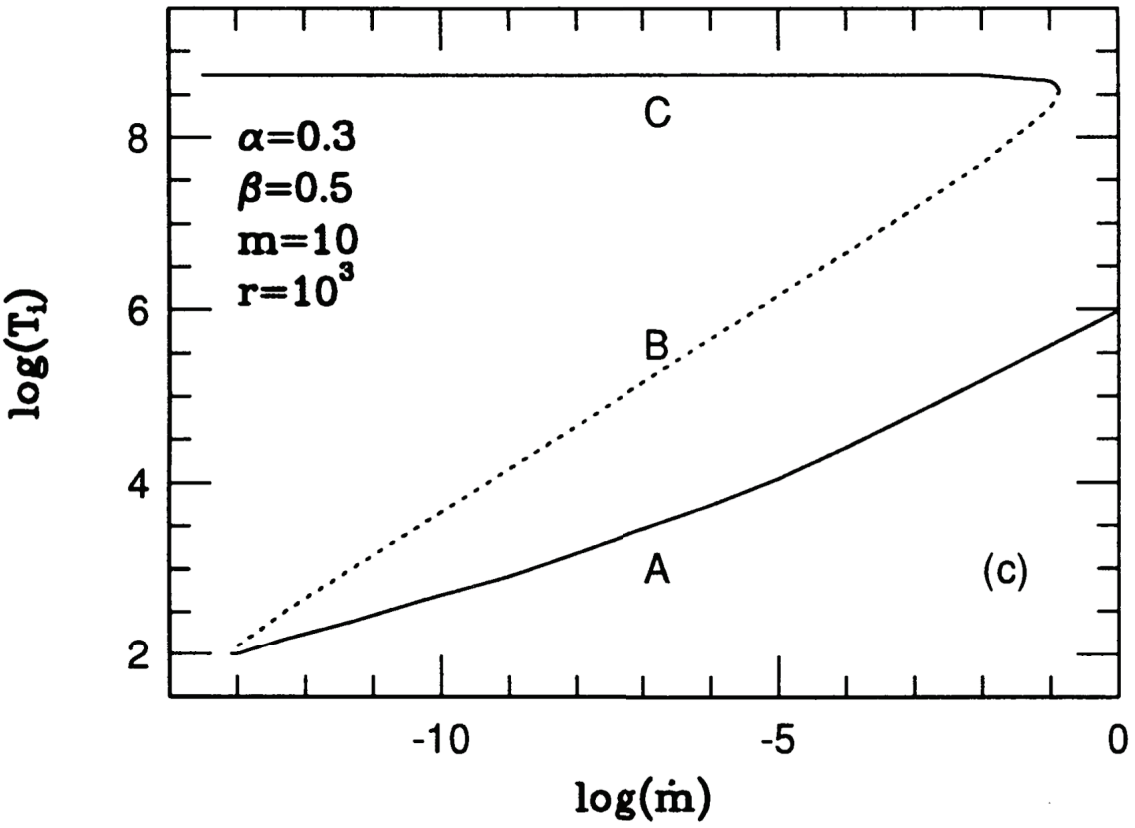

Fig. 7.1 Three solution branches for an accreting black hole. The uppermost branch is the advection-dominated branch discussed in **?** (C). Note that $T \sim cons. \sim 10^9$ K for this branch. In fact in this region the most of the dissipated energy is advected with the flow. The lowermost branch corresponds to the standard cooling-dominated thin accretion disk solution (**?**) (A). These two stable branches are connected by an unstable middle brach, indicated by a dotted line (B), which corresponds to the hot solution discovered originally by **?**.

energy is advected with the flow. If there is no exchange of energy between ions and electrons, the system tends to heat up. The lowermost branch has a very low value of T and it is therefore dominated by cooling. This solution has a low temperature, is optically thick, and corresponds to the standard thin accretion disk solution (**?**, **?**). Both these branches are stable at this radius. In addiction there is a middle branch, which is thermodynamically unstable and which is indicated with dotted line in Figure **??**. This solution has a low value of T and it is therefore cooling dominated. However this solution is much hotter than the thin disk branch and it can be the unstable (the SLE hot solution (**?**)). In figure **??**, the presence of a $\dot{m}_c$ for which the advection-dominated flows do not extend above is also clear.

With the assumption of radiation pressure dominance, **?** obtained a model with a definitely not disc-like morphology. The ADAF structure, indeed, is nearly spherical and it is generally much larger than a standard thin disc ($H \sim R$).

The system is highly under-luminous relatively to its mass accretion rate. The emitted radiation is not a black body, because the hot gas is optically thin. Its emission is instead dominated by processes like cyclo-synchrotron, bremsstrahlung and inverse Compton scattering. **?** and **?** described for the first time the details of the emitted spectrum of an ADAF. They assumed spherical accretion and calculated the spectrum as divided into three components: the cyclosynchrotron component, and the bremsstrahlung and the inverse-Compton component. The result of the spectrum is shown in Figure **??**. The first peak of the spectrum is produced by synchrotron emission from thermal electrons. This emission is self-absorbed and is very sensitive to the electron temperature. Synchrotron photons are Compton up-scattered by the hot electrons, producing hard radiation. The importance of this Compton component depends on $\dot{m} = \dot{M}/\dot{M}_{\rm Edd}$: at high values of $\dot{m}$ it dominates the spectrum, but as $\dot{m}$ decreases it becomes softer and bolometrically weaker. At sufficiently low $\dot{m}$, the hard-X-ray spectrum is dominated by the bremsstrahlung emission, since the inverse Compton component becomes less luminous and softer (in fact $T_e \sim 10^9 K$, as in figure **??**).

The dominant cooling process, therefore, strongly depends on the accretion rate. Under this condition, the radiation efficiency depends on the accretion rate too, instead of being just a fixed value.

To summarize, when $\dot{m} \gtrsim 10^{-2}$, a standard accretion disk is expected that is geometrically thin, optically thick, and radiatively efficient. In contrast, when $\dot{m} \lesssim 10^{-2}$, a transition to radiative inefficient accretion flow (RIAF) is supported by both theory and observations (**?**). In RIAFs, the density of the accretion flow is low enough that thermal protons cannot transfer their energy effectively to thermal electrons via collisional processes. As a

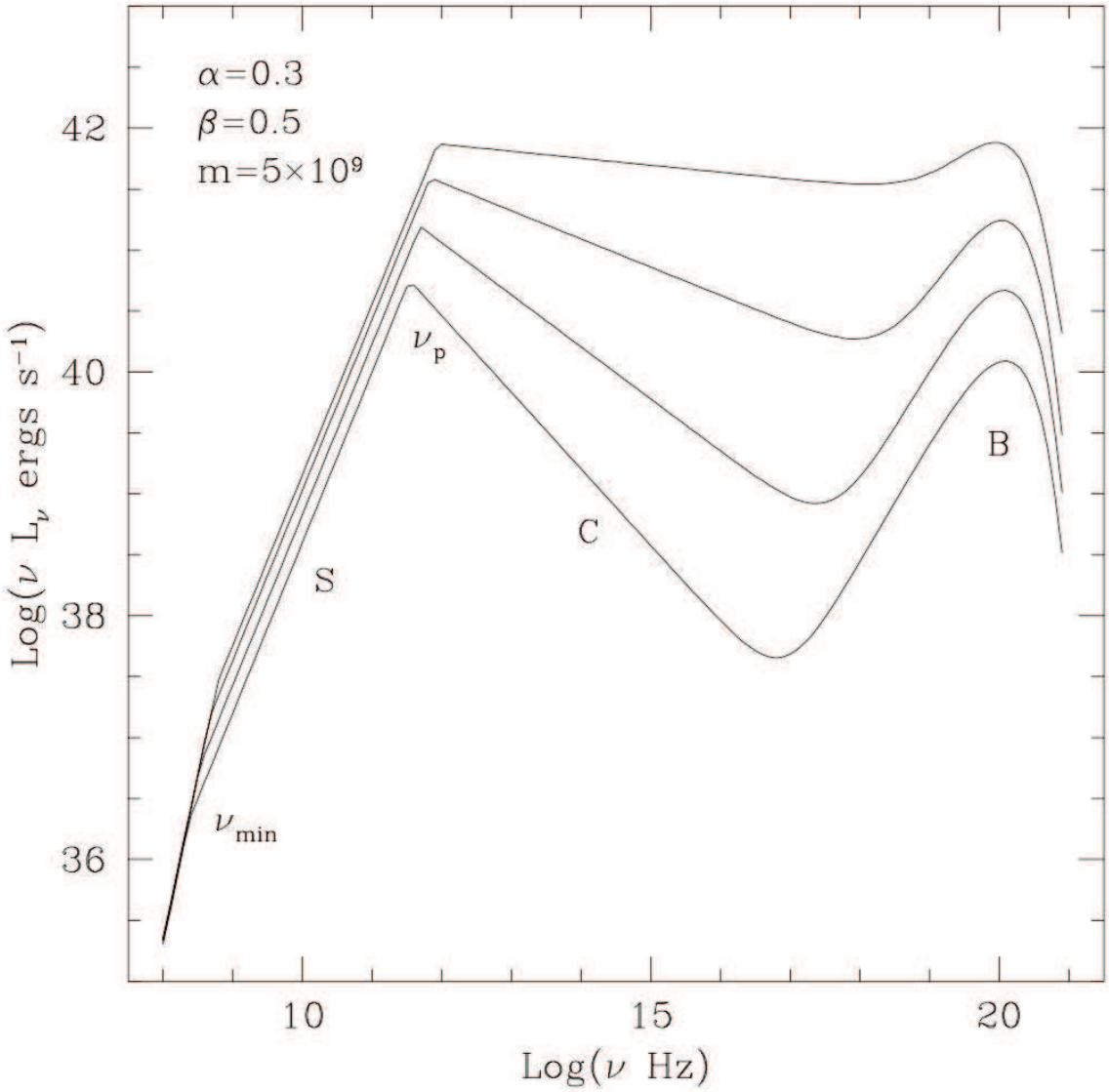

Fig. 7.2 Spectrum produced by an advection-dominated disk with $\alpha = 0.3$, $\beta = 0.5$, mass $m = 5 \times 10^9$ $M_\odot$, and $\dot{m} = (3,6,12,24) \times 10^{-4}$. The plots are calculated numerically by the method described in **?**. The three labels correspond to the three cooling processes: synchrotron cooling (S), Compton cooling (C), and bremsstrahlung cooling (B). ν_p and $\nu_{\min}$ correspond to the radio frequencies from the region $3 < r < 10^3$.

consequence, the proton temperature remains close to the virial value, much hotter than in standard accretion disks, and the flow becomes geometrically thick and optically thin while radiating inefficiently.

The systematic trends in the observed phenomenology of FSRQs and BL Lacs have been adequately interpreted in terms of a sequence in the total power (energy flux) in the jet $P_{\rm jet}$ correlated with $\dot{M}$, together with a transition from standard accretion disks in the nuclei of FSRQs to RIAFs in those of BL Lacs (e.g. Ghisellini et al. 2009). Within the BL Lac population, the trends among LBLs, IBLs and HBLs may also be understood as a sequence in $P_{\rm jet}$ and $\dot{M}$. Here we discuss the emission expected from RIAFs for each BL Lac subclass.

7.2 ADAF and neutrino emission

BL Lacs are relatively less powerful then FSRQs, and display weak or no emission lines, indicating the lack of strong external radiation fields. Their γ-ray luminosity is comparable to the synchrotron luminosity, but extends to higher energies then in FSRQs. BL Lacs can be further subdivided depending on the peak energy of their SED components, with low-synchrotron-peak BL Lacs (LBLs) emitting up to hundreds of GeV, and high-synchrotron-peak BL Lacs (HBLs) up to tens of TeV **?**[1]. The γ-rays observed in BL Lacs can generally be well explained as synchrotron self-Compton (SSC) emission, i.e. IC emission by electrons accelerated in the jet upscattering their own synchrotron emission. Given their low power and inferred weak radiation fields, the neutrino production efficiency for BL Lacs has often been thought to be low (**?**; see however, Sec. 5).

The recent finding that the likely counterpart of the ~300 TeV neutrino IceCube-170922A is TXS 0506+056, a BL Lac (Aartsen et al. 2018), is therefore not trivial to interpret. Note that TXS 0506+056 is likely an LBL or possibly an intermediate-synchrotron-peak BL Lac (IBL; see below). The picture is further complicated by the fact that the HBLs Mkn 421 and Mkn 501 are still undetected in high-energy neutrinos, despite being more prominent γ-ray emitters **?**).

In this context, a potential source of external photons for BL Lacs that has hardly been discussed in the literature is advection-dominated accretion flows (ADAFs), or more generally, radiatively inefficient accretion flows (RIAFs). As discussed above, it is quite plausible that the nuclei of BL Lacs host RIAFs (e.g. **?**), which are expected when the mass accretion rate $\dot{M}$ onto the central SMBH is lower than a critical value In the following we explore the role of RIAFs as external target photons for $p\gamma$ neutrino production in BL Lacs,

[1] Note that the abbreviations here differ from "HSP", "ISP" and "LSP" used in **?**.

	$\log < L_{\rm bol} >$ $\log$ (erg s^{-1})	α_1	α_2	α_3	$\nu_{\rm t}$ Hz	$\nu_{\rm S}$ Hz	$\nu_{\rm C}$ Hz	$\nu_{\rm cut,S}$ Hz	$\nu_{\rm cut,C}$ Hz	$\nu_{\rm S} L(\nu_{\rm S})$ erg s^{-1}	CD	N
LBL	47.2	0.65	1.3	0.62	3e11	1e12	3e21	5e16	7e26	1e46	1	71
IBL	46.2	0.7	1.3	0.8	2.5e11	5e14	1e23	6e18	8e26	8e44	0.7	21
HBL	45.8	0.68	1.2	0.8	1e11	9e16	5e24	4e19	5e27	4e44	0.4	18

Table 7.1 Parameters for the phenomenological SEDs plotted in Fig. **??**, where $\alpha_{\rm R} = -0.1$ was fixed. See G17 for detailed definition of the parameters.

which can have various interesting implications, including marked differences between LBLs and HBLs.

7.3 BL Lac spectral energy distributions

As reported in Section **??**, using a sample of 747 blazars (299 BL Lacs and 448 FSRQs) detected by *Fermi*-LAT with known redshifts from the 3LAC catalog (**?**), **?** (hereafter G17) confirmed the evidence for a spectral sequence, a systematic trend among the SEDs of all blazars that had been found in previous studies (**?**). To parameterise their average SEDs, G17 used a phenomenological function consisting of two broken power laws connecting with a power law describing the radio emission. We found that with increasing luminosity, BL Lacs have lower peak frequency, softer γ-ray slope and larger dominance of the high-energy component.

? proposed a subclassification among BL Lacs, based on the peak frequency ν_S of the synchrotron SED component:

- LBLs with $\nu_S < 10^{14}$ Hz,
- IBLs with 10^{14} Hz $< \nu_S < 10^{15}$ Hz, and
- HBLs with $\nu_S > 10^{15}$ Hz.

This "*Fermi*" classification scheme can be applied to 110 out of the 299 BL Lacs in G17 with sufficient data, resulting in 71 LBLs, 21 IBLs and 18 HBLs.

For the purpose of estimating typical values of the observed bolometric luminosity, intrinsic radiative power, and jet power for each BL Lac subclass, we parameterize the average SEDs of their non-thermal emission, using the phenomenological model of G17 and assuming $\alpha_R = -0.1$ for the radio spectral index. For each subclass, the model is compared with the data in Fig.**??**, and the ten model parameters that were determined are listed in Tab. **??**. From the model, it is straightforward to evaluate the average, isotropic-equivalent bolometric luminosity $L_{\rm bol}$. Assuming a jet bulk Lorenz factor $\Gamma_j = 20$ **?**, the

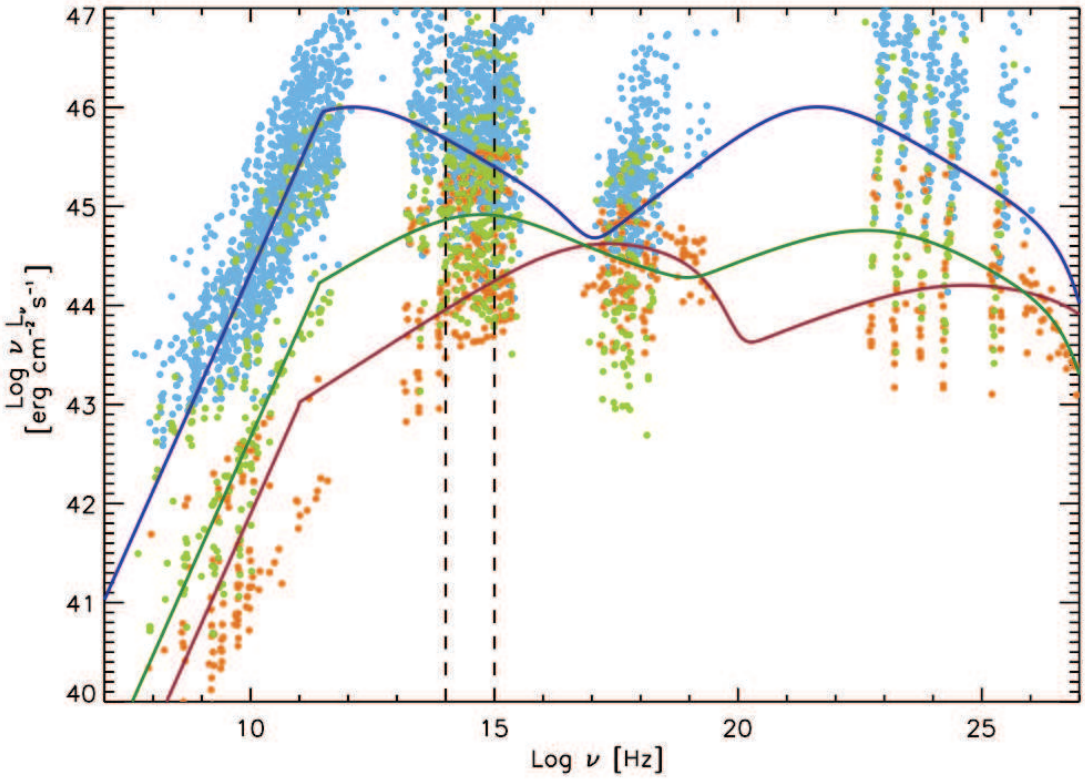

Fig. 7.3 Observed SEDs (filled circles) compared with average parameterized models for the three subclasses of BL Lacs: LBL (top, blue), IBL (middle, green), HBL (bottom, orange).

beaming-corrected power in radiation can be estimated as $P_{\rm rad} = L_{\rm bol}/\Gamma_j^2$ (e.g. **?**), with values listed in Table **??**. LBLs approximately have $L_{\rm bol}$ three times larger than IBLs, and $P_{\rm rad}$ three times larger than HBLs. We note that our aim here is not detailed spectral modelling of these SEDs.

Then, we adopt a simple scaling between $P_{\rm jet}$ and $\dot{M}$ (e.g. **?**),

$$P_{\rm jet} \approx \eta_j \dot{M} c^2, \tag{7.3}$$

where a value $\eta_j \sim 1$ is supported for the jet formation efficiency through modeling of *Fermi*-LAT blazars (Ghisellini et al. 2014) as well as numerical simulations of magnetically-driven jet formation (**?**) . On the other hand, a relation on average between $P_{\rm jet}$ and $P_{\rm rad}$ as derived from the SEDs in Sec. 2 is indicated by several studies (**?**, **?**, **?**),

$$P_{\rm jet} \approx P_{\rm rad}/\eta_{\rm rad}, \tag{7.4}$$

with $\eta_{\rm rad} \sim 0.1$. Assuming for simplicity fixed values of $M_{\rm BH} = 10^9 M_\odot$ and $\eta_{\rm acc} = 0.1$[2], $\dot{m}$ can be estimated for each BL Lac subclass from the average $P_{\rm rad}$ as

$$\dot{m} \approx \frac{\eta_{\rm acc}}{\eta_j}\frac{P_{\rm jet}}{L_{\rm Edd}} \approx \frac{\eta_{\rm acc}}{\eta_j \eta_{\rm rad}}\frac{P_{\rm rad}}{L_{\rm Edd}}, \tag{7.5}$$

resulting in $\dot{m} = 10^{-3}$, 3×10^{-3} and 10^{-4} for LBLs, IBLs and LBLs, respectively.

Although the details of the emission from RIAFs can be model-dependent **?**, for concreteness, we adopt the advection-dominated accretion flow (ADAF) model of **?**, who provide simple prescriptions for calculating the expected broadband spectra for different parameters. We assume viscosity parameter $\alpha = 0.3$, ratio of gas pressure to total pressure $\beta = 0.5$, minimum radius $r_{\rm min} = 3r_S$ and maximum radius $r_{\rm max} = 10^3 r_S$ in units of $r_S = 2GM_{\rm BH}/c^2$ (for more details, see **?**).

7.4 Neutrino emission induced by RIAFs

For the three subclasses of BL Lacs, Fig. **??** shows the expected RIAF spectra. As discussed above, they comprise three components: a hard power law below 10^{12} Hz due to cyclo-synchrotron emission, a softer power law covering IR to soft-X rays due to multiple IC upscattering by semi-relativistic electrons, and a bump peaking in soft γ-rays due to bremsstrahlung. With increasing $\dot{m}$, a conspicuous hardening of the IC component in

[2]We remember that $\eta_{\rm acc}$ is a normalization factor that do not contains physics proprieties.

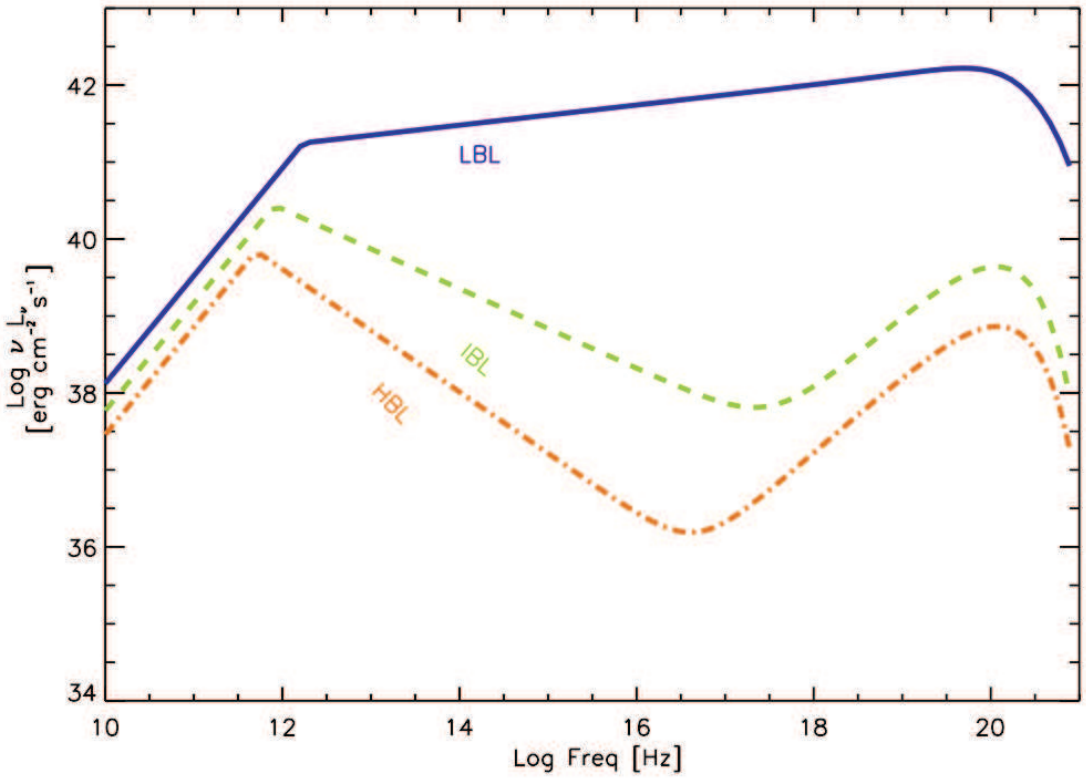

Fig. 7.4 RIAF spectra expected for the three subclasses of BL Lacs: LBL (solid blue), IBL (dashed green) and HBL (dot-dashed orange).

the UV to X-ray range can be seen, besides the overall increase in the luminosity. This is a robust prediction of ADAF models, and reasonably representative of RIAFs in general (**?**). The significant differences in the RIAF spectra among the BL Lac subclasses have key consequences for their neutrino emission.

We now discuss the neutrino emission from BL Lacs, considering RIAFs as sources of external target photons for $p\gamma$ interactions with protons accelerated inside their jets. the calculation follows the same lines discussed in Section **??**.

1. Considering a region in the jet with radius $R_j = 10^{16}$ cm moving with bulk Lorentz factor $\Gamma_j = 20$, accelerated protons are injected isotropically in the jet frame with luminosity L'_p, distributed in energy E'_p as a power-law with a maximum cutoff:

$$L'_p(E'_p) = k_p E_p^{'-n} \exp\left(-\frac{E'_p}{E'_{p,\max}}\right); \qquad E'_p > E'_{p,\min} \tag{7.6}$$

Type	$P_{\rm rad}$ erg s^{-1}	$P_{\rm jet}$ erg s^{-1}	$\dot{m}$ (10^{-3})	$L'_{\rm p}$ erg s^{-1}	R_{ν_μ} 7 yr
LBL	$6.3\cdot10^{44}$	$6.3\cdot10^{45}$	5.7	$5\cdot10^{44}$	1
IBL	$6.3\cdot10^{43}$	$6.3\cdot10^{44}$	0.5	$4.5\cdot10^{43}$	$8\cdot10^{-5}$
HBL	$2.5\cdot10^{43}$	$2.5\cdot10^{44}$	0.3	$1.8\cdot10^{43}$	$8\cdot10^{-7}$

Table 7.2 Radiative power, jet power, normalized accretion rate, proton power and neutrino detection rate for the three subclasses of BL Lacs.

where, for definiteness, we set $E'_{p,\rm max} = 10^{17}$ eV, $E'_{p,\rm min} = 3\cdot10^{11}$eV and $n = 2$. Heavier nuclei are neglected.

2. The photomeson production efficiency $f_{p\gamma}(E'_p)$ is determined by the ratio between the dynamical timescale $t'_{\rm dyn} \approx R_j/c$ and $t'_{p\gamma}(E'_p)$, the energy loss timescale for protons via $p\gamma$ interactions.

3. The neutrino luminosity L'_ν in the jet frame is:

$$E'_\nu L'_\nu(E'_\nu) \approx \frac{3}{8} f_{p\gamma}(E'_p) E'_p L'_p(E'_p); \qquad E'_\nu = 0.05 E'_p. \tag{7.7}$$

Using the Doppler factor of the emission region $\delta = [\Gamma_j(1-\beta_j\cos\theta)]^{-1}$, where $\beta_j = (1 - 1/\Gamma_j^2)^{1/2}$ and $\theta \approx 1/\Gamma_j$ is the viewing angle with respect to the jet axis, the luminosity of *muon* neutrinos L_{ν_μ} in the observer frame is

$$E_\nu L_{\nu_\mu}(E_\nu) = \frac{1}{3} E'_\nu L'_\nu(E'_\nu)\delta^4; \qquad E_\nu = \delta E'_\nu. \tag{7.8}$$

Note that the factor 1/3 accounts for equipartition among the flavors due to neutrino oscillations during propagation.

4. To evaluate $t'_{p\gamma}(E'_p)$ for this work, we account for both internal synchrotron photons from electrons accelerated in the jet, and external photons from the RIAF. For the internal photons, we utilize the SED models for the observed non-thermal emission described in §2, assume that it originates co-spatially with the protons and isotropically in the jet frame, and convert the SEDs into photon density in the jet frame using δ.

The resulting neutrino spectra for each BL Lac subclass are compared in Fig. **??**, which also shows the contributions from external RIAF and internal photons separately. To highlight the effect of the different RIAF spectra, here $L'_p = 10^{45}$ erg s^{-1} has been fixed. Most notably, the neutrino luminosity of LBLs at $E_\nu \sim 0.1$-1 PeV is ~ 4 orders of magnitude larger than that of HBLs, primarily due to the significant difference in the density of external RIAF photons in the soft X-ray range, which serve as the main $p\gamma$ targets for protons with $E_p \sim 2$-20 PeV. We also see that while internal photons are the most prevalent

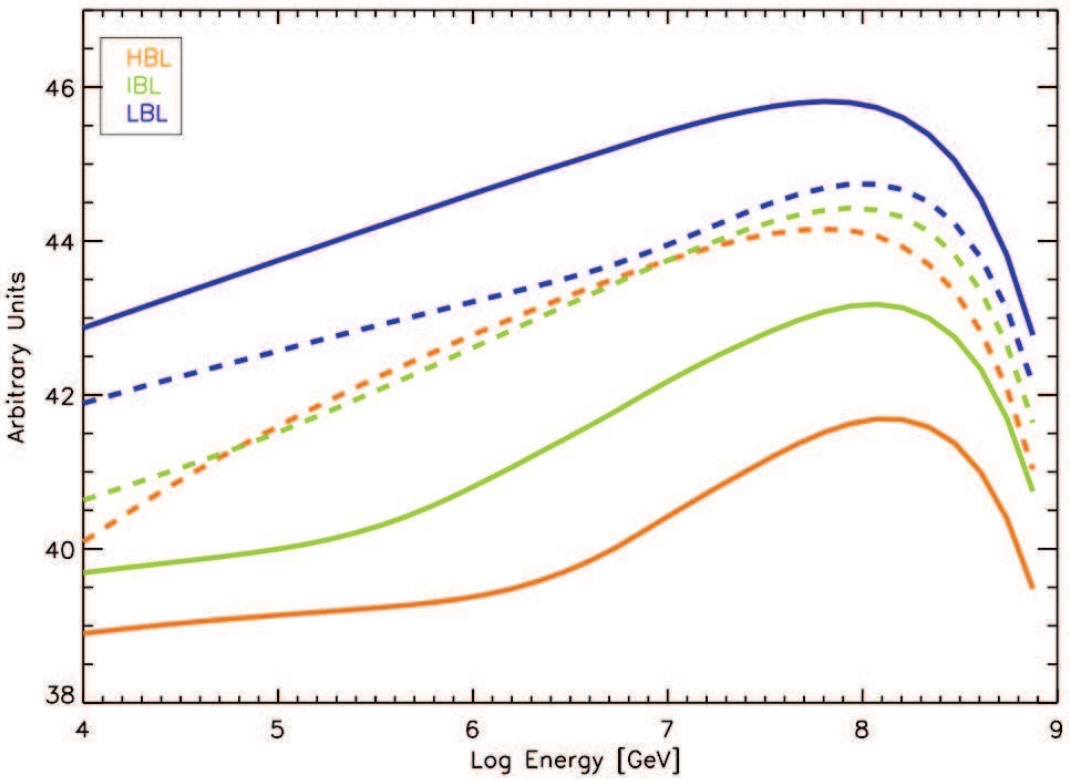

Fig. 7.5 Neutrino spectra due to $p\gamma$ interactions between protons with fixed $L'_p = 10^{45}$ erg s^{-1} and external RIAF photons for the three subclasses of BL Lacs: LBL (solid blue), IBL (dashed green), HBLs (dot-dashed orange). Contributions from internal photons as $p\gamma$ targets are also shown (dotted blue, green and orange for LBL, IBL, HBL, respectively).

$p\gamma$ targets in HBLs, external RIAF photons become relatively more important in IBLs, and completely dominate in LBLs.

More realistically, L'_p is likely linked to $P_{\rm jet}$ and is expected to vary among the BL Lac subclasses. An important test case is the BL Lac TXS 0506+056, potentially associated with IceCube-170922A, a ~300 TeV neutrino **?**. While TXS 0506+056 may be classifiable as an IBL from the observed ν_S alone, its observed luminosity is more representative of an LBL, especially in terms of our SED classification discussed in §2. We assume that TXS 0506+056 is a typical LBL, emitting neutrinos according to our model that includes external RIAF photons. With the measured redshift of $z = 0.3365 \pm 0.0010$ **?** and the IceCube effective area appropriate for the declination of TXS 0506+056 **?**, its neutrino flux must be high enough to result in at least one ν_μ detection during 7 years of IceCube observations in the energy range 60 TeV - 10 PeV, roughly corresponding to uncertainty for IceCube-170922A. This translates into a constraint on L'_p for LBLs. The values for IBLs and HBLs follow by assuming $L'_p \propto P_{\rm jet}$. With these values of L'_p for the different BL Lac subclasses, their neutrino spectra can be predicted as shown in Fig. **??**, together with the corresponding SEDs of the electromagnetic emission from the jet and RIAF. Tab. **??** lists the values of L'_p and R_{ν_μ}, the neutrino detections expected in 7 years.

Compared to the case assuming constant L'_p, the differences between LBLs and the other, less luminous subclasses is naturally magnified. As above, RIAFs play a significant role only for LBLs. In this scheme, only LBLs may be sufficiently powerful neutrino emitters to be observationally relevant. These inferences for the RIAF model are particularly interesting in view of the fact that the LBL TXS 0506+056 is likely the first identified source of high-energy neutrinos, while HBLs such as Mkn 421 and Mkn 501 are yet to be detected by IceCube, despite being conspicuous, nearby γ-ray emitters with some predictions of detectability (e.g. **?**). Although the relevant statistics is currently limited, stronger tests of this picture through further observations are anticipated.

7.5 Discussion

We have conducted a first study of the role of RIAFs as sources of external target photons for $p\gamma$ neutrino production in BL Lacs, finding that they can be particularly relevant for the subclass of LBLs, but less so for IBLs or HBLs. These results have interesting implications for interpreting the potential association of IceCube-170922A with the LBL TXS 0506+056, and the non-detections by IceCube so far of HBLs such as Mkn 421 and Mkn 501.

As an exploratory step, many simplifying assumptions were made concerning various aspects, which deserve more detailed and comprehensive considerations in the future. We

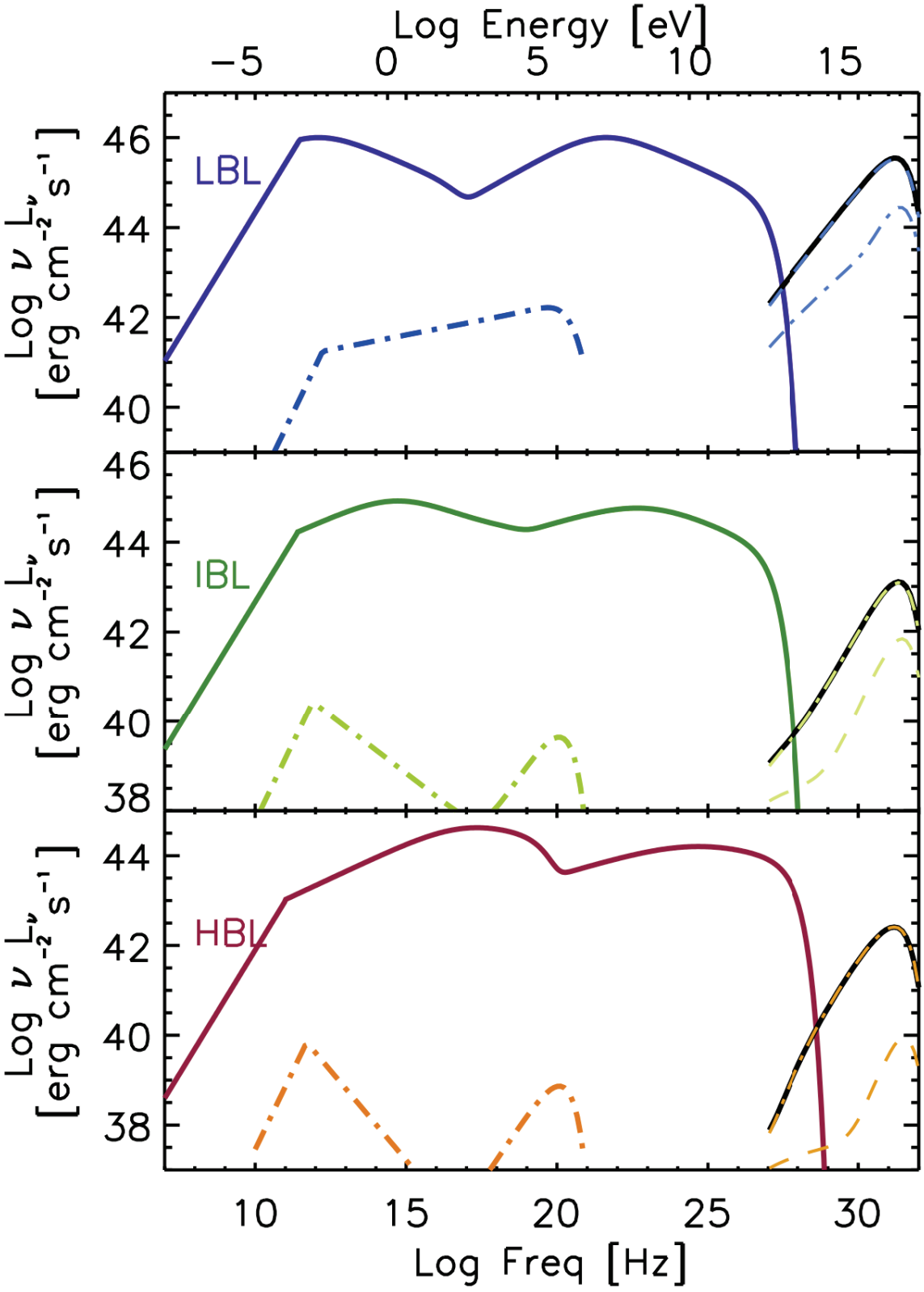

Fig. 7.6 SEDs for the three subclasses of BL Lacs: LBL (top), IBL (middle), HBL (bottom), showing the electromagnetic components from the jet (solid colored) and RIAF (dot-dashed), and the neutrino components due to internal photons (dotted), external RIAF photons (dashed), and their sum (solid black). Note the different scales for luminosity between the panels.

have assumed rudimentary scaling relations between $P_{\rm rad}$, $P_{\rm jet}$ and $\dot{M}$, and fixed quantities such as $M_{\rm BH}$ for simplicity. A more realistic study obviously needs to account for the distribution and scatter of these variables. Although our description of the non-thermal electromagnetic emission was entirely phenomenological, more physical modelling is warranted, including the potential effects of EC emission induced by RIAFs, hadronic emission components triggered by $p\gamma$ interactions, etc.

The simple ADAF prescription of **?** that we employed can be updated with more advanced RIAF models (**?**). Since the RIAF is geometrically thick, with different spatial dependences for each of its spectral components, accurate evaluations require a more proper treatment of the spatial and angular distribution of the RIAF photons impinging into the jet, which can also be affected by electron scattering in the jet vicinity. Such calculations may reveal non-trivial beaming patterns for both the EC and neutrino emission, with potentially important observational implications (see relevant discussion in **?**).

Chapter 8

Conclusions

This report summarizes the work done for my PhD thesis performed in collaboration between the University of Insubria and the National Institute for Astrophysics (INAF)-Observatory of Brera.

In this thesis I have addressed the problem of the identification of the source(s) of astrophysical neutrinos detected by IceCube with a specific focus on BL Lacs. The understanding of the neutrino emission (especially at the $\sim$ 100 TeV energy scale) within astrophysical sources is an issue of fundamental importance to shed light on the structure and dynamics of the source itself. Neutrinos are, in fact, able to escape from dense region, thanks to the small cross-section, thus providing information about regions otherwise not observable with other particles. The detection of a high-energy neutrino from a source allows to have indirect informations about the cosmic rays sources. During the last decade $\sim$ 80 events above 60 TeV were detected by IceCube, a 1 km cubic detector at South Pole. The main features of high-energy neutrino are presented in this thesis in *Chapter 1*.

Blazars are a subclass of active galactic nuclei (AGNs) with the relativistic jet pointing to the Earth. They are natural accelerators of particles, as witnessed by the strong non-thermal emission, and this makes them good candidate sources for extragalactic cosmic rays and neutrinos at high-energy. The main features of the two subclasses of Blazars (Flat Spectrum Radio Quasars, FSRQs, and BL Lacs) are presented in *Chapter 3*. The recent detection of a muon track event by IceCube, in the direction of a flaring BL Lac (with a chance coincidence statistically disfavoured at the level of $\sim 3\sigma$) offers a unique opportunity to explore the interplay between energetic photons, neutrinos and cosmic rays in the jet (see **??**, **??** and **??** for details).

The most significant results of my work concern the neutrino emission from BL Lacs. However, I also took part in other projects focused on the characterization of Blazars. In particular, I joined a spectroscopic campaign carried out at the 10 m Gran Telescopio

Canarias (GTC) of a sample of 22 BL Lac objects detected (or candidates) at TeV energies, aiming at determining or constraining their redshift (**?**, *Chapter 3*). The redshift is a fundamental parameter for models, and then for the interpretation of the emission from Blazars, for population studies and it is also mandatory for studying the interaction of high-energy photons with the extragalactic background light using TeV sources.

Moreover I worked on a reconsideration of the so-called *blazar sequence*, that is the trend characterising the SED of FSRQs and BL Lacs (**?**, *Chapter 3*). In particular, for the *new* sequence we confirm the main results of the original blazar sequence found in **?**. The presence of a trend of the SEDs of the two subclasses of Blazars puts some constraints on the physical proprieties of the objects and suggests an evolution from a subclass (FSRQs, high z, high luminosity) to the other (BL Lacs, low z, less powerful than FSRQs but with the SED peaked at higher energy).

Among the main topics of my work I started the study of BL Lacs as neutrino emitters. Based on a simple theoretically-motivated framework inspired by the structured jet scenario for these sources, we postulated a direct proportionality between the high-energy γ-ray flux produced through the inverse Compton inside a structured jet of BL Lac and the (hypotetical) neutrino flux. In this way, even if γ-rays and neutrinos have different origins, their fluxes can be correlated and a neutrino flux for each BL Lac can be estimated. This work (**?**) is presented in *Chapter 5* with the assumption that BL Lacs account for the entire neutrino diffuse emission. We derived the expected count rate for all BL Lacs objects of the 2FHL Fermi catalogue (sources detected above 50 GeV), obtaining a value above 1 event per year only for few sources.

According to this scheme, the brightest γ-ray BL Lacs, such as Mkn 421, Mkn 501 or PG 1553+113, are expected to be the brightest neutrino emitters. However, the non detection after ~ 8 years of these sources by IceCube is not in conflict with our result if one considers the background signal coming from the same direction of the source (see **?**). One of the main assumption of **?**, is to assume the 2FHL BL Lacs as the unique contributors to the neutrino spectrum observed by IceCube. This hypothesis should be relaxed assuming that BL Lacs contribute to only a fraction of the neutrino emission as suggested by many authors (see e.g. **?**, **?**, **?**).

As natural consequence of this work, we started an observational campaign for few selected BL Lac sources aimed at identifying any similarity on the SED of BL Lac candidate neutrino emitters (see *Chapter 6*, **?**). In particular, from the event lists released by the IceCube Collaboration, we selected those BL Lacs of the 2FHL catalogue alone in the angular uncertainty of high energy starting events (HESE), or close, $< 2.5°$, to the direction

of track events. With these constraints we obtained a sample of 8 sources including TXS 0506+056, and two well known TeV sources (PG 1553+113 and 1ES 0414+009).

The analysis of the SED and the γ-ray light-curves does not highlight any common feature for the objects. In fact, even they belong to different subclasses of BL Lac (HBL, IBL or LBL). This means that their SED is peaking at different frequency in a $\nu L(\nu)$ plot. Moreover, their γ-ray light-curves do not present a significant increase of flux in correspondence of the neutrino detection.

Starting from September 2017 I took part in the TeV observation (with the MAGIC Collaboration), the multiwavelength analysis and the physical interpretation of the coincidence event between the neutrino IC22092017A and the BL Lac TXS0506+056. With the MAGIC Collaboration, we applied the spine-layer scenario to the SED of TXS 0506+056 founding good agreement with the observational data. The model includes the hadronic component (cascades, proton synchrotron emission and Bethe-Heitler pair cascades) showing that the electromagnetic SED can be explained with the leptonic component (synchrotron emission from the relativistic electrons inside the spine and Inverse Compton of the same electrons with the synchrotron radiation emitted by the layer). The electromagnetic component coming from the photo-meson reaction interacts inside the jet and produces a cascade at lower energy. It can be significant at low energies (UV-X-ray band, through Bethe-Heitler emission and through cascade, see Section **??** and Figure **??**) or at high-energy (TeV band, through cascade, see Figure **??**).

From the model of TXS 0506+056 the important role of the X-ray band came up. In fact, in this band there are both hadronic and leptonic contributions. The slope of the continuum in this spectral region can suggest which contribution is dominant; for example a flat shape suggests an hadronic dominant emission (through Bethe-Heitler emission or photo-meson cascades). In other words, the X-ray band becomes relevant to distinguish the hadronic or leptonic emission. Except for **?** that considers the pp channel to model the SED of TXS 0506+056, other models agree on the lepto-hadronic view of the emission.

The non detection of neutrinos associated to the brightest BL Lacs such as Mkn 421 or Mkn 501 starts to put some constraints on the neutrino emission models. As reported in *Chapter 6* there are no clear evidences of a neutrino emission from these BL Lacs. These sources have the second peak of the SED at high-energy (above 50 GeV); for this reason it is natural to expect a large neutrino rate because their capability to reach high-energy in the electromagnetic spectrum. On a first approximation, the expected neutrino flux is at the same level of the γ-ray peak, that corresponds to a factor ~ 10 of the TXS 0506+056.

This puts some constraints on the expected neutrino flux from HBL objects. We developed an alternative scenario to justify the neutrino emission from sources TXS-like

(LBL/IBL) that at the same time penalises the neutrino emission from HBL objects. In this alternative model the photon target involved in the $p\gamma$ reaction comes from the accretion flow (see *Chapter 7*, **?**).

The accretion flow for BL Lac is considered inefficient due to the weak or absent emission lines. A confirmation of this idea is given by the inferred radiatively inefficient accretion rate for FR-I radiogalaxies, that in the unification scheme are considered the misaligned version of BL Lacs. From the relation between the BLR luminosity and the disc luminosity (e.g. **?**, **?**), it can be concluded that the accretion flow is not the optically thick and geometrically thin disc usually expected (**?**), but an accretion flow radiatively less efficient. In particular **?** suggested that at low accretion rate $\dot{m}$, the accretion flow becomes radiatively inefficient, optically thin and geometrically spheric, the so-called Advection Dominated Accretion Flow (ADAF) solution. The structure and the emission of the ADAF is described in *Chapter 7*. The main feature is the strong dependence of the emission in the UV-soft-X band on the accretion rate.

Our work discusses the possibility that the population of photons involved in the $p\gamma$ interaction come from the ADAF region. Dividing the BL Lac detected with Fermi into the different subclasses (LBL, IBL and HBL)[1], we obtain a different accretion rate for each subclass and then a different ADAF spectrum. We found that the radiation field of the ADAF is potentially dense enough to dominate the neutrino production in the case of low-energy peaked BL Lacs. For highly-peaked BL Lacs (comprising the famous high-energy γ-ray emitters Mkn 421 and Mkn 501) the contribution of the ADAF is instead comparable or smaller than that of the local radiation field of the jet and thus too low to allow powerful neutrino emission.

The general status and results can be with the following points:

- Blazar objects are potential sources for high-energy neutrinos. Their jet pointing to us is a natural accelerator of particles and the presence of radiation at all frequencies, in particular in the UV-soft-X band, produced inside the jet itself or in the environment, allows the $p\gamma$ interaction and then the neutrino emission.

- Despite the fact that they have been often considered poor neutrino emitters, a major role for BL Lacs, a subclass of Blazars, was argued in **?**, **?** and **?**, based on the possibility that their output is boosted by the presence of a structured jet, in which the slow external portions of the jet provide the main target for the photo-meson reactions.

[1] It is common also the expression LSP, ISL and HSP BL Lacs.

- While the above works considered BL Lacs as the main neutrino emitters, it is more plausible that they contribute to a fraction of the entire neutrino diffuse emission detected by IceCube. (e.g. **?**, **?**)

- The detection of a neutrino event in spatial and temporal coincidence with the flaring BL Lac TXS 0506+056 strengthen the case for BL Lac to be contributors of the neutrino diffuse intensity. The common feature that comes up from the models of the SED of this source is that the high-energy electromagnetic emission is dominated by leptonic emission (Inverse Compton), while the radiation emitted via hadronic processes (Bethe-Heitler cascade, synchrotron by relativistic protons and cascade of photo-meson reaction) is not relevant. The reprocessed hadronic component can come up in the X-ray band (between the two peaks of the SED) and at high-energy (TeV band). The shape of the X-ray spectrum could give information on the relative role of leptonic and hadronic processes.

- The absence of a clear detection of neutrinos associated to HBL objects (the brightest γ-ray BL Lacs), points out the problem of the emission processes inside BL Lac objects. The ADAF scenario proposed in **?** is a valid alternative to explain the neutrino emission from *TXS-like* sources and, at the same time, to disfavour the emission from HBL sources.

- One of the possible extensions of my works is a deeper investigation of the candidate sources. Blazars are expected to contribute only $\sim 20\%$ of the entire neutrino diffuse emission, the association of September 22 2017 between a track and a BL Lac is the only coincidence with a significance above 3σ. Then other candidate BL Lac sources *TXS-like* can be searched in the new *Fermi* catalogues, such as the 3FHL that contains all the sources detected in the range 10 GeV - 2 TeV in the first 7 years of data taking.

- Another important issue which could be reconsidered is the jet composition.While in the previous chapters we focused on the role of the photon target population, we cannot exclude that the differences among the BL Lacs are related to the hadrons. In fact a theoretical study on the proton acceleration mechanism or the proton-lepton ratio inside the jet and their dependence on the jet type, can be performed in order to give an alternative interpretation of the *non-detection* of neutrinos from HBL sources.

References

M. G. Aartsen and M. G. Aartsen. Erratum: Constraints on Ultrahigh-Energy Cosmic-Ray Sources from a Search for Neutrinos Above 10 PeV with IceCube [Phys. Rev. Lett. 117, 241101 (2016)]. *Physical Review Letters*, 119(25):259902, December 2017. doi: 10.1103/PhysRevLett.119.259902.

M. G. Aartsen, R. Abbasi, M. Ackermann, J. Adams, J. A. Aguilar, M. Ahlers, D. Altmann, C. Arguelles, J. Auffenberg, X. Bai, and et al. Energy reconstruction methods in the IceCube neutrino telescope. *Journal of Instrumentation*, 9:P03009, March 2014a. doi: 10.1088/1748-0221/9/03/P03009.

M. G. Aartsen, M. Ackermann, J. Adams, J. A. Aguilar, M. Ahlers, M. Ahrens, D. Altmann, T. Anderson, C. Arguelles, T. C. Arlen, and et al. Observation of High-Energy Astrophysical Neutrinos in Three Years of IceCube Data. *Physical Review Letters*, 113(10):101101, September 2014b. doi: 10.1103/PhysRevLett.113.101101.

M. G. Aartsen, K. Abraham, M. Ackermann, J. Adams, J. A. Aguilar, M. Ahlers, M. Ahrens, D. Altmann, T. Anderson, M. Archinger, and et al. Evidence for Astrophysical Muon Neutrinos from the Northern Sky with IceCube. *Physical Review Letters*, 115(8):081102, August 2015a. doi: 10.1103/PhysRevLett.115.081102.

M. G. Aartsen, K. Abraham, M. Ackermann, J. Adams, J. A. Aguilar, M. Ahlers, M. Ahrens, D. Altmann, T. Anderson, M. Archinger, and et al. A Combined Maximum-likelihood Analysis of the High-energy Astrophysical Neutrino Flux Measured with IceCube. *Astrophysical Journal*, 809:98, August 2015b. doi: 10.1088/0004-637X/809/1/98.

M. G. Aartsen, M. Ackermann, J. Adams, J. A. Aguilar, M. Ahlers, M. Ahrens, D. Altmann, T. Anderson, M. Archinger, C. Arguelles, and et al. Searches for Time-dependent Neutrino Sources with IceCube Data from 2008 to 2012. *Astrophysical Journal*, 807:46, July 2015c.

M. G. Aartsen, M. Ackermann, J. Adams, J. A. Aguilar, M. Ahlers, M. Ahrens, D. Altmann, T. Anderson, C. Arguelles, T. C. Arlen, and et al. Atmospheric and astrophysical neutrinos above 1 TeV interacting in IceCube. *Physical Review D*, 91(2):022001, January 2015d. doi: 10.1103/PhysRevD.91.022001.

M. G. Aartsen, K. Abraham, M. Ackermann, J. Adams, J. A. Aguilar, M. Ahlers, M. Ahrens, D. Altmann, K. Andeen, T. Anderson, and et al. Observation and Characterization of a Cosmic Muon Neutrino Flux from the Northern Hemisphere Using Six Years of IceCube Data. *Astrophysical Journal*, 833:3, December 2016a. doi: 10.3847/0004-637X/833/1/3.

M. G. Aartsen, K. Abraham, M. Ackermann, J. Adams, J. A. Aguilar, M. Ahlers, M. Ahrens, D. Altmann, K. Andeen, T. Anderson, and et al. Constraints on Ultrahigh-Energy Cosmic-Ray Sources from a Search for Neutrinos above 10 PeV with IceCube. *Physical Review Letters*, 117(24):241101, December 2016b. doi: 10.1103/PhysRevLett.117.241101.

M. G. Aartsen, K. Abraham, M. Ackermann, J. Adams, J. A. Aguilar, M. Ahlers, M. Ahrens, D. Altmann, T. Anderson, I. Ansseau, and et al. An All-sky Search for Three Flavors of Neutrinos from Gamma-ray Bursts with the IceCube Neutrino Observatory. *Astrophysical Journal*, 824:115, June 2016c. doi: 10.3847/0004-637X/824/2/115.

M. G. Aartsen, K. Abraham, M. Ackermann, J. Adams, J. A. Aguilar, M. Ahlers, M. Ahrens, D. Altmann, K. Andeen, T. Anderson, and et al. All-sky Search for Time-integrated Neutrino Emission from Astrophysical Sources with 7 yr of IceCube Data. *Astrophysical Journal*, 835:151, February 2017a. doi: 10.3847/1538-4357/835/2/151.

M. G. Aartsen, K. Abraham, M. Ackermann, J. Adams, J. A. Aguilar, M. Ahlers, M. Ahrens, D. Altmann, K. Andeen, T. Anderson, and et al. The Contribution of Fermi-2LAC Blazars to Diffuse TeV-PeV Neutrino Flux. *Astrophysical Journal*, 835:45, January 2017b. doi: 10.3847/1538-4357/835/1/45.

M. G. Aartsen, M. Ackermann, J. Adams, J. A. Aguilar, M. Ahlers, M. Ahrens, D. Altmann, K. Andeen, T. Anderson, I. Ansseau, and et al. The IceCube realtime alert system. *Astroparticle Physics*, 92:30–41, June 2017c. doi: 10.1016/j.astropartphys.2017.05.002.

A. A. Abdo, M. Ackermann, M. Ajello, L. Baldini, J. Ballet, G. Barbiellini, D. Bastieri, K. Bechtol, R. Bellazzini, B. Berenji, and et al. Fermi Large Area Telescope Observations of Markarian 421: The Missing Piece of its Spectral Energy Distribution. *Astrophysical Journal*, 736:131, August 2011. doi: 10.1088/0004-637X/736/2/131.

M. A. Abramowicz, B. Czerny, J. P. Lasota, and E. Szuszkiewicz. Slim accretion disks. *Astrophysical Journal*, 332:646–658, September 1988. doi: 10.1086/166683.

M. A. Abramowicz, X. Chen, S. Kato, J.-P. Lasota, and O. Regev. Thermal equilibria of accretion disks. *Astrophysical Journal, Letters*, 438:L37–L39, January 1995. doi: 10.1086/187709.

A. Abramowski, F. Acero, F. Aharonian, A. G. Akhperjanian, G. Anton, A. Balzer, A. Barnacka, Y. Becherini, J. Becker, K. Bernlöhr, E. Birsin, J. Biteau, A. Bochow, C. Boisson, J. Bolmont, P. Bordas, J. Brucker, F. Brun, P. Brun, T. Bulik, I. Büsching, S. Carrigan, S. Casanova, M. Cerruti, P. M. Chadwick, A. Charbonnier, R. C. G. Chaves, A. Cheesebrough, G. Cologna, J. Conrad, C. Couturier, M. Dalton, M. K. Daniel, I. D. Davids, B. Degrange, C. Deil, H. J. Dickinson, A. Djannati-Ataï, W. Domainko, L. O. Drury, G. Dubus, K. Dutson, J. Dyks, M. Dyrda, K. Egberts, P. Eger, P. Espigat, L. Fallon, S. Fegan, F. Feinstein, M. V. Fernandes, A. Fiasson, G. Fontaine, A. Förster, M. Füßling, M. Gajdus, Y. A. Gallant, T. Garrigoux, H. Gast, L. Gérard, B. Giebels, J. F. Glicenstein, B. Glück, D. Göring, M.-H. Grondin, S. Häffner, J. D. Hague, J. Hahn, D. Hampf, J. Harris, M. Hauser, S. Heinz, G. Heinzelmann, G. Henri, G. Hermann, A. Hillert, J. A. Hinton, W. Hofmann, P. Hofverberg, M. Holler, D. Horns, A. Jacholkowska, C. Jahn, M. Jamrozy, I. Jung, M. A. Kastendieck, K. Katarzyński, U. Katz, S. Kaufmann, B. Khélifi, D. Klochkov, W. Kluźniak, T. Kneiske, N. Komin, K. Kosack, R. Kossakowski, F. Krayzel, H. Laffon,

G. Lamanna, J.-P. Lenain, D. Lennarz, T. Lohse, A. Lopatin, C.-C. Lu, V. Marandon, A. Marcowith, J. Masbou, G. Maurin, N. Maxted, M. Mayer, T. J. L. McComb, M. C. Medina, J. Méhault, R. Moderski, M. Mohamed, E. Moulin, C. L. Naumann, M. Naumann-Godo, M. de Naurois, D. Nedbal, D. Nekrassov, N. Nguyen, B. Nicholas, J. Niemiec, S. J. Nolan, S. Ohm, E. de Oña Wilhelmi, B. Opitz, M. Ostrowski, I. Oya, M. Panter, M. Paz Arribas, N. W. Pekeur, G. Pelletier, J. Perez, P.-O. Petrucci, B. Peyaud, S. Pita, G. Pühlhofer, M. Punch, A. Quirrenbach, M. Raue, A. Reimer, O. Reimer, M. Renaud, R. de los Reyes, F. Rieger, J. Ripken, L. Rob, S. Rosier-Lees, G. Rowell, B. Rudak, C. B. Rulten, V. Sahakian, D. A. Sanchez, A. Santangelo, R. Schlickeiser, A. Schulz, U. Schwanke, S. Schwarzburg, S. Schwemmer, F. Sheidaei, J. L. Skilton, H. Sol, G. Spengler, Ł. Stawarz, R. Steenkamp, C. Stegmann, F. Stinzing, K. Stycz, I. Sushch, A. Szostek, J.-P. Tavernet, R. Terrier, M. Tluczykont, K. Valerius, C. van Eldik, G. Vasileiadis, C. Venter, A. Viana, P. Vincent, H. J. Völk, F. Volpe, S. Vorobiov, M. Vorster, S. J. Wagner, M. Ward, R. White, A. Wierzcholska, M. Zacharias, A. Zajczyk, A. A. Zdziarski, A. Zech, H.-S. Zechlin, and H. E. S. S. Collaboration. Spectral Analysis and Interpretation of the γ-Ray Emission from the Starburst Galaxy NGC 253. *Astrophysical Journal*, 757:158, October 2012. doi: 10.1088/0004-637X/757/2/158.

F. Acero, M. Ackermann, M. Ajello, A. Albert, W. B. Atwood, M. Axelsson, L. Baldini, J. Ballet, G. Barbiellini, D. Bastieri, A. Belfiore, R. Bellazzini, E. Bissaldi, R. D. Blandford, E. D. Bloom, J. R. Bogart, R. Bonino, E. Bottacini, J. Bregeon, R. J. Britto, P. Bruel, R. Buehler, T. H. Burnett, S. Buson, G. A. Caliandro, R. A. Cameron, R. Caputo, M. Caragiulo, P. A. Caraveo, J. M. Casandjian, E. Cavazzuti, E. Charles, R. C. G. Chaves, A. Chekhtman, C. C. Cheung, J. Chiang, G. Chiaro, S. Ciprini, R. Claus, J. Cohen-Tanugi, L. R. Cominsky, J. Conrad, S. Cutini, F. D'Ammando, A. de Angelis, M. DeKlotz, F. de Palma, R. Desiante, S. W. Digel, L. Di Venere, P. S. Drell, R. Dubois, D. Dumora, C. Favuzzi, S. J. Fegan, E. C. Ferrara, J. Finke, A. Franckowiak, Y. Fukazawa, S. Funk, P. Fusco, F. Gargano, D. Gasparrini, B. Giebels, N. Giglietto, P. Giommi, F. Giordano, M. Giroletti, T. Glanzman, G. Godfrey, I. A. Grenier, M.-H. Grondin, J. E. Grove, L. Guillemot, S. Guiriec, D. Hadasch, A. K. Harding, E. Hays, J. W. Hewitt, A. B. Hill, D. Horan, G. Iafrate, T. Jogler, G. Jóhannesson, R. P. Johnson, A. S. Johnson, T. J. Johnson, W. N. Johnson, T. Kamae, J. Kataoka, J. Katsuta, M. Kuss, G. La Mura, D. Landriu, S. Larsson, L. Latronico, M. Lemoine-Goumard, J. Li, L. Li, F. Longo, F. Loparco, B. Lott, M. N. Lovellette, P. Lubrano, G. M. Madejski, F. Massaro, M. Mayer, M. N. Mazziotta, J. E. McEnery, P. F. Michelson, N. Mirabal, T. Mizuno, A. A. Moiseev, M. Mongelli, M. E. Monzani, A. Morselli, I. V. Moskalenko, S. Murgia, E. Nuss, M. Ohno, T. Ohsugi, N. Omodei, M. Orienti, E. Orlando, J. F. Ormes, D. Paneque, J. H. Panetta, J. S. Perkins, M. Pesce-Rollins, F. Piron, G. Pivato, T. A. Porter, J. L. Racusin, R. Rando, M. Razzano, S. Razzaque, A. Reimer, O. Reimer, T. Reposeur, L. S. Rochester, R. W. Romani, D. Salvetti, M. Sánchez-Conde, P. M. Saz Parkinson, A. Schulz, E. J. Siskind, D. A. Smith, F. Spada, G. Spandre, P. Spinelli, T. E. Stephens, A. W. Strong, D. J. Suson, H. Takahashi, T. Takahashi, Y. Tanaka, J. G. Thayer, J. B. Thayer, D. J. Thompson, L. Tibaldo, O. Tibolla, D. F. Torres, E. Torresi, G. Tosti, E. Troja, B. Van Klaveren, G. Vianello, B. L. Winer, K. S. Wood, M. Wood, S. Zimmer, and Fermi-LAT Collaboration. Fermi Large Area Telescope Third Source Catalog. *Astronomy and Astrophysics, Supplement*, 218:23, June 2015. doi: 10.1088/0067-0049/218/2/23.

A. Achterberg, M. Ackermann, J. Adams, J. Ahrens, K. Andeen, D. W. Atlee, J. N. Bahcall, X. Bai, B. Baret, M. Bartelt, and et al. Limits on the muon flux from neutralino anni-

hilations at the center of the Earth with AMANDA. *Astroparticle Physics*, 26:129–139, September 2006. doi: 10.1016/j.astropartphys.2006.05.007.

M. Ackermann, J. Ahrens, X. Bai, R. Bay, M. Bartelt, S. W. Barwick, T. Becka, K. H. Becker, J. K. Becker, E. Bernardini, D. Bertrand, D. J. Boersma, S. Böser, O. Botner, A. Bouchta, O. Bouhali, J. Braun, C. Burgess, T. Burgess, T. Castermans, D. Chirkin, B. Collin, J. Conrad, J. Cooley, D. F. Cowen, A. Davour, C. de Clercq, T. De Young, P. Desiati, P. Ekström, T. Feser, T. K. Gaisser, R. Ganugapati, H. Geenen, L. Gerhardt, A. Goldschmidt, A. Groß, A. Hallgren, F. Halzen, K. Hanson, D. Hardtke, R. Hardtke, T. Harenberg, T. Hauschildt, K. Helbing, M. Hellwig, P. Herquet, G. C. Hill, J. Hodges, D. Hubert, B. Hughey, P. O. Hulth, K. Hultqvist, S. Hundertmark, J. Jacobsen, K. H. Kampert, A. Karle, J. L. Kelley, M. Kestel, G. Kohnen, L. Köpke, M. Kowalski, M. Krasberg, K. Kuehn, H. Leich, M. Leuthold, I. Liubarsky, J. Lundberg, J. Madsen, P. Marciniewski, H. S. Matis, C. P. McParland, T. Messarius, Y. Minaeva, P. Miočinović, R. Morse, K. Münich, R. Nahnhauer, J. W. Nam, T. Neunhöffer, P. Niessen, D. R. Nygren, H. Ögelman, P. Olbrechts, C. Pérez de Los Heros, A. C. Pohl, R. Porrata, P. B. Price, G. T. Przybylski, K. Rawlins, E. Resconi, W. Rhode, M. Ribordy, S. Richter, J. Rodríguez Martino, H. G. Sander, K. Schinarakis, S. Schlenstedt, D. Schneider, R. Schwarz, A. Silvestri, M. Solarz, G. M. Spiczak, C. Spiering, M. Stamatikos, D. Steele, P. Steffen, R. G. Stokstad, K. H. Sulanke, I. Taboada, O. Tarasova, L. Thollander, S. Tilav, W. Wagner, C. Walck, M. Walter, Y. R. Wang, C. Wendt, C. H. Wiebusch, R. Wischnewski, H. Wissing, K. Woschnagg, and G. Yodh. Search for extraterrestrial point sources of high energy neutrinos with AMANDA-II using data collected in 2000 2002. *Physical Review D*, 71(7):077102, April 2005. doi: 10.1103/PhysRevD.71.077102.

M. Ackermann, A. Albert, W. B. Atwood, L. Baldini, J. Ballet, G. Barbiellini, D. Bastieri, R. Bellazzini, E. Bissaldi, R. D. Blandford, E. D. Bloom, E. Bottacini, T. J. Brandt, J. Bregeon, P. Bruel, R. Buehler, S. Buson, G. A. Caliandro, R. A. Cameron, M. Caragiulo, P. A. Caraveo, E. Cavazzuti, C. Cecchi, E. Charles, A. Chekhtman, J. Chiang, G. Chiaro, S. Ciprini, R. Claus, J. Cohen-Tanugi, J. Conrad, S. Cutini, F. D'Ammando, A. de Angelis, F. de Palma, C. D. Dermer, S. W. Digel, L. Di Venere, E. d. C. e. Silva, P. S. Drell, C. Favuzzi, E. C. Ferrara, W. B. Focke, A. Franckowiak, Y. Fukazawa, S. Funk, P. Fusco, F. Gargano, D. Gasparrini, S. Germani, N. Giglietto, F. Giordano, M. Giroletti, G. Godfrey, G. A. Gomez-Vargas, I. A. Grenier, S. Guiriec, D. Hadasch, A. K. Harding, E. Hays, J. W. Hewitt, X. Hou, T. Jogler, G. Jóhannesson, A. S. Johnson, W. N. Johnson, T. Kamae, J. Kataoka, J. Knödlseder, D. Kocevski, M. Kuss, S. Larsson, L. Latronico, F. Longo, F. Loparco, M. N. Lovellette, P. Lubrano, D. Malyshev, A. Manfreda, F. Massaro, M. Mayer, M. N. Mazziotta, J. E. McEnery, P. F. Michelson, W. Mitthumsiri, T. Mizuno, M. E. Monzani, A. Morselli, I. V. Moskalenko, S. Murgia, R. Nemmen, E. Nuss, T. Ohsugi, N. Omodei, M. Orienti, E. Orlando, J. F. Ormes, D. Paneque, J. H. Panetta, J. S. Perkins, M. Pesce-Rollins, V. Petrosian, F. Piron, G. Pivato, S. Rainò, R. Rando, M. Razzano, S. Razzaque, A. Reimer, O. Reimer, M. Sánchez-Conde, M. Schaal, A. Schulz, C. Sgrò, E. J. Siskind, G. Spandre, P. Spinelli, Ł. Stawarz, A. W. Strong, D. J. Suson, M. Tahara, H. Takahashi, J. B. Thayer, L. Tibaldo, M. Tinivella, D. F. Torres, G. Tosti, E. Troja, Y. Uchiyama, G. Vianello, M. Werner, B. L. Winer, K. S. Wood, M. Wood, and G. Zaharijas. The Spectrum and Morphology of the Fermi Bubbles. *Astrophysical Journal*, 793:64, September 2014. doi: 10.1088/0004-637X/793/1/64.

M. Ackermann, M. Ajello, W. B. Atwood, L. Baldini, J. Ballet, G. Barbiellini, D. Bastieri, J. Becerra Gonzalez, R. Bellazzini, E. Bissaldi, R. D. Blandford, E. D. Bloom, R. Bonino,

E. Bottacini, T. J. Brandt, J. Bregeon, R. J. Britto, P. Bruel, R. Buehler, S. Buson, G. A. Caliandro, R. A. Cameron, M. Caragiulo, P. A. Caraveo, B. Carpenter, J. M. Casandjian, E. Cavazzuti, C. Cecchi, E. Charles, A. Chekhtman, C. C. Cheung, J. Chiang, G. Chiaro, S. Ciprini, R. Claus, J. Cohen-Tanugi, L. R. Cominsky, J. Conrad, S. Cutini, R. D'Abrusco, F. D'Ammando, A. de Angelis, R. Desiante, S. W. Digel, L. Di Venere, P. S. Drell, C. Favuzzi, S. J. Fegan, E. C. Ferrara, J. Finke, W. B. Focke, A. Franckowiak, L. Fuhrmann, Y. Fukazawa, A. K. Furniss, P. Fusco, F. Gargano, D. Gasparrini, N. Giglietto, P. Giommi, F. Giordano, M. Giroletti, T. Glanzman, G. Godfrey, I. A. Grenier, J. E. Grove, S. Guiriec, J. W. Hewitt, A. B. Hill, D. Horan, R. Itoh, G. Jóhannesson, A. S. Johnson, W. N. Johnson, J. Kataoka, T. Kawano, F. Krauss, M. Kuss, G. La Mura, S. Larsson, L. Latronico, C. Leto, J. Li, L. Li, F. Longo, F. Loparco, B. Lott, M. N. Lovellette, P. Lubrano, G. M. Madejski, M. Mayer, M. N. Mazziotta, J. E. McEnery, P. F. Michelson, T. Mizuno, A. A. Moiseev, M. E. Monzani, A. Morselli, I. V. Moskalenko, S. Murgia, E. Nuss, M. Ohno, T. Ohsugi, R. Ojha, N. Omodei, M. Orienti, E. Orlando, A. Paggi, D. Paneque, J. S. Perkins, M. Pesce-Rollins, F. Piron, G. Pivato, T. A. Porter, S. Rainò, R. Rando, M. Razzano, S. Razzaque, A. Reimer, O. Reimer, R. W. Romani, D. Salvetti, M. Schaal, F. K. Schinzel, A. Schulz, C. Sgrò, E. J. Siskind, K. V. Sokolovsky, F. Spada, G. Spandre, P. Spinelli, L. Stawarz, D. J. Suson, H. Takahashi, T. Takahashi, Y. Tanaka, J. G. Thayer, J. B. Thayer, L. Tibaldo, D. F. Torres, E. Torresi, G. Tosti, E. Troja, Y. Uchiyama, G. Vianello, B. L. Winer, K. S. Wood, and S. Zimmer. The Third Catalog of Active Galactic Nuclei Detected by the Fermi Large Area Telescope. *Astrophysical Journal*, 810:14, September 2015. doi: 10.1088/0004-637X/810/1/14.

M. Ackermann, M. Ajello, A. Albert, W. B. Atwood, L. Baldini, J. Ballet, G. Barbiellini, D. Bastieri, K. Bechtol, R. Bellazzini, E. Bissaldi, R. D. Blandford, E. D. Bloom, R. Bonino, J. Bregeon, R. J. Britto, P. Bruel, R. Buehler, G. A. Caliandro, R. A. Cameron, M. Caragiulo, P. A. Caraveo, E. Cavazzuti, C. Cecchi, E. Charles, A. Chekhtman, J. Chiang, G. Chiaro, S. Ciprini, J. Cohen-Tanugi, L. R. Cominsky, F. Costanza, S. Cutini, F. D'Ammando, A. de Angelis, F. de Palma, R. Desiante, S. W. Digel, M. Di Mauro, L. Di Venere, A. Domínguez, P. S. Drell, C. Favuzzi, S. J. Fegan, E. C. Ferrara, A. Franckowiak, Y. Fukazawa, S. Funk, P. Fusco, F. Gargano, D. Gasparrini, N. Giglietto, P. Giommi, F. Giordano, M. Giroletti, G. Godfrey, D. Green, I. A. Grenier, S. Guiriec, E. Hays, D. Horan, G. Iafrate, T. Jogler, G. Jóhannesson, M. Kuss, G. La Mura, S. Larsson, L. Latronico, J. Li, L. Li, F. Longo, F. Loparco, B. Lott, M. N. Lovellette, P. Lubrano, G. M. Madejski, J. Magill, S. Maldera, A. Manfreda, M. Mayer, M. N. Mazziotta, P. F. Michelson, W. Mitthumsiri, T. Mizuno, A. A. Moiseev, M. E. Monzani, A. Morselli, I. V. Moskalenko, S. Murgia, M. Negro, E. Nuss, T. Ohsugi, C. Okada, N. Omodei, E. Orlando, J. F. Ormes, D. Paneque, J. S. Perkins, M. Pesce-Rollins, V. Petrosian, F. Piron, G. Pivato, T. A. Porter, S. Rainò, R. Rando, M. Razzano, S. Razzaque, A. Reimer, O. Reimer, T. Reposeur, R. W. Romani, M. Sánchez-Conde, J. Schmid, A. Schulz, C. Sgrò, D. Simone, E. J. Siskind, F. Spada, G. Spandre, P. Spinelli, D. J. Suson, H. Takahashi, J. B. Thayer, L. Tibaldo, D. F. Torres, E. Troja, G. Vianello, M. Yassine, and S. Zimmer. Resolving the Extragalactic γ -Ray Background above 50 GeV with the Fermi Large Area Telescope. *Physical Review Letters*, 116(15): 151105, April 2016a. doi: 10.1103/PhysRevLett.116.151105.

M. Ackermann, M. Ajello, A. Albert, W. B. Atwood, L. Baldini, J. Ballet, G. Barbiellini, D. Bastieri, K. Bechtol, R. Bellazzini, E. Bissaldi, R. D. Blandford, E. D. Bloom, R. Bonino, J. Bregeon, R. J. Britto, P. Bruel, R. Buehler, G. A. Caliandro, R. A. Cameron, M. Caragiulo, P. A. Caraveo, E. Cavazzuti, C. Cecchi, E. Charles, A. Chekhtman, J. Chiang, G. Chiaro, S. Ciprini, J. Cohen-Tanugi, L. R. Cominsky, F. Costanza, S. Cutini, F. D'Ammando, A. de

Angelis, F. de Palma, R. Desiante, S. W. Digel, M. Di Mauro, L. Di Venere, A. Domínguez, P. S. Drell, C. Favuzzi, S. J. Fegan, E. C. Ferrara, A. Franckowiak, Y. Fukazawa, S. Funk, P. Fusco, F. Gargano, D. Gasparrini, N. Giglietto, P. Giommi, F. Giordano, M. Giroletti, G. Godfrey, D. Green, I. A. Grenier, S. Guiriec, E. Hays, D. Horan, G. Iafrate, T. Jogler, G. Jóhannesson, M. Kuss, G. La Mura, S. Larsson, L. Latronico, J. Li, L. Li, F. Longo, F. Loparco, B. Lott, M. N. Lovellette, P. Lubrano, G. M. Madejski, J. Magill, S. Maldera, A. Manfreda, M. Mayer, M. N. Mazziotta, P. F. Michelson, W. Mitthumsiri, T. Mizuno, A. A. Moiseev, M. E. Monzani, A. Morselli, I. V. Moskalenko, S. Murgia, M. Negro, E. Nuss, T. Ohsugi, C. Okada, N. Omodei, E. Orlando, J. F. Ormes, D. Paneque, J. S. Perkins, M. Pesce-Rollins, V. Petrosian, F. Piron, G. Pivato, T. A. Porter, S. Rainò, R. Rando, M. Razzano, S. Razzaque, A. Reimer, O. Reimer, T. Reposeur, R. W. Romani, M. Sánchez-Conde, J. Schmid, A. Schulz, C. Sgrò, D. Simone, E. J. Siskind, F. Spada, G. Spandre, P. Spinelli, D. J. Suson, H. Takahashi, J. B. Thayer, L. Tibaldo, D. F. Torres, E. Troja, G. Vianello, M. Yassine, and S. Zimmer. Resolving the Extragalactic γ -Ray Background above 50 GeV with the Fermi Large Area Telescope. *Physical Review Letters*, 116(15): 151105, April 2016b. doi: 10.1103/PhysRevLett.116.151105.

M. Ackermann, M. Ajello, W. B. Atwood, L. Baldini, J. Ballet, G. Barbiellini, D. Bastieri, J. Becerra Gonzalez, R. Bellazzini, E. Bissaldi, R. D. Blandford, E. D. Bloom, R. Bonino, E. Bottacini, T. J. Brandt, J. Bregeon, P. Bruel, R. Buehler, S. Buson, G. A. Caliandro, R. A. Cameron, R. Caputo, M. Caragiulo, P. A. Caraveo, E. Cavazzuti, C. Cecchi, E. Charles, A. Chekhtman, C. C. Cheung, J. Chiang, G. Chiaro, S. Ciprini, J. M. Cohen, J. Cohen-Tanugi, L. R. Cominsky, J. Conrad, A. Cuoco, S. Cutini, F. D'Ammando, A. de Angelis, F. de Palma, R. Desiante, M. Di Mauro, L. Di Venere, A. Domínguez, P. S. Drell, C. Favuzzi, S. J. Fegan, E. C. Ferrara, W. B. Focke, P. Fortin, A. Franckowiak, Y. Fukazawa, S. Funk, A. K. Furniss, P. Fusco, F. Gargano, D. Gasparrini, N. Giglietto, P. Giommi, F. Giordano, M. Giroletti, T. Glanzman, G. Godfrey, I. A. Grenier, M.-H. Grondin, L. Guillemot, S. Guiriec, A. K. Harding, E. Hays, J. W. Hewitt, A. B. Hill, D. Horan, G. Iafrate, D. Hartmann, T. Jogler, G. Jóhannesson, A. S. Johnson, T. Kamae, J. Kataoka, J. Knödlseder, M. Kuss, G. La Mura, S. Larsson, L. Latronico, M. Lemoine-Goumard, J. Li, L. Li, F. Longo, F. Loparco, B. Lott, M. N. Lovellette, P. Lubrano, G. M. Madejski, S. Maldera, A. Manfreda, M. Mayer, M. N. Mazziotta, P. F. Michelson, N. Mirabal, W. Mitthumsiri, T. Mizuno, A. A. Moiseev, M. E. Monzani, A. Morselli, I. V. Moskalenko, S. Murgia, E. Nuss, T. Ohsugi, N. Omodei, M. Orienti, E. Orlando, J. F. Ormes, D. Paneque, J. S. Perkins, M. Pesce-Rollins, V. Petrosian, F. Piron, G. Pivato, T. A. Porter, S. Rainò, R. Rando, M. Razzano, S. Razzaque, A. Reimer, O. Reimer, T. Reposeur, R. W. Romani, M. Sánchez-Conde, P. M. Saz Parkinson, J. Schmid, A. Schulz, C. Sgrò, E. J. Siskind, F. Spada, G. Spandre, P. Spinelli, D. J. Suson, H. Tajima, H. Takahashi, M. Takahashi, T. Takahashi, J. B. Thayer, D. J. Thompson, L. Tibaldo, D. F. Torres, G. Tosti, E. Troja, G. Vianello, K. S. Wood, M. Wood, M. Yassine, G. Zaharijas, and S. Zimmer. 2FHL: The Second Catalog of Hard Fermi-LAT Sources. *Astrophysical Journal, Supplement*, 222:5, January 2016c. doi: 10.3847/0067-0049/222/1/5.

M. Ackermann, M. Ajello, W. B. Atwood, L. Baldini, J. Ballet, G. Barbiellini, D. Bastieri, J. Becerra Gonzalez, R. Bellazzini, E. Bissaldi, R. D. Blandford, E. D. Bloom, R. Bonino, E. Bottacini, T. J. Brandt, J. Bregeon, P. Bruel, R. Buehler, S. Buson, G. A. Caliandro, R. A. Cameron, R. Caputo, M. Caragiulo, P. A. Caraveo, E. Cavazzuti, C. Cecchi, E. Charles, A. Chekhtman, C. C. Cheung, J. Chiang, G. Chiaro, S. Ciprini, J. M. Cohen, J. Cohen-Tanugi, L. R. Cominsky, J. Conrad, A. Cuoco, S. Cutini, F. D'Ammando, A. de Angelis, F. de Palma, R. Desiante, M. Di Mauro, L. Di Venere, A. Domínguez, P. S. Drell, C. Favuzzi, S. J.

Fegan, E. C. Ferrara, W. B. Focke, P. Fortin, A. Franckowiak, Y. Fukazawa, S. Funk, A. K. Furniss, P. Fusco, F. Gargano, D. Gasparrini, N. Giglietto, P. Giommi, F. Giordano, M. Giroletti, T. Glanzman, G. Godfrey, I. A. Grenier, M.-H. Grondin, L. Guillemot, S. Guiriec, A. K. Harding, E. Hays, J. W. Hewitt, A. B. Hill, D. Horan, G. Iafrate, D. Hartmann, T. Jogler, G. Jóhannesson, A. S. Johnson, T. Kamae, J. Kataoka, J. Knödlseder, M. Kuss, G. La Mura, S. Larsson, L. Latronico, M. Lemoine-Goumard, J. Li, L. Li, F. Longo, F. Loparco, B. Lott, M. N. Lovellette, P. Lubrano, G. M. Madejski, S. Maldera, A. Manfreda, M. Mayer, M. N. Mazziotta, P. F. Michelson, N. Mirabal, W. Mitthumsiri, T. Mizuno, A. A. Moiseev, M. E. Monzani, A. Morselli, I. V. Moskalenko, S. Murgia, E. Nuss, T. Ohsugi, N. Omodei, M. Orienti, E. Orlando, J. F. Ormes, D. Paneque, J. S. Perkins, M. Pesce-Rollins, V. Petrosian, F. Piron, G. Pivato, T. A. Porter, S. Rainò, R. Rando, M. Razzano, S. Razzaque, A. Reimer, O. Reimer, T. Reposeur, R. W. Romani, M. Sánchez-Conde, P. M. Saz Parkinson, J. Schmid, A. Schulz, C. Sgrò, E. J. Siskind, F. Spada, G. Spandre, P. Spinelli, D. J. Suson, H. Tajima, H. Takahashi, M. Takahashi, T. Takahashi, J. B. Thayer, D. J. Thompson, L. Tibaldo, D. F. Torres, G. Tosti, E. Troja, G. Vianello, K. S. Wood, M. Wood, M. Yassine, G. Zaharijas, and S. Zimmer. 2FHL: The Second Catalog of Hard Fermi-LAT Sources. *Astrophysical Journal, Supplement*, 222:5, January 2016d. doi: 10.3847/0067-0049/222/1/5.

S. Adrián-Martínez, M. Ageron, F. Aharonian, S. Aiello, A. Albert, F. Ameli, E. Anassontzis, M. Andre, G. Androulakis, M. Anghinolfi, and et al. Letter of intent for KM3NeT 2.0. *Journal of Physics G Nuclear Physics*, 43(8):084001, August 2016. doi: 10.1088/0954-3899/43/8/084001.

M. Ageron, J. A. Aguilar, I. Al Samarai, A. Albert, F. Ameli, M. André, M. Anghinolfi, G. Anton, S. Anvar, M. Ardid, and et al. ANTARES: The first undersea neutrino telescope. *Nuclear Instruments and Methods in Physics Research A*, 656:11–38, November 2011. doi: 10.1016/j.nima.2011.06.103.

F. A. Aharonian. TeV gamma rays from BL Lac objects due to synchrotron radiation of extremely high energy protons. *New Astronomy*, 5:377–395, November 2000. doi: 10.1016/S1384-1076(00)00039-7.

M. Ahlers and F. Halzen. High-energy cosmic neutrino puzzle: a review. *Reports on Progress in Physics*, 78(12):126901, December 2015. doi: 10.1088/0034-4885/78/12/126901.

M. Ahlers and F. Halzen. Opening a new window onto the universe with IceCube. *Progress in Particle and Nuclear Physics*, 102:73–88, September 2018. doi: 10.1016/j.ppnp.2018.05.001.

M. Ahlers and K. Murase. Probing the Galactic origin of the IceCube excess with gamma rays. *Physical Review D*, 90(2):023010, July 2014a. doi: 10.1103/PhysRevD.90.023010.

M. Ahlers and K. Murase. Probing the Galactic origin of the IceCube excess with gamma rays. *Physical Review D*, 90(2):023010, July 2014b. doi: 10.1103/PhysRevD.90.023010.

M. Ahlers, Y. Bai, V. Barger, and R. Lu. Galactic neutrinos in the TeV to PeV range. *Physical Review D*, 93(1):013009, January 2016. doi: 10.1103/PhysRevD.93.013009.

A. Albert, M. André, M. Anghinolfi, G. Anton, M. Ardid, J.-J. Aubert, J. Aublin, T. Avgitas, B. Baret, J. Barrios-Martí, S. Basa, B. Belhorma, V. Bertin, S. Biagi, R. Bormuth, J. Boumaaza, S. Bourret, M. C. Bouwhuis, H. Brânzaş, R. Bruijn, J. Brunner, J. Busto,

A. Capone, L. Caramete, J. Carr, S. Celli, M. Chabab, R. Cherkaoui El Moursli, T. Chiarusi, M. Circella, J. A. B. Coelho, A. Coleiro, M. Colomer, R. Coniglione, H. Costantini, P. Coyle, A. Creusot, A. F. Díaz, A. Deschamps, C. Distefano, I. Di Palma, A. Domi, R. Donà, C. Donzaud, D. Dornic, D. Drouhin, T. Eberl, I. El Bojaddaini, N. El Khayati, D. Elsässer, A. Enzenhöfer, A. Ettahiri, F. Fassi, I. Felis, P. Fermani, G. Ferrara, L. Fusco, P. Gay, H. Glotin, T. Grégoire, R. G. Ruiz, K. Graf, S. Hallmann, H. van Haren, A. J. Heijboer, Y. Hello, J. J. Hernández-Rey, J. Hößl, J. Hofestädt, G. Illuminati, M. de Jong, M. Jongen, M. Kadler, O. Kalekin, U. Katz, N. R. Khan-Chowdhury, A. Kouchner, M. Kreter, I. Kreykenbohm, V. Kulikovskiy, C. Lachaud, R. Lahmann, D. Lefèvre, E. Leonora, M. Lotze, S. Loucatos, M. Marcelin, A. Margiotta, A. Marinelli, J. A. Martínez-Mora, R. Mele, K. Melis, P. Migliozzi, A. Moussa, S. Navas, E. Nezri, A. Nuñez, M. Organokov, G. E. Păvălaş, C. Pellegrino, P. Piattelli, V. Popa, T. Pradier, L. Quinn, C. Racca, N. Randazzo, G. Riccobene, A. Sánchez-Losa, M. Saldaña, I. Salvadori, D. F. E. Samtleben, M. Sanguineti, P. Sapienza, F. Schüssler, M. Spurio, T. Stolarczyk, M. Taiuti, Y. Tayalati, A. Trovato, B. Vallage, V. Van Elewyck, F. Versari, D. Vivolo, J. Wilms, D. Zaborov, J. D. Zornoza, J. Zúñiga, and ANTARES Collaboration. The Search for Neutrinos from TXS 0506+056 with the ANTARES Telescope. *Astrophysical Journal, Letters*, 863:L30, August 2018. doi: 10.3847/2041-8213/aad8c0.

J. Aleksić, E. A. Alvarez, L. A. Antonelli, P. Antoranz, M. Asensio, M. Backes, J. A. Barrio, D. Bastieri, J. Becerra González, W. Bednarek, A. Berdyugin, K. Berger, E. Bernardini, A. Biland, O. Blanch, R. K. Bock, A. Boller, G. Bonnoli, D. Borla Tridon, I. Braun, T. Bretz, A. Cañellas, E. Carmona, A. Carosi, P. Colin, E. Colombo, J. L. Contreras, J. Cortina, L. Cossio, S. Covino, F. Dazzi, A. De Angelis, G. De Caneva, E. De Cea del Pozo, B. De Lotto, C. Delgado Mendez, A. Diago Ortega, M. Doert, A. Domínguez, D. Dominis Prester, D. Dorner, M. Doro, D. Elsaesser, D. Ferenc, M. V. Fonseca, L. Font, C. Fruck, R. J. García López, M. Garczarczyk, D. Garrido, G. Giavitto, N. Godinović, D. Hadasch, D. Häfner, A. Herrero, D. Hildebrand, D. Höhne-Mönch, J. Hose, D. Hrupec, B. Huber, T. Jogler, H. Kellermann, S. Klepser, T. Krähenbühl, J. Krause, A. La Barbera, D. Lelas, E. Leonardo, E. Lindfors, S. Lombardi, M. López, A. López-Oramas, E. Lorenz, M. Makariev, G. Maneva, N. Mankuzhiyil, K. Mannheim, L. Maraschi, M. Mariotti, M. Martínez, D. Mazin, M. Meucci, J. M. Miranda, R. Mirzoyan, H. Miyamoto, J. Moldón, A. Moralejo, P. Munar-Adrover, D. Nieto, K. Nilsson, R. Orito, I. Oya, D. Paneque, R. Paoletti, S. Pardo, J. M. Paredes, S. Partini, M. Pasanen, F. Pauss, M. A. Perez-Torres, M. Persic, L. Peruzzo, M. Pilia, J. Pochon, F. Prada, P. G. Prada Moroni, E. Prandini, I. Puljak, I. Reichardt, R. Reinthal, W. Rhode, M. Ribó, J. Rico, S. Rügamer, A. Saggion, K. Saito, T. Y. Saito, M. Salvati, K. Satalecka, V. Scalzotto, V. Scapin, C. Schultz, T. Schweizer, M. Shayduk, S. N. Shore, A. Sillanpää, J. Sitarek, D. Sobczynska, F. Spanier, S. Spiro, V. Stamatescu, A. Stamerra, B. Steinke, J. Storz, N. Strah, T. Surić, L. Takalo, H. Takami, F. Tavecchio, P. Temnikov, T. Terzić, D. Tescaro, M. Teshima, O. Tibolla, D. F. Torres, A. Treves, M. Uellenbeck, H. Vankov, P. Vogler, R. M. Wagner, Q. Weitzel, V. Zabalza, F. Zandanel, R. Zanin, S. Buson, D. Horan, S. Larsson, and F. D'Ammando. PG 1553+113: Five Years of Observations with MAGIC. *Astrophysical Journal*, 748:46, March 2012. doi: 10.1088/0004-637X/748/1/46.

R. Aloisio, V. Berezinsky, and A. Gazizov. Transition from galactic to extragalactic cosmic rays. *Astroparticle Physics*, 39:129–143, December 2012. doi: 10.1016/j.astropartphys.2012.09.007.

R. Aloisio, P. Blasi, I. De Mitri, and S. Petrera. *Selected Topics in Cosmic Ray Physics*, page 1. 2018a. doi: 10.1007/978-3-319-65425-6_1.

R. Aloisio, E. Coccia, and F. Vissani. *Multiple Messengers and Challenges in Astroparticle Physics*. 2018b. doi: 10.1007/978-3-319-65425-6.

J. Alvarez-Muñiz and P. Mészáros. High energy neutrinos from radio-quiet active galactic nuclei. *Physical Review D*, 70(12):123001, December 2004. doi: 10.1103/PhysRevD.70.123001.

E. Amato and P. Blasi. A kinetic approach to cosmic-ray-induced streaming instability at supernova shocks. *Monthly Notices of the RAS*, 392:1591–1600, February 2009. doi: 10.1111/j.1365-2966.2008.14200.x.

L. A. Anchordoqui, T. C. Paul, L. H. M. da Silva, D. F. Torres, and B. J. Vlcek. What IceCube data tell us about neutrino emission from star-forming galaxies (so far). *Physical Review D*, 89(12):127304, June 2014. doi: 10.1103/PhysRevD.89.127304.

S. Ansoldi, L. A. Antonelli, C. Arcaro, D. Baack, A. Babić, B. Banerjee, P. Bangale, U. Barres de Almeida, J. A. Barrio, J. Becerra González, W. Bednarek, E. Bernardini, R. C. Berse, A. Berti, J. Besenrieder, W. Bhattacharyya, C. Bigongiari, A. Biland, O. Blanch, G. Bonnoli, R. Carosi, G. Ceribella, A. Chatterjee, S. M. Colak, P. Colin, E. Colombo, J. L. Contreras, J. Cortina, S. Covino, P. Cumani, V. D'Elia, P. Da Vela, F. Dazzi, A. De Angelis, B. De Lotto, M. Delfino, J. Delgado, F. Di Pierro, A. Domínguez, D. Dominis Prester, D. Dorner, M. Doro, S. Einecke, D. Elsaesser, V. Fallah Ramazani, A. Fattorini, A. Fernández-Barral, G. Ferrara, D. Fidalgo, L. Foffano, M. V. Fonseca, L. Font, C. Fruck, S. Gallozzi, R. J. García López, M. Garczarczyk, M. Gaug, P. Giammaria, N. Godinović, D. Guberman, D. Hadasch, A. Hahn, T. Hassan, M. Hayashida, J. Herrera, J. Hoang, D. Hrupec, S. Inoue, K. Ishio, Y. Iwamura, Y. Konno, H. Kubo, J. Kushida, A. Lamastra, D. Lelas, F. Leone, E. Lindfors, S. Lombardi, F. Longo, M. López, C. Maggio, P. Majumdar, M. Makariev, G. Maneva, M. Manganaro, K. Mannheim, L. Maraschi, M. Mariotti, M. Martínez, S. Masuda, D. Mazin, K. Mielke, M. Minev, J. M. Miranda, R. Mirzoyan, A. Moralejo, V. Moreno, E. Moretti, V. Neustroev, A. Niedzwiecki, M. Nievas Rosillo, C. Nigro, K. Nilsson, D. Ninci, K. Nishijima, K. Noda, L. Nogués, S. Paiano, J. Palacio, D. Paneque, R. Paoletti, J. M. Paredes, G. Pedaletti, P. Peñil, M. Peresano, M. Persic, K. Pfrang, P. G. Prada Moroni, E. Prandini, I. Puljak, J. R. Garcia, W. Rhode, M. Ribó, J. Rico, C. Righi, A. Rugliancich, L. Saha, T. Saito, K. Satalecka, T. Schweizer, J. Sitarek, I. Šnidarić, D. Sobczynska, A. Stamerra, M. Strzys, T. Surić, F. Tavecchio, P. Temnikov, T. Terzić, M. Teshima, N. Torres-Albá, S. Tsujimoto, G. Vanzo, M. Vazquez Acosta, I. Vovk, J. E. Ward, M. Will, D. Zarić, and M. Cerruti. The Blazar TXS 0506+056 Associated with a High-energy Neutrino: Insights into Extragalactic Jets and Cosmic-Ray Acceleration. *Astrophysical Journal, Letters*, 863:L10, August 2018. doi: 10.3847/2041-8213/aad083.

R. R. J. Antonucci and J. S. Miller. Spectropolarimetry and the nature of NGC 1068. *Astrophysical Journal*, 297:621–632, October 1985. doi: 10.1086/163559.

W. D. Apel, J. C. Arteaga-Velàzquez, K. Bekk, M. Bertaina, J. Blümer, H. Bozdog, I. M. Brancus, E. Cantoni, A. Chiavassa, F. Cossavella, K. Daumiller, V. de Souza, F. Di Pierro, P. Doll, R. Engel, J. Engler, M. Finger, B. Fuchs, D. Fuhrmann, H. J. Gils, R. Glasstetter, C. Grupen, A. Haungs, D. Heck, J. R. Hörandel, D. Huber, T. Huege, K.-H. Kampert, D. Kang, H. O.

Klages, K. Link, P. Łuczak, M. Ludwig, H. J. Mathes, H. J. Mayer, M. Melissas, J. Milke, B. Mitrica, C. Morello, J. Oehlschläger, S. Ostapchenko, N. Palmieri, M. Petcu, T. Pierog, H. Rebel, M. Roth, H. Schieler, S. Schoo, F. G. Schröder, O. Sima, G. Toma, G. C. Trinchero, H. Ulrich, A. Weindl, J. Wochele, M. Wommer, and J. Zabierowski. Ankle-like feature in the energy spectrum of light elements of cosmic rays observed with KASCADE-Grande. *Physical Review D*, 87(8):081101, April 2013. doi: 10.1103/PhysRevD.87.081101.

A. M. Atoyan and C. D. Dermer. Neutral Beams from Blazar Jets. *Astrophysical Journal*, 586:79–96, March 2003. doi: 10.1086/346261.

A. D. Avrorin, A. V. Avrorin, V. M. Aynutdinov, R. Bannasch, I. A. Belolaptikov, D. Y. Bogorodsky, V. B. Brudanin, N. M. Budnev, I. A. Danilchenko, S. V. Demidov, G. V. Domogatsky, A. A. Doroshenko, A. N. Dyachok, Z.-A. M. Dzhilkibaev, S. V. Fialkovsky, A. R. Gafarov, O. N. Gaponenko, K. V. Golubkov, T. I. Gress, Z. Honz, K. G. Kebkal, O. G. Kebkal, K. V. Konischev, E. N. Konstantinov, A. V. Korobchenko, A. P. Koshechkin, F. K. Koshel, A. V. Kozhin, V. F. Kulepov, D. A. Kuleshov, V. I. Ljashuk, M. B. Milenin, R. A. Mirgazov, E. R. Osipova, A. I. Panfilov, L. V. Pan'kov, A. A. Perevalov, E. N. Pliskovsky, V. A. Poleschuk, M. I. Rozanov, V. F. Rubtzov, E. V. Rjabov, B. A. Shaybonov, A. A. Sheifler, A. V. Shkurihin, A. A. Smagina, O. V. Suvorova, B. A. Tarashansky, S. A. Yakovlev, A. V. Zagorodnikov, V. A. Zhukov, and V. L. Zurbanov. Search for neutrino emission from relic dark matter in the sun with the Baikal NT200 detector. *Astroparticle Physics*, 62:12–20, March 2015. doi: 10.1016/j.astropartphys.2014.07.006.

Y. Bai, R. Lu, and J. Salvado. Geometric compatibility of IceCube TeV-PeV neutrino excess and its galactic dark matter origin. *Journal of High Energy Physics*, 1:161, January 2016. doi: 10.1007/JHEP01(2016)161.

M. Baloković, D. Paneque, G. Madejski, A. Furniss, J. Chiang, M. Ajello, D. M. Alexander, D. Barret, R. D. Blandford, S. E. Boggs, and et al. Multiwavelength Study of Quiescent States of Mrk 421 with Unprecedented Hard X-Ray Coverage Provided by NuSTAR in 2013. *Astrophysical Journal*, 819:156, March 2016. doi: 10.3847/0004-637X/819/2/156.

M. V. Barkov, F. A. Aharonian, S. V. Bogovalov, S. R. Kelner, and D. Khangulyan. Rapid TeV Variability in Blazars as a Result of Jet-Star Interaction. *Astrophysical Journal*, 749:119, April 2012. doi: 10.1088/0004-637X/749/2/119.

J. Becker Tjus, B. Eichmann, F. Halzen, A. Kheirandish, and S. M. Saba. High-energy neutrinos from radio galaxies. *Physical Review D*, 89(12):123005, June 2014. doi: 10.1103/PhysRevD.89.123005.

M. C. Begelman. Can a spherically accreting black hole radiate very near the Eddington limit. *Monthly Notices of the RAS*, 187:237–251, April 1979. doi: 10.1093/mnras/187.2.237.

M. C. Begelman and D. L. Meier. Thick accretion disks - Self-similar, supercritical models. *Astrophysical Journal*, 253:873–896, February 1982. doi: 10.1086/159688.

M. C. Begelman, R. D. Blandford, and M. J. Rees. Theory of extragalactic radio sources. *Reviews of Modern Physics*, 56:255–351, April 1984. doi: 10.1103/RevModPhys.56.255.

A. R. Bell. Turbulent amplification of magnetic field and diffusive shock acceleration of cosmic rays. *Monthly Notices of the RAS*, 353:550–558, September 2004. doi: 10.1111/j.1365-2966.2004.08097.x.

A. R. Bell. The interaction of cosmic rays and magnetized plasma. *Monthly Notices of the RAS*, 358:181–187, March 2005. doi: 10.1111/j.1365-2966.2005.08774.x.

A. R. Bell, K. M. Schure, B. Reville, and G. Giacinti. Cosmic-ray acceleration and escape from supernova remnants. *Monthly Notices of the RAS*, 431:415–429, May 2013. doi: 10.1093/mnras/stt179.

V. S. Berezinsky, T. K. Gaisser, F. Halzen, and T. Stanev. Diffuse radiation from cosmic ray interactions in the galaxy. *Astroparticle Physics*, 1:281–287, July 1993. doi: 10.1016/0927-6505(93)90014-5.

P. L. Biermann and P. A. Strittmatter. Synchrotron emission from shock waves in active galactic nuclei. *Astrophysical Journal*, 322:643–649, November 1987. doi: 10.1086/165759.

R. D. Blandford and D. G. Payne. Hydromagnetic flows from accretion discs and the production of radio jets. *Monthly Notices of the RAS*, 199:883–903, June 1982. doi: 10.1093/mnras/199.4.883.

R. D. Blandford and R. L. Znajek. Electromagnetic extraction of energy from Kerr black holes. *Monthly Notices of the RAS*, 179:433–456, May 1977. doi: 10.1093/mnras/179.3.433.

R. D. Blandford, C. F. McKee, and M. J. Rees. Super-luminal expansion in extragalactic radio sources. *Nature*, 267:211–216, May 1977. doi: 10.1038/267211a0.

P. Blasi. The origin of galactic cosmic rays. *Astronomy and Astrophysics Reviews*, 21:70, November 2013. doi: 10.1007/s00159-013-0070-7.

M. Błażejowski, M. Sikora, R. Moderski, and G. M. Madejski. Comptonization of Infrared Radiation from Hot Dust by Relativistic Jets in Quasars. *Astrophysical Journal*, 545:107–116, December 2000. doi: 10.1086/317791.

S. D. Bloom and A. P. Marscher. An Analysis of the Synchrotron Self-Compton Model for the Multi–Wave Band Spectra of Blazars. *Astrophysical Journal*, 461:657, April 1996. doi: 10.1086/177092.

G. R. Blumenthal. Energy Loss of High-Energy Cosmic Rays in Pair-Producing Collisions with Ambient Photons. *Physical Review D*, 1:1596–1602, March 1970. doi: 10.1103/PhysRevD.1.1596.

G. Bonnoli, G. Ghisellini, L. Foschini, F. Tavecchio, and G. Ghirlanda. The γ-ray brightest days of the blazar 3C 454.3. *Monthly Notices of the RAS*, 410:368–380, January 2011. doi: 10.1111/j.1365-2966.2010.17450.x.

M. Böttcher, A. Reimer, K. Sweeney, and A. Prakash. Leptonic and Hadronic Modeling of Fermi-detected Blazars. *Astrophysical Journal*, 768:54, May 2013. doi: 10.1088/0004-637X/768/1/54.

J. Braun, A. Karle, and T. Montaruli. Neutrino Point Source Search Strategies for AMANDA-II and Results from 2005. *International Cosmic Ray Conference*, 5:1437–1440, 2008.

J. Braun, M. Baker, J. Dumm, C. Finley, A. Karle, and T. Montaruli. Time-dependent point source search methods in high energy neutrino astronomy. *Astroparticle Physics*, 33: 175–181, April 2010. doi: 10.1016/j.astropartphys.2010.01.005.

D. N. Burrows, J. E. Hill, J. A. Nousek, J. A. Kennea, A. Wells, J. P. Osborne, A. F. Abbey, A. Beardmore, K. Mukerjee, A. D. T. Short, G. Chincarini, S. Campana, O. Citterio, A. Moretti, C. Pagani, G. Tagliaferri, P. Giommi, M. Capalbi, F. Tamburelli, L. Angelini, G. Cusumano, H. W. Bräuninger, W. Burkert, and G. D. Hartner. The Swift X-Ray Telescope. *Space Science Reviews*, 120:165–195, October 2005. doi: 10.1007/s11214-005-5097-2.

A. Capone, P. Lipari, and F. Vissani. *Neutrino Astronomy*, page 195. 2018. doi: 10.1007/978-3-319-65425-6_4.

A. Celotti and G. Ghisellini. The power of blazar jets. *Monthly Notices of the RAS*, 385: 283–300, March 2008. doi: 10.1111/j.1365-2966.2007.12758.x.

M. Cerruti, A. Zech, C. Boisson, and S. Inoue. A hadronic origin for ultra-high-frequency-peaked BL Lac objects. *Monthly Notices of the RAS*, 448:910–927, March 2015. doi: 10.1093/mnras/stu2691.

M. Cerruti, A. Zech, C. Boisson, G. Emery, S. Inoue, and J.-P. Lenain. Lepto-hadronic single-zone models for the electromagnetic and neutrino emission of TXS 0506+056. *ArXiv e-prints*, July 2018.

X.-C. Chang and X.-Y. Wang. The Diffuse Gamma-Ray Flux Associated with Sub-PeV/PeV Neutrinos from Starburst Galaxies. *Astrophysical Journal*, 793:131, October 2014. doi: 10.1088/0004-637X/793/2/131.

X. Chen, M. A. Abramowicz, J.-P. Lasota, R. Narayan, and I. Yi. Unified description of accretion flows around black holes. *Astrophysical Journal, Letters*, 443:L61–L64, April 1995. doi: 10.1086/187836.

M. Chiaberge, A. Celotti, A. Capetti, and G. Ghisellini. Does the unification of BL Lac and FR I radio galaxies require jet velocity structures? *Astronomy and Astrophysics*, 358: 104–112, June 2000.

I. Cholis. Searching for the high-energy neutrino counterpart signals: The case of the Fermi bubbles signal and of dark matter annihilation in the inner Galaxy. *Physical Review D*, 88(6):063524, September 2013. doi: 10.1103/PhysRevD.88.063524.

K. Cleary and C. R. Lawrence. The Agn Radius-luminosity And Mass-luminosity Relationships In The Mid-infrared. In *American Astronomical Society Meeting Abstracts #210*, volume 39 of *Bulletin of the American Astronomical Society*, page 330, July 2007.

J. J. Condon, W. D. Cotton, E. W. Greisen, Q. F. Yin, R. A. Perley, G. B. Taylor, and J. J. Broderick. The NRAO VLA Sky Survey. *Astronomical Journal*, 115:1693–1716, May 1998. doi: 10.1086/300337.

R. M. Crocker and F. Aharonian. Fermi Bubbles: Giant, Multibillion-Year-Old Reservoirs of Galactic Center Cosmic Rays. *Physical Review Letters*, 106(10):101102, March 2011. doi: 10.1103/PhysRevLett.106.101102.

P. D'Avanzo. Short gamma-ray bursts: A review. *Journal of High Energy Astrophysics*, 7: 73–80, September 2015. doi: 10.1016/j.jheap.2015.07.002.

C. D. Dermer and G. Menon. *High Energy Radiation from Black Holes: Gamma Rays, Cosmic Rays, and Neutrinos*. 2009.

C. D. Dermer and R. Schlickeiser. Model for the High-Energy Emission from Blazars. *Astrophysical Journal*, 416:458, October 1993. doi: 10.1086/173251.

C. D. Dermer, S. J. Sturner, and R. Schlickeiser. Multiwavelength Spectral Modeling of Blazars. In *American Astronomical Society Meeting Abstracts*, volume 27 of *Bulletin of the American Astronomical Society*, page 1350, December 1995.

L. Dondi and G. Ghisellini. Gamma-ray-loud blazars and beaming. *Monthly Notices of the RAS*, 273:583–595, April 1995. doi: 10.1093/mnras/273.3.583.

J. S. Dunlop, R. J. McLure, M. J. Kukula, S. A. Baum, C. P. O'Dea, and D. H. Hughes. Quasars, their host galaxies and their central black holes. *Monthly Notices of the RAS*, 340:1095–1135, April 2003. doi: 10.1046/j.1365-8711.2003.06333.x.

W. Essey, O. E. Kalashev, A. Kusenko, and J. F. Beacom. Secondary Photons and Neutrinos from Cosmic Rays Produced by Distant Blazars. *Physical Review Letters*, 104(14):141102, April 2010. doi: 10.1103/PhysRevLett.104.141102.

C. Evoli, D. Grasso, and L. Maccione. Diffuse neutrino and gamma-ray emissions of the galaxy above the TeV. *Journal of Cosmology and Astroparticle Physics*, 6:003, June 2007. doi: 10.1088/1475-7516/2007/06/003.

B. L. Fanaroff and J. M. Riley. The morphology of extragalactic radio sources of high and low luminosity. *Monthly Notices of the RAS*, 167:31P–36P, May 1974. doi: 10.1093/mnras/167.1.31P.

E. P. Farina, R. Decarli, R. Falomo, A. Treves, and C. M. Raiteri. The optical spectrum of PKS 1222+216 and its black hole mass. *Monthly Notices of the RAS*, 424:393–398, July 2012. doi: 10.1111/j.1365-2966.2012.21209.x.

Y. Farzan and A. Y. Smirnov. Coherence and oscillations of cosmic neutrinos. *Nuclear Physics B*, 805:356–376, December 2008. doi: 10.1016/j.nuclphysb.2008.07.028.

G. Fossati, L. Maraschi, A. Celotti, A. Comastri, and G. Ghisellini. A unifying view of the spectral energy distributions of blazars. *Monthly Notices of the RAS*, 299:433–448, September 1998. doi: 10.1046/j.1365-8711.1998.01828.x.

J. Frank, A. King, and D. J. Raine. *Accretion Power in Astrophysics: Third Edition*. January 2002.

T. K. Gaisser. Neutrino Astronomy 2017. *ArXiv e-prints*, January 2018.

T. K. Gaisser, T. Stanev, S. A. Bludman, and H. Lee. Flux of atmospheric neutrinos. *Physical Review Letters*, 51:223–226, July 1983. doi: 10.1103/PhysRevLett.51.223.

T. K. Gaisser, F. Halzen, and T. Stanev. Particle astrophysics with high energy neutrinos. *Physics Reports*, 258:173–236, July 1995. doi: 10.1016/0370-1573(95)00003-Y.

R. Gandhi, C. Quigg, M. Hall Reno, and I. Sarcevic. Ultrahigh-energy neutrino interactions. *Astroparticle Physics*, 5:81–110, August 1996. doi: 10.1016/0927-6505(96)00008-4.

R. Gandhi, C. Quigg, M. H. Reno, and I. Sarcevic. Neutrino interactions at ultrahigh energies. *Physical Review D*, 58(9):093009, November 1998. doi: 10.1103/PhysRevD.58.093009.

S. Gao, A. Fedynitch, W. Winter, and M. Pohl. Interpretation of the coincident observation of a high energy neutrino and a bright flare. *ArXiv e-prints*, July 2018.

M. Georganopoulos and D. Kazanas. Decelerating Flows in TeV Blazars: A Resolution to the BL Lacertae-FR I Unification Problem. *Astrophysical Journal, Letters*, 594:L27–L30, September 2003. doi: 10.1086/378557.

G. Ghisellini, editor. *Radiative Processes in High Energy Astrophysics*, volume 873 of *Lecture Notes in Physics, Berlin Springer Verlag*, 2013. doi: 10.1007/978-3-319-00612-3.

G. Ghisellini and A. Celotti. Relativistic large-scale jets and minimum power requirements. *Monthly Notices of the RAS*, 327:739–743, November 2001. doi: 10.1046/j.1365-8711.2001.04700.x.

G. Ghisellini and P. Madau. On the origin of the gamma-ray emission in blazars. *Monthly Notices of the RAS*, 280:67–76, May 1996. doi: 10.1093/mnras/280.1.67.

G. Ghisellini and F. Tavecchio. The blazar sequence: a new perspective. *Monthly Notices of the RAS*, 387:1669–1680, July 2008. doi: 10.1111/j.1365-2966.2008.13360.x.

G. Ghisellini and F. Tavecchio. Canonical high-power blazars. *Monthly Notices of the RAS*, 397:985–1002, August 2009. doi: 10.1111/j.1365-2966.2009.15007.x.

G. Ghisellini, F. Tavecchio, and M. Chiaberge. Structured jets in TeV BL Lac objects and radiogalaxies. Implications for the observed properties. *Astronomy and Astrophysics*, 432:401–410, March 2005. doi: 10.1051/0004-6361:20041404.

G. Ghisellini, L. Maraschi, and F. Tavecchio. The Fermi blazars' divide. *Monthly Notices of the RAS*, 396:L105–L109, June 2009a. doi: 10.1111/j.1745-3933.2009.00673.x.

G. Ghisellini, L. Maraschi, and F. Tavecchio. The Fermi blazars' divide. *Monthly Notices of the RAS*, 396:L105–L109, June 2009b. doi: 10.1111/j.1745-3933.2009.00673.x.

G. Ghisellini, F. Tavecchio, L. Foschini, G. Ghirlanda, L. Maraschi, and A. Celotti. General physical properties of bright Fermi blazars. *Monthly Notices of the RAS*, 402:497–518, February 2010. doi: 10.1111/j.1365-2966.2009.15898.x.

G. Ghisellini, C. Righi, L. Costamante, and F. Tavecchio. The Fermi blazar sequence. *Monthly Notices of the RAS*, 469:255–266, July 2017. doi: 10.1093/mnras/stx806.

P. Giommi and P. Padovani. A simplified view of blazars: contribution to the X-ray and γ-ray extragalactic backgrounds. *Monthly Notices of the RAS*, 450:2404–2409, July 2015. doi: 10.1093/mnras/stv793.

P. Giommi, P. Padovani, G. Polenta, S. Turriziani, V. D'Elia, and S. Piranomonte. A simplified view of blazars: clearing the fog around long-standing selection effects. *Monthly Notices of the RAS*, 420:2899–2911, March 2012. doi: 10.1111/j.1365-2966.2011.20044.x.

G. Giovannini, L. Feretti, T. Venturi, W. D. Cotton, and L. Lara. VLBI Observations of Mrk421 and Mrk501. In L. O. Takalo and A. Sillanpää, editors, *BL Lac Phenomenon*, volume 159 of *Astronomical Society of the Pacific Conference Series*, page 439, 1999.

M. Giroletti, G. Giovannini, L. Feretti, W. D. Cotton, P. G. Edwards, L. Lara, A. P. Marscher, J. R. Mattox, B. G. Piner, and T. Venturi. Parsec-Scale Properties of Markarian 501. *Astrophysical Journal*, 600:127–140, January 2004. doi: 10.1086/379663.

P. Grandi, L. Maraschi, C. M. Urry, A. E. Wehrle, M. F. Aller, H. D. Aller, T. J. Balonek, J. Jason, I. M. McHardy, R. C. Hartman, E. Pian, J. A. Stevens, A. C. Sadun, H. Terasränta, and A. Treves. Long term variability of 3C279. *Advances in Space Research*, 15, May 1995. doi: 10.1016/0273-1177(94)00029-Z.

F. Halzen and D. Hooper. High energy neutrinos from the TeV Blazar 1ES 1959 + 650. *Astroparticle Physics*, 23:537–542, July 2005. doi: 10.1016/j.astropartphys.2005.03.007.

F. Halzen and S. R. Klein. Invited Review Article: IceCube: An instrument for neutrino astronomy. *Review of Scientific Instruments*, 81(8):081101–081101, August 2010. doi: 10.1063/1.3480478.

G. Henri and G. Pelletier. Relativistic electron-positron beam formation in the framework of the two-flow model for active galactic nuclei. *Astrophysical Journal, Letters*, 383: L7–L10, December 1991. doi: 10.1086/186228.

S. Hümmer, M. Maltoni, W. Winter, and C. Yaguna. Energy dependent neutrino flavor ratios from cosmic accelerators on the Hillas plot. *Astroparticle Physics*, 34:205–224, November 2010a. doi: 10.1016/j.astropartphys.2010.07.003.

S. Hümmer, M. Rüger, F. Spanier, and W. Winter. Simplified Models for Photohadronic Interactions in Cosmic Accelerators. *Astrophysical Journal*, 721:630–652, September 2010b. doi: 10.1088/0004-637X/721/1/630.

IceCube Collaboration. Evidence for High-Energy Extraterrestrial Neutrinos at the IceCube Detector. *Science*, 342:1242856, November 2013. doi: 10.1126/science.1242856.

IceCube Collaboration, M. G. Aartsen, R. Abbasi, Y. Abdou, M. Ackermann, J. Adams, J. A. Aguilar, M. Ahlers, D. Altmann, J. Auffenberg, and et al. The IceCube Neutrino Observatory Part II: Atmospheric and Diffuse UHE Neutrino Searches of All Flavors. *ArXiv e-prints*, September 2013.

IceCube Collaboration, M. G. Aartsen, M. Ackermann, J. Adams, J. A. Aguilar, M. Ahlers, M. Ahrens, I. A. Samarai, D. Altmann, K. Andeen, and et al. The IceCube Neutrino Observatory - Contributions to ICRC 2017 Part II: Properties of the Atmospheric and Astrophysical Neutrino Flux. *ArXiv e-prints*, October 2017a.

IceCube Collaboration, M. G. Aartsen, M. Ackermann, J. Adams, J. A. Aguilar, M. Ahlers, M. Ahrens, I. A. Samarai, D. Altmann, K. Andeen, and et al. The IceCube Neutrino Observatory - Contributions to ICRC 2017 Part I: Searches for the Sources of Astrophysical Neutrinos. *ArXiv e-prints*, October 2017b.

IceCube Collaboration, M. G. Aartsen, M. Ackermann, J. Adams, J. A. Aguilar, M. Ahlers, M. Ahrens, I. Al Samarai, D. Altmann, K. Andeen, and et al. Multimessenger observations of a flaring blazar coincident with high-energy neutrino IceCube-170922A. *Science*, 361: eaat1378, July 2018a. doi: 10.1126/science.aat1378.

IceCube Collaboration, M. G. Aartsen, M. Ackermann, J. Adams, J. A. Aguilar, M. Ahlers, M. Ahrens, I. A. Samarai, D. Altmann, K. Andeen, and et al. Neutrino emission from the direction of the blazar TXS 0506+056 prior to the IceCube-170922A alert. *Science*, 361: 147–151, July 2018b. doi: 10.1126/science.aat2890.

S. Ichimaru. Bimodal behavior of accretion disks - Theory and application to Cygnus X-1 transitions. *Astrophysical Journal*, 214:840–855, June 1977. doi: 10.1086/155314.

G. Ingelman and M. Thunman. Particle Production in the Interstellar Medium. *ArXiv High Energy Physics - Phenomenology e-prints*, April 1996.

J. C. Joshi, W. Winter, and N. Gupta. How many of the observed neutrino events can be described by cosmic ray interactions in the Milky Way? *Monthly Notices of the RAS*, 439: 3414–3419, April 2014. doi: 10.1093/mnras/stu189.

M. Kachelriess and S. Ostapchenko. Neutrino yield from Galactic cosmic rays. *Physical Review D*, 90(8):083002, October 2014. doi: 10.1103/PhysRevD.90.083002.

A. Karle and for the IceCube Collaboration. IceCube - status and recent results. *ArXiv e-prints*, January 2014.

N. Karlsson and for the VERITAS collaboration. Discovery of VHE Gamma-ray Emission from the Starburst Galaxy M82. *ArXiv e-prints*, December 2009.

J. I. Katz. X-rays from spherical accretion onto degenerate dwarfs. *Astrophysical Journal*, 215:265–275, July 1977. doi: 10.1086/155355.

A. Keivani, K. Murase, M. Petropoulou, D. B. Fox, S. B. Cenko, S. Chaty, A. Coleiro, J. J. DeLaunay, S. Dimitrakoudis, P. A. Evans, J. A. Kennea, F. E. Marshall, A. Mastichiadis, J. P. Osborne, M. Santander, A. Tohuvavohu, and C. F. Turley. A Multimessenger Picture of the Flaring Blazar TXS 0506+056: implications for High-Energy Neutrino Emission and Cosmic Ray Acceleration. *ArXiv e-prints*, July 2018.

K. I. Kellermann, R. C. Vermeulen, J. A. Zensus, and M. H. Cohen. Sub-Milliarcsecond Imaging of Quasars and Active Galactic Nuclei. *Astrophysical Journal*, 115:1295–1318, April 1998. doi: 10.1086/300308.

S. R. Kelner and F. A. Aharonian. Energy spectra of gamma rays, electrons, and neutrinos produced at interactions of relativistic protons with low energy radiation. *Physical Review D*, 78(3):034013, August 2008. doi: 10.1103/PhysRevD.78.034013.

S. R. Kelner, F. A. Aharonian, and V. V. Bugayov. Energy spectra of gamma rays, electrons, and neutrinos produced at proton-proton interactions in the very high energy regime. *Physical Review D*, 74(3):034018, August 2006. doi: 10.1103/PhysRevD.74.034018.

S. S. Kimura, K. Murase, and K. Toma. Neutrino and Cosmic-Ray Emission and Cumulative Background from Radiatively Inefficient Accretion Flows in Low-luminosity Active Galactic Nuclei. *Astrophysical Journal*, 806:159, June 2015. doi: 10.1088/0004-637X/806/2/159.

S. S. Komissarov. A theoretical model of Fanaroff-Riley I jets. *Astrophysics and Space Science*, 171:105–114, September 1990. doi: 10.1007/BF00646828.

C. Kopper, W. Giang, and N. Kurahashi. Observation of Astrophysical Neutrinos in Four Years of IceCube Data. In *34th International Cosmic Ray Conference (ICRC2015)*, volume 34 of *International Cosmic Ray Conference*, page 1081, July 2015.

Y. Y. Kovalev, M. L. Lister, D. C. Homan, and K. I. Kellermann. The Inner Jet of the Radio Galaxy M87. *Astrophysical Journal Letter*, 668:L27–L30, October 2007. doi: 10.1086/522603.

M. Kowalski. Status of High-Energy Neutrino Astronomy. In *Journal of Physics Conference Series*, volume 632 of *Journal of Physics Conference Series*, page 012039, August 2015. doi: 10.1088/1742-6596/632/1/012039.

B. C. Lacki, T. A. Thompson, E. Quataert, A. Loeb, and E. Waxman. On the GeV and TeV Detections of the Starburst Galaxies M82 and NGC 253. *Astrophysical Journal*, 734:107, June 2011. doi: 10.1088/0004-637X/734/2/107.

R. A. Laing. Relativistic flow in low luminosity radio jets. In R. J. Davis and R. S. Booth, editors, *Sub-arcsecond Radio Astronomy*, page 346, 1993.

A. Lamastra, F. Fiore, D. Guetta, L. A. Antonelli, S. Colafrancesco, N. Menci, S. Puccetti, A. Stamerra, and L. Zappacosta. Galactic outflow driven by the active nucleus and the origin of the gamma-ray emission in NGC 1068. *Astronomy and Astrophysics*, 596:A68, December 2016. doi: 10.1051/0004-6361/201628667.

M. Landoni, R. Falomo, A. Treves, B. Sbarufatti, M. Barattini, R. Decarli, and J. Kotilainen. ESO Very Large Telescope Optical Spectroscopy of BL Lacertae Objects. IV. New Spectra and Properties of the Full Sample. *Astronomical Journal*, 145:114, April 2013. doi: 10.1088/0004-6256/145/4/114.

J. G. Learned and S. Pakvasa. Detecting $\nu_?$ oscillations at PeV energies. *Astroparticle Physics*, 3:267–274, May 1995. doi: 10.1016/0927-6505(94)00043-3.

P. Lipari. Cosmic ray astrophysics and hadronic interactions. *Nuclear Physics B Proceedings Supplements*, 122:133–148, July 2003. doi: 10.1016/S0920-5632(03)80370-5.

R.-Y. Liu, X.-Y. Wang, S. Inoue, R. Crocker, and F. Aharonian. Diffuse PeV neutrinos from EeV cosmic ray sources: Semirelativistic hypernova remnants in star-forming galaxies. *Physical Review D*, 89(8):083004, April 2014. doi: 10.1103/PhysRevD.89.083004.

A. Loeb and E. Waxman. The cumulative background of high energy neutrinos from starburst galaxies. *Journal of Cosmology and Astroparticle Physics*, 5:003, May 2006. doi: 10.1088/1475-7516/2006/05/003.

M. S. Longair. *High Energy Astrophysics*. February 2011.

F. Lucarelli, C. Pittori, F. Verrecchia, I. Donnarumma, M. Tavani, A. Bulgarelli, A. Giuliani, L. A. Antonelli, P. Caraveo, P. W. Cattaneo, S. Colafrancesco, F. Longo, S. Mereghetti, A. Morselli, L. Pacciani, G. Piano, A. Pellizzoni, M. Pilia, A. Rappoldi, A. Trois, and S. Vercellone. AGILE Detection of a Candidate Gamma-Ray Precursor to the ICECUBE-160731 Neutrino Event. *Astrophysical Journal*, 846:121, September 2017a. doi: 10.3847/1538-4357/aa81c8.

F. Lucarelli, C. Pittori, F. Verrecchia, S. Vercellone, A. Bulgarelli, M. Tavani, P. Munar-Adrover, G. Minervini, G. Piano, A. Ursi, I. Donnarumma, V. Fioretti, A. Zoli, E. Striani, M. Cardillo, F. Gianotti, M. Trifoglio, A. Giuliani, S. Mereghetti, P. Caraveo, F. Perotti, A. Chen, A. Argan, E. Costa, E. Del Monte, Y. Evangelista, M. Feroci, F. Lazzarotto, I. Lapshov, L. Pacciani, P. Soffitta, S. Sabatini, V. Vittorini, G. Pucella, M. Rapisarda, G. Di Cocco, F. Fuschino, M. Galli, C. Labanti, M. Marisaldi, A. Pellizzoni, M. Pilia, A. Trois, G. Barbiellini, E. Vallazza, F. Longo, A. Morselli, P. Picozza, M. Prest, P. Lipari, D. Zanello, P. W. Cattaneo, A. Rappoldi, S. Colafrancesco, N. Parmiggiani, A. Ferrari, F. Paoletti, A. Antonelli, P. Giommi, L. Salotti, G. Valentini, and F. D'Amico. AGILE confirmation of enhanced gamma-ray activity from NGC 1275. *The Astronomer's Telegram*, 9934, January 2017b.

C. Lunardini and S. Razzaque. High Energy Neutrinos from the Fermi Bubbles. *Physical Review Letters*, 108(22):221102, June 2012. doi: 10.1103/PhysRevLett.108.221102.

C. Lunardini, S. Razzaque, K. T. Theodoseau, and L. Yang. Neutrino events at IceCube and the Fermi bubbles. *Physical Review D*, 90(2):023016, July 2014. doi: 10.1103/PhysRevD.90.023016.

C. Lunardini, S. Razzaque, and L. Yang. Multimessenger study of the Fermi bubbles: Very high energy gamma rays and neutrinos. *Physical Review D*, 92(2):021301, July 2015. doi: 10.1103/PhysRevD.92.021301.

D. Lynden-Bell and J. E. Pringle. The evolution of viscous discs and the origin of the nebular variables. *Monthly Notices of the RAS*, 168:603–637, September 1974. doi: 10.1093/mnras/168.3.603.

R. Mahadevan. Scaling Laws for Advection-dominated Flows: Applications to Low-Luminosity Galactic Nuclei. *Astrophysical Journal*, 477:585–601, March 1997. doi: 10.1086/303727.

K. Mannheim. γ rays and neutrinos from a powerful cosmic accelerator. *Physical Review D*, 48:2408–2414, September 1993. doi: 10.1103/PhysRevD.48.2408.

K. Mannheim and P. L. Biermann. Gamma-ray flaring of 3C 279 - A proton-initiated cascade in the jet? *Astronomy and Astrophysics*, 253:L21–L24, January 1992.

L. Maraschi, G. Ghisellini, and A. Celotti. A jet model for the gamma-ray emitting blazar 3C 279. *Astrophysical Journal, Letter*, 397:L5–L9, September 1992. doi: 10.1086/186531.

A. Margiotta. The KM3NeT deep-sea neutrino telescope. *Nuclear Instruments and Methods in Physics Research A*, 766:83–87, December 2014. doi: 10.1016/j.nima.2014.05.090.

A. Marscher. Variability of Blazars and Blazar Models over 38 Years. *Galaxies*, 4:37, September 2016. doi: 10.3390/galaxies4040037.

P. Mertsch and S. Sarkar. Fermi Gamma-Ray "Bubbles" from Stochastic Acceleration of Electrons. *Physical Review Letters*, 107(9):091101, August 2011. doi: 10.1103/PhysRevLett.107.091101.

P. Mertsch, M. Rameez, and I. Tamborra. Detection prospects for high energy neutrino sources from the anisotropic matter distribution in the local Universe. *Journal of Cosmology and Astroparticle Physics*, 3:011, March 2017. doi: 10.1088/1475-7516/2017/03/011.

P. Mészáros. Astrophysical Sources of High-Energy Neutrinos in the IceCube Era. *Annual Review of Nuclear and Particle Science*, 67:45–67, October 2017. doi: 10.1146/annurev-nucl-101916-123304.

J. S. Miller and B. F. Goodrich. Multi-directional Views of the Nucleus of NGC 1068. In *Bulletin of the American Astronomical Society*, volume 18 of *Bulletin of the AAS*, page 1001, September 1986.

R. Mirzoyan. MAGIC detection of a giant flaring activity from NGC 1275 at very-high-energy gamma rays. *The Astronomer's Telegram*, 9929, January 2017.

A. Mücke and R. J. Protheroe. A proton synchrotron blazar model for flaring in Markarian 501. *Astroparticle Physics*, 15:121–136, March 2001. doi: 10.1016/S0927-6505(00)00141-9.

A. Mücke, R. J. Protheroe, R. Engel, J. P. Rachen, and T. Stanev. BL Lac objects in the synchrotron proton blazar model. *Astroparticle Physics*, 18:593–613, March 2003. doi: 10.1016/S0927-6505(02)00185-8.

K. Murase. High energy neutrino early afterglows from gamma-ray bursts revisited. *Physical Review D*, 76(12):123001, December 2007. doi: 10.1103/PhysRevD.76.123001.

K. Murase and K. Ioka. TeV-PeV Neutrinos from Low-Power Gamma-Ray Burst Jets inside Stars. *Physical Review Letters*, 111(12):121102, September 2013. doi: 10.1103/PhysRevLett.111.121102.

K. Murase and E. Waxman. Constraining high-energy cosmic neutrino sources: Implications and prospects. *Physical Review D*, 94(10):103006, November 2016. doi: 10.1103/PhysRevD.94.103006.

K. Murase, Y. Inoue, and C. D. Dermer. Diffuse neutrino intensity from the inner jets of active galactic nuclei: Impacts of external photon fields and the blazar sequence. *Physical Review D*, 90(2):023007, July 2014. doi: 10.1103/PhysRevD.90.023007.

K. Murase, D. Guetta, and M. Ahlers. Hidden Cosmic-Ray Accelerators as an Origin of TeV-PeV Cosmic Neutrinos. *Physical Review Letters*, 116(7):071101, February 2016. doi: 10.1103/PhysRevLett.116.071101.

K. Murase, F. Oikonomou, and M. Petropoulou. Blazar Flares as an Origin of High-Energy Cosmic Neutrinos? *ArXiv e-prints*, July 2018.

H. Nagai, T. Haga, G. Giovannini, A. Doi, M. Orienti, F. D'Ammando, M. Kino, M. Nakamura, K. Asada, K. Hada, and M. Giroletti. Limb-brightened Jet of 3C 84 Revealed by the 43 GHz Very-Long-Baseline-Array Observation. *Astrophysical Journal*, 785:53, April 2014. doi: 10.1088/0004-637X/785/1/53.

R. Narayan and I. Yi. Advection-dominated accretion: A self-similar solution. *Astrophysical Journal, Letters*, 428:L13–L16, June 1994. doi: 10.1086/187381.

R. Narayan and I. Yi. Advection-dominated accretion: Self-similarity and bipolar outflows. *Astrophysical Journal*, 444:231–243, May 1995a. doi: 10.1086/175599.

R. Narayan and I. Yi. Advection-dominated Accretion: Underfed Black Holes and Neutron Stars. *Astrophysical Journal*, 452:710, October 1995b. doi: 10.1086/176343.

L. Nellen, K. Mannheim, and P. L. Biermann. Neutrino production through hadronic cascades in AGN accretion disks. *Physical Review D*, 47:5270–5274, June 1993. doi: 10.1103/PhysRevD.47.5270.

R. S. Nemmen, M. Georganopoulos, S. Guiriec, E. T. Meyer, N. Gehrels, and R. M. Sambruna. A Universal Scaling for the Energetics of Relativistic Jets from Black Hole Systems. *Science*, 338:1445, December 2012. doi: 10.1126/science.1227416.

M. Nenkova, Ž. Ivezić, and M. Elitzur. Dust Emission from Active Galactic Nuclei. *Astrophysical Journal, Letters*, 570:L9–L12, May 2002. doi: 10.1086/340857.

A. Neronov and M. Ribordy. IceCube sensitivity for neutrino flux from Fermi blazars in quiescent states. *Physical Review D*, 80(8):083008, October 2009. doi: 10.1103/PhysRevD.80.083008.

H. M. Niederhausen, M. Lesiak-Bzdak, and A. Stoessl. High energy astrophysical neutrino flux characteristics for neutrino-induced cascades using IC79 and IC86-string IceCube conf. In *34th International Cosmic Ray Conference (ICRC2015)*, volume 34 of *International Cosmic Ray Conference*, page 1109, July 2015.

I. D. Novikov and K. S. Thorne. Astrophysics of black holes. In C. Dewitt and B. S. Dewitt, editors, *Black Holes (Les Astres Occlus)*, pages 343–450, 1973.

F. N. Owen, P. E. Hardee, and T. J. Cornwell. High-resolution, high dynamic range VLA images of the M87 jet at 2 centimeters. *Astrophysical Journal*, 340:698–707, May 1989. doi: 10.1086/167430.

P. Padovani. The blazar sequence: validity and predictions. *Astrophysics and Space Science*, 309:63–71, June 2007. doi: 10.1007/s10509-007-9455-2.

P. Padovani, P. Giommi, and A. Rau. The discovery of high-power high synchrotron peak blazars. *Monthly Notices of the RAS*, 422:L48–L52, May 2012. doi: 10.1111/j.1745-3933.2012.01234.x.

P. Padovani, E. Resconi, P. Giommi, B. Arsioli, and Y. L. Chang. Extreme blazars as counterparts of IceCube astrophysical neutrinos. *Monthly Notices of the RAS*, 457:3582–3592, April 2016. doi: 10.1093/mnras/stw228.

P. Padovani, P. Giommi, E. Resconi, T. Glauch, B. Arsioli, N. Sahakyan, and M. Huber. Dissecting the region around IceCube-170922A: the blazar TXS 0506+056 as the first cosmic neutrino source. *Monthly Notices of the RAS*, 480:192–203, October 2018. doi: 10.1093/mnras/sty1852.

S. Paiano, M. Landoni, R. Falomo, A. Treves, R. Scarpa, and C. Righi. On the Redshift of TeV BL Lac Objects. *Astrophysical Journal*, 837:144, March 2017. doi: 10.3847/1538-4357/837/2/144.

S. Paiano, R. Falomo, A. Treves, and R. Scarpa. The Redshift of the BL Lac Object TXS 0506+056. *Astrophysical Journal, Letters*, 854:L32, February 2018. doi: 10.3847/2041-8213/aaad5e.

A. Palladino. A multi-component model for the IceCube neutrino events. *ArXiv e-prints*, July 2017.

A. Palladino and F. Vissani. Extragalactic plus Galactic Model for IceCube Neutrino Events. *Astrophysical Journal*, 826:185, August 2016. doi: 10.3847/0004-637X/826/2/185.

A. Palladino and W. Winter. A multi-component model for observed astrophysical neutrinos. *Astronomy and Astrophysics*, 615:A168, August 2018. doi: 10.1051/0004-6361/201832731.

E. S. Perlman, C. A. Padgett, M. Georganopoulos, D. M. Worrall, J. H. Kastner, G. Franz, M. Birkinshaw, F. Dulwich, C. P. O'Dea, S. A. Baum, W. B. Sparks, J. A. Biretta, L. Lara, S. Jester, and A. Martel. A Multi-Wavelength Spectral and Polarimetric Study of the Jet of 3C 264. *Astrophysical Journal*, 708:171–187, January 2010. doi: 10.1088/0004-637X/708/1/171.

M. Petropoulou and A. Mastichiadis. Bethe-Heitler emission in BL Lacs: filling the gap between X-rays and γ-rays. *Monthly Notices of the RAS*, 447:36–48, February 2015. doi: 10.1093/mnras/stu2364.

M. Petropoulou, S. Dimitrakoudis, P. Padovani, A. Mastichiadis, and E. Resconi. Photohadronic origin of γ -ray BL Lac emission: implications for IceCube neutrinos. *Monthly Notices of the RAS*, 448:2412–2429, April 2015. doi: 10.1093/mnras/stv179.

M. Petropoulou, S. Coenders, and S. Dimitrakoudis. Time-dependent neutrino emission from Mrk 421 during flares and predictions for IceCube. *Astroparticle Physics*, 80:115–130, July 2016. doi: 10.1016/j.astropartphys.2016.04.001.

T. Piran, D. Guetta, and M. Rodriguez-Martinez. Gamma-Ray Bursts and New Physics. *Progress of Theoretical Physics Supplement*, 163:23–37, 2006. doi: 10.1143/PTPS.163.23.

C. M. Raiteri, F. Nicastro, A. Stamerra, M. Villata, V. M. Larionov, D. Blinov, J. A. Acosta-Pulido, M. J. Arévalo, A. A. Arkharov, R. Bachev, G. A. Borman, M. I. Carnerero, D. Carosati, M. Cecconi, W.-P. Chen, G. Damljanovic, A. Di Paola, S. A. Ehgamberdiev,

A. Frasca, M. Giroletti, P. A. González-Morales, A. B. Griñon-Marín, T. S. Grishina, P.-C. Huang, S. Ibryamov, S. A. Klimanov, E. N. Kopatskaya, O. M. Kurtanidze, S. O. Kurtanidze, A. Lähteenmäki, E. G. Larionova, L. V. Larionova, C. Lázaro, G. Leto, I. Liodakis, C. Martínez-Lombilla, B. Mihov, D. O. Mirzaqulov, A. A. Mokrushina, J. W. Moody, D. A. Morozova, S. V. Nazarov, M. G. Nikolashvili, J. M. Ohlert, G. V. Panopoulou, A. Pastor Yabar, F. Pinna, C. Protasio, N. Rizzi, A. C. Sadun, S. S. Savchenko, E. Semkov, L. A. Sigua, L. Slavcheva-Mihova, A. Strigachev, M. Tornikoski, Y. V. Troitskaya, I. S. Troitsky, A. A. Vasilyev, R. J. C. Vera, O. Vince, and R. Zanmar Sanchez. Synchrotron emission from the blazar PG 1553+113. An analysis of its flux and polarization variability. *Monthly Notices of the RAS*, 466:3762–3774, April 2017. doi: 10.1093/mnras/stw3333.

S. Razzaque. Galactic Center origin of a subset of IceCube neutrino events. *Physical Review D*, 88(8):081302, October 2013. doi: 10.1103/PhysRevD.88.081302.

S. Razzaque, P. Mészáros, and E. Waxman. High Energy Neutrinos from Gamma-Ray Bursts with Precursor Supernovae. *Physical Review Letters*, 90(24):241103, June 2003. doi: 10.1103/PhysRevLett.90.241103.

M. J. Rees. Appearance of Relativistically Expanding Radio Sources. *Nature*, 211:468–470, July 1966. doi: 10.1038/211468a0.

M. Ribordy. Methods and problems in neutrino observatories. *ArXiv e-prints*, May 2012.

C. Righi and F. Tavecchio. On the detectability of BL Lac objects by IceCube. *ArXiv e-prints*, August 2017.

C. Righi, F. Tavecchio, and D. Guetta. High-energy emitting BL Lacs and high-energy neutrinos. Prospects for the direct association with IceCube and KM3NeT. *Astronomy & Astrophysics*, 598:A36, February 2017. doi: 10.1051/0004-6361/201629412.

C. Righi, F. Tavecchio, and S. Inoue. Neutrino emission from BL Lac objects: the role of radiatively inefficient accretion flows. *ArXiv e-prints*, July 2018a.

C. Righi, F. Tavecchio, and L. Pacciani. A multiwavelength view of BL Lacs neutrino candidates. *ArXiv e-prints*, July 2018b.

P. W. A. Roming, T. E. Kennedy, K. O. Mason, J. A. Nousek, L. Ahr, R. E. Bingham, P. S. Broos, M. J. Carter, B. K. Hancock, H. E. Huckle, S. D. Hunsberger, H. Kawakami, R. Killough, T. S. Koch, M. K. McLelland, K. Smith, P. J. Smith, J. C. Soto, P. T. Boyd, A. A. Breeveld, S. T. Holland, M. Ivanushkina, M. S. Pryzby, M. D. Still, and J. Stock. The Swift Ultra-Violet/Optical Telescope. *Space Science Reviews*, 120:95–142, October 2005. doi: 10.1007/s11214-005-5095-4.

P. Rossi, A. Mignone, G. Bodo, S. Massaglia, and A. Ferrari. Formation of dynamical structures in relativistic jets: the FRI case. *Astronomy & Astrophysics*, 488:795–806, September 2008. doi: 10.1051/0004-6361:200809687.

G. B. Rybicki and A. P. Lightman. *Radiative Processes in Astrophysics*. June 1986.

N. Sahakyan. Lepto-hadronic γ-ray and neutrino emission from the jet of TXS 0506+056. *ArXiv e-prints*, August 2018.

R. M. Sambruna, C. M. Urry, G. Ghisellini, and L. Maraschi. Spectral Variability of the X-Ray–bright BL Lacertae Object PKS 2005-489. *Astrophysical Journal*, 449:567, August 1995. doi: 10.1086/176080.

R. M. Sambruna, M. Gliozzi, D. Donato, L. Maraschi, F. Tavecchio, C. C. Cheung, C. M. Urry, and J. F. C. Wardle. Deep Chandra and Multicolor HST Follow-up of the Jets in Two Powerful Radio Quasars. *Astrophysical Journal*, 641:717–731, April 2006. doi: 10.1086/500526.

T. Sbarrato, P. Padovani, and G. Ghisellini. The jet-disc connection in AGN. *Monthly Notices of the RAS*, 445:81–92, November 2014. doi: 10.1093/mnras/stu1759.

D. J. Schlegel, D. P. Finkbeiner, and M. Davis. Maps of Dust Infrared Emission for Use in Estimation of Reddening and Cosmic Microwave Background Radiation Foregrounds. *Astrophysical Journal*, 500:525–553, June 1998. doi: 10.1086/305772.

N. Senno, P. Mészáros, K. Murase, P. Baerwald, and M. J. Rees. Extragalactic Star-forming Galaxies with Hypernovae and Supernovae as High-energy Neutrino and Gamma-ray Sources: the case of the 10 TeV Neutrino data. *Astrophysical Journal*, 806:24, June 2015. doi: 10.1088/0004-637X/806/1/24.

C. K. Seyfert. New Emission Objects. *Publications of the ASP*, 59:35–36, February 1947. doi: 10.1086/125897.

N. I. Shakura and R. A. Sunyaev. Black holes in binary systems. Observational appearance. *Astronomy and Astrophysics*, 24:337–355, 1973.

S. L. Shapiro, A. P. Lightman, and D. M. Eardley. A two-temperature accretion disk model for Cygnus X-1 - Structure and spectrum. *Astrophysical Journal*, 204:187–199, February 1976. doi: 10.1086/154162.

M. Sikora, M. C. Begelman, and M. J. Rees. Comptonization of diffuse ambient radiation by a relativistic jet: The source of gamma rays from blazars? *Astrophysical Journal*, 421: 153–162, January 1994. doi: 10.1086/173633.

M. F. Skrutskie, R. M. Cutri, R. Stiening, M. D. Weinberg, S. Schneider, J. M. Carpenter, C. Beichman, R. Capps, T. Chester, J. Elias, J. Huchra, J. Liebert, C. Lonsdale, D. G. Monet, S. Price, P. Seitzer, T. Jarrett, J. D. Kirkpatrick, J. E. Gizis, E. Howard, T. Evans, J. Fowler, L. Fullmer, R. Hurt, R. Light, E. L. Kopan, K. A. Marsh, H. L. McCallon, R. Tam, S. Van Dyk, and S. Wheelock. The Two Micron All Sky Survey (2MASS). *Astronomical Journal*, 131:1163–1183, February 2006. doi: 10.1086/498708.

M. Stalevski, J. Fritz, M. Baes, T. Nakos, and L. Č. Popović. 3D radiative transfer modelling of the dusty tori around active galactic nuclei as a clumpy two-phase medium. *Monthly Notices of the RAS*, 420:2756–2772, March 2012. doi: 10.1111/j.1365-2966.2011.19775.x.

F. W. Stecker. Diffuse fluxes of cosmic high-energy neutrinos. *Astrophysical Journal*, 228: 919–927, March 1979. doi: 10.1086/156919.

F. W. Stecker, C. Done, M. H. Salamon, and P. Sommers. High-energy neutrinos from active galactic nuclei. *Physical Review Letters*, 66:2697–2700, May 1991. doi: 10.1103/PhysRevLett.66.2697.

M. Su, T. R. Slatyer, and D. P. Finkbeiner. Giant Gamma-ray Bubbles from Fermi-LAT: Active Galactic Nucleus Activity or Bipolar Galactic Wind? *Astrophysical Journal*, 724: 1044–1082, December 2010. doi: 10.1088/0004-637X/724/2/1044.

M. R. Swain, A. H. Bridle, and S. A. Baum. Internal Structure of the Jets in 3C 353. *Astrophysical Journal, Letters*, 507:L29–L33, November 1998. doi: 10.1086/311663.

I. Tamborra, S. Ando, and K. Murase. Star-forming galaxies as the origin of diffuse high-energy backgrounds: gamma-ray and neutrino connections, and implications for starburst history. *Journal of Cosmology and Astroparticle Physics*, 9:043, September 2014. doi: 10.1088/1475-7516/2014/09/043.

F. Tavecchio. Gamma rays from blazars. In *6th International Symposium on High Energy Gamma-Ray Astronomy*, volume 1792 of *American Institute of Physics Conference Series*, page 020007, January 2017. doi: 10.1063/1.4968892.

F. Tavecchio and G. Ghisellini. High-energy cosmic neutrinos from spine-sheath BL Lac jets. *Monthly Notices of the RAS*, 451:1502–1510, August 2015. doi: 10.1093/mnras/stv1023.

F. Tavecchio and G. Ghisellini. On the magnetization of BL Lac jets. *Monthly Notices of the RAS*, 456:2374–2382, March 2016. doi: 10.1093/mnras/stv2790.

F. Tavecchio, L. Maraschi, and G. Ghisellini. Constraints on the Physical Parameters of TeV Blazars. *Astrophysical Journal*, 509:608–619, December 1998. doi: 10.1086/306526.

F. Tavecchio, G. Ghisellini, G. Bonnoli, and G. Ghirlanda. Constraining the location of the emitting region in Fermi blazars through rapid γ-ray variability. *Monthly Notices of the RAS*, 405:L94–L98, June 2010. doi: 10.1111/j.1745-3933.2010.00867.x.

F. Tavecchio, G. Ghisellini, and D. Guetta. Structured Jets in BL Lac Objects: Efficient PeV Neutrino Factories? *Astrophysical Journal, Letters*, 793:L18, September 2014. doi: 10.1088/2041-8205/793/1/L18.

F. Tavecchio, C. Righi, A. Capetti, P. Grandi, and G. Ghisellini. High-energy neutrinos from FR0 radio galaxies? *Monthly Notices of the RAS*, 475:5529–5534, April 2018. doi: 10.1093/mnras/sty251.

A. Tchekhovskoy, R. Narayan, and J. C. McKinney. Efficient generation of jets from magnetically arrested accretion on a rapidly spinning black hole. *Monthly Notices of the RAS*, 418:L79–L83, November 2011. doi: 10.1111/j.1745-3933.2011.01147.x.

The IceCube Collaboration, M. G. Aartsen, K. Abraham, M. Ackermann, J. Adams, J. A. Aguilar, M. Ahlers, M. Ahrens, D. Altmann, T. Anderson, and et al. The IceCube Neutrino Observatory - Contributions to ICRC 2015 Part I: Point Source Searches. *ArXiv e-prints*, October 2015a.

The IceCube Collaboration, M. G. Aartsen, K. Abraham, M. Ackermann, J. Adams, J. A. Aguilar, M. Ahlers, M. Ahrens, D. Altmann, T. Anderson, and et al. The IceCube Neutrino Observatory - Contributions to ICRC 2015 Part II: Atmospheric and Astrophysical Diffuse Neutrino Searches of All Flavors. *ArXiv e-prints*, October 2015b.

T. A. Thompson, E. Quataert, E. Waxman, N. Murray, and C. L. Martin. Magnetic Fields in Starburst Galaxies and the Origin of the FIR-Radio Correlation. *Astrophysical Journal*, 645:186–198, July 2006. doi: 10.1086/504035.

C. M. Urry. An Overview of Blazar Variability. In H. R. Miller, J. R. Webb, and J. C. Noble, editors, *Blazar Continuum Variability*, volume 110 of *Astronomical Society of the Pacific Conference Series*, page 391, 1996.

C. M. Urry and P. Padovani. Unified Schemes for Radio-Loud Active Galactic Nuclei. *Publications of the ASP*, 107:803, September 1995. doi: 10.1086/133630.

D. vanden Berk, C. Yip, A. Connolly, S. Jester, and C. Stoughton. Luminosity and Redshift Dependence of Quasar Spectral Properties. In G. T. Richards and P. B. Hall, editors, *AGN Physics with the Sloan Digital Sky Survey*, volume 311 of *Astronomical Society of the Pacific Conference Series*, page 21, June 2004.

M. Vietri. The Acceleration of Ultra–High-Energy Cosmic Rays in Gamma-Ray Bursts. *Astrophysical Journal*, 453:883, November 1995. doi: 10.1086/176448.

F. Vissani, G. Pagliaroli, and F. L. Villante. The fraction of muon tracks in cosmic neutrinos. *Journal of Cosmology and Astroparticle Physics*, 9:017, September 2013. doi: 10.1088/1475-7516/2013/09/017.

L. V. Volkova. Energy Spectra and Angular Distributions of Atmospheric Neutrinos. *Soviet Journal of Nuclear Physics*, 31, 1980.

K. Wang, R.-Y. Liu, Z. Li, X.-Y. Wang, and Z.-G. Dai. Jet-cloud/star interaction as an interpretation of neutrino outburst from the blazar TXS 0506+056. *ArXiv e-prints*, September 2018.

E. Waxman. Cosmological Gamma-Ray Bursts and the Highest Energy Cosmic Rays. *Physical Review Letters*, 75:386–389, July 1995. doi: 10.1103/PhysRevLett.75.386.

E. Waxman and J. Bahcall. High Energy Neutrinos from Cosmological Gamma-Ray Burst Fireballs. *Physical Review Letters*, 78:2292–2295, March 1997. doi: 10.1103/PhysRevLett.78.2292.

E. Waxman and J. Bahcall. High energy neutrinos from astrophysical sources: An upper bound. *Physical Review D*, 59(2):023002, January 1999. doi: 10.1103/PhysRevD.59.023002.

D. Xu and for the IceCube Collaboration. Search for Astrophysical Tau Neutrinos with IceCube. *ArXiv e-prints*, February 2017.

L. Yacobi, D. Guetta, and E. Behar. Constraints on the Hadronic Content of Gamma Ray Bursts. *Astrophysical Journal*, 793:48, September 2014. doi: 10.1088/0004-637X/793/1/48.

R.-z. Yang, F. Aharonian, and R. Crocker. The Fermi bubbles revisited. *Astronomy and Astrophysics*, 567:A19, July 2014. doi: 10.1051/0004-6361/201423562.

F. Yuan and R. Narayan. Hot Accretion Flows Around Black Holes. *Annual Review of Astron and Astrophys*, 52:529–588, August 2014. doi: 10.1146/annurev-astro-082812-141003.

M. Zacharias. Time-dependent injection as a model for rapid blazar flares. In *34th International Cosmic Ray Conference (ICRC2015)*, volume 34 of *International Cosmic Ray Conference*, page 903, July 2015.

Acknowledgements

Finalmente arriva il momento di ringraziare. Questi tre anni sono stati pieni di esperienze, che mi hanno portato a crescere dal punto di vista scientifico, ma sopratutto personale. E di persone da ringraziare ce ne sono davvero tante. Prima di tutto vorrei ringraziare di cuore il mio relatore Fabrizio, da cui non si smette mai di imparare e che mi ha permesso di fare molte esperienze durante tutto il periodo del dottorato. Insieme a lui devo ringraziare Gabriele che é stata una figura paterna anche fuori dal lavoro. Un ringraziamento va a tutto il gruppo di Alte Energie, al gruppo del Golem ed in generale a tutte le persone che ho avuto modo di conoscere all'interno dell'Osservatorio di Brera. Un grazie speciale alla foresteria ed a tutti gli amici che sono passati di li di cui conservo bellissimi ricordi. Grazie anche agli amici di Genova, che mi hanno sempre accolto i weekend in cui tornavo a casa e che mi hanno sopportato durante le mie perenni lamentele.